Title

Next Generation Membranes for Selective Water Purification

Author

Anderson, Mackenzie Babetta

Publication Date

2022

UNIVERSITY OF CALIFORNIA

Los Angeles

Next Generation Membranes for Selective Water Purification

A dissertation submitted in partial satisfaction of the

requirements for the degree Doctor of Philosophy

in Chemistry

by

Mackenzie Babetta Anderson

2022

ABSTRACT OF THE DISSERTATION

Next Generation Membranes for Selective Water Purification

by

Mackenzie Babetta Anderson

Doctor of Philosophy in Chemistry

University of California, Los Angeles

Professor Richard B. Kaner, Chair

This body of work addresses the ways in which water interacts with materials on a molecular scale and the scalable fabrication of membranes for water purification applications.

Threats to water security including global population growth, climate change, environmental pollution, and decades of unsustainable water usage making the generation of new freshwater sources imperative. Seawater desalination along with beneficial purification and reuse of municipal, agricultural, and industrial wastewaters is crucial to achieve water-stress alleviation.

These aqueous separations are now almost universally achieved using reverse osmosis (RO) membrane technology, which offers lower energy and cost than thermal distillation technologies; and hence, RO is now widely deployed throughout the world in these applications. Still, there is a lot of interest in improving the performance of RO membrane processes through engineering, and membrane capabilities through materials science. Better materials could improve liquid and solid recovery from complex aqueous and non-aqueous solutions and overcome some of the ongoing problems facing membrane operations.

In particular, improved membrane materials can help reduce the cost, extend the lifespan, and broaden the applicability of membrane processes for water recovery. Not only can new materials be better suited for removal of a particular solute and have particular selectivity, but the robustness (chemical and physical) of membranes can be improved to reduce the amount of pre-treatment and membrane passes required to generate potable water. Chapter 1 of this work, addresses one approach to these challenges taken by developing a new membrane fabrication technique that enables the employment of almost any functional material as a membrane active layer. An in-depth discussion of the development of support-layer chemistry to resist compaction and optimization of support layer chemistry for the lift-off of thin films is provided.

Beginning with the development of this technique, advances were made in the use of epoxy-based membranes as both a supporting material for thin-film composite membranes and for standalone membranes. A demonstration of how porogens can be used while curing and their effect on the resulting microstructure of membranes is provided along with other factors relevant to the membrane industry such as flux, compaction, and solute removal. Chapter 2 builds on this chemistry through the development of "all-epoxy" membranes. A series of membranes are developed and using similar technology to that discussed in Chapter 1, are optimized to achieve high-performance nanofiltration membranes. A proposal for new, more sustainable membranes is made that utilizes our newly developed techniques and including monomers with reversible bonds.

Conjugated polymers have access to multiple charged states and are interesting in the development of salt-rejecting membranes. Unlike the nanofiltration membranes discussed in Chapter 2 where membrane selectivity is largely governed by the pore-flow model, reverse-osmosis membrane separation mechanisms are based on the solution-diffusion model, where a molecule's solubility in a dense membrane material in addition to its diffusivity determines the efficiency of its removal. Chelation effects, hydrogen bonding, and charge-charge interactions are all important components to the rejection mechanism of a membrane. There is still a lot of room for building an improved understanding of membrane separation mechanisms. By systematically tuning structure and performance of novel materials, mechanistic relationships between these and a physical understanding of transport through them can be elucidated.

Chapter 3 contains studies of active-layer materials, in particular, approaches to their fabrication and the surface properties that affect membrane performance. Polybenzimidazoles and Polyimides are difficult to process polymers, but of great interest due to their chemical tolerance. They produce very dense films and often highly crystalline networks. A number of membranes are made using these materials and some are tested for desalination of waters with different degrees of acidity. Correlations between interfacial surface tension components and rejection of NaCl at 0.20% NaCl and 3.5% NaCl, as well as the potential to predict the performance of particular materials using these correlations, are discussed.

Water treatment and energy go hand-in-hand. Membrane treatment requires large amounts of power and energy and the optimization of materials to reduce energy requirements have thermodynamic limits. Chapter 4 discusses the development of inexpensive electrochemical capacitors, utilizing many of the characterization techniques discussed earlier in this work.

In Chapter 5 of this work, a technique to create functionally graded materials is discussed. The method involves the casting of graphene-oxide films onto foils of metals that have different reduction potentials. The films then undergo graded conversion to reduced graphene oxide and the foil may be recovered for continued use. The electrochemical and actuation characteristics of these materials are discussed, but these novel methods of making functional materials are very important to creating scalable, roll-to-roll methods for fabricating materials for novel membranes.

The dissertation of Mackenzie Babetta Anderson is approved.

Shaily Mahendra

Paula Diaconsecu

Chong Liu

Richard B. Kaner, Committee Chair

University of California, Los Angeles

2022

Dedicated in Loving Memory

to

Mary Ellen Anderson (1927-2020)

TABLE OF CONTENTS

LIST OF FIGURES

LIST OF TABLES

ACKNOWLEDGEMENTS

Over the past 9 years of undergraduate and graduate study, I was able to work on an array of projects ranging from membrane fabrication, to photochemical modification of surfaces, to electrochemical capacitors. In the midst of all of this, I was developing as an individual and facing the challenges we are all uniquely dealt. In research, as in life, you need to be resilient and determined. When this was difficult, I was so fortunate as to have many people along the way providing advice and offering opportunities that got me here.

First of all, I thank my dad, Sean Anderson for loving me from the start and never letting me give in the face of failure or setbacks.

I thank Professor Veronica Jaramillo for giving me the opportunity to lead, develop my love of teaching, and remaining my mentor to this day. Without these experiences, I may not have found a home in science.

I want to thank Marc Baum and other Oak Crest Family for the 3+ years for the chance to pursue research as an undergrad, prepare for graduate school, and become more engaged in the local community.

I want to thank my go-to undergrad homies Kevin Swartz, Jesús Iñiguez, Zach Gvildys, Vince Aguirre, and Eugene Wong for spending endless hours studying and completing assignments and providing the best support system during those 4 years and beyond.

I am most incredibly grateful to Ric Kaner for welcoming me into his lab as a transfer student in 2015 and for continuing to support me and encourage me to excel as a scientist throughout my graduate career. Thank you to Eric Hoek for being an amazing resource throughout my graduate research and letting me chip in on so many different projects. Thank you to Paula Diaconescu for her amazing influence throughout both undergrad and graduate school. Thank you to Maher El Kady for giving me the opportunity to work hard, contribute to the Kaner Lab, and feel at home at UCLA back in 2015.

I want to thank Brian McVerry for introducing me to the field of membrane science, teaching me so much as an undergrad, encouraging me to create my own projects, and standing up for me always. Ignacio Martini, for being so supportive from the first time I learned SEM in 2016 through to today. Going way back, I want to thank Heather Audesirk for taking time away from Caltech to put up with us highschool students and for teaching me what grad school was and helping me discover that I could succeed at research, even when I felt I didn't belong.

I want to thank the entire Kaner Lab. Chris Turner, for being the most resourceful member of our group. Thanks to Na He, Ethan Rao, and Brian McVerry for being the greatest office trio over the years. Mitt Muni, for making the COVID lockdowns just a little better and always being willing to talk. Thank you to current and former members Reza Rizvi, Volker Strauss, Dayong Chen, Lisa Pangilinan, Cheng-Wei Lin, Matt Kowal, Shanlin Hu, Helen Huang, Xueying Chang, Chenxiang Wang, Haosen Wang, Francis Jimoh, and everyone else for creating such a positive lab atmosphere.

I want to thank Donald Argus for supporting me as I explored a new field and learned so many valuable skills during my time at JPL and JIFRESSEE.

I want to thank my dearest friends Yhardfah, Patricia, and Janty and my four legged family Pete, Phil, Crookshanks, Heisenberg, Feynman, and Master for their ongoing support.

Special thanks to my lovely undergraduate assistants Clayton, Riley, and Aryan.

This thesis is comprised of a number of works published and in preparation.

Chapter 1 includes work that is reprinted (adapted) with permission from McVerry, B., Anderson, M., He, N., Kweon, H., Ji, C., Xue, S., Rao, E., Lee, C., Lin, C.-W., Chen, D., Jun, D., Sant, G., & Kaner, R. B. (2019). Next-Generation Asymmetric Membranes Using Thin-Film Liftoff. *Nano Letters*. 19(8), 5036–5043. Copyright 2019 American Chemical Society

Chapter 1 includes work that is reprinted (adapted) with permission from Xue, S., Ji, C., Kowal, M. D., Molas, J. C., Lin, C.-W., McVerry, B. T., Turner, C. L., Mak, W. H., Anderson, M., Muni, M., V Hoek, E. M., Xu, Z.-L., & Kaner, R. B. (2020). Nanostructured Graphene Oxide Composite Membranes with Ultrapermeability and Mechanical Robustness. *Nano Letters*. 17, 31. Copyright 2020 American Chemical Society

Chapter 4 includes work that is reprinted (adapted) with permission from Strauss, V., Anderson, M., Turner, C. L., & Kaner, R. B. (2019). Fast response electrochemical capacitor electrodes created by laser-reduction of carbon nanodots. *Materials Today Energy*. 11, 114–119. Copyright 2019 Elsevier

Chapter 5 includes work that is reprinted (adapted) with permission from Bhatkar, O., Smith, D., Kowal, M. D., Anderson, M., Rizvi, R., & Kaner, R. B. (2019). Self-Assembled Functionally Graded Graphene Films with Tunable Compositions and Their Applications in Transient Electronics and Actuation. *ACS Applied Materials and Interfaces.*11, 2346-23473. Copyright 2018 American Chemical Society

VITAE

2017-2022	Graduate Student Researcher with Prof. Richard Kaner University of California, Los Angeles
2018- 2022	National Science Foundation Innovation at the Nexus of Food, Energy, and Water Systems Trainee University of California, Los Angeles
2021-2022	Year-Round Intern with Dr. Donald F. Argus NASA Jet Propulsion Laboratory
2020-2022	Adjunct Chemistry Instructor Pasadena City College
2017-2021	Teaching Assistant University of California, Los Angeles
2021	Chemistry and Biochemistry Dissertation year Fellowship University of California, Los Angeles
2020	Southern California Salinity Coalition Fellowship National Water Research Institute
2020	Joint Institute for Regional Earth System Science and Engineering Summer Intern University of California, Los Angeles
2020	Chemistry and Biochemistry Instructional Division Graduate Student Researcher University of California, Los Angeles
2019	Division 33: Communications, Tracking, and Radar Visiting Student Researcher NASA Jet Propulsion Laboratory Pasadena, California
2019	Honorable Mention National Science Foundation
2018	United Stated Bureau of Reclamation Fellowship American Membrane Technology Association
2015-2017	Research Associate/Analytical Chemist Oak Crest Institute of Science
	Undergraduate Research Fellow
2016-2017	University of California, Los Angeles
2015-2017	Bachelor of Science in Chemistry/Materials Science, Organic Materials Concentration University of California, Los Angeles
2016	Affordable Desalination Collaboration Fellowship American Membrane Technology Association
2015	Research Assistant Nanotech Energy
2015	Rose Hills Research Fellow Oak Crest Institute of Science
2013-2015	Associate in Arts in Natural Sciences Pasadena City College
2014-2015	Pasadena City College ACS Student Chapter Outreach Coordinator Pasadena, California
2014	Alice and Don Slater Memorial Scholarship Pasadena City College Foundation

LIST OF PUBLICATIONS

1. McVerry, B., Polasko, A., Rao, E., Haghniaz, R., Chen, D., He, N., Ramos, P., Hayashi, J., Curson, P., Wu, C.-Y., Bandaru, P., Anderson, M., Bui, B., Sayegh, A., Mahendra, S., Carlo, D. Di, Kreydin, E., Khademhosseini, A., Sheikhi, A., & Kaner, R. B. (**2022**). A Readily Scalable, Clinically Demonstrated, Antibiofouling Zwitterionic Surface Treatment for Implantable Medical Devices. *Advanced Materials*. 2200254.

2. Jishan Wu, by, Jung, B., Anvari, A., Im, S., Anderson, M., Zheng, X., Jassby, D., Kaner, R. B., Dlamini, D., Edalat, A., & Hoek, E. M. (**2022**). Reverse Osmosis Membrane Compaction and Embossing at Ultra-High Pressure Operation. *Desalination*. DES-D-22-00277.
3. Huang, A., El-Kady, M. F., Chang, X., Anderson, M., Lin, C.-W., Turner, C. L., Kaner, R. B., Huang, A., El-Kady, M. F., Chang, X., Anderson, M., Lin, C., Turner, C. L., & Kaner, R. B. (**2021**). Facile Fabrication of Multivalent VOx/Graphene Nanocomposite Electrodes for High-Energy-Density Symmetric Supercapacitors. *Advanced Energy Materials*. 11(26), 2100768.
4. Chang, X., El-Kady, M. F., Huang, A., Lin, C.-W., Aguilar, S., Anderson, M., Zi Jie Zhu, J., Kaner, R. B., Chang, X., El-Kady, M. F., Huang, A., Lin, C., Aguilar, S., Anderson, M., J Zhu, J. Z., & Kaner, R. B. (**2021**). 3D Graphene Network with Covalently Grafted Aniline Tetramer for Ultralong-Life Supercapacitors. *Advanced Functional Materials*. 31(32), 2102397.
5. , H., Delacroix, S., Osswald, O., Anderson, M., Heil, T., Lepre, E., Lopez-Salas, N., Kaner, R. B., Smarsly, B., & Strauss, V. (**2021**). Laser-carbonization: Peering into the formation of micro-thermally produced (N-doped) carbons. *Carbon*. 176, 500–510.
6. Strauss, V., Anderson, M., Turner, C. L., & Kaner, R. B. (**2019**). Fast response electrochemical capacitor electrodes created by laser-reduction of carbon nanodots. *Materials Today Energy*. 11, 114–119.
7. Ji, C., Xue, S., Lin, C.-W., Mak, W. H., Mcverry, B. T., Turner, C. L., Anderson, M., Molas, J. C., Xu, Z., & Kaner, R. B. (**2020**). Ultrapermeable Organic Solvent Nanofiltration Membranes with Precisely Tailored Support Layers Fabricated Using Thin-Film Liftoff. *ACS Applied Materials and Interfaces*. 12, 30796–30804.
8. Xue, S., Ji, C., Kowal, M. D., Molas, J. C., Lin, C.-W., McVerry, B. T., Turner, C. L., Mak, W. H., Anderson, M., Muni, M., V Hoek, E. M., Xu, Z.-L., & Kaner, R. B. (**2019**). *Nanostructured Graphene Oxide Composite Membranes with Ultrapermeability and Mechanical Robustness*. 17, 31.
9. McVerry[*], B., Anderson[*], M., He, N., Kweon, H., Ji, C., Xue, S., Rao, E., Lee, C., Lin, C.-W., Chen, D., Jun, D., Sant, G., & Kaner, R. B. (**2019**). Next-Generation Asymmetric Membranes Using Thin-Film Liftoff. *Nano Letters*, *19*(8), 5036–5043. [*]These authors contributed equally to this work.
10. Wang, H., Yu, Z., El-Kady, M. F., Anderson, M., Kowal, M. D., Li, M., & Kaner, R. B. (**2019**). Graphene/oligoaniline based supercapacitors: Towards conducting polymer materials with high rate charge storage. *Energy Storage Materials*, *19*, 137–147.
11. Borenstein, A., Strauss, V., Kowal, M. D., Anderson, M., & Kaner, R. B. (**2019**). Carbon Nanodots: Laser-Assisted Lattice Recovery of Graphene by Carbon Nanodot Incorporation (Small 52/2019). *Small*. 15(52), 1970285.
12. Borenstein, A., Strauss, V., Kowal, M. D., Yoonessi, M., Muni, M., Anderson, M., & Kaner, R. B. (**2018**). Laser-reduced graphene-oxide/ferrocene: a 3-D redox-active composite for supercapacitor electrodes. *Journal of Materials Chemistry A. 6*(41).
13. Rao, E., McVerry, B., Borenstein, A., Anderson, M., Jordan, R. S., & Kaner, R. B. (**2018**). Roll-to-Roll Functionalization of Polyolefin Separators for High-Performance Lithium-Ion Batteries. *ACS Applied Energy Materials*. 1(7), 3292–3300.
14. Strauss, V., Anderson, M., Wang, C., Borenstein, A., & Kaner, R. B. (**2018**). Carbon Nanodots as Feedstock for a Uniform Hematite-Graphene Nanocomposite. *Small*. 14(51).
15. Pangilinan, L. E., Turner, C. L., Akopov, G., Anderson, M., Mohammadi, R., & Kaner, R. B. (**2018**). Superhard Tungsten Diboride-Based Solid Solutions. *Inorganic Chemistry*. 57(24), 15305–15313.
16. Strauss, V., Anderson, M., Turner, C. L., & Kaner, R. B. (**2019**). Fast response electrochemical capacitor electrodes created by laser-reduction of carbon nanodots. *Materials Today Energy*. 11, 114–119.
17. Bock, N., Baum, M. M., Anderson, M. B., Pesta, A., & Northrop, W. F. (**2017**). Dicarboxylic Acid Emissions from Aftertreatment Equipped Diesel Engines. *ACS Environmental Science and Technology*. 51, 13036-13043.

CHAPTER 1: Thin-Film Lift Off

Reprinted (adapted) with permission from McVerry, B., Anderson, M., He, N., Kweon, H., Ji, C., Xue, S., Rao, E., Lee, C., Lin, C.-W., Chen, D., Jun, D., Sant, G., & Kaner, R. B. (2019). Next-Generation Asymmetric Membranes Using Thin-Film Liftoff. *Nano Letters*. 19(8), 5036–5043. Copyright 2019 American Chemical Society

Reprinted (adapted) with permission from Xue, S., Ji, C., Kowal, M. D., Molas, J. C., Lin, C.-W., McVerry, B. T., Turner, C. L., Mak, W. H., Anderson, M., Muni, M., V Hoek, E. M., Xu, Z.-L., & Kaner, R. B. (2020). Nanostructured Graphene Oxide Composite Membranes with Ultrapermeability and Mechanical Robustness. *Nano Letters*. 17, 31 . Copyright 2020 American Chemical Society

INTRODUCTION

Thin-film asymmetric membranes, often employed in water purification yet applicable to several other applications, consist of a thin-film called the active layer (AL) on top of a support layer (SL). Nonporous or dense membranes are used to separate solutes from their solvent by allowing solvent to pass through the dense film much more slowly than the solute. Rather than separating based on size like porous membranes, these membranes perform separations by maximizing the differences in diffusivity of one substance in a material relative to another.

According to the solution-diffusion model for membrane separation processes, water flux through a membrane is dependent on the osmotic pressure differential across the membrane ($\Delta\pi_m$), the applied hydraulic pressure differential (ΔP), and a constant A as derived from Fick's law[1]:

$$J_w = A(\Delta P - \Delta\pi_m)$$

Equation 1-1

A is intrinsic to the membrane and summarized as the product of the water permeability of the membrane (P_w) and the total volume of water held by the membrane (V_w) over the product of the thickness of the membrane's active layer (δ_m), the gas constant (R_g), and the temperature of the water (T)(1).[1]

$$A = \frac{P_w V_w}{\delta_m R_g T}$$

Equation 1-2

Here *w* represents "water" but is essentially any solvent (liquid or gas) in which the solute, s, is dissolved. The solute flux (J_s) through the membrane is summarized in Equation 1-3, where C_R and C_P are the concentration of salt on the retentate and permeate sides of the membrane, respectively, and a constant B.

$$J_s = B(C_R - C_P)$$

Equation 1-3

B is also intrinsic to the membrane and is simply the permeability of salt in the membrane material (P_s) over the thickness of the membrane.

$$B = \frac{P_s}{\delta_m}$$

Equation 1-4

Optimizing P_s and/or P_w for a particular separation under specific feed conditions is the main tenet of membrane materials research and distills down to the intermolecular forces between solute, solvent, and membrane. By combining Equations 1.1 – 1.4, we get the *A/B* ratio, often referred to as the permeability-selectivity or "permselectivity" of a membrane:

$$\frac{A}{B} = \frac{J_w(C_r - C_p)}{J_s(\Delta P - \Delta\pi_m)}$$

Equation 1-5

Ultimately, the performance of a membrane process is summarized as:

$$R_s = 1 - \frac{C_r}{C_p}$$

Equation 1-6

where (R_s) the rejection of a solute.

The *A/B* ratio of a membrane is not dependent on the active layer thickness, while flux values are. By minimizing the film thickness, flux increases or you can minimize the hydraulic pressure needed, while not altering the rejection potential of the membrane (*A/B*).

In addition to the chemical and physical properties of a membrane's active layer (AL), the support payer (SL) is crucial to creating functional membranes that behave well under hydraulic pressure by preventing compaction, without hindering the passage of solvent through the film. The lamination of AL and SL results in a thin-film composite membrane.

Composites are made by combining two or more materials to create a new material with properties of both components proportional to the amount of each component. Most relevant to this work, composites can be made by fabricating functional materials including polymeric membranes for filtration applications and for the essential components of energy storage devices. Here is discussed the synthesis, fabrication, characterization, and performance of a variety of materials for use in composites.

Thin-Film Lift Off

Based on porosity alone, there are three major types of thin-film composite membranes: porous, nonporous, and dense, each with increasing ability to separate out smaller and smaller solutes. Porous membranes, for filtering out larger particles, can be made by stretching, track etching, template leaching, or phase inversion.[2] Nonporous membranes are primarily made my phase inversion, more specifically, nonsolvent induced phase separation(NIPS). NIPS is a technique in which a solution of polymer is cast onto a substrate and then contacted to a nonsolvent causing the precipitation of the polymer onto the substrate (often a woven fabric). The side of the film that is in contact with the non-solvent is very dense due to its immediate precipitation. After initial precipitation, the nonsolvent permeates through the dense layer to slowly precipitate the rest of the polymer film. This portion, precipitated upon diffusion, is largely porous. The shape and size of these pores is dependent on the solvent-nonsolvent system.[3]

Phase inversion can also be achieved by slow solvent evaporation, vapor phase deposition, or precipitation based on a thermal gradient. These types of membranes are good for nanofiltration and ultrafiltration applications. For applications like desalination, the removal of ions from water, dense polymeric membranes are needed. These films often have a much lower flux than non-porous membranes made by immersion precipitation and are made using techniques such as spin-coating and interfacial polymerization.[2]

Interfacial polymerization is by far the most common technique for the fabrication of dense polymeric membranes. A supporting fabric or non-dense membrane is placed at the interface of a nonsolvent and solvent. Monomers from one solvent diffuse into the other causing polymerization at the interface of the solvent, around the supporting membrane. Right at the interface, a very dense thin film is made, then diffusion of monomer through the dense film leads to subsequent polymerization and a less dense supporting part of the membrane forms. Typically polyamide membranes are made by contacting a solution of meta phenylene diamine and trimesoyl chloride to form partially or fully aromatic polyamide membranes used for applications ranging from the refinement of dairy products to industrial-scale desalination of seawater. Because of the success of this interfacial polymerization process and the reactivity of these monomers, polyamide is widely researched and highly optimized.

As we move toward even more intensive needs to purify a wide range of aqueous and non-aqueous residential and industrial discharges, as well as utilize non-conventional sources of surface water and groundwater, membranes need to become more and more selective.[1] One approach to this selectivity is to use a wider array of polymeric materials including more robust polymers, inorganic media, and "inorganic carbon", which are not amenable to interfacial polymerization or other phase inversion techniques. The first portion of this chapter presents a method of making membranes that is amenable to all of the materials listed above. Other portions will be dedicated to specific aspects of the technique. Here we will specifically discuss the development of the technique and the concept of its use as a platform to study specific materials. Examples of applications to desalination, organic solvent nanofiltration, and gas separation will be given. Optimization of chemistries that affect the selectivity of the membranes and the rate at which water passed through the membranes are detailed in future chapters.

Polymeric thin-film membranes have emerged as a leading technology for separations, because of their exceptional transport properties, large surface area/small footprint, and low cost of fabrication.[1] A major breakthrough in membrane technology occurred when Loeb and Sourirajan developed the first asymmetric membrane,[5] made from cellulose acetate (CA), that demonstrated superior permeation flux, when compared to dense CA membrane films.[5] Because the separation ability of a membrane is independent of its thickness,[4] a thin separation layer imparts higher permeability to a membrane compared to a thick layer, while theoretically maintaining the same rejection capabilities.[7] To improve on this work, Cadotte et al. developed asymmetric thin-film composite (TFC) membranes with polyamide active layers made via interfacial polymerization.[7] Today, TFC membranes are the state-of-the-art technology used for nanofiltration, and brackish and seawater desalination. The pore sizes of these membranes can be readily tailored for different applications: membranes with larger pores are used in wastewater treatment and kidney dialysis (ultrafiltration), while nonporous membranes are used in nanofiltration, seawater desalination, and gas separation.[7]

Despite their great performance, today's polymeric thin-film composite membranes have several limitations. Placing a thin active layer (~150 nm) on top of a porous support membrane (typically made from polysulfone) is achieved using interfacial polymerization, which limits membrane precursors to highly reactive acyl chlorides and polyamines or polyols that react on contact.(8) Moreover, the rapid reaction rate of interfacial polymerization[8-20] leads to a rough active layer that creates sites that initiate membrane fouling.[22] Because the active layer is formed on the already made support membrane, the properties of the support membrane must be considered before forming the active layer. For example, solution casting of thin films onto a support membrane often causes issues with dissolution of the support polymer or leads to poor lamination between the two layers. Many polymers known for their chlorine tolerance or pH stability must be thermally cured at higher temperatures than the support membrane can withstand, which limits the current curing conditions to relatively mild temperatures.[18] In this contribution, we present a new thin-film liftoff (T-FLO) technique to fabricate robust thin-film composite membranes, which opens the door to the use of a variety of polymers and carbon materials as active layers.

With T-FLO, an active layer precursor is first cast onto a substrate using a doctor blade to form a thin film, followed by solvent evaporation or curing. Next, a thermosetting resin is cast directly on top of the active layer and thermally cured to form a microporous support. As the support cures and hardens, the polymerization simultaneously generates covalent interactions with the active layer that enables the defect-free delamination of the active layer from the underlying substrate (Figure 1-1).

When choosing a porous support material to lift-off the active layer, several criteria must be considered:

(1) The support must form strong interactions with the active layer to resist delamination during the lift-off process;

(2) The material must be able to be made into a tunable porous network that is highly permeable; and

(3) The material must be mechanically flexible and robust so it can be handled easily and used under pressurized conditions since RO is performed at 200−800 psi.

After screening several different polymer systems, thermosetting epoxy resins were found to be most suitable for T-FLO membrane fabrication. Cross-linked epoxy networks are known for their high strength and good chemical stability. Their bulk properties can be readily modified by selecting different polyamine hardeners, changing stoichiometric ratios of hardeners to the resin, or adjusting the cure temperature/duration.[24] Epoxy resins are used widely across several industries, primarily in adhesive and structural applications. Because of this, the materials for making epoxies are widely available and relatively cheap. Highly reactive epoxide groups make the hardening of the resin rapid compared to other adhesives/structural materials. For T-FLO, the highly reactive epoxide groups also enable the curing network to covalently bind to functional groups on an active layer. Furthermore, fabricating porous epoxy membranes can be readily achieved by adding water-soluble polyglycol porogens into the uncured resin solution.[22] After curing, the membrane is submerged into a water bath that serves two functions. The water removes the porogen from the cured epoxy network, forming the porous support membrane, and simultaneously, in the case of T-FLO membranes, the water slowly swells the active layer to enable delamination of the entire composite from the underlying substrate.

Because the active layer is cast separately from the support, the physical and chemical properties of the active layer can be investigated independently from the membrane composite. As long as these techniques are nondestructive, the active layer can be directly fabricated into thin-film composite membranes with the T-FLO technique and studied during operation in a pressurized cell.

To produce T-FLO composite membranes with comparable permeability to commercial membranes, both the active layer and the support layer must be thin. This can be achieved by casting thin films on glass plates or aluminum sheets using a doctor blade with a fixed height. Figure 1-2 includes 3 cross-sectional images of T-FLO membranes. Here, we demonstrate the T- FLO technique using several different polymers and carbon- based materials to produce membranes for different applications. A major challenge that had to be overcome was curing the epoxy support at a specific height due the change in viscosity of the resin mixture during curing. Our solution to this problem was to create a sandwich structure between two panes of glass using strips of ~65-μm-thick electrical tape as a spacer to ensure a uniform thickness. Despite fabricating suitable samples for cross-sectional analysis, the process of separating two panes of glass that were held together by the epoxy resin was arduous (Figure 1-3 A-B).

We adopted a simpler approach by using a thin nonwoven fabric veil that was made of glass, carbon, or polymer fibers to use as a membrane template for the epoxy resin. The liquid epoxy infuses directly into the thin veil, and upon curing, forms a fiber-reinforced plastic film that can be easily handled. Fiber-reinforced plastics are well-known commercially for their lightweight and high strength and are the basis for carbon-fiber composites, body armor, and high-performance sports equipment, and have been implemented extensively in the automotive and aerospace industries.[24]

Several materials were considered and screened for the selection of a compatible support fabric. The optimal materials were chemically inert to the epoxide chemistry within the resin, had low thermal expansion coefficients, and were flexible. We observed that nonwoven glass fiber, carbon fiber, and polyester veils with an areal weight of 12 g/m^2 provided the best balance of mechanical and transport properties in the resulting composite membranes.

Optimization of Epoxy Support Membranes Based on Porogen

Experimental

Epoxy Solutions

The diamine was dissolved in the porogen in a 20 mL scintillation vial and stirred with a magnetic stir bar until fully dissolved. The diglycidyl ether was then added to the solution, with stirring until fully dissolved. The solution was degassed under vacuum. Table 1-1 summarizes the epoxy preparation for membranes in Figures 1-8, 1-9, 1-10, and 1-11.

The epoxy pre-preg solution was prepared above and poured onto an active layer film on a glass plate. 12.5 µm electrical tape was placed on the edges of the glass pane that acts as a spacer. A second glass plate coated with Epoxyease (McMaster-Carr, Santa Fe Springs, CA) was then gently placed on the glass plate to form a sandwich structure, spaced by the electrical tape. The glass plates were uniformly heated on a hot plate to cure the T-FLO membranes using the same curing conditions as above. The glass plates were separated with a wedge and the glass plate containing the active layer and membrane was placed in a DI water bath to lift-off the membrane and remove the porogen. The membrane was allowed to dry and freeze-fractured to enable SEM observation.

Figure 1-4 illustrates the reaction of Bisphenol A digylicylether (BADGE) with 4,4′-methylene-bis-cyclohexylamine (MBCA) in the presence of PEG during the curing of the support layer. First, the mixture of monomers reacts to produce linear polymers from the reaction of the epoxides and the diamines to form a resin. The secondary amines and resulting hydroxyl groups react with additional BADGE to form the hardened cross-linked network.

Structural characterization of highly crosslinked polymer networks can be limited considering you cannot perform techniques like NMR or mass spec that can be used for finite molecules/polymers. Therefore, the final structure of the cured polymer network using different molecular weight PEGs was investigated using infrared-attenuated total internal reflection (IR-ATR) spectroscopy and X-ray photoelectron spectroscopy (XPS). In Figure 1-5, blue vertical traces indicate the region of particular functional groups and the numbers along each indicate the peak intensity at that energy. *Smaller* numbers indicate a stronger signal for that group. Changes in the OH and C-H regions indicate an increase in OH groups when PEG200 is used as the porogen and a change in the carbon environments. Oxirane decreases with more PEG 200 and secondary alcohol presence appears to increase. Additional hydroxy groups would indicate more linear polymerization since hydroxy groups are formed with the reaction of epoxide groups. The increase in the N-H bend when PEG 400 is used as the porogen may suggest that, although the linear polymerization was less productive due to reduced catalytic OH groups, having more epoxide groups during the curing process led to more crosslinking. There were more unopened epoxides that could react with the secondary amines.

XPS was used to determine elemental composition and elucidate oxidation states of atoms. Types of bonds can also be estimated by deconvoluting peaks at hi-resolution (Figure -6). These deconvolutions can be overinterpreted in many cases as different peaks are assigned specific types of carbon bonds. The simplest interpretation here is that PEG 400 samples contain more electron-deprived carbons, there is a shift toward higher energy peaks, which may mean there are more epoxides remaining in the structure as more PEG 400 is used as the porogen. Survey scans of our films show less oxygen detected at the surface for PEG 200 resins as opposed to PEG 400. Since XPS only observed the first few nanometers of a substance, this could be due to some form of hydrophobic recovery in the more linear polymers as opposed to the more crosslinked ones that resist hydrophobic recovery.

Despite these theories regarding the functional groups of the epoxy membranes, differential scanning calorimetry (DSC) shows very similar traces when cycled from 30 °C to 300 °C, indicating that the glass-transition temperature (T_g) of the polymer is not significantly affected by the type of porogen used (Figure 1-7). Therefore, it is likely that differences in the mechanical and transport properties of the epoxy membranes are largely due to the resulting pore macrostructure, as opposed to slight changes in the cross-linking density of the epoxy network.

Most evident of changes to the epoxy systems is the difference in pore structures based on the porogen system. In Figure 1-8, four images of resins taken at the same magnification (19000x) show that porosity decreases as the relative amount of PEG 200 decreases from 100% to 25%. This is also evident in the appearance of membranes. Membranes with larger pores appear opaque when wet, are flexible, and have higher permeabilities, compared to membranes with smaller pores that are transparent and brittle.

Most importantly, flux and compaction properties of the epoxy support layer can be readily optimized by changing the ratio of polyethylene glycols. Table 1-2 has, in each column, the % porogen that is PEG 200 and % porogen that is 400 along with initial flux, final flux, and % compaction. Membrane compaction is the flow rate of water through a membrane at the beginning of operation divided by the flow rate of water after the flow rate stops changing. Ideally there will be no compaction that occurs when the membrane is put under pressure. More realistically, water flux through a membrane will quickly reduce at the beginning of a run and reach an asymptote after which no further change occurs. The worst-case scenario is when a membrane’s flux decreases slowly until the flux is 0. This demonstrates extreme compaction of pores. Resins with less that 50% PEG 400 had extremely high flux such that measuring compaction would require much more than 300 mL of water to pass through the membrane, the capacity of the DEC. The 25% PEG 200 membrane appears to have the least compaction. The negative compaction value for the 37.5% PEG 200 sample may mean that additional pores opened up when pressure was applied.

Figure 1-9 demonstrates the correlation between control of pore size by porogen composition and control of flux and compaction. In addition, we have observed that these properties are maintained when a dense active layer is present in the composite. The effect of the porogen, PEG compounds with different molecular weights, on the support membrane morphology originated from the density of hydroxyl groups in the porogen. The catalytic effect of various small-molecule alcohols on the kinetics of epoxy network formation is well understood; hydrogen bonding stabilizes the ring opening of epoxides as the resin cures.[26] In our system, a similar effect is achieved with the terminal −OH groups on the PEG porogens used to dissolve the resin and create pores in the cured structure (Figure 1-4 B). A higher density of −OH groups per unit mass of porogen, such as 3.25 g of PEG200, compared to 3.25 g of PEG400, has a greater catalytic effect on the mixture. The more rapid reaction of polymer, especially during the linear polymerization phase, leads to a more open/porous structure resulting in more flexible membranes with higher permeability.

Methyl-capped polyethylene oxide experiments

In order to investigate the effect of the density of hydroxyl moieties in the porogen on the morphology of the support layer, poly(ethylene glycol) dimethyl ether (Me-PEO, avg. MW:250), was used in place of polyethylene glycol or in combination with PEG 200 to make epoxy support membranes as described in Section 2 of the SI. Unlike PEG, Me-PEO cannot have a hydrogen bond stabilizing effect with the oxygen of the epoxide ring (S1 A, S1 B). This significantly increases the activation barrier, reducing the rate of polymerization and crosslinking of the resin. With slower curing times, the growing polymer network does not phase separate quickly, resulting in a dense, non-porous membrane support film. Based on our results, we conclude that, within this range of MW, the hydroxyl-group concentration plays the largest role in the curing rate of the epoxy support layer. In

S1 C, D and E, films are shown made with differing amounts of Me-PEG relative to PEG 200. When Me-PEO is used as the porogen, a viable freestanding porous membrane is not formed under the same curing conditions. Rather, the viscous resin precipitates on the glass substrate Figure 1-11 C. By blending in PEG 200 at different weight %, we were able to establish similar trends in flux to those shown in Figure 1-9 although with much lower water permeability films made from a >50 wt% Me-PEO porogen. Viable films were only successfully fabricated with at least 50% PEG 200 relative to Me-PEO. The relative differences in pore size of the films can be observed from the opacity of the film (Figure 1-11). A less dense membrane with larger pores scatters more light, resulting in the formation of an opaque film. A dense film with small pores is transparent. Therefore, greater amounts of Me-PEO used in the porogen produced transparent films with very low permeability. The permeability can be increased by adding higher wt.% hydroxyl groups from PEG 200.

Selection of Nonwoven Fabrics for Epoxy Support Layer Composites

While the T-FLO fabrication described earlier in this chapter is very useful for fundamental studies of the materials for membrane, separating two panes of glass that were held together by the epoxy resin was arduous. We developed a simpler approach by implementing a thin nonwoven fabric veil that was made of glass, carbon, or polymer fibers to use as a framework to cure the epoxy resin. The liquid epoxy infuses directly into the thin veil, and upon curing, forms a fiber-reinforced plastic film that can be easily handled. Fiber-reinforced plastics are well-known commercially for their lightweight and high strength and are the basis for carbon-fiber composites, body armor, and high-performance sports equipment, and have been implemented extensively in the automotive and aerospace industries.[27]

When selecting the fabric to be used in T-FLO membranes, we considered the chemical and physical interaction of the support fabric with the epoxy resin when curing as well as the effect on compaction.

Experimental

Nonwoven Fiber-Reinforced Membranes

For standalone epoxy supports, a glass substrate was coated with a thin layer of Slide Epoxease or a pre-prepared active layer. An 11 cm x 14 cm non-woven fabric sheet was placed on top of the active layer to absorb the epoxy solution and reinforce the cured membrane. Uniform heat was applied through an industrial hotplate for 3 hr. to cure the epoxy solution into a porous film. Once cured, the glass plate supporting the membrane was allowed to cool and placed into a DI water bath to delaminate the membrane from the glass substrate and remove the porogen. The membranes were stored in DI water before further use.

Discussion/Conclusions

Nonwoven materials used as support fabrics included glass fiber, polyester fiber, and aramid fiber. While the aramid fiber worked as a nonwoven material, the epoxy reacts with the amide bonds, making it difficult to isolate chemical features of the fabrication process and is also subject to degradation by chlorine. Polyester fibers also worked as a support material and endowed the films with much more flexibility. Unfortunately, expansion/deformation upon heating occurs. Since the fibers are inevitably heated when the epoxy resin is cured, this was a non-ideal option. The 25 g/m^2 polyester fiber in Table 1-3 showed minimal compaction. A slight increase is seen in flux is observed (Table 1-3) which could be due to additional pores in the membrane opening up with applied pressure. Figure 1-12-F shows the SEM cross-section of the 25 g/m^2 polyester fiber composite. The fibers can be seen poking out of the resin on either end, which could minimize resin contact with an active later upon curing, but also cause large surface pores surrounding the un-encased fiber. A larger amount of resin could be used to encase the fibers or a smaller area of fabric, but we focused on one variable to avoid increasing the total mass/thickness of the membranes. Lower density polyester veils were more difficult to work with than the higher density veils because, rather than holding the epoxy in place, the fibers moved easily with the epoxy causing uneven films to form with the slightest disturbance prior/during curing.

In terms of fabrication, glass fibers were the most convenient because the resin wicks quickly into the veil due to its relative hydrophilicity (compared to PE). The 6 g/m^2 glass veil produced flexible films and, by SEM only, the 6 g/m^2 veil shows fibers well-encased by the epoxy compared to heavier veils. Unfortunately, it showed extreme compaction (Table 1-3), which is not favorable as a standalone membrane or as a supporting membrane. A 12 g/m^2 glass veil was selected for general use.

Later in development of T-FLO, glass fiber became less favorable when using a cross-flow format and ultimately a 6 g/m^2 veil was selected as a more inert and more flexible alternative to the glass fiber. Though a systematic study is not included here, membranes with this support fabric are discussed in Chapters 2 and 3 of this work.

Figure 1-13 summarizes the process of developing membranes using T-FLO. Selection of an AL structure or chemistry is based on the types of bonds, functional groups, crystallinity, crosslink density, etc. T-FLO enables the structure be simply cast onto a substrate which may be followed by further chemical treatments such as thermally-induced crosslinking, graphitization using a laser, addition of additional AL materials, or chemical treatment to optimize flux or lift-off capability. Processing also involves the optimization of the epoxy SL chemistry to lift-off the AL. Performance testing including solvent flux and rejection measurements give an evaluation of the AL structure and the efficacy of the optimized SL. Finally, the chemical and structural properties of AL and SL can be evaluated and inform what changes in the chemical structure of the AL will be both compatible with processing and enhance performance.

Applications of T-FLO: Gas Separation

Using nonwoven fabrics, T-FLO was much more practical and we began investigating its use to make composite membranes with active layers that otherwise could not be made using traditional membrane casting techniques. One of these was a gas-separation membrane based on a polyaniline-graphene oxide. Gas separations can be performed using dense polymeric films, but cryogenic fractionation and adsorption are more common separation techniques, even though they are more energy-intensive processes.[28] Tunable gas separations have been demonstrated previously using polyaniline, but the difficulty in processing polyaniline limits its applications.[31]

Methods

Active layer polymer solutions were prepared by dissolving the selected polymer(s) in a suitable solvent to form a viscous solution. The solutions were further centrifuged at 13,000 rpm to remove agglomerates and the supernatant cast onto clean glass plates using a fixed height (7.62 micrometer wet film thickness, GardCo) doctor blade. A uniform film formed upon evaporation of the solvent. For higher boiling solvents, gentle heat can be applied underneath the glass substrate to aid in evaporation. Higher curing temperature treatment can be performed for imidization or cross-linking reactions.

Polyaniline (PANI) films with graphene oxide (GO, added for improved permeability) were cast on glass plates and dried in a vacuum oven at 80 °C for 36 h. since no additional mass loss was observed with further drying. Afterward, the PANI membrane films were submerged in DI water and separated from their substrates. Before testing the PANI film and PANI support membrane were degassed in the membrane cell unit, using a vacuum oven at 80 °C for 36 hrs until no additional mass loss was observed with further drying.

Results and Discussion Processing and handling thinner films (in this case, 500 nm) is made possible using T-FLO. This enables the isolation of physical and chemical parameters when investigating new materials, as well as improving the performance of known materials. By measuring the pressure difference between the inlet and permeate sides of both epoxy membranes and epoxy membranes with covalently bound PANI active layers, the advantages of T-FLO for gas separation becomes evident. As shown in Figure 1-14-A, the epoxy support does not affect the gas permeability in the presence of the active layer. Figure 1-14-A also illustrates how the selectivity for particular gases can be optimized by changing the active-layer film's thickness, thus accentuating the flux difference of CO_2 vs. N_2 which grows by about 200 Barrers. Processing and handling thinner films, in this case 500 nm, is made possible using T-FLO. This enables the isolation of physical and chemical parameters when investigating new materials as well as for improving the performance of known materials. The permeability of pure CO_2 and N_2 gases was calculated as:

$$\mathrm{P} = 10^{10} \times \frac{VL}{P_{permeate}ART} \times \frac{dp(t)}{dt}$$

Equation 1-7

where P is the gas permeability (in Barrers) where 1 Barrer = 10^{-10} cm^3(STP)cm/cm^2 s cm Hg, $P_{permeate}$ is the upstream pressure (cm Hg), dp/dt is the steady-state permeate-side pressure increase (cm Hg/s), V is the calibrated permeate volume (cm^3), L is the membrane thickness (cm), A is the effective membrane area (cm^2), T is the operating temperature (K), and R is the gas constant [0.278 cm^3 cm Hg /cm^3(STP) K].

The ideal selectivity (α) is determined from the ratio of permeability coefficients.

$$\alpha_{A/B} = \frac{P_A}{P_B} = \frac{P_{CO_2}}{P_{N_2}}$$

Equation 1-8

where P_A and P_B refer to the permeability coefficients of the pure gases CO_2 and N_2, respectively. Figure 1-15-A shows the comparison of the CO_2 permeance of the membranes with and without the epoxy layer. The pure CO_2 and N_2 permeance were measured at 7 psi (0.048 MPa) feed pressure. The CO_2 permeability of the PANI film membrane (without the epoxy layer) is only slightly higher than that measured for the PANI support membrane alone. However, the difference in CO_2 and N_2 permeance was insignificant, which indicates that CO_2 and N_2 permeance were not affected by the epoxy layer as its large pores do not reduce the penetration of the gases.

Applications of T-FLO: Organic Solvent Nanofiltration

Organic solvent nanofiltration (OSN) provides a complementary technique or alternative to traditional solvent purification methods (i.e., distillation, chromatography, extraction). Using OSN, desirable solutes can be readily concentrated or waste products can be rejected to purify solvents by passing them through a membrane. Current membranes for OSN are made using traditional membrane fabrication techniques that limit the selection of polymers for the membrane active layers.

Methods

For organic solvent nanofiltration membranes, a commercial solution of celazole polybenzimidazole (Performance Products Inc.), (PBI), 10% in dimethylacetamide (DMAc) was diluted and then cast onto a glass substrate and heated to 60 °C to remove solvent. 12 g/m^2 nonwoven glass fiber was used as the supporting fabric. 100% PEG 400 was used as the support resin porogen. Rejection of methylene blue and flux of ethanol through OSN membranes was performed in a 300 ml, dead-end, stirred cell pressurized using compressed nitrogen gas.

Results and Discussion

Because epoxy-based polymers have good chemical stability and an array of cross-linked or selectively insoluble polymers can be utilized, T-FLO membranes can be tuned for OSN applications.[34-39] We demonstrate this feasibility by fabricating T-FLO membrane composites and selecting polybenzimidazole (PBI) as the active layer material. PBI is well known for its chemical stability, stiffness and toughness at elevated temperatures.[29] Furthermore, Valtcheva *et al.* have demonstrated that PBI membranes formed using phase-inversion exhibit great OSN capability and minimal degradation even under extreme conditions. However, non-solvent induced phase-inversion offers little control over the active layer thickness.(47) Using the T-FLO technique, the membrane thickness can be precisely controlled through changing the casting solution concentration. The epoxy support layer can be tuned independently of the active layer using T-FLO enabling optimization of polybenzimidazole for OSN applications separate from other aqueous separations. To demonstrate the membrane OSN capabilities, a solution of ethanol containing methylene blue and a solute was pressurized and passed through a T-FLO membrane (Figure 1-16). The membrane rejected ~90% of the dye solute in a single pass and steady-state permeability was observed at operating pressures up to 300 psi.

Graphene Oxide Membranes

Although most membranes created claiming to utilize the unique properties of carbon materials like GO receive a lot of attention, many of their designs are not practical for large scale membrane manufacture nor have the robustness needed for real-world membranes.[31-42] Using our method of membrane fabrication discussed earlier for polymeric active layers we attempted to overcome these challenges.

Methods Following this basic method for thin-film lift off (T-FLO); epoxide groups were reacted with functional groups on the graphene oxide sheets, fixing them in place upon resin cure before delaminating upon submersion in a water solvent exchange bath. These films are denoted T-FLO-GO ("lifted GO) and are compared to "conventional" GO (C-GO) films made by filtering GO solutions through a pre-made polymer support.

Results and Discussion

Single layered graphite, known as graphene, is popular in materials research for energy storage and composite applications because of its high conductivity and large surface area. It is of interest for water purification because of the way that water can rapidly permeate through a network of graphene sheets. Graphene oxide (GO), commonly used as a precursor to reduced graphene oxide, which has similar properties to graphene, can be made in large batches from graphite through an exfoliation process. Unlike graphene, GO has many oxygen functionalities that make the material more hydrophilic and offer handles for chemical modification. Using our thin-film lift off (T-FLO) method, epoxy resin was reacted with the oxygen moieties on the GO and then converted to a porous membrane support for the GO layer.

Figure 1-17 shows the top surface of a T-FLO GO film using scanning electron microscopy. This image shows a smooth, continuous active layer with no large pinholes. The thickness of the active layer can be controlled by the concentration of GO in solution. Figure 1-18 shows a cross-section of a T-FLO GO film indicating an active layer smaller than 100 nm. The porous support voids appear to be greater than or equal to 100 nm. Atomic force microscopy (AFM) has been used to study the topography of the T-FLO GO films. The surfaces were found to be quite smooth. X-ray photoelectron spectroscopy (XPS) has been used to characterize the surface of T-FLO GO membranes. The deconvolution of the C1s peak approximates the different C-O bonds found on the surface of the T-FLO GO film, which, show only minimal differences from the GO sample from which the membrane sample was made. This indicates that the characterization of GO before film formation is an accurate reflection, with only minor functionality changes, of the GO that makes up the active layer.

GO suspended in water at concentrations of 2.5 mg/g, 5 mg/g, 7.5 mg/g and 10 mg/g were cast onto glass substrates forming dry films 32 nm to 131 nm thick (measured using step profilometry and/or scanning electron microscopy). An epoxy-resin solution containing bisphenol A diglycidyl ether, bisphenol A propoxylate diglycidyl ether, piperazine, and 1-(2-aminoethyl) piperazine dissolved in polyethylene glycol (MW 400), which acts as a porogen, was then cast onto nonwoven glass fiber placed atop GO films. Films were cured as described earlier in this chapter.

X-ray diffraction patterns are generated as X-rays from a monochromatic beam constructively or destructively interfere after they interact with a crystalline material at varying angles. In the case of graphene and graphene oxide, we are mostly concerned with the spacing between monolayer thick sheets of carbon atoms which can be calculated by the angle of maximum constructive interference. The large number of oxygen functionalities on the surface of GO sheets cause the material to swell when wet thus increasing the spaces between the sheets. Because the heat treatment processes lead to some thermal reduction (loss of oxygen functionalities) of the GO, T-FLO-GO has an overall smaller interlayer spacing compared to C-GO as observed by the difference of peak positions in their X-ray diffraction patterns.

In order to find out what type of water contaminants might be removed using this type of film, rejection of different dyes as well as salts covering a range of hydrated radii (a measurement of how large the particles are in water when surrounded by a layer of water molecules) was tested in a pressurized dead-end cell. As can be seen in Figure 1-19-B, high rejection (>98%), was maintained for solutes with hydrated radii of 4.87 angstroms or larger, while rejection diminished for solutes with smaller radii, including salts. Figure1-19-B shows the relationship between film thickness, percent rejection of dyes and permeability of solvent through the films. Membrane permeability is a function of film thickness, while rejection is a function of the material. From these experiments we can infer that membrane perm-selectivity is dictated by the dense GO layers.

Tolerance of Reverse Osmosis Membranes

Pressure-driven reverse osmosis has emerged as the leading technology for desalination of seawater and brackish water because of its continuous operation, small footprint, and low-energy cost compared to other desalination technologies. Despite their superior performance, polymeric thin film membranes foul due to organic and biological materials in the feed that adhere to the membrane surfaces. These biofilms restrict the passage of water through the membrane, increasing resistance and lower efficiency. Chlorination of feed water is a common way to control the formation and growth of biofilms. However, state-of-the-art thin-film composite membranes are highly susceptible to degradation with even trace amounts of chlorine present in the feed solution. The amide bonds that make up the backbone of the rejecting layer rapidly hydrolyze, thus compromising the initial high salt rejection of the polyamide membranes.[25,26] Treatment plants must remove virtually all sodium hypochlorite from the feed water before exposure to the RO membranes, enabling fouling to occur and creating additional steps that increase the cost of desalination.[55,56]

Polymerization of meta-phenylene diamine (MPD) with trimesoyl chloride (TMC) at the interface of an organic and aqueous layer around a supporting membrane leads to a fully-aromatic polyamide membrane. The mechanism of the degradation of polyamide membranes is still debated, but is essentially a cleavage of the amide bond. This may happen either by cleavage directly after N-chlorination at the amide bond, or through the mechanism of N-chlorination followed by Orton rearrangement. The latter leads to the generation of chlorine gas and electrophilic substitution onto the position ortho to the two amide bonds due to the electron withdrawing effects of the two amides. This chlorination further draws electron density out of the benzene's pi system, essentially weakening the N-C bond of the amide, allowing for ease of hydrolysis.[53,54]

If amide bonds are replaced with other types of bonds, such as imides, or other tertiary amine, you can greatly reduce degradation. This can be done by substituting out the MPD with monomers such as piperazine or polyimides and polybenzimidazoles which covalently bind to epoxy resin T-FLO supports once glycidyl ether groups in the support resin react with secondary amines in the cured active layer polymer. In the case of polyimides, secondary amines arise due to incomplete cyclization of the polyamic acid precursor when it is cured to form polyimide, whereas in polybenzimidazole, the imidazole functionalities serve as reaction sites.

Methods

Desalination membranes were made by casting thin films of polystyrene sulfonic acid in water (PSSA, Sigma Aldrich, 1-% w/v) onto clean glass substrates. Gentle heating was applied to evaporate the solvent followed by casting of a PBI solution in DMAc and THF directly atop the PSSA layer. THF was used as a co-solvent to encourage faster solvent evaporation that enabled higher film quality due to a reduction in the number of defects that can form upon prolonged drying or rapid evaporation of a higher boiling solvent. Acid-base interactions occurred upon contact followed by curing for 4 hr at 180 °C to induce crosslinking. 12 g/m^2 carbon fiber was used in the support membrane. 100% PEG 400 was used as the support resin porogen. Rejection of salt and flux of water through RO membranes was performed in a 300 ml, dead-end, stirred cell pressurized using compressed nitrogen gas.

Circular membrane coupons (5 cm in diameter) punched out from flat sheets were tested for salt rejection at 55 bar of applied pressure using a 300-mL, stirred dead-end cell apparatus. Pressure was applied using compressed nitrogen gas. Accelerated chlorine tolerance tests were performed by dipping already-tested coupons into an 8.5% commercial solution of sodium hypochlorite (NaClO) for 5 min.

Discussion/Conclusion As illustrated in Figure 1-20, a T-FLO film containing a layered PBI/PSSA membrane is crosslinked at the interface. Once made into a membrane using T-FLO, membranes were imaged, as shown in Figure 1-21. Table 1-4 contains the O:S ratio for PBI, PBI-PSSA mixture, and PBI/PSSA after curing. After curing the O:S ratio increases, thus supporting the crosslinking reaction illustrated in Figure 1-20.

The increase in hydrophilicity after treatment of PBI with PSSA and the following decrease in hydrophilicity after curing also supports the suggested crosslinking reaction. As the O-H is removed, removing the potential for charged O on the polymer backbone and hydrogen bonding, the hydrophilicity will reduce (Figure 1-21).

Unlike with XPS and CA, chemical changes tracked using IR spectroscopy showed only minor changes in functional groups. The reduction of the C=N (near 1600 cm^{-1}) stretch with treatment with PSSA is observed and partially recovered upon curing (Figure 1-22).

SEM images of the PBI-PSSA membrane used in this study is shown in Figure 1-21. The fibers are well encased in the epoxy. The 50:50 PEG200:PEG400 support appears very dense with fibers well encased in the epoxy and the active layer well adhered to the support.

The high-resolution XPS spectra of the Cl 2p region shows trace amounts of Cl on the surface of only the chlorine treated PA membrane (Figure 1-24). The survey spectra show chlorine present on both the PA and PBI/PSSA membranes, unusual due to the lower resolution of the survey scans. Since there is also trace amounts of Na on the surface of the PA membrane, some of the Cl may be due to NaCl that was not adequately removed after soaking membranes in DI. The increase in oxygen after treatment of the PA with NaClO may be due to the generation of COOH groups upon cleavage of the amide bonds. The PBI/PSSA survey scans do not indicate the presence of sulfur after treatment with NaClO. This may be due to rearrangement of polymer chains on addition of NaClO or due to the photooxidation of the sulfonate groups due to the presence of both NaClO and NaOH in the commercial bleach solution.[57]

Hi-resolution scans of the O1s region of the DOW SWXLW membrane before treatment with NaClO (Figure 1-27-A) compared with after treatment with NaClO (Figure 1-27-C) show a shift in the relative binding energy from 529 eV to 527 eV. PBI/PSSA has a relatively similar distribution of O 1s peaks before (Figure 1-27-B) and after (Figure 1-27-D) treatment with NaClO. The lower-energy peak is typically associated with C-O-H type bonds while the higher-energy peak with O=C. This difference correlate with an increasing amount of O-H due to amide bond cleavage. Alternatively, the oxygen atoms in an amide bond would be more electron deficient than in a carboxylic acid. Therefore, a shift from more-electron-deficient oxygen atoms to less electron deficient oxygens also correlates with bond cleavage.

The greatest evidence for degradation were the changes in salt rejection before and after treatment with NaClO. The PBI/PSSA active layer maintained a high salt rejection of 2000 ppm of NaCl when exposed to sodium hypochlorite, because the polymers used for the active layer have great oxidative stability. In comparison, the salt rejection of a commercial Dow SWXLE membrane substantially decreased due to degradation of the polyamide active layer that is known to rapidly deteriorate when exposed to even trace amounts of sodium hypochlorite (Figure 1-25). The lower-than-usual rejection for the commercial membrane prior to chlorine treatment is likely due to operation in DEC format rather than a fault with the product.

Figure 1-26 includes rejection data for 10% NaCl for a polyimide membrane made using T-FLO and a Dow SWXLE membrane under neutral feed conditions; a PBI/PSSA membrane and DOW SWXLE at high pH; and those same PBI/PSSA and Dow membranes tested at pH 11 after treatment with NaClO. The reduction in rejection is much greater for the Dow SWXLE membrane when compared with the same experiment at neutral pH. We hypothesize that the formation of the n-chlorinated polyamide would produce a weaker polymer network for desalination, but only undergo some cleavage in the neutral salt environment, while immediate exposure to low pH would lead to more rapid hydrolysis due to the hydroxide nucleophiles present in the solution. Since making this comparison was not the original intent of the two studies in Figures 1-25 and 1-26, additional controlled experiments at equivalent salt concentrations are needed to confirm this theory.

Optimization of Thin-Film Delamination through adjustment of active layer and support layer chemistries.

Discussed previously was the optimization of a novel, scalable, top-down thin film lift off (T-FLO) fabrication technique for making thin film composite (TFC) membranes with dense active layers (AL). One of the challenges is generalizing this technique as successful: useful for composite formation between active and support layers among a variety of AL formulations. In this work, epoxy resins with varying 4,4’ methylenebiscyclohelylamine (MBCA) content are prepared, which are proposed to cause weak delamination (poor AL-SL interaction), destructive delamination (AL-SL interaction causes destruction of composite membrane), or an optimized formulation for a particular AL type. Scanning electron microscopy is used to investigate active layer support layer adhesion in each case showing an intermediate concentration of epoxy hardener as forming the best composite. Variable-pressure water flux data were obtained and suggest a correlation between improved flux and true composite formation.

Earlier in this chapter the optimization of a support layer through kinetic and structural components that enables high water flux through a dense polybenzimidazole (PBI) thin film was discussed. Capacity to tune AL-SL adhesion independently from pore formation, to create a similarly optimized membrane with a PI rather than PBI thin film is discussed. PI films with more electron deficient nitrogen thus require additional tuning of both the active layer and the support in order to use T-FLO.

In order for T-FLO to work, covalent bonding between the epoxide sites in the support with pendant amine groups on the thin active layer and sufficient swelling of the AL upon exposure to salt water enabling non-destructive delamination from a glass substrate must both occur. In addition to reacting with itself, epoxy sites are taken up by the hardener present. We take advantage of these properties to make TFLO compatible with polyimide films, which show higher selectivity in separation processes.

In this work, three epoxy resins adapted from Minehara *et al.* with varying MBCA content are prepared that are known to cause weak delamination (poor AL-SL interaction, S1; destructive delamination (AL-SL interaction causes destruction of composite membrane), S2; and an optimized formulation for the delamination of PI-PBI blend, S3. S1 and S2 typically failed to delaminate PI/0.1PBI films but two were carefully treated for the purpose of this study. A third trial is demonstrated that by following the same iterative process a fully aromatic thin film PI can also be delaminated via this process.

Experimental

Polyimide Films

Polyamic acid was formed by suspending 206 mg of 3,5 diaminobenzoic acid and 2.66 mg of tris-aminomethylphenylamine in 2.5 ml of anhydrous THF by sonication. 300 mg of pyromellitic dianhydride, sublimed under vacuum at 280 °C was added to the mixture stirred with a magnetic stir bar. The monomers were allowed to react for ~3 hr during which the soluble precursors polymerize to form the THF soluble polyamic acid. 2.5 ml of THF were added to dilute the overall solution to ~15% total solids. The mixture was then centrifuged at 3000 rpm for 5 min to separate any residual, insoluble precursors. The solution was then decanted onto a clean, acid washed, glass plate and cast using a 0.15 mil doctor blade. Films were then cured at 300 °C for 4 hr.

Polyimide-Polybenzimidazole Blend

PI was prepared as described as above where 2.5 ml of dimethylacetamide DMAc and 100 μL of 10 wt% solution of PBI in DMAc instead of an additional 2.5 ml of THF.

Epoxy Resin

4,4 methylenebiscyclohexylamine (stored under argon, MBCA) was dissolved in 3.25 g of PEG 200 at room temperature and under ambient atmosphere. 1.11 g of Bisphenol A Diglycidylether (BPA-DGE) was added followed by 10 min of stirring at 700 rpm until completely dissolved. The sample was then degassed under vacuum. An ~11 cm x 7 cm 12 g/m^2 carbon fiber nonwoven fabric was placed atop a clean glass substrate with thermally cured thin film AL. Epoxy resin was then allowed to absorb to the full dimensions of the fabric.

Three resin formulations were made differing by the amount of diamine present in the resin summarized in Table 1-6.

The resin was then cured by heating on a hot plate for 2 hr at 60 ^{o}C followed by heating at 120^{o}C for 2hr.

Scanning Electron Microscopy (SEM)

Samples were prepared by drying out membranes (usually kept wet) and freeze fracturing them under liquid nitrogen to avoid excessive damage to the pore structure and cross sections. SEM images were acquired on a NOVA 230 (ThermoFisher Sci.) SEM (UCLA Engineering V) and JEOL JSM-6700F FE-Scanning Electron Microscope (UCLA Chemistry and Biochemistry). Due to the insulating nature of these polymers, membrane samples were plasma sputtered to form a 1 nm thick gold layer. Low voltage was used to prevent excessive surface charging. Images were taken at a 45° tilt angle and varying magnification.

Variable Pressure, Flux and Compaction Experiments

Compaction experiments were performed in a Sterlitech 300 ml DEC with stirring pressurized by nitrogen gas at 50 psi increments beginning at 50 psi with max pressure of 500 psi. Flux was tracked gravimetrically and recorded on a computer. The average and standard deviation of all flux data points for a given pressure were taken excluding those within ~2-3 min of pressure change.

X-ray Photoelectron Spectroscopy XPS spectra were obtained using Kratos Axis Ultra XPS (UCLA Chemistry and Biochemistry). Survey scans were taken at a pass energy of 160 eV and high-resolution scans taken at a pass energy of 20 eV for N, C, and O. Bonding environments were analyzed by spectra deconvolution using a casaXPS program.

Results and Discussion

SEM Images

Although, for this study S1 and S3 were available for testing, films with these compositions were difficult to obtain due to typically poor adhesion to the active layer, or inability to delaminate. While originally, we thought reduction of hardener would open up sites in the epoxy support for binding to the AL as opposed to the hardener, to yield more successful adhesion, SEM lends evidence to similar patterns of AL failure in both the amine rich S1 and amine deficient S3.

In order to obtain SEM images, the complete membranes had to be dried thoroughly, taking them out of their functional state. Figure 1-30 reveals folds in the AL of S1, showing poor chemical adhesion to the SL. The folds may have formed while the epoxy was curing or possibly when the films were soaked in brine solution. While these folds may not diminish membrane rejection, they provide sites for foulant accumulation and may affect flux due to surface turbulence or higher resistance for permeation as water will face additional resistance through that region or no flux at all.

Additionally, Figure 1-30-c shows that along the freeze-fractured edge, the membrane is peeling off of the SL. Small fragments of support appear on the underside of the AL suggesting not poor SL-AL adhesion, but perhaps lower cohesion of the very dense SL (relative to S2) leading to crumbling. SEM images from S2 show a well adhered support layer. Figure 1-30-a shows a profile view of the AL-SL interface where a measurement of AL thickness is captured. Unlike in S1, the active layer remains taught against the SL rather than peeling off and the underlying SL(Figure 1-30-d-f) appears more porous. Figure 1-30-d shows the freeze-fractured edge of S2 where the active layer remains flesh against the SL and the carbon fibers encapsulated by the epoxy compared to Figures 1-30-c and 1-30-b where the fibers are detached from the composite. Fiber incorporation and AL adhesion are indicative of a true composite, where the mechanical (and perhaps diffusion) properties of the material reinforce one another. SEM images of S3, even though the MBCA content is much lower, are not indicative of enhanced AL-SL adhesion as expected due to less competition for epoxy sites between AL and MBCA. S3 has many of the same features as S1 as shown in Figure 1-30-a-b.

When using fully aromatic PI active layer without the 1%v/v addition of PBI, SL2 did not fully delaminate suggesting adhesion similar to that observed in S1. Using the same iterative approach to composite formation for the PI/.01PBI, the MBCA mass was adjusted to 77%, midway between S2 and S3 amounts, to yield full delamination of fully aromatic PI. This film's flux data is shown alongside that of the optimized PBI film. As expected, the film has a reduced flux, but the compaction resistance, a sought-after property in membranes, remains even at high pressures.

XPS analysis is needed to probe the chemical nature of the SL-AL interface. XPS was used to analyze the chemical environment directly beneath the AL. Survey scans were used to obtain the data summarized in Table 1-7. The atomic percentages of C, N, and O are similar, as would be expected, but it can be noted that the concentration of O and N at the interface is slightly higher for the films that showed successful delamination using an optimized formulation, S2 and S-PI as opposed to S1 and S3. Analysis of the high-resolution scans of the C1s and O1s spectral regions show some differences in bonding environments (Figure 1-30). It is inconclusive whether these data can provide insight into AL-SL adhesion.

Conclusions

We have proposed a general approach to the fabrication of functional membranes from a variety of non-traditional membrane materials and demonstrated adaptability of the technique to two different amine rich AL's using an epoxy-based support layer.

The T-FLO method was optimized to create high-flux and low compaction membranes with a PBI active layer and then, using the same materials, tuned to create membranes with PI active layers. SEM imaging paired with flux analysis and XPS helped elucidate the differences among membranes during SL optimization with 3 identical AL.

SEM images reveal several surface defects present in membranes made with the same active layers but differ in amine additive to the epoxy-based support. Differences in membrane flux can be identified but, the overall compaction resistance of the original optimized membrane is retained, given that a membrane can be successfully delaminated from the substrate.

Tables

Table 1-1: Parameters for T-FLO Membranes Without Nonwoven Fiber Reinforcement

Parameter	**Value**
4,4 methylene(bis)cyclohexylamine	330 mg
polyethylene glycol (PEG 400 and PEG 200 combined as noted in text)	3.25 g
bisphenol A diglycidylether	1.14 g
Stir time at 700 rpm	1.5 hr
Cure Time	4 hr
Cure Temp.	120 °C

Table 1-5: Summary of compaction data dependent on the ration of PEG200 and PEG 400 used as the porogen measured using a dead-end cell pressurized with N_2 gas.

%PEG 200	100	75	50	50 (3hr)	37.5	25	0
% PEG 400	0	25	50	50 (3hr)	62.5	75	100
Start Flux $L\cdot m^{-2}\cdot hr^{-1}\cdot bar^{-1}$	High	High	59.0	23.4	19.6	15.5	7.1
Final Flux $L\cdot m^{-2}\cdot hr^{-1}\cdot bar^{-1}$	--	--	43.5	9.0	20.5	15.2	6.9
% Compaction	--	--	26.3	61.4	-4.4	1.9	2.9

Table 1- 6: Table of values for initial flux, final flux, and % compaction for different materials used as a support fabric.

Veil Density & Material	**6 g/m^2 glass**	**10 g/m^2 glass**	**17 g/m^2 glass**	**22 g/m^2 glass**	**25 g/m^2 PE**
Initial Flux L·m^{-2}·hr^{-1}·bar^{-1}	93.3	11.3	6.0	8.2	4.2
Final Flux L·m^{-2}·hr^{-1}·bar^{-1}	3.0	2.7	0.5	4.2	4.3
%Compaction	96.7	76.1	92.1	48.4	-3.1

Table 1-4: O:S Ratios Derived from XPS Survey Spectra

Sample	**O:S**
PBI control	38.41:1
PSSA treated	13.46:1
PSSA treated + cured	5.22:1

Table 1-5: Elemental Compositions Derived from XPS Survey Scans for Membranes Before and After Treatment with NaClO

Atomic %	**C 1s**	**N 1s**	**O 1s**	**S 2p**	**Cl 2p**	**Na 1s**	**Ca 2p**
PA	81.44	4.14	14.42	0.00	0.00	0.00	0.00
PA-NaClO	79.02	3.86	15.24	0.00	1.53	0.34	0.00
PBI-PSSA	74.94	6.52	15.79	1.35	0.00	0.00	1.39
PBI-PSSA-NaClO	82.10	3.67	13.45	0.00	0.78	0.00	0.00

Table 1-7: Mass of MBCA in each SL Formulation

Sample	**MBCA (mg)**
S1	247.0
S2	210.4
S3	172.9

Table 1-8: Elemental Compositions of Support Layer Directly Beneath the Active Layer

Sample	**C 1s %**	**N 1s %**	**O 1s %**
S1	86.7	1.6	11.7
S2	83.0	3.1	14.0
S3	84.7	2.2	13.1
S4-PI	80.2	3.7	16.1

Figures

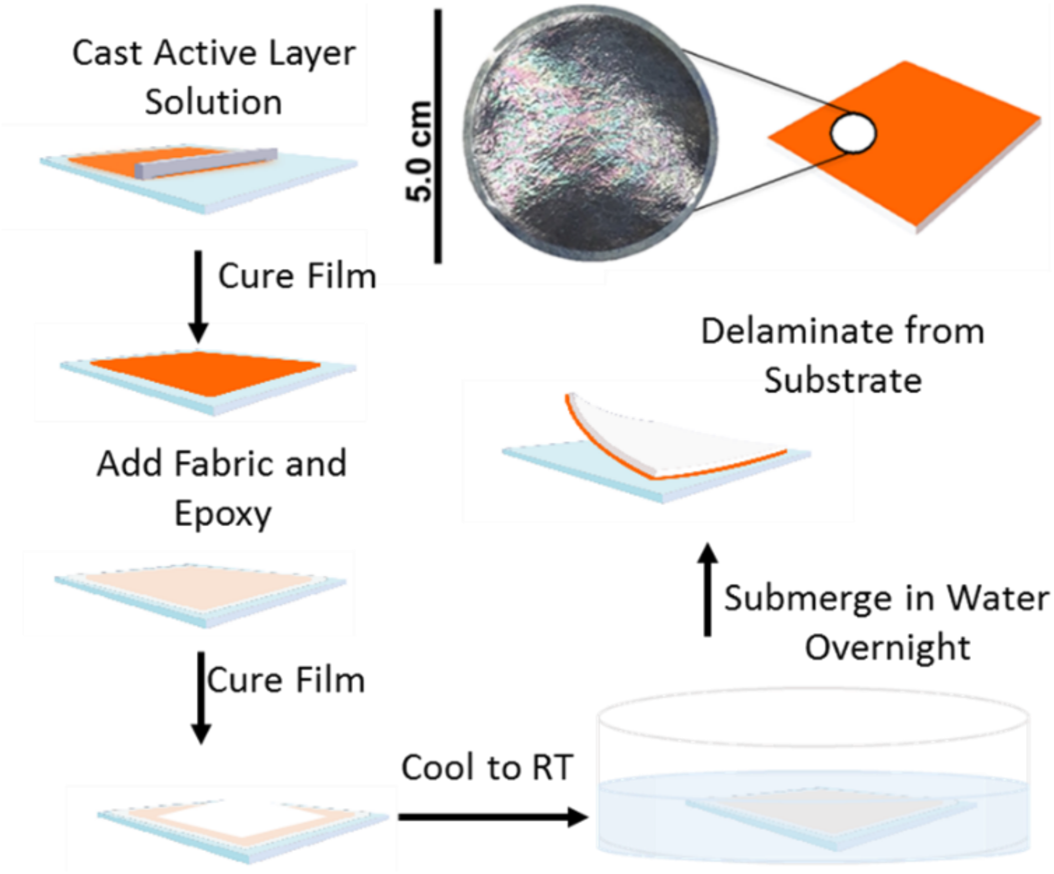

Figure 1-1: The steps for using T-FLO to make thin-film composite membrane.

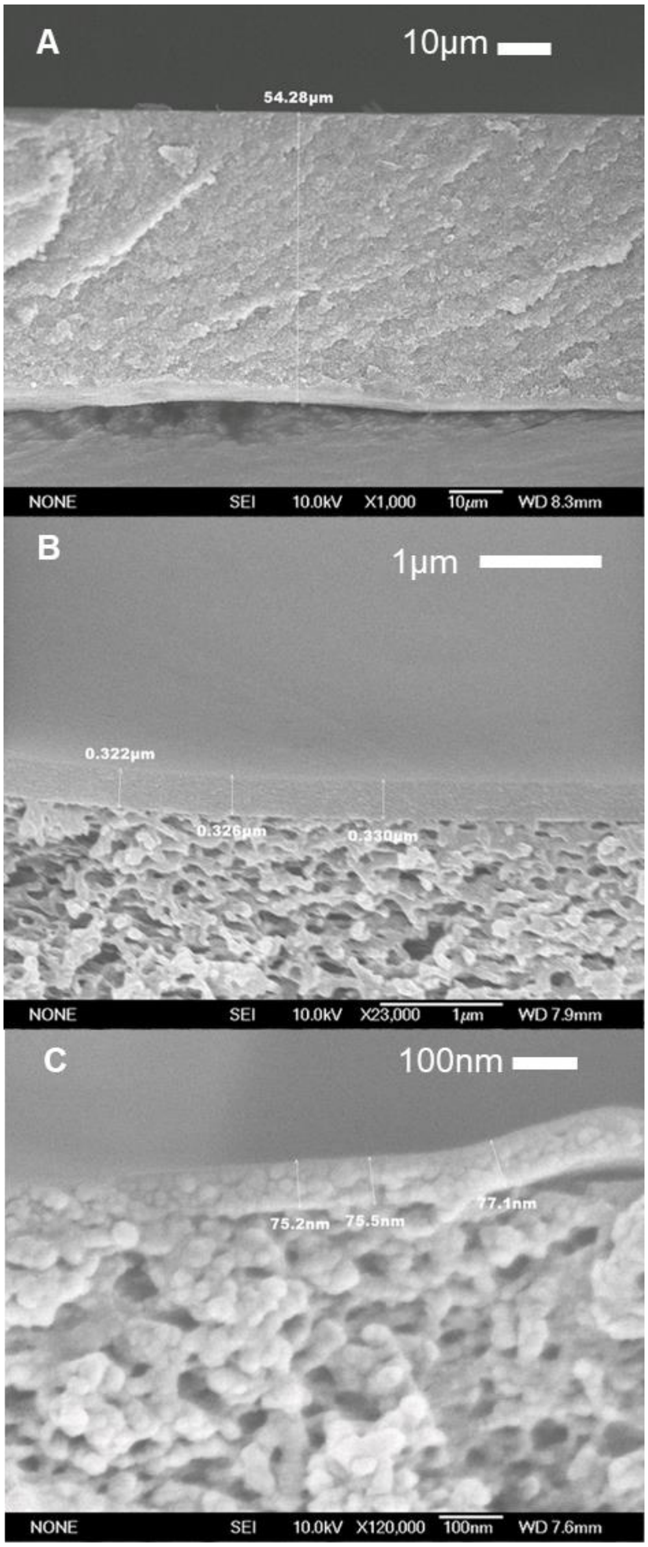

Figure 1-2: (A) SEM cross-section of T-FLO membrane 1,000x (B) Cross-section with active layer thickness, 23,000x (C) Cross-section with active layer thickness, 120,000x.

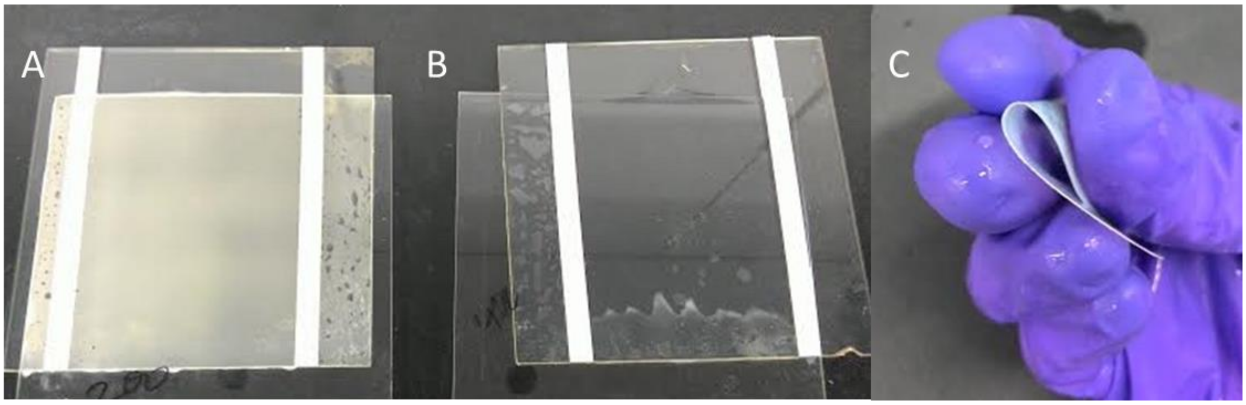

Figure 1-3: (A) Glass plates with tape spacer making a porous resin-support. (B) Glass plates with tape spacer making a less-porous resin-support. (C) A membrane made using the original T-FLO method being bent to show flexibility.

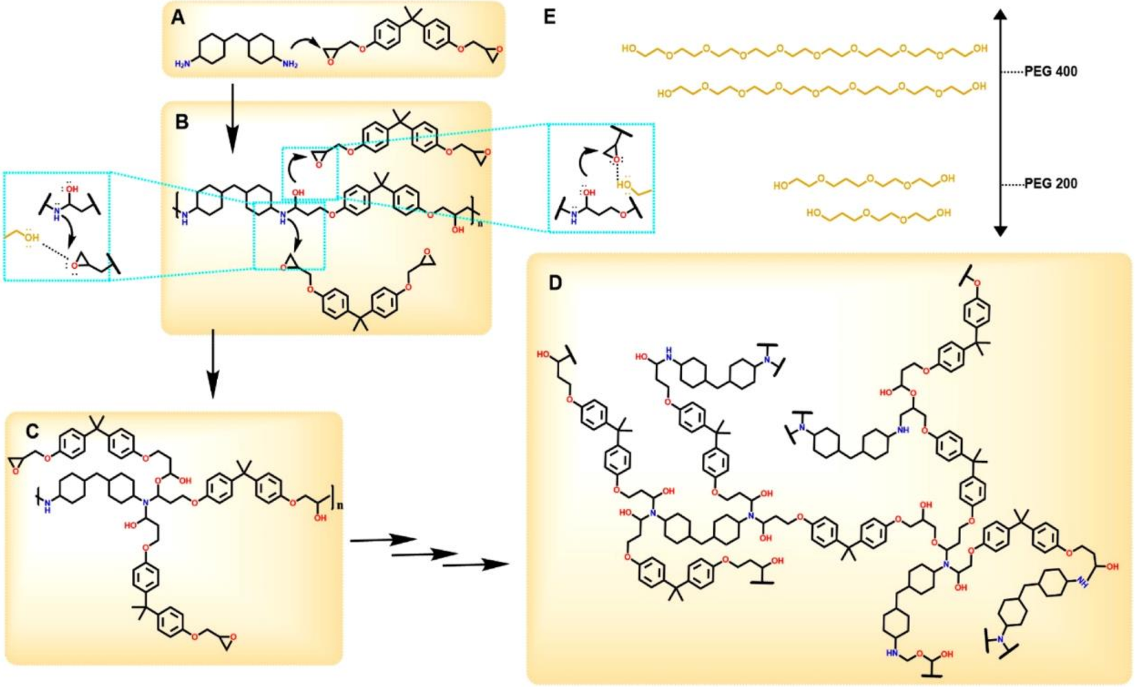

Figure 1-4: (A) Monomers MBCA (left) and BADGE (right) used for support layers. Tan regions represent PEG porogen. (B) After initial reaction of the monomers to form linear polymers, excess BADGE leads to secondary reactions between epoxy groups and alcohol or secondary amine groups to form branches and crosslinks. Insets show role of PEG in stabilizing the ring opening. With these reactions, PEG becomes displaced to form large or small pores. (C) Backbone with BADGE partially reacted. (D) Representation of support layer chemical structure. (E) Primary chemical structures of PEG 200 or PEG 400 represented by beige shading within the figure.

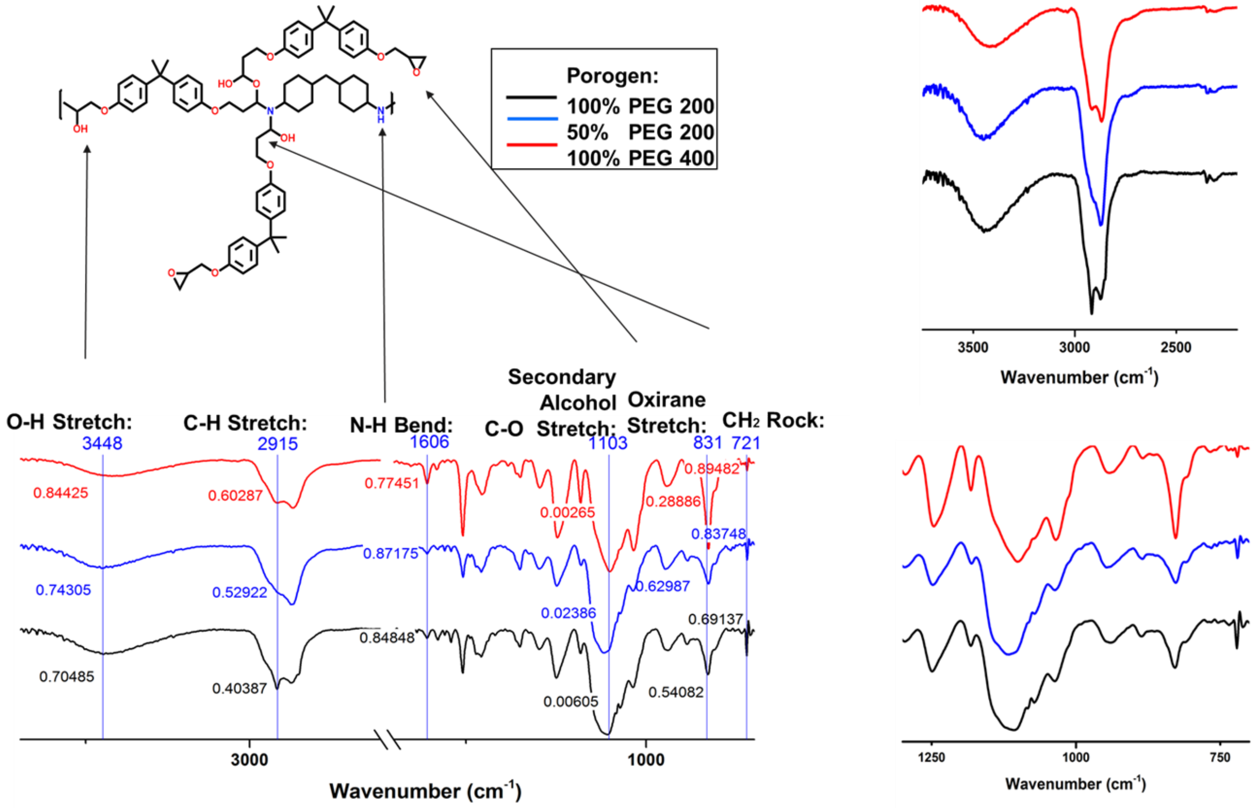

Figure 1-5: IR spectra of three epoxy samples made with different porogen compositions. Blue vertical traces indicate the region of particular functional groups and the numbers along each indicate the peak intensity at that energy. Smaller numbers indicate a stronger signal for that group. Changes in the OH and C-H regions indicate an increase in OH groups when PEG200 is used as the porogen and a change in the carbon environments. Oxirane decreases with more PEG 200 and secondary alcohol presence appears to increase.

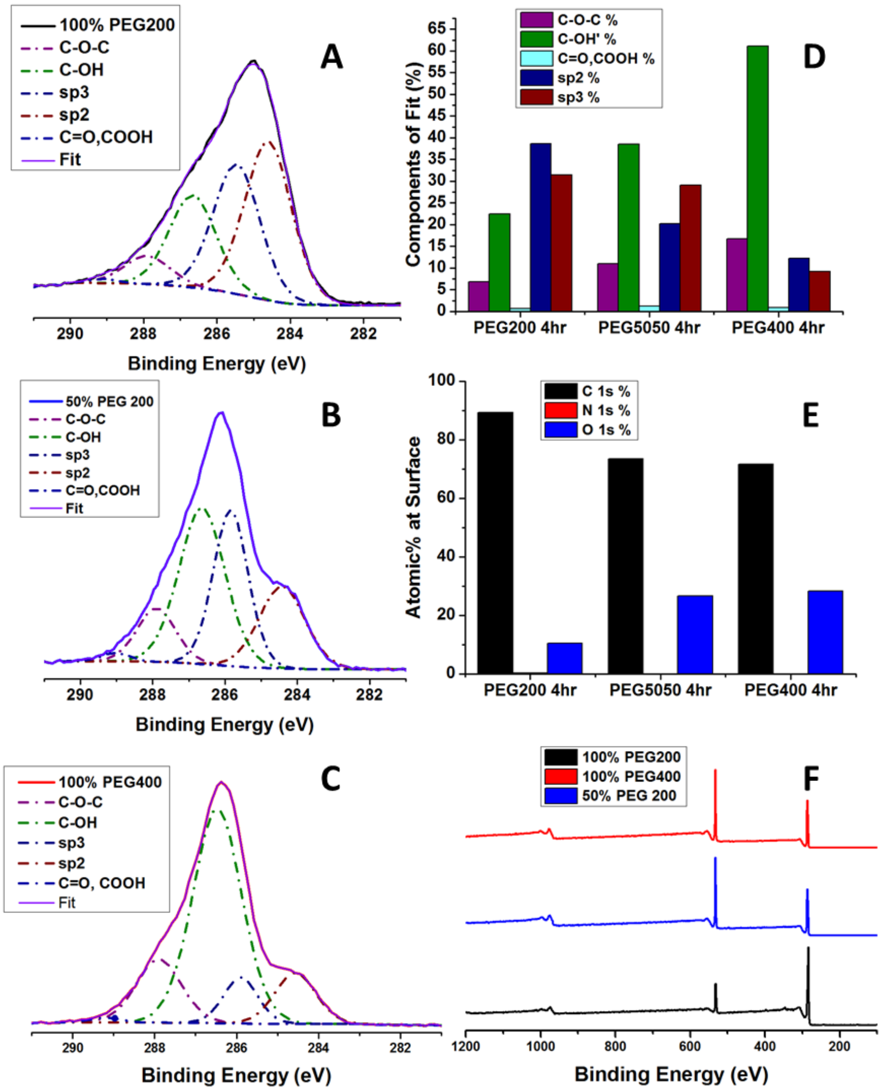

Figure 1-6: (A)-(C) High resolution XPS scans of the C1s region of epoxy samples cured with different PEG porogens, PEG200, 1:1 PEG200:PEG400, and PEG400. PEG was removed from epoxy before analysis. Increase in the presence of stabilizing OH groups shows a shift from more electron deficient carbons such as those in epoxide groups toward a more normal sp^3 bonding environment as in carbons bound to hydroxyl groups. (D) Graph showing relative areas of components of fits to XPS spectra in (A)-(C). While this is not precise quantitation of groups present, various trends for each component shows trends in carbon bonding environments that result from different resin curing environments. (E) Graph indicating relative concentrations of C, N, and O at the surface of epoxy samples. (F) Full spectrum scan of epoxy samples.

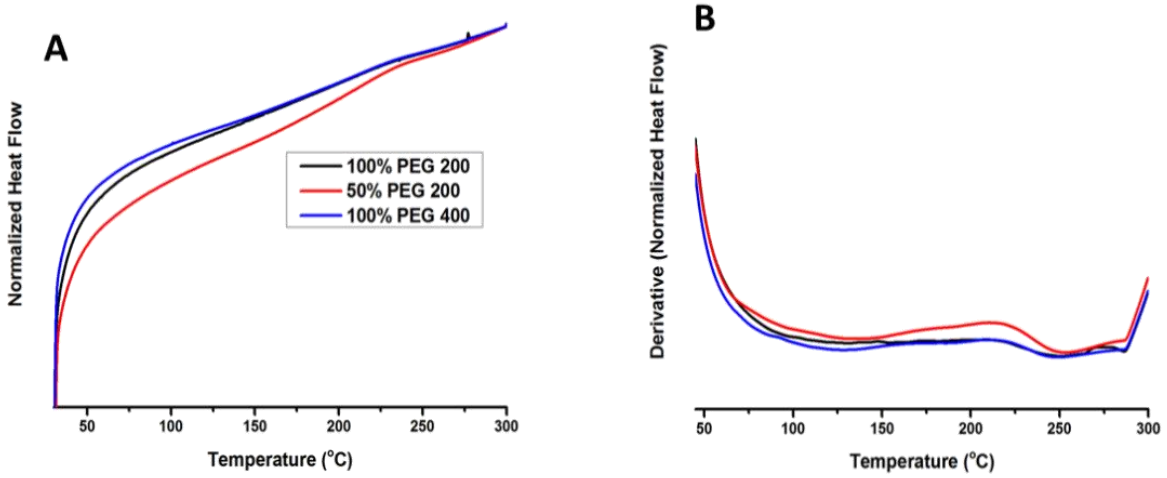

Figure 1-7: DSC traces of three epoxy samples made with different porogen compositions. (A) Normalized heat flow vs. Temperature (°C) (B) First derivative of normalized heat flow showing glass transition at approximately 245 °C for all three samples.

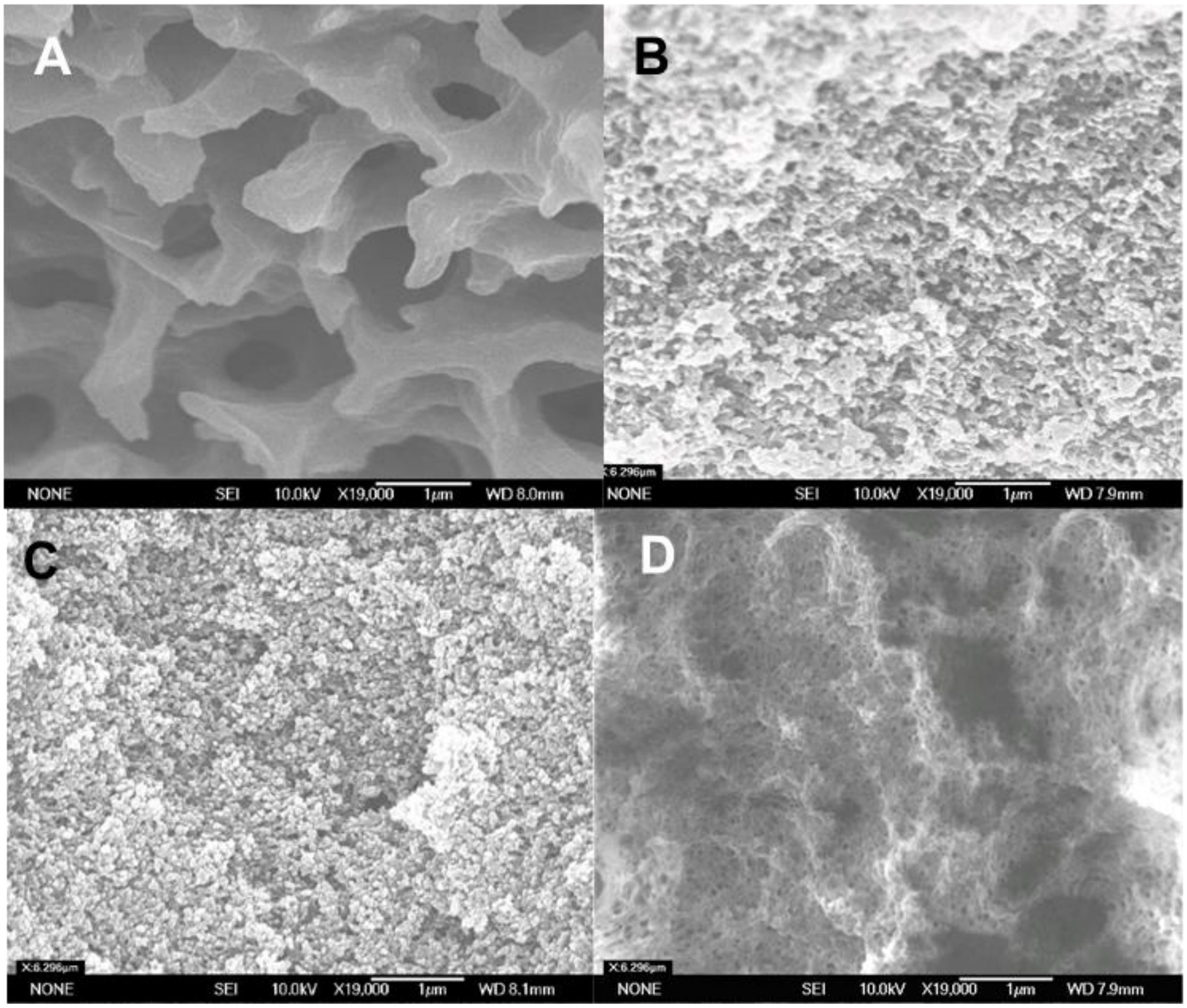

Figure 1-8: (A) membrane with 100% PEG 200 used as porogen. (B) membrane with 3:1 PEG 200 to PEG 400 used as porogen. (C) membrane with 1:3 PEG 200 to PEG 400 used as porogen and (D) membrane with 100% PEG 400 used as porogen.

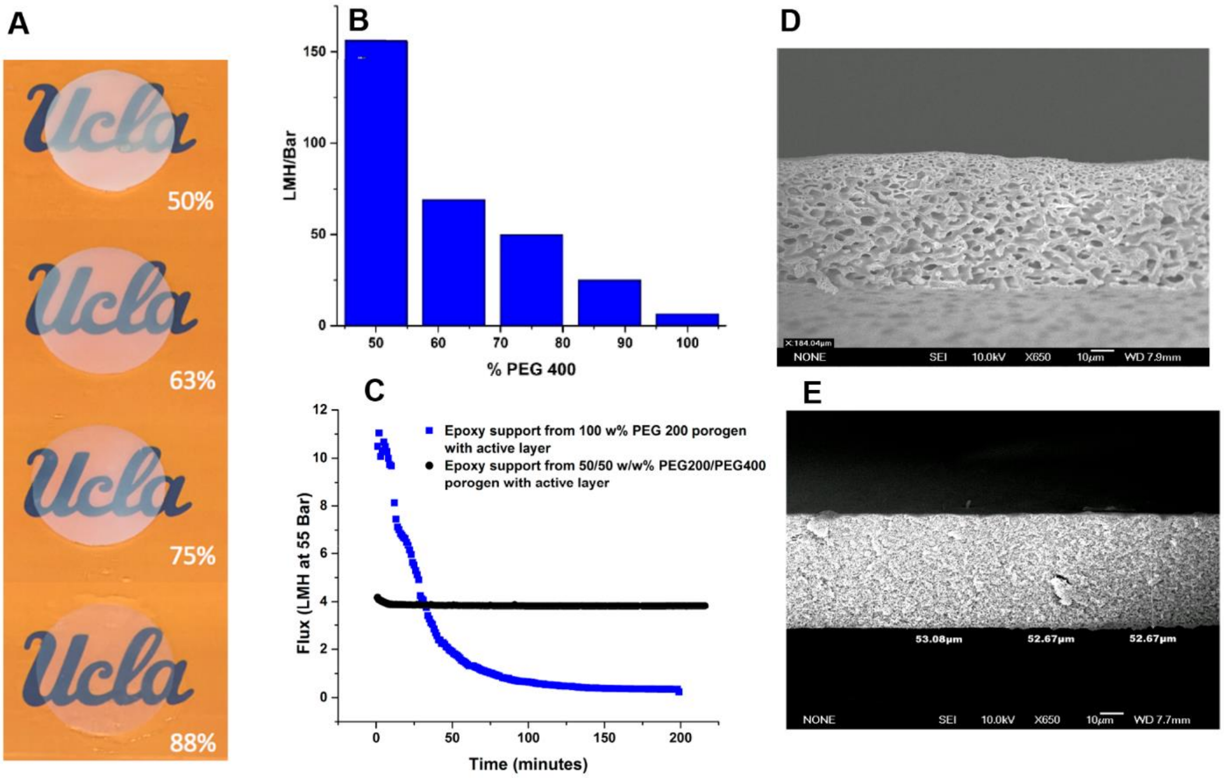

Figure 1-9: (A) Higher concentrations of porogen PEG400 produces membranes with enhanced density that appear more transparent when wet (Percentage of PEG400 in the porogen mixture stated in white) (B) Increasing the weight percentage of PEG400 in the porogen mixture produces denser epoxy support membranes that decrease permeability. (C) Denser epoxy support membranes improve compaction resistance. (D) SEM cross section images show an open pore structure and larger pores are observed in the support made from the 100% PEG200 porogen (E) and a denser pore structure with smaller pores are observed in the support made from 50/50 wt.% PEG200/PEG400 porogen.

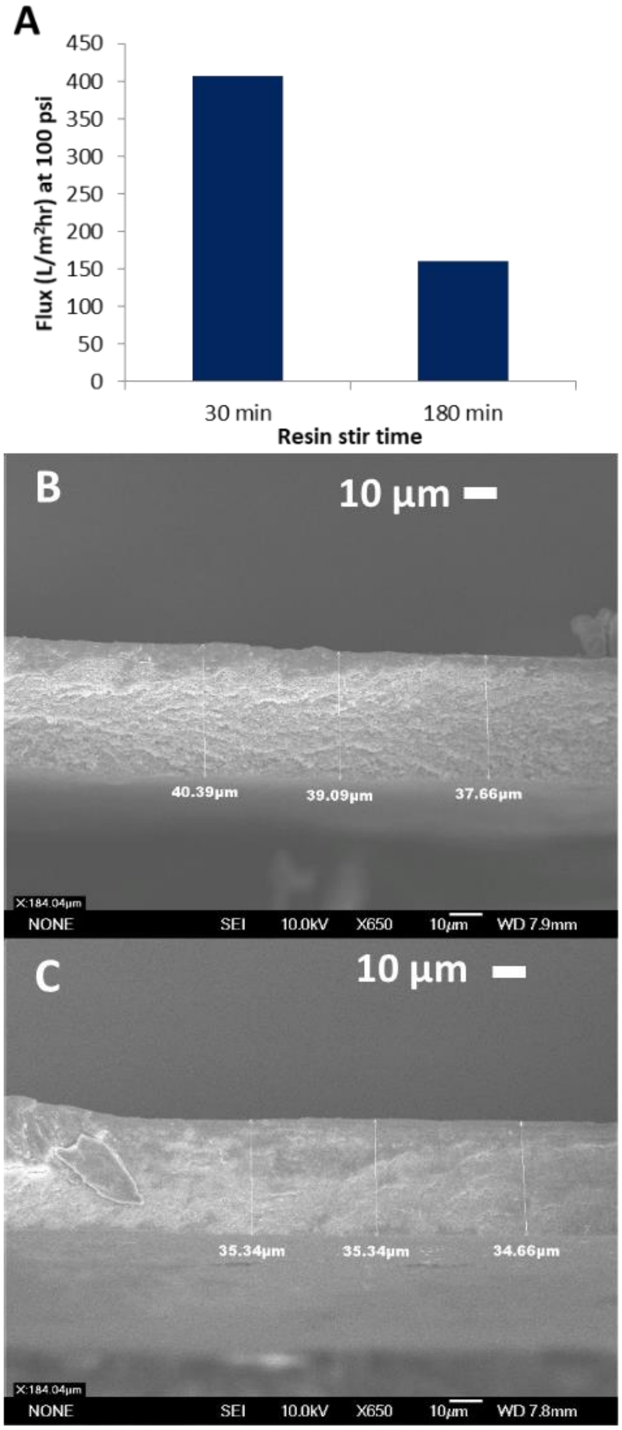

Figure 1-10: (A) Flux for resin stirred at 700 rpm for 30 minutes and 180 minutes prior to curing. (B) cross-sectional image of epoxy film from resin stirred for 30 min. (C) cross-sectional image of film from resin stirred for 180 min.

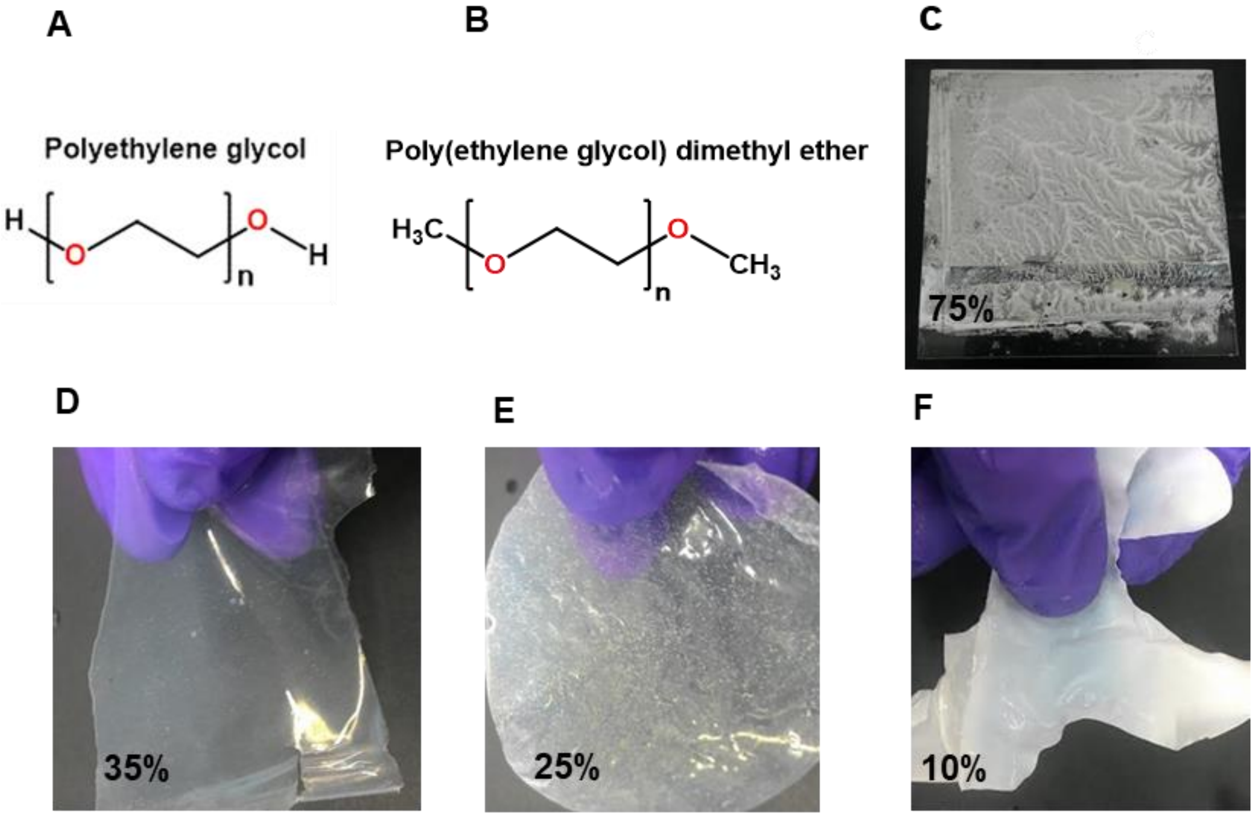

Figure 1-11: (A) Polyethylene glycol (B) Poly(ethylene glycol) dimethyl ether (C) Partially cured epoxy on glass substrate after porogen (75% Me-PEO Mn = 250 25% PEG Mn=200) removal resulting in a poor film quality that could not be removed from substrate. (D) Support membrane achieved with 35% Me-PEO Mn = 250 65% PEG Mn = 200. (E) Support membrane achieved with 25% Me-PEO Mn=250 75% PEG Mn = 200. (F) Support membrane achieved with 10% Me-PEO Mn = 25 90% PEG Mn = 200.

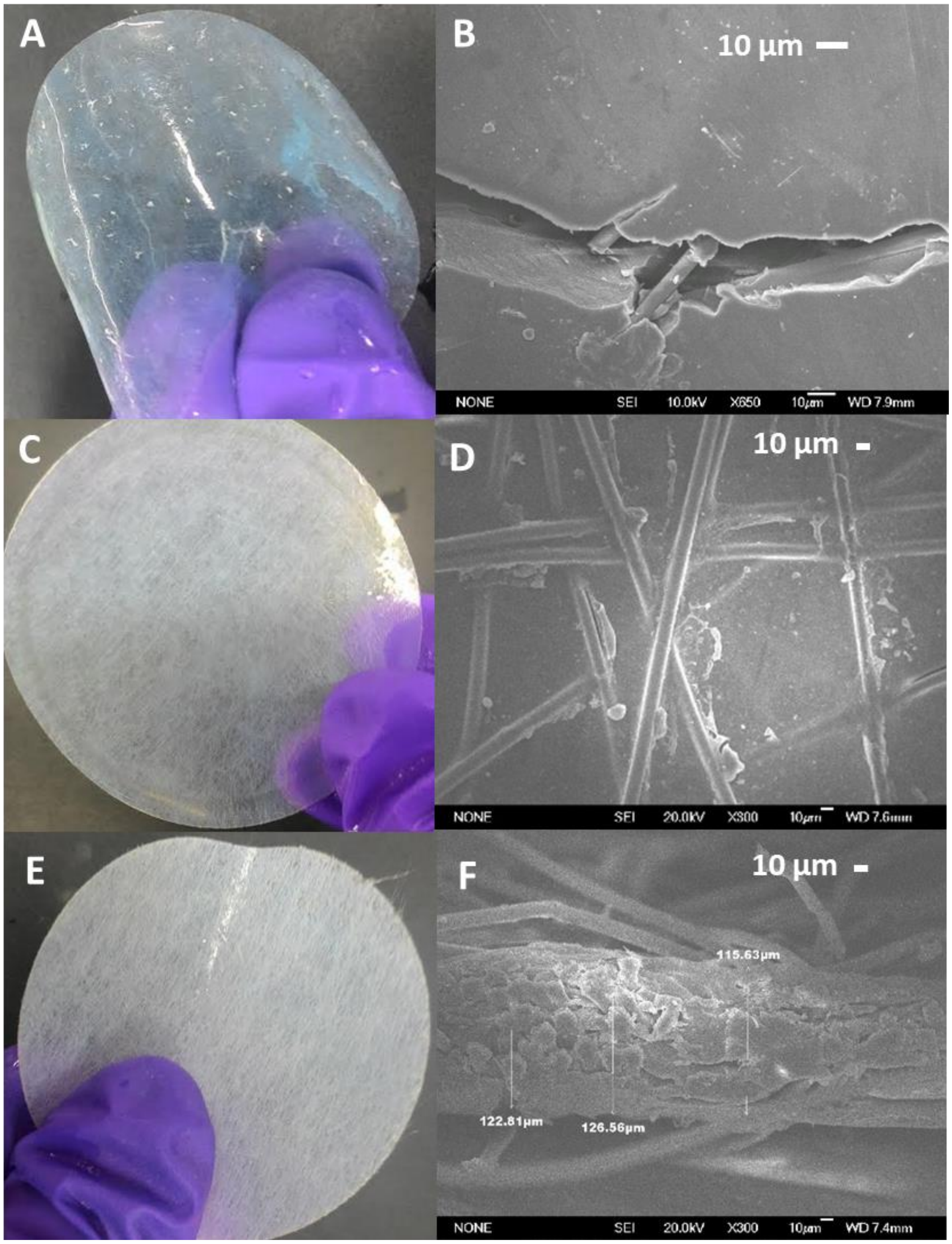

Figure 1-12: (A),(C),(E) 5 cm diameter membrane coupons with 6 g/m^2 glass veil, 22 g/m^2 glass veil, and 25 g/m^2 polyester. (B) surface of (A) at 250x magnification with fibers only visible in defect. (C) surface 30,000x (F) cross-section of (E) with fibers protruding out of the epoxy.

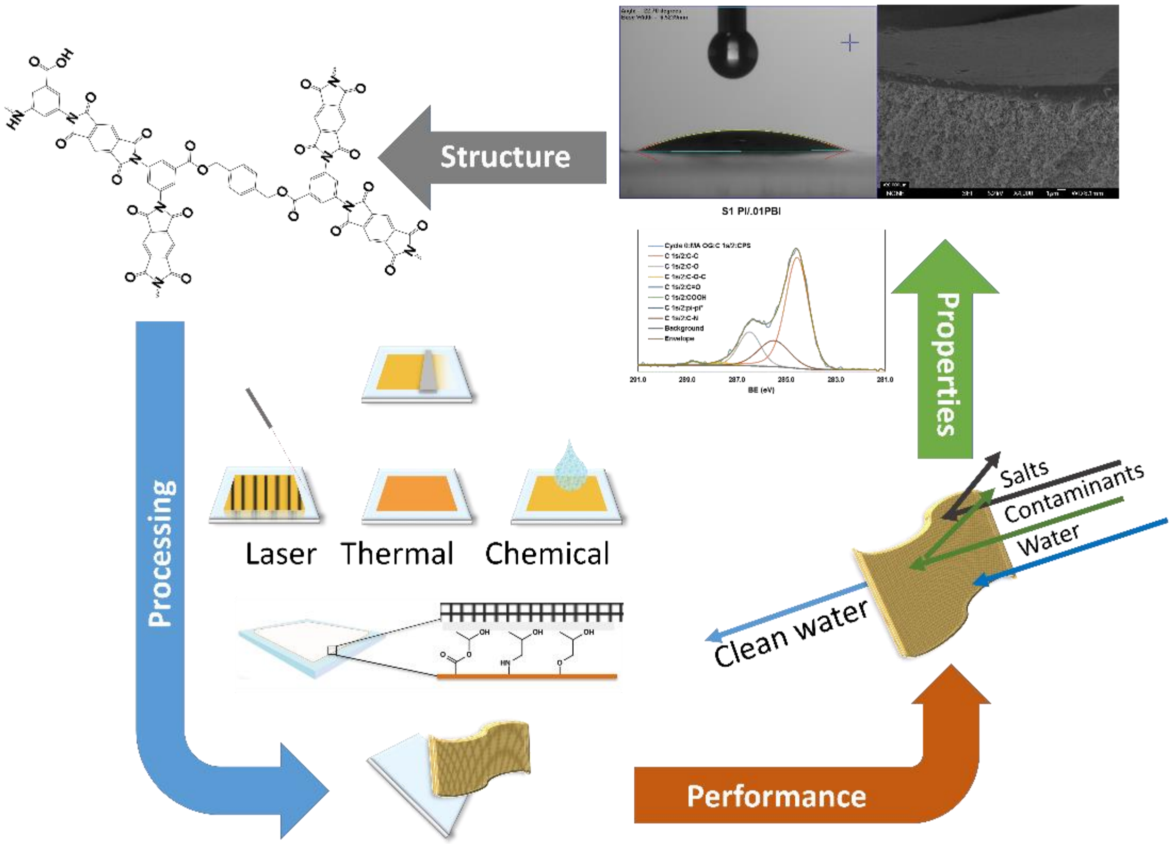

Figure 1-13: Process of using T-FLO for membrane discovery through a materials science framework.

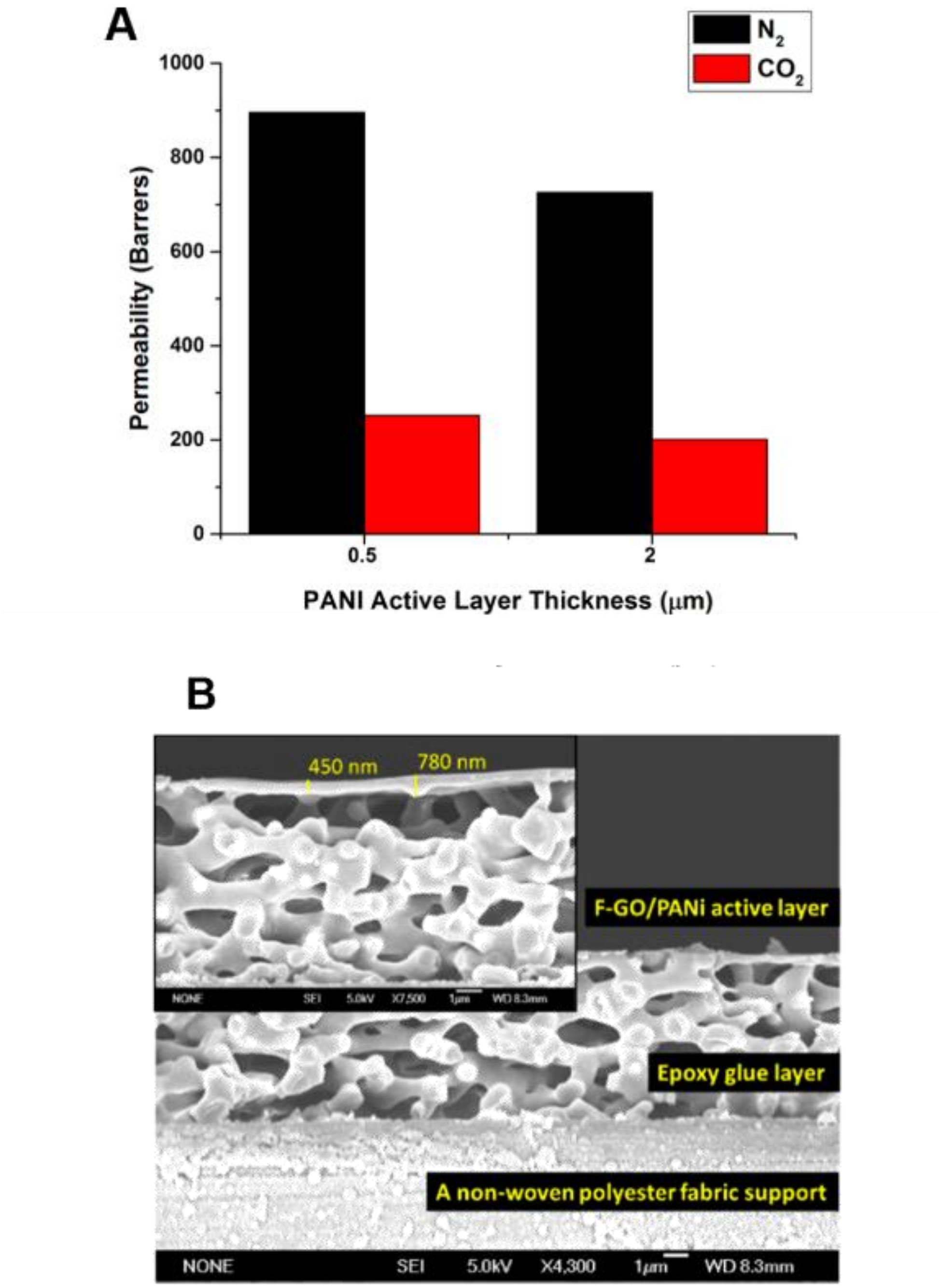

Figure 1-2: (A) Selectivity data for polyaniline (PANI) thin films with and without a support membrane. (B) SEM image of a sample PANI membrane cross section.

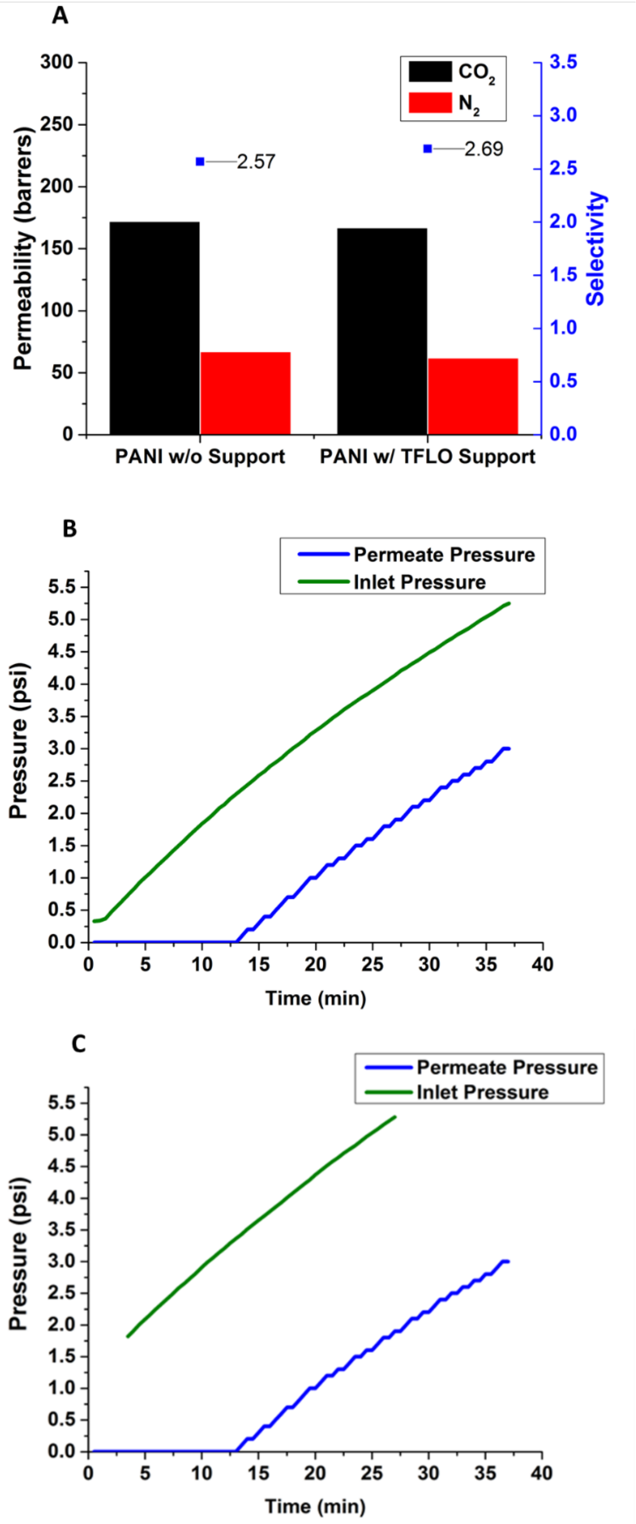

Figure 1-15: (A) Permeability of CO_2 and N_2 in PANI-GO membranes with and without a support layer (°C) (B) Inlet/outlet pressure without support (C) Inlet/outlet pressure with T-FLO support.

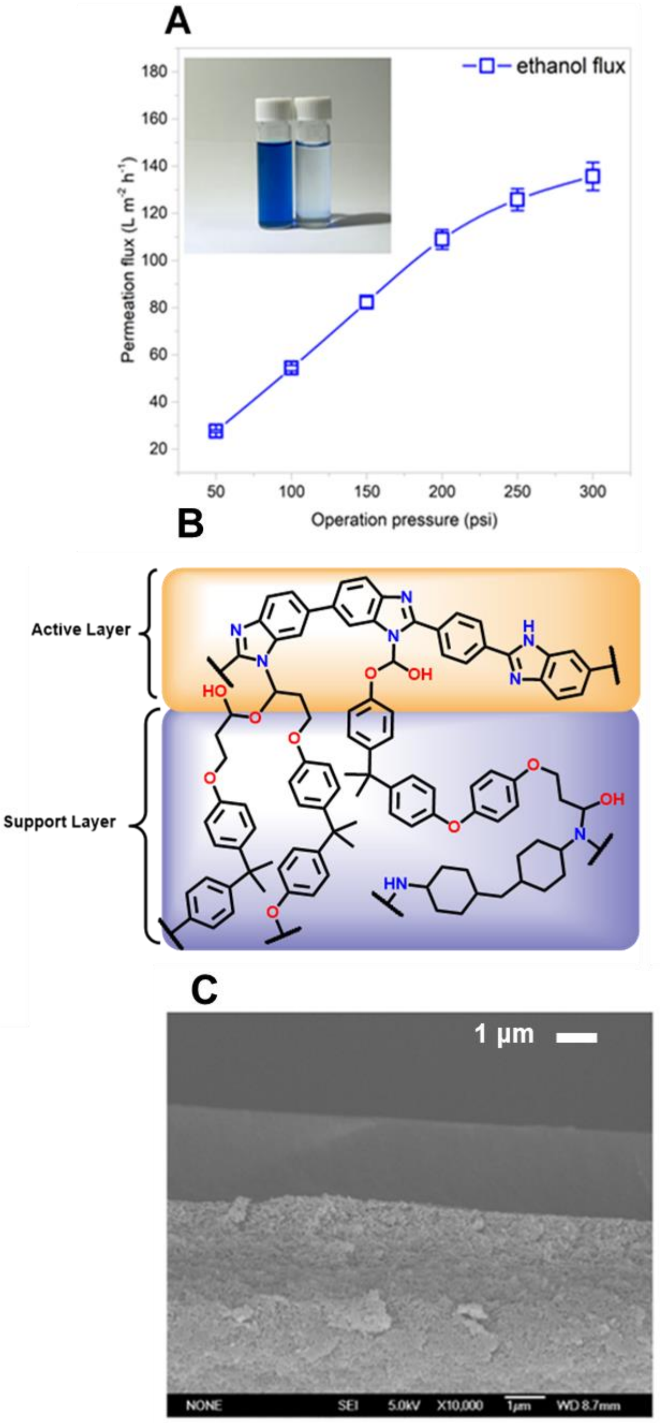

Figure 1-16: (A) Ethanol flux through a PBI OSN membrane. (B) Schematic of the active layer/support layer interface. (C) SEM image SEM cross-section of a PBI OSN membrane at 10 000× magnification.

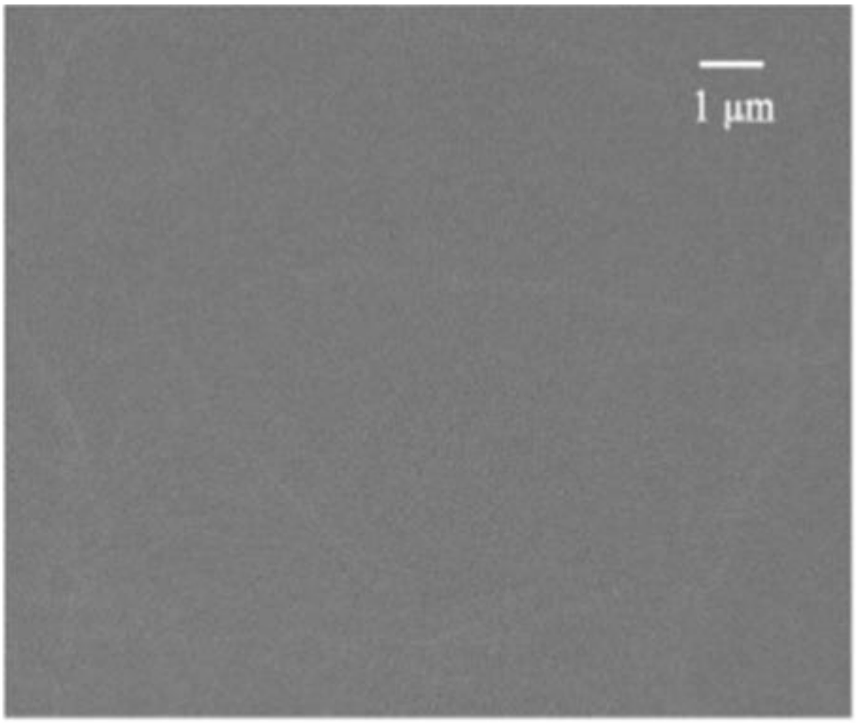

Figure 1-17: Surface of T-FLO RGO Membrane

(a) 10 mg/g

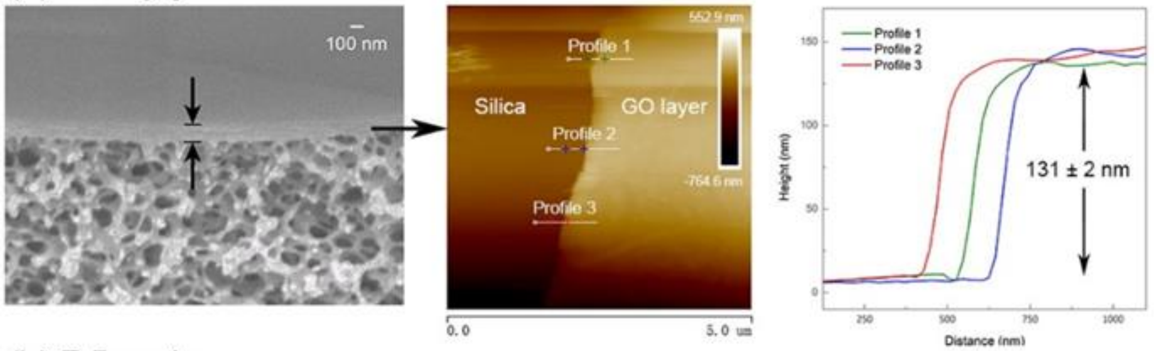

(b) 7.5 mg/g

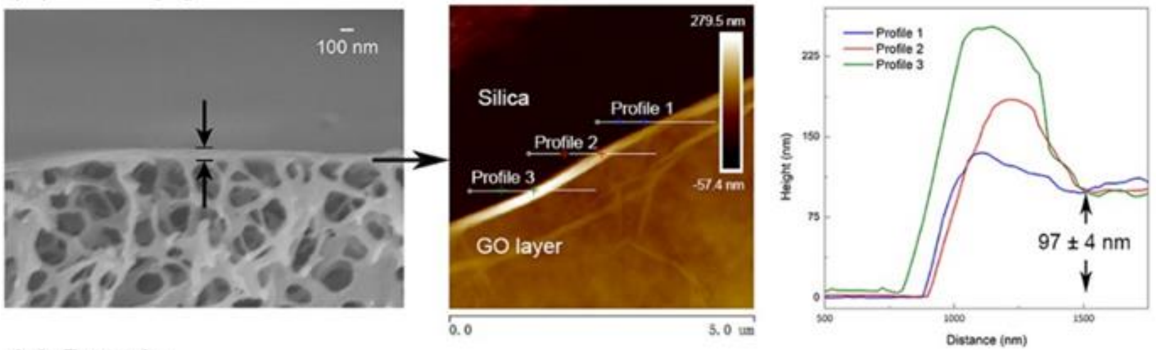

(c) 5 mg/g

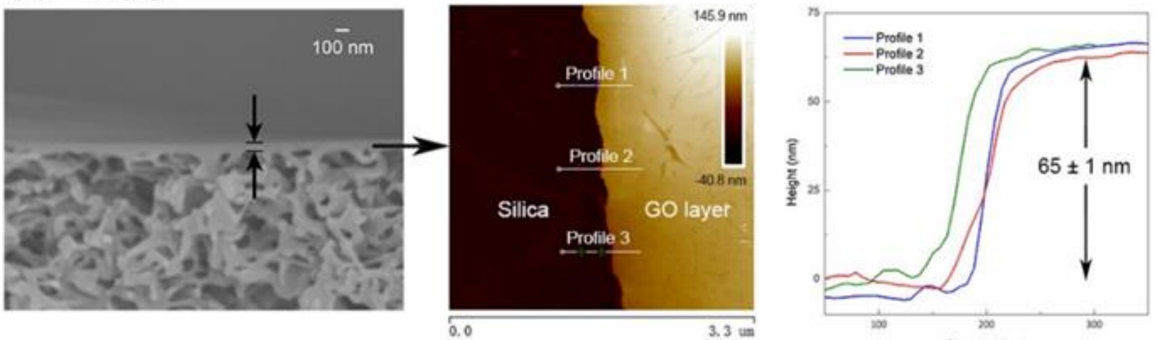

(d) 2.5 mg/g

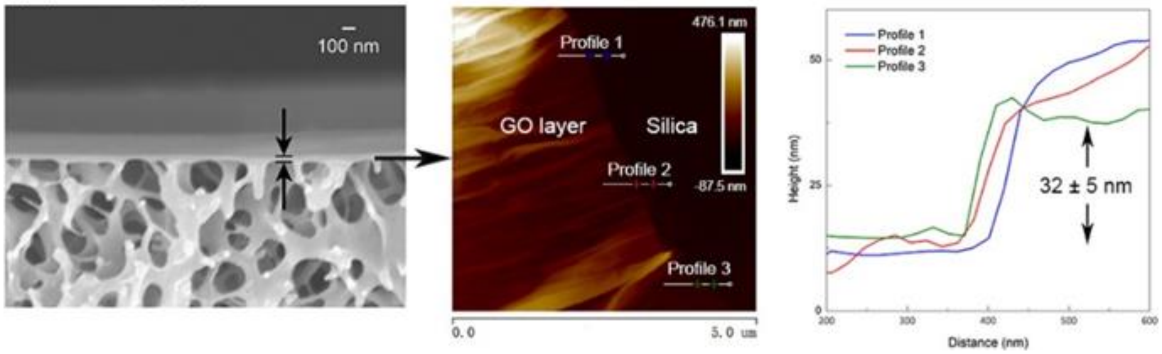

Figure 1-18: SEM images, AFM micrographs, and profilometric measurements of graphene-membranes made using T-FLO with different membrane thicknesses (a)-(d).

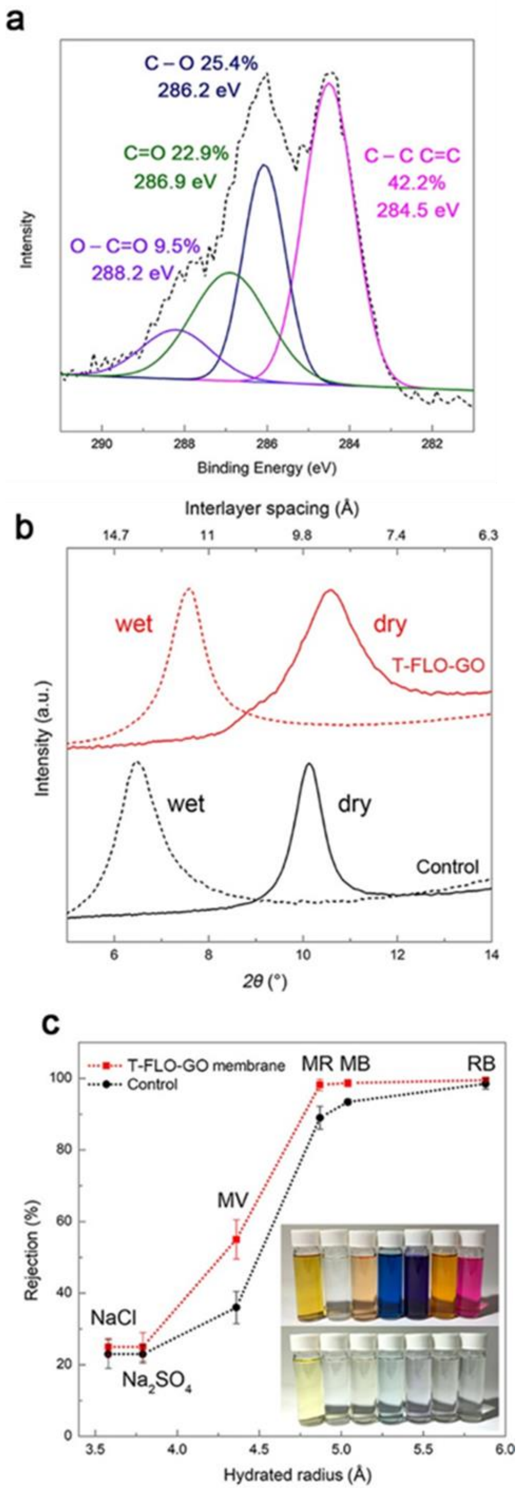

Figure 1-19: (A) XPS high-resolution scan of the C1s region deconvoluted. (B) XRD spectra for T-FLO GO and filtered GO. (C). rejection of salts and dyes by T-FLO GO membranes and filtered (conventional) GO membranes.

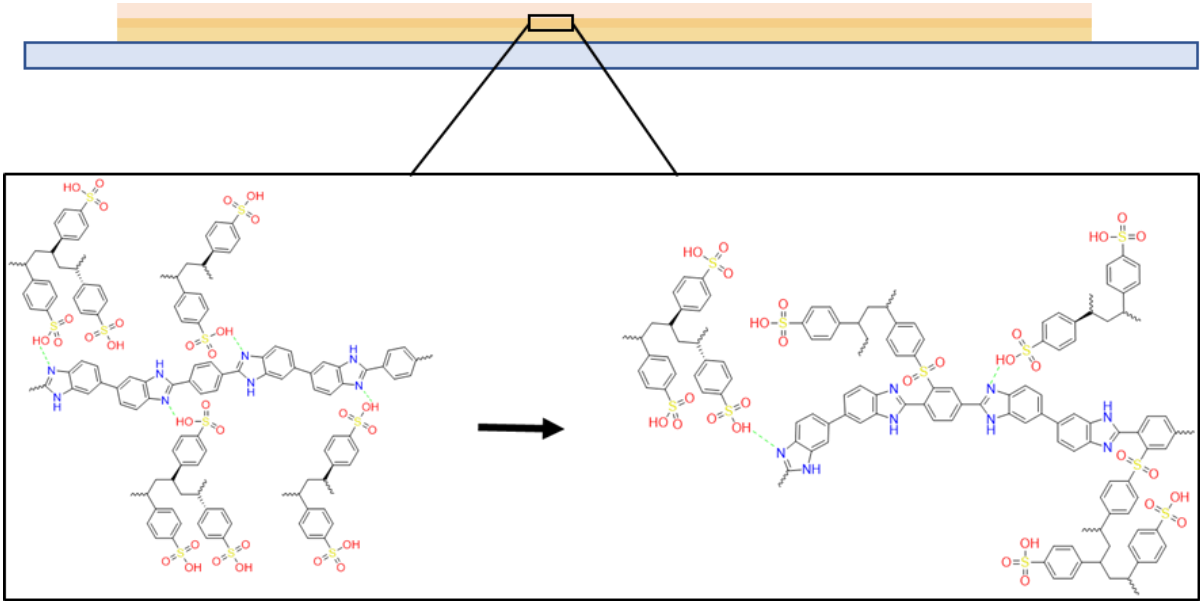

Figure 1-20: Schematic of PSSA(pink) film cast onto PBI(yellow) film atop a glass substrate. Crosslinking chemistry at the interface of the film.

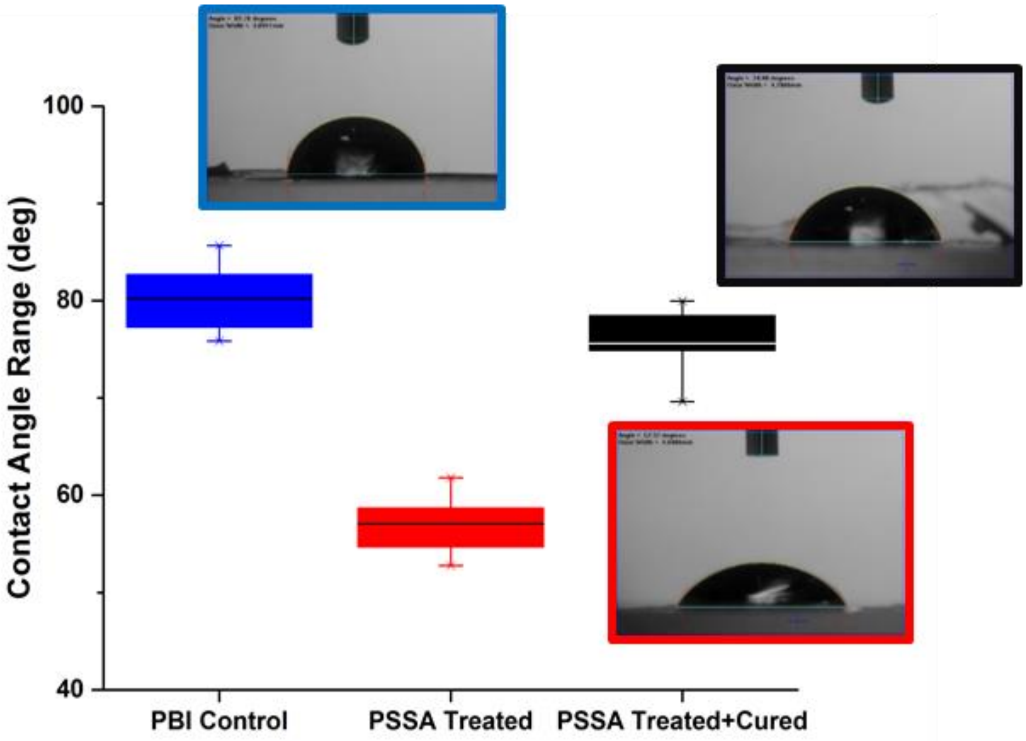

Figure 1-21: Contact angels for PBI, PBI w/PSSA, and the cured laminate. Pictures of representative water drops used in measurement.

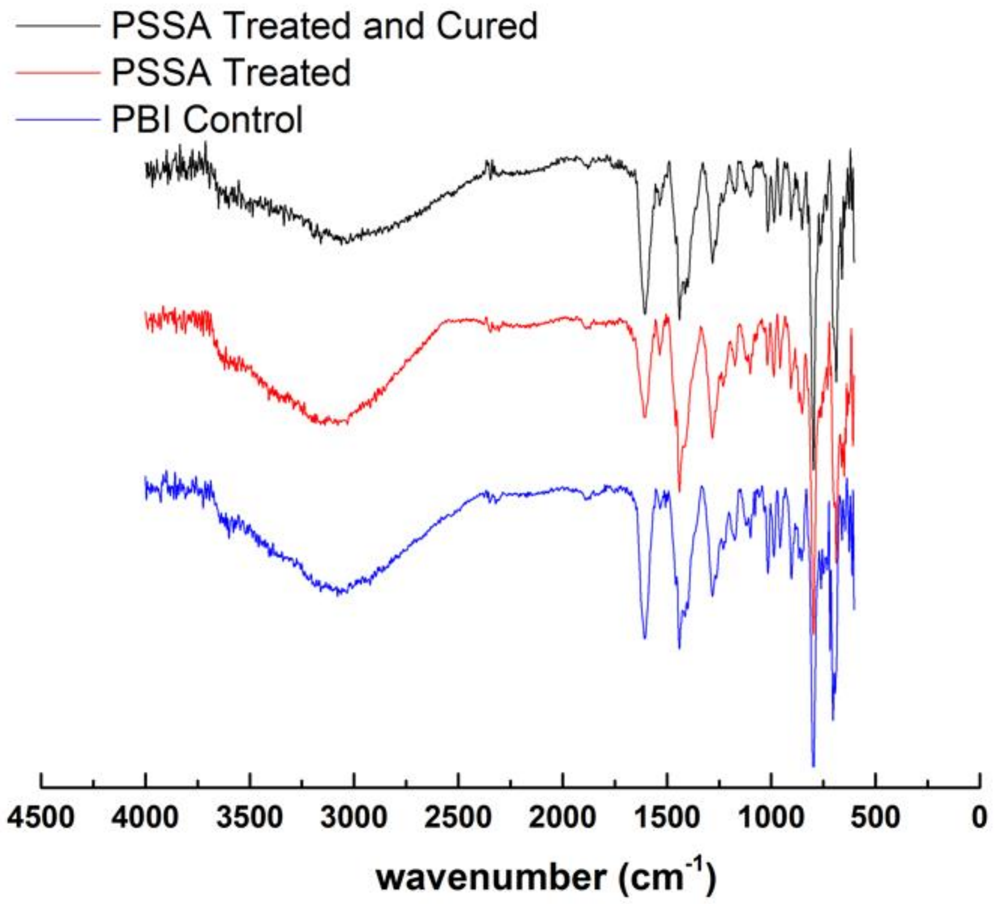

Figure 1-22: IR spectra of PBI, PSSA treated PBI, and cured PBI/PSSA laminate.

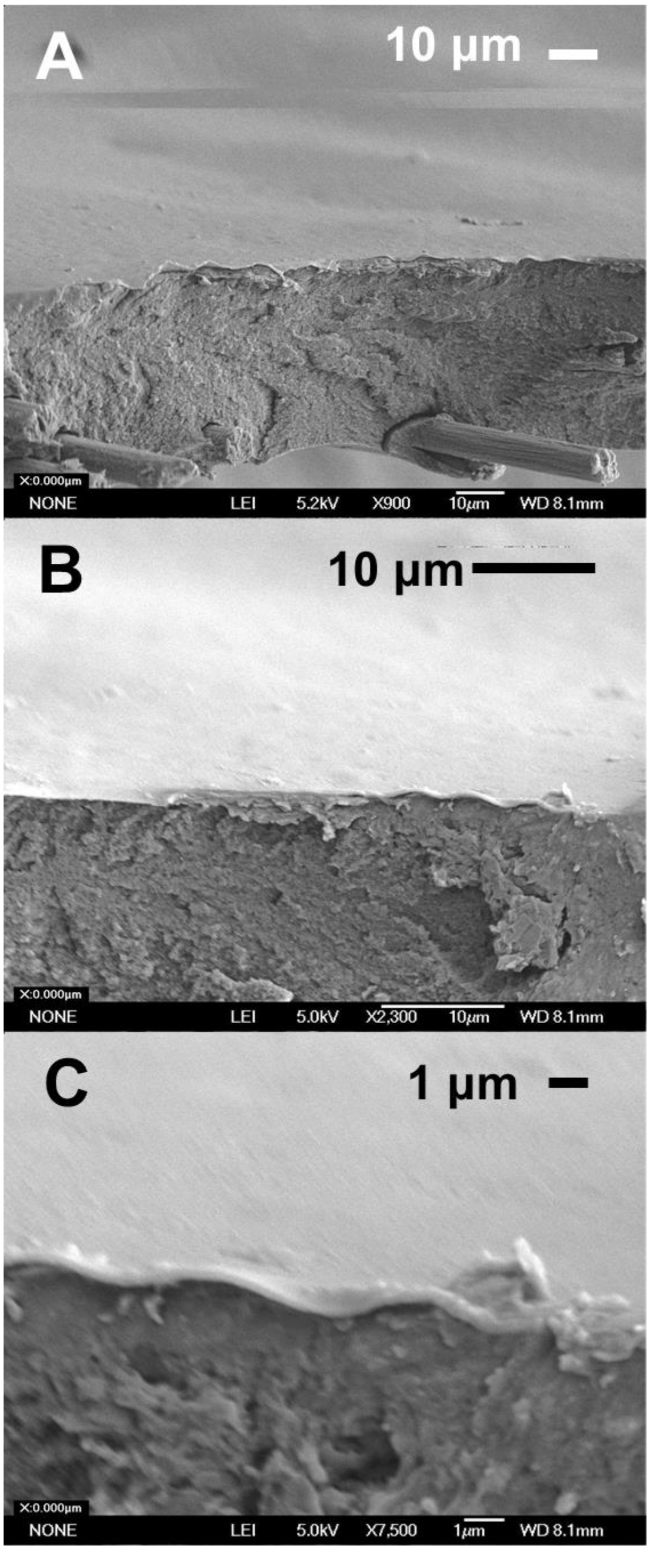

Figure 1-23: SEM images of PBI/PSSA membranes.

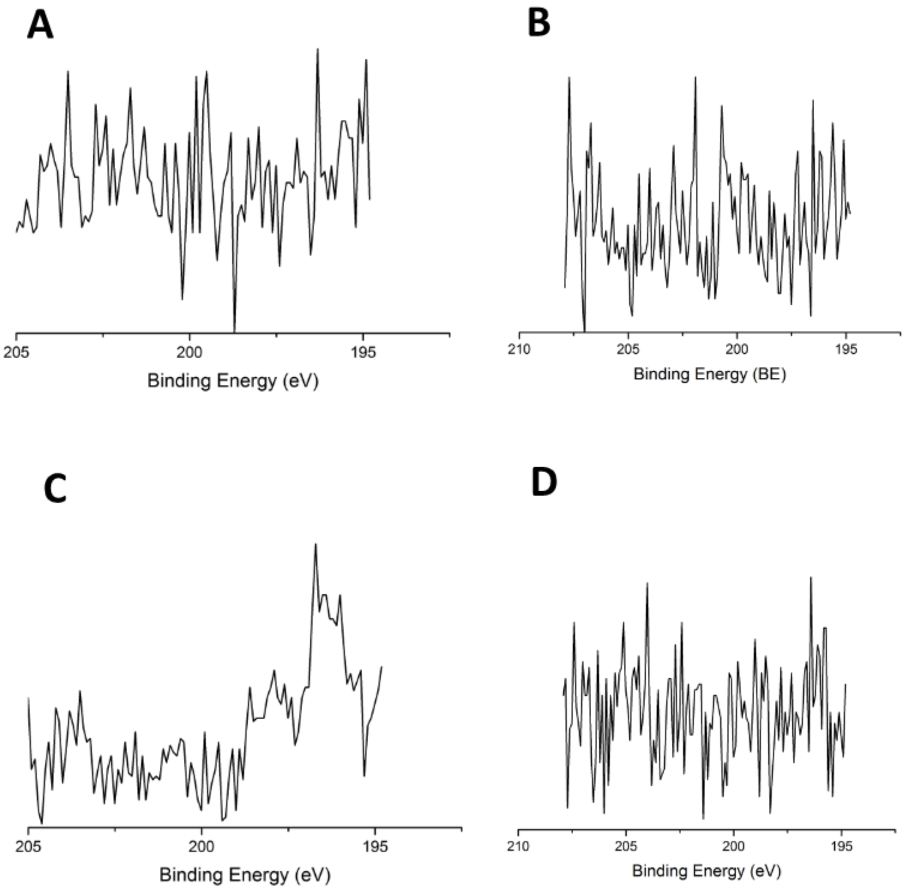

Figure 1-24: Polyamide (A) and PBI/PSSA (B) membranes before treatment with NaClO and after exposure (C)-(D).

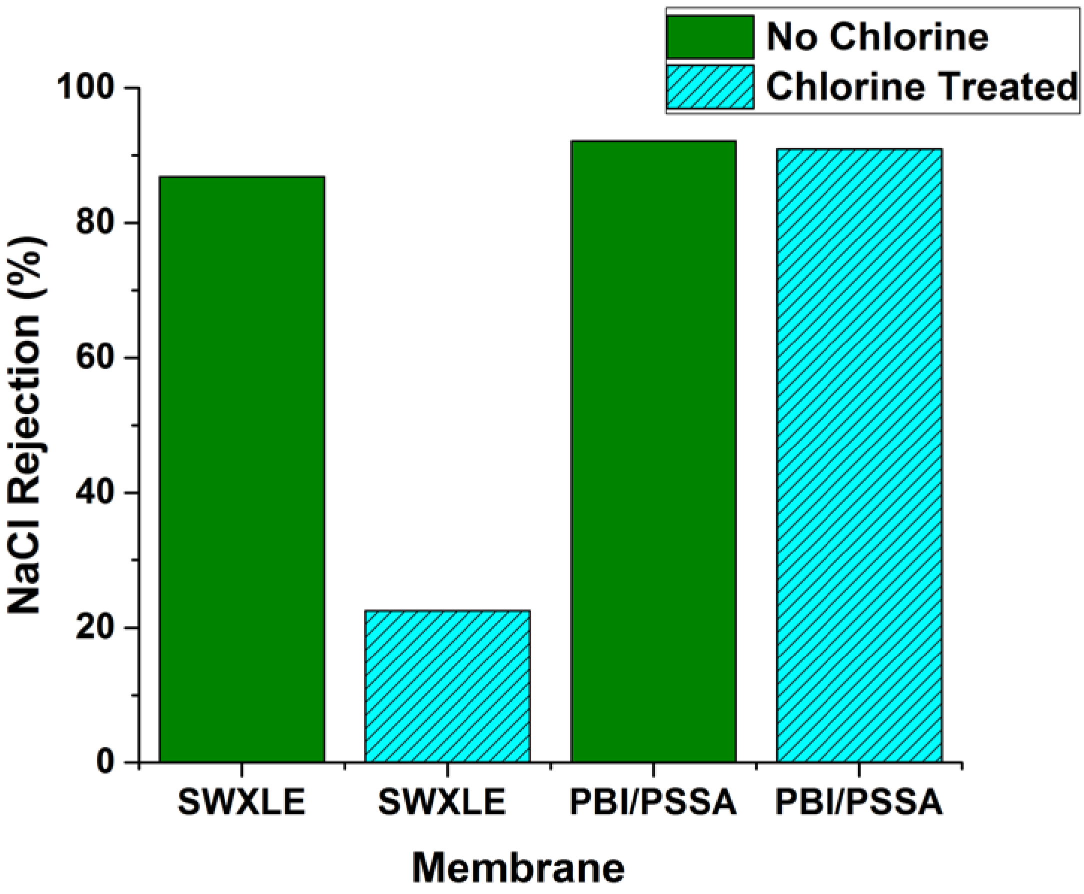

Figure 1-25: Rejection of 0.20% NaClO

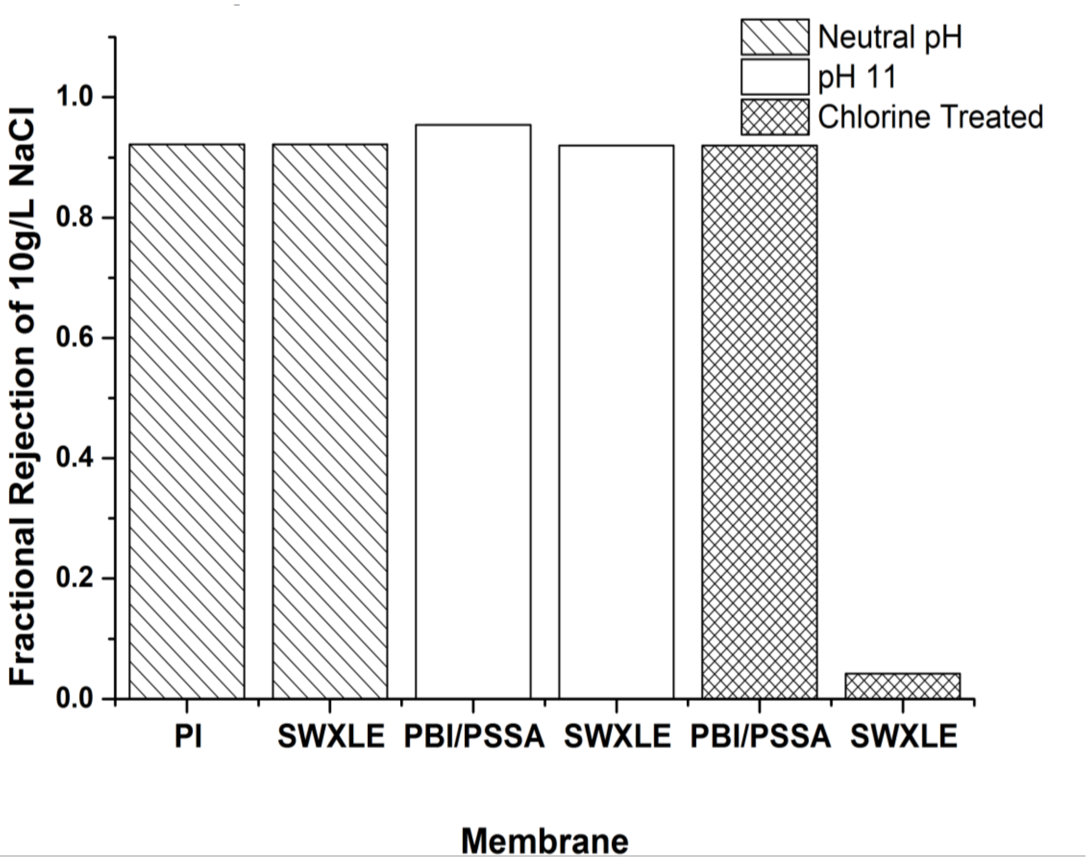

Figure 1-26: Membranes' rejection of 10.0g/L NaCl before and after chlorine degradation at high pH.

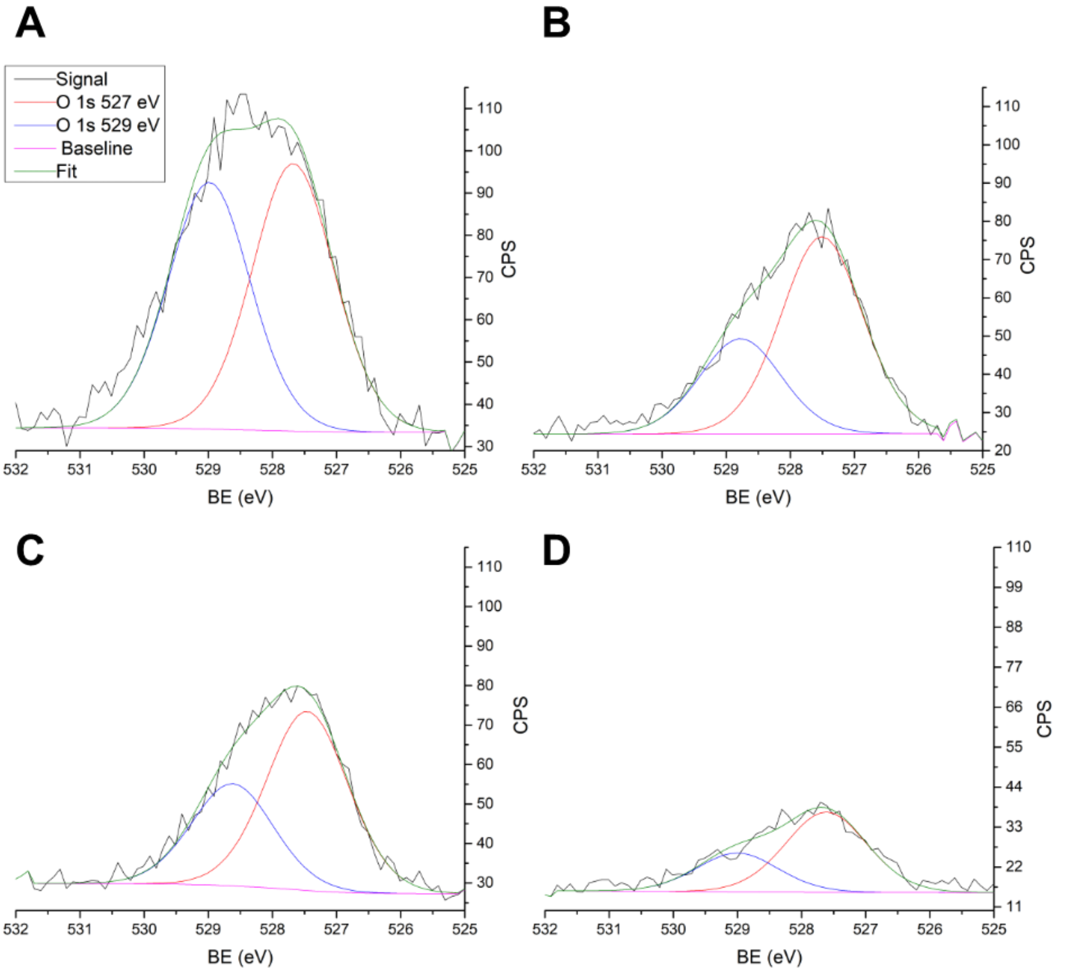

Figure 1-27: Hi-resolution scans of the O1s region for (A) DOW SWXLE and (B) PBI/PSSA membranes before treatment with NaClO. (C) DOW SWXLE and (D) PBI/PSSA after treatment with NaClO.

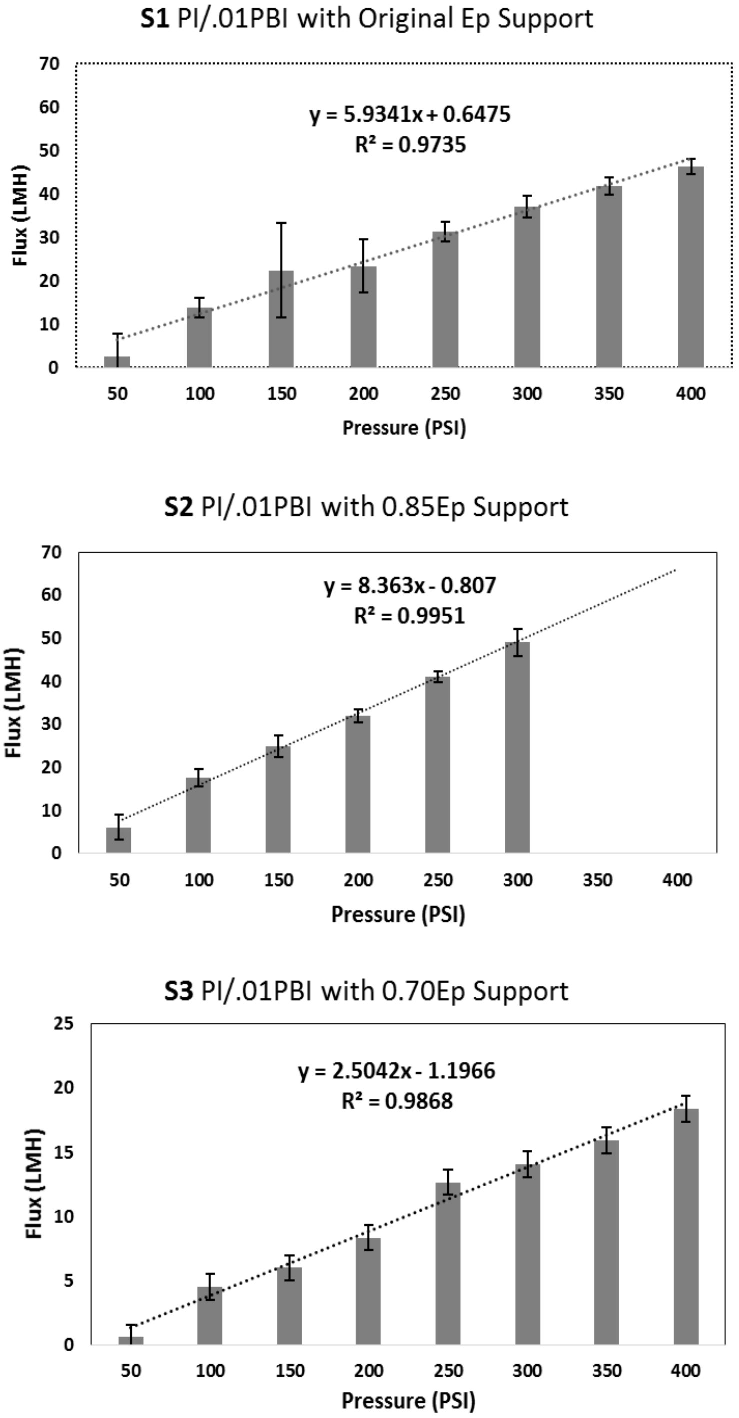

Figure 1-28: S1, S2, and S3 flux at 50-400 psi. R^2 value represents compaction resistance and slope represents normalized flux.

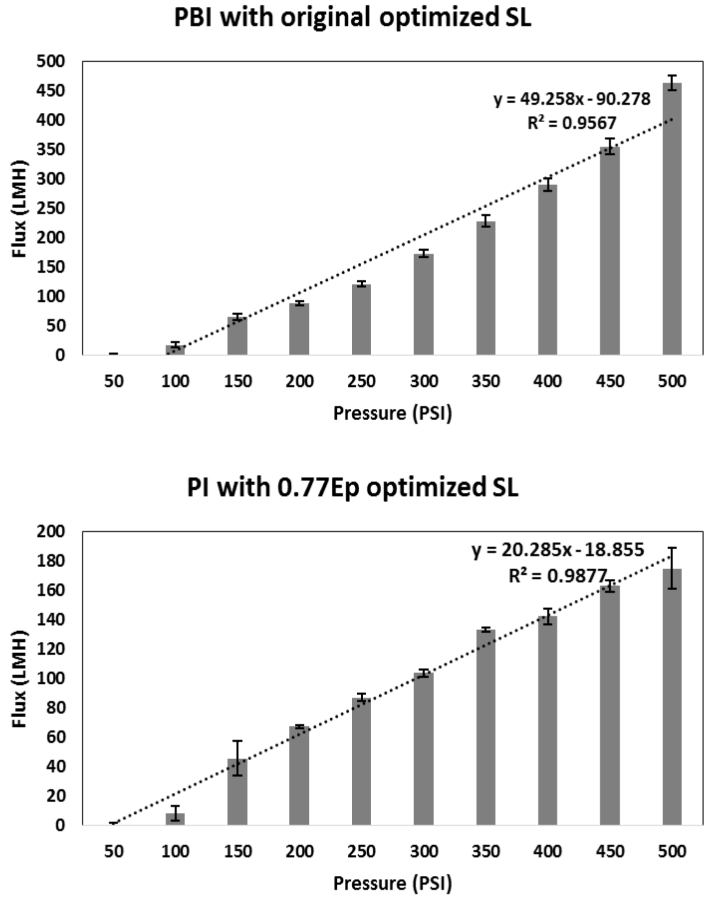

Figure 1-29: Flux for various psi for optimized PBI, which was the basis for all other optimizations and the final PI membrane.

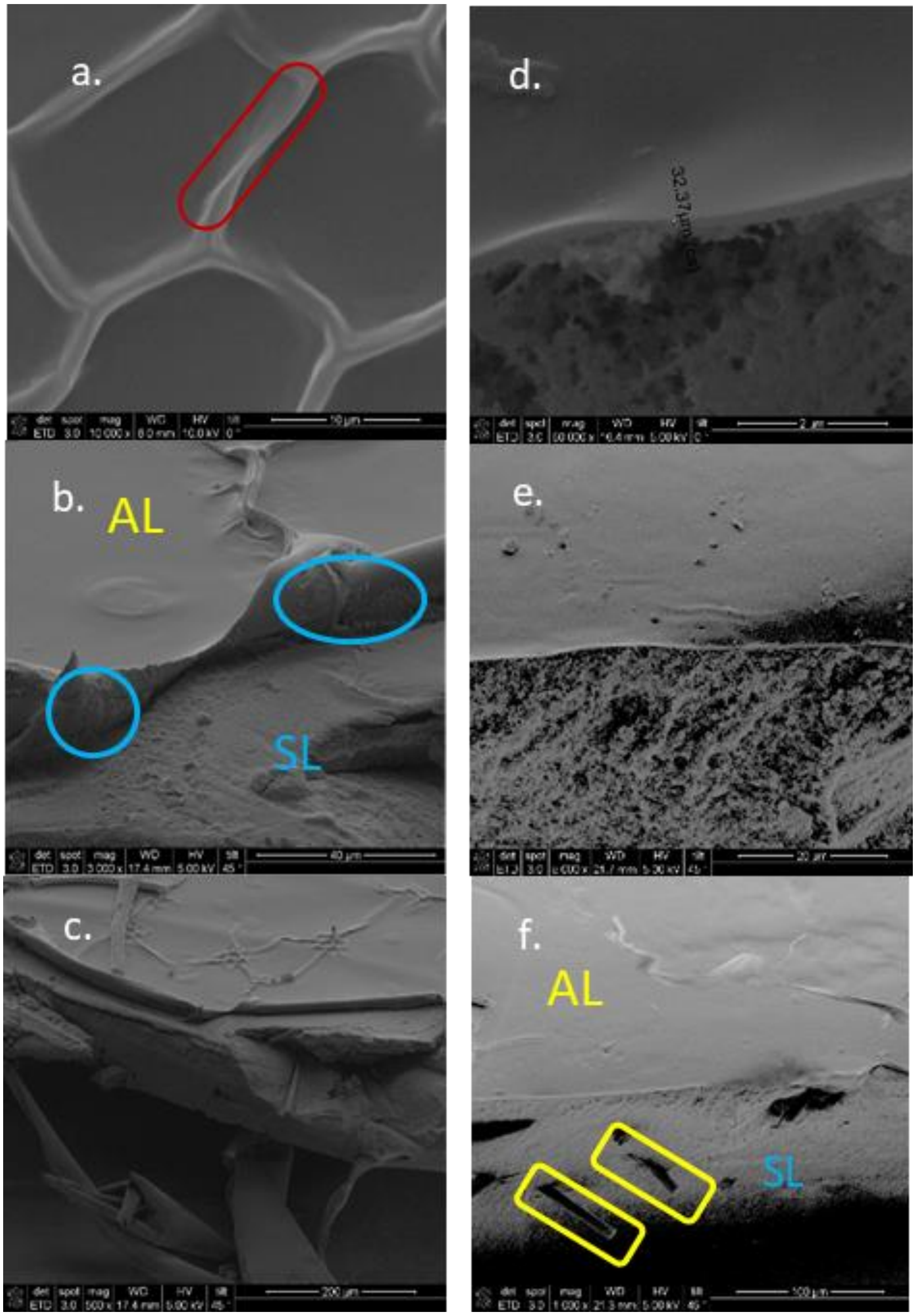

Figure 1-30: (a) S1 AL with AL fold emphasized with red outline. (b) edge of S1AL peeling off SL with folds. SL adhesion to AL underside is emphasized with blue circles (c)Image showing S1 edge and folds. (d). S2 AL edge with <u>32.4 micron</u> thickness (e). S2 smooth active layer and porous SL. (f) S2 smooth AL with no peeling from SL and well encapsulated carbon fibers emphasized with yellow boxes.

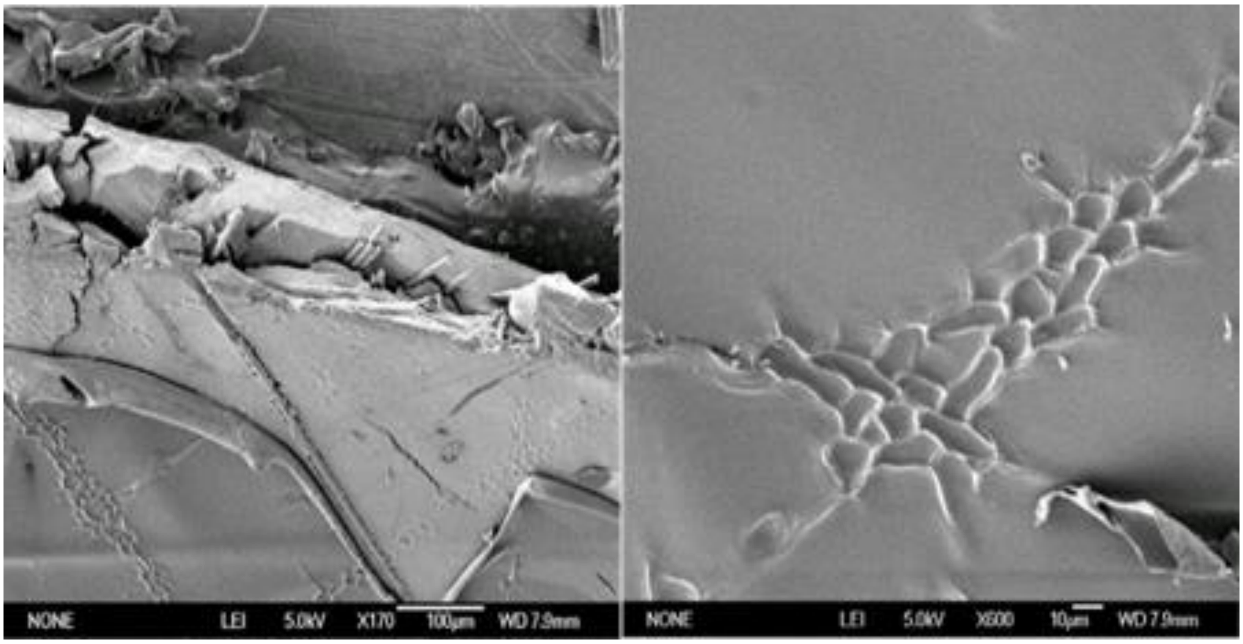

Figure 1-31 S3 images showing splitting SL around carbon fibers and surface folds.

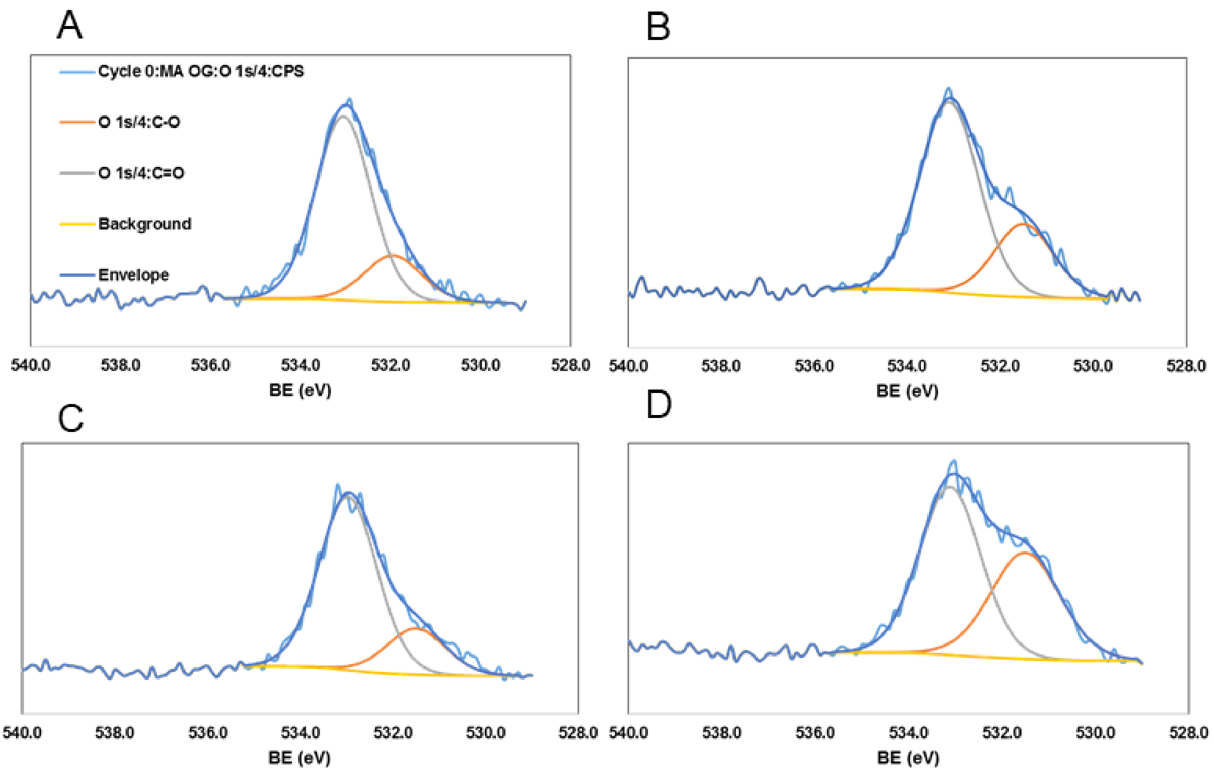

Figure 1-32 High-resolution scans of O1s region with deconvolution.(A) S1 PI/0.10 PBI (B) S2 PI/0.10 PBI (C) S3 PI/0.20 (D) S4 77% PI.

References

(1) Werber, J. R., Osuji, C. O., & Elimelech, M. (2016). Materials for next-generation desalination and water purification membranes. *Nature Reviews Materials*. *1*(5), 16018.

(2) Thomas, S., Wilson, R., S., A. K., George, S. C., Abitha, V. K., & Thomas, S. (2018). Fabrication Methods: Polymer Membranes for Liquid Transport. *Transport Properties of Polymeric Membranes*, 35–50.

(3) Hołda, A. K., & Vankelecom, I. F. J. (2015). Understanding and guiding the phase inversion process for synthesis of solvent resistant nanofiltration membranes. *Journal of Applied Polymer Science.* 42130, 1-17.

(4) Lee, K. P., Arnot, T. C., & Mattia, D. (2011). A review of reverse osmosis membrane materials for desalination-Development to date and future potential. *Journal of Membrane Science*. 370(1–2), 1–22.

(5) Loeb, S. (2018). The Loeb-Sourirajan Membrane: How It Came About. *ACS Symposium Series.* 23, 1-9.

(6) Reid, C. E., & Breton, E. J. (1959). Water and ion flow across cellulosic membranes. *Journal of Applied Polymer Science*. 1(2), 133–143.

(7) Geise, G. M., Paul, D. R., & Freeman, B. D. (2014). Fundamental water and salt transport properties of polymeric materials. *Progress in Polymer Science*. 39(1), 1–42.

(8) Wang, J., Dlamini, D. S., Mishra, A. K., Pendergast, M. T. M., Wong, M. C. Y., Mamba, B. B., Freger, V., Verliefde, A. R. D., & Hoek, E. M. V. (2014). A critical review of transport through osmotic membranes. *Journal of Membrane Science*. 454, 516–537.

(9) Petersen, R. J., Cadotte, J. E., Porter, M. E., (1990) Eds. Handbook of Industrial Membrane Technology; *Noyes Publications*, 307.

(10) Petersen, R. J. (1993). Composite reverse osmosis and nanofiltration membranes. *Journal of Membrane Science*, *83*(1), 81–150.

(11) Nowbahar, A., Mansard, V., Mecca, J. M., Paul, M., Arrowood, T., & Squires, T. M. (2018). Measuring Interfacial Polymerization Kinetics Using Microfluidic Interferometry. *J. Am. Chem. Soc*. 140, 43.

(12) Chai, G. Y., & Krantz, W. B. (1994). Formation and characterization of polyamide membranes via interfacial polymerization. *Journal of Membrane Science*, *93*(2), 175–192.

(13) Rao, A. P., Desai, N. V., & Rangarajan, R. (1997). Interfacially synthesized thin film composite RO membranes for seawater desalination. *Journal of Membrane Science*. 124(2),

(14) Rao, A. P., Joshi, S. V., Trivedi, J. J., Devmurari, C. V., & Shah, V. J. (2003). Structure–performance correlation of polyamide thin film composite membranes: effect of coating conditions on film formation. *Journal of Membrane Science*. 211(1), 13–24.

(15) Song, Y., Sun, P., Henry, L. L., & Sun, B. (2005). Mechanisms of structure and performance controlled thin film composite membrane formation via interfacial polymerization process. *Journal of Membrane Science*. 251(1–2), 67–79.

(16) Ba, C., & Economy, J. (2010). Preparation of PMDA/ODA polyimide membrane for use as substrate in a thermally stable composite reverse osmosis membrane. *Journal of Membrane Science*. 363(1–2), 140–148.

(17) Ghosh, A. K., Jeong, B. H., Huang, X., & Hoek, E. M. V. (2008). Impacts of reaction and curing conditions on polyamide composite reverse osmosis membrane properties. *Journal of Membrane Science*. 311(1–2), 34–45.

(18) Liu, M., Yu, S., Tao, J., & Gao, C. (2008). Preparation, structure characteristics and separation properties of thin-film composite polyamide-urethane seawater reverse osmosis membrane. *Journal of Membrane Science*. 325(2), 947–956.

(19) Jin, Y., & Su, Z. (2009). Effects of polymerization conditions on hydrophilic groups in aromatic polyamide thin films. *Journal of Membrane Science*. 330(1–2), 175–179.

(20) Xie, W., Geise, G. M., Freeman, B. D., Lee, H. S., Byun, G., & McGrath, J. E. (2012). Polyamide interfacial composite membranes prepared from m-phenylene diamine, trimesoyl chloride and a new disulfonated diamine. *Journal of Membrane Science*. 403–404, 152–161.

(21) Klaysom, C., Hermans, S., Gahlaut, A., Van Craenenbroeck, S., & Vankelecom, I. F. J. (2013). Polyamide/Polyacrylonitrile (PA/PAN) thin film composite osmosis membranes: Film optimization, characterization and performance evaluation. *Journal of Membrane Science*. 445, 25–33.

(22) Hoek, E. M. V, Bhattacharjee, S., & Elimelech, M. (2003). Effect of Membrane Surface Roughness on Colloid-Membrane DLVO Interactions. *Langmuir.* 19, 11, 4836–4847.

(23) Hong, S., Kim, I.-C., Tak, T., & Kwon, Y.-N. (2013). Interfacially synthesized chlorine-resistant polyimide thin film composite (TFC) reverse osmosis (RO) membranes. *Desalination*. 309, 18–26.

(24) Jin, F.-L., Li, X., & Park, S.-J. (2015). Synthesis and application of epoxy resins: A review. *Journal of Industrial and Engineering Chemistry*. *29*, 1–11.

(25) Kawaguchi, Y.; Hiro, A.; Harada, N.; Hayashi, O.; Mizuike, A.; Ishii, K. U.S. Patent No. 0174723, July 21, 2011.

(26) Shechter, L., Wynstra, J., & Kurkjy, R. P. (n.d.). Glycidyl Ether Reactions with Amines. *Industrial and Engineering Chemistry*. 48(1), 94–97.

(27) Meier, U. (1995). Strengthening of structures using carbon fibre/epoxy composites. *Construction and Building Materials*. 9(6), 341–351.

(28) Liu, C., Greer, D. W., & O'Leary, B. W. (2016). Advanced Materials and Membranes for Gas Separations: The UOP Approach. *ACS Symposium Series*. *1224*, 119–135.

(29) Fang, J., Kita, H., & Okamoto, K. (2000). Hyperbranched polyimides for gas separation applications. 1. Synthesis and characterization. *Macromolecules*. 33, 13, 4639–4646.

(30) Anderson, M. R., Matres, B. R., Reiss, H., & Kaner, R. B. (2017). Conjugated Polymer Films for Gas Separations. *American Association for the Advancement of Science*. *252*(5011), 1412–1415.

(31) Jia, Z., & Wang, Y. (2015). Covalently crosslinked graphene oxide membranes by esterification reactions for ions separation. *Journal of Materials Chemistry A: Materials for Energy and Sustainability*. 3, 4405–4412.

(32) Kim, H. J., Lim, M. Y., Jung, K. H., Kim, D. G., & Lee, J. C. (2015). High-performance reverse osmosis nanocomposite membranes containing the mixture of carbon nanotubes and graphene oxides. *Journal of Materials Chemistry A*. 3(13), 6798–6809.

(33) Xu, Y., Bai, H., Lu, G., Li, C., & Shi, G. (2008). Flexible Graphene Films via the Filtration of Water-Soluble Noncovalent Functionalized Graphene Sheets. *Journal of the American Chemical Society*. 130(18), 5856-5857.

(34) Muscatello, J., Jaeger, F., Matar, O. K., & Müller, E. A. (2016). Optimizing Water Transport through Graphene-Based Membranes: Insights from Nonequilibrium Molecular Dynamics. *ACS Applied Materials & Interfaces*. 8, 19, 12330–12336.

(35) Geim, A. K., & Nair, R. R. (2014). Precise and Ultrafast Molecular Oxide Membranes. *Science*. 343(6172), 752–755.

(36) Beydaghi, H., Javanbakht, M., & Kowsari, E. (2014). Synthesis and Characterization of Poly (vinyl alcohol)/ Sulfonated Graphene Oxide Nanocomposite Membranes for Use in Proton Exchange Membrane Fuel Cells (PEMFCs). *Industrial and Engineering Chemistry Research*. 53, 43, 16621–16632.

(37) Boukhvalov, D. W., Katsnelson, M. I., & Son, Y. (2013). Origin of Anomalous Water Permeation through Graphene Oxide Membrane. *Nano Letters*. 13(8), 3930-3935.

(38) Hu, M., & Mi, B. (2013). Enabling Graphene Oxide Nanosheets as Water Separation Membranes. *Environmental Science and Technology*. 13(8), 3930–3935.

(39) Xu, G., Wang, J., & Li, C. (2013). Strategies for improving the performance of the polyamide thin film composite (PA-TFC) reverse osmosis (RO) membranes: Surface modifications and nanoparticles incorporations. *Desalination*. 328, 83–100.

(40) Han, Y., Xu, Z., & Gao, C. (2013). Ultrathin Graphene Nanofiltration Membrane for Water Purification. *Advanced. Functional Materials*. 23, 3693–3700

(41) Yang, G., Xie, Z., Zhang, S., Zheng, H., Cai, K., Cran, M., Ng, D., Wu, C., & Gray, S. (2020). Functionalized carbon nanotube-mediated transport in membranes containing fixed-site carriers for fast pervaporation desalination. *ACS Applied Materials and Interfaces*. 12, 45, 50918–50928.

(42) Park, H. B., Freeman, B. D., Zhang, Z., Sankir, M., & Mcgrath, J. E. (2008). Highly Chlorine-Tolerant Polymers for Desalination. *Angewandte Chemie*. 47, 6019 –6024.

(43) Vanherck, K., Koeckelberghs, G., & Vankelecom, I. F. J. (2013). Crosslinking polyimides for membrane applications: A review. *Progress in Polymer Science*. 38, 874–896.

(44) Walch, A., Lukas, H., Kimmek, A. (1974). Structure and Hyperfiltration Properties of Polyimide Membranes. *Angewandte Chemie Polymer Letters Edition*. 12, 697–710.

(45) Shechter, L., Wynstra, J., & Kurkjy, R. P. (n.d.). Glycidyl Ether Reactions with Amines. *Industrial and Engineering Chemistry*. 48(1), 94–97.

(46) Yun, H. K., Cho, K., Kim, J. K., Park, C. E., Sim, S. M., Oh, S. Y., & Park, J. M. (1997). Adhesion polyimide polyimide improvement of epoxy resin / polyimide joints by amine treatment of surface. *Polymer*. 38(4), 827–834.

(47) Valtcheva, I. B., Kumbharkar, S. C., Kim, J. F., Bhole, Y., & Livingston, A. G. (2014). Beyond polyimide: Crosslinked polybenzimidazole membranes for organic solvent nanofiltration (OSN) in harsh environments. *Journal of Membrane Science*. 457, 62–72.

(48) Valtcheva, I. B., Marchetti, P., & Livingston, A. G. (2015). Crosslinked polybenzimidazole membranes for organic solvent nanofiltration (OSN): Analysis of crosslinking reaction mechanism and effects of reaction parameters. *Journal of Membrane Science*. 493, 568–579.

(49) Cong, S., Wang, J., Wang, Z., & Liu, X. (2020). Polybenzimidazole (PBI) and benzimidazole-linked polymer (BILP) membranes. *Green Chemical Engineering*. 2, 44-56.

(50) da Silva Burgal, J., Peeva, L. G., Kumbharkar, S., & Livingston, A. (2015). Organic solvent resistant poly(ether-ether-ketone) nanofiltration membranes. *Journal of Membrane Science*. 479, 105–116.

(51) Aburabie, J., Neelakanda, P., Karunakaran, M., & Peinemann, K. V. (2015). Thin-film composite crosslinked polythiosemicarbazide membranes for organic solvent nanofiltration (OSN). *Reactive and Functional Polymers*. 86, 225–232.

(52) Minehara et al. US Patent Pub. No.: US 2013/0313186 A1

(53) Jamaly, S., Darwish, N. N., Ahmed, I., & Hasan, S. W. (2014). A short review on reverse osmosis pretreatment technologies. *Desalination*. 354, 30–38.

(54) Isaias, N. P. (2001). Experience in reverse osmosis pretreatment. *Desalination*, 139(1–3), 57–64.

(55) Barassi, G., & Borrmann, T. (2012). N-chlorination and Orton Rearrangement of Aromatic Polyamides, Revisited. *Journal of Membrane Science & Technology*. 02(02), 2–4.

(56) Do, V. T., Tang, C. Y., Reinhard, M., & Leckie, J. O. (2012). Degradation of polyamide nanofiltration and reverse osmosis membranes by hypochlorite. *Environmental Science and Technology*. 46(2), 852–859.

(57) Kimura, M., & Ogata, Y. (2006). Photooxidation of Some Aromatic Sulfonic Acids with Alkaline Hypochlorite. *The Chemical Society of Japan*. 56(2), 471–473.

CHAPTER 2: Toward Sustainable Manufacture of Chemically-Tolerant Ultrafiltration Membranes

All-Epoxy Membranes for Ultrafiltration Applications

Despite being high-performance in separations and adaptable to many applications, polyamide (PA) membranes, made by interfacial polymerization of meta-phenylene diamine (MPD) and trimesoyl chloride (TMC), are not resistant to harsh chemical environments.[1-4] This forces the need for robust pretreatment of feed solutions before being contacted to the PA. Addressing this shortcoming, Verbeke *et al.* proposed a novel synthesis of a polyether epoxide TFC membrane, translating traditionally bulk syntheses to an interfacial polymerization of EPON™ Resin 1031 (EPON).[5] They demonstrated how an EPON active layer was highly resistant to caustic environments, which, although the poly(epoxyether) layer was undamaged, the polyimide (PI) support membrane was susceptible to degradation. They therefore proposed that an alternative membrane be used. In a later publication, Verbeke *et al*. demonstrated that key to the separation capacity of these TFC membranes is the solvent annealing of the PI support layer and that the poly(epoxyether) active layer is only significant for the smallest of organic separations.[6] Here we present a novel "all-epoxy" membrane, addressing both the need for a chemically robust support membrane and other environmental factors as discussed below.

In Chapter 1, it was demonstrated how thin-film composite membranes made using a method called Thin-Film Lift-Off (T-FLO), are highly resistant to chemical degradation by NaClO and highly alkaline solutions. A polybenzimidazole-polystyrene sulfonic acid-based active layer upon a finely tuned poly(epoxyether) support was used to separate NaCl from water at brackish water concentrations. The epoxy chemistry was tuned to be used for a variety of filtration applications by adhering to thin films of various active layers.[7] In subsequent publications, it is demonstrated that the

T-FLO technique is amenable to graphene oxide (GO) and polybenzimidazole (PBI) for nanofiltration membranes in both organic and aqueous feed solutions.[8] Still, this technology has not yet utilized the standalone epoxy membranes to their full extent.

The importance of the support layer for the active layer has been demonstrated in several publications using the most prevalent membrane formation technique, the interfacial polymerization of MPD and TMC. The primary factors in formation of the active layer include the support layer's pore sizes, surface porosity (number of pores per surface area), pore size distribution and the relative hydrophobicity/hydrophilicity.[9- 14] These factors affect the diffusion of reactants (MPD and TMC) and products (HCl) to and from the organic-aqueous interface, affecting both the kinetics of film formation and the resulting physical and chemical properties. Generally, smaller pore sizes lead to a more uniform and thicker active layer as the diffusion of MPD into the organic TMC layer is slower and more controlled, therefore less of the polyamide forms in the pores of the support.[9,10] This also leads to a more crosslinked membrane as the diffusion path of MPD to TMC throughout the reaction is shorter.[11] With large pores, the diffusion is less controlled and the movement of MPD more rapid, resulting in a rougher active layer as well as polymerization occurring in the pores. There tends to be less crosslinking due to PA layers forming inside the pores, increasing the diffusion path of MPD to reach the organic layer.[11] Therefore, the smaller-pores of the active layer give a more crosslinked and thus, more selective active layer. In addition to pore size, the number of pores per unit area affects the active layer morphology and thickness.[9] Generally, higher surface porosity enables continuous film formation with higher crosslinking density when compared to membranes with support layers with lower surface porosity.[9,10] What is discovered here is that using monolithic EPON and BADGE-based epoxy resins, rather than interfacial polymerization, membranes can achieve low molecular weight cutoff without an active layer or a woven support. While useful for understanding the interfacial polymerization process, this discovery also addresses a second, very important challenge facing the membrane industry, the large volumes of organic solvents used in synthesis/fabrication.

Membrane fabrication, whether formed by nonsolvent immersion precipitation (NIPS) or interfacial polymerization, requires the use of large amounts of organic solvents for dissolving polymer solutions and dissolving monomers, respectively. This use has negative effects on health and equipment while reducing the sustainability of the field.[15] This problem has been addressed by attempting to minimize solvent use,[15] using safer solvents,[15] using fewer volatile solvents[16,17] or eliminating the need for solvents altogether.[18,19] Interfacial polymerization of both MPD-TMC and the EPON used here require large amounts of organic solvent, which dissolves the TMC and EPON and forms the aqueous-organic interface. The epoxy system developed in Chapter 1 requires only PEG as a solvent and porogen and a water bath for PEG removal. PEG is generally considered safe, appearing in many products including cosmetics,[20] laxatives,[21] and contact lenses.[22] Additionally, PEG can be removed using nanofiltration membranes, unlike other solvents that may require distillation to separate solvent mixtures.[23] Therefore, monolithic membranes using only PEG and water could be a solution for reducing the environmental impact of ultrafiltration and nanofiltration membrane manufacture.

Herein is demonstrated the importance of the support layer in an all-epoxy system. Membranes capable of high rejection of small molecule dyes are fabricated. By altering both the porogen and the epoxide monomer, the flux and rejection of membranes can be finely tuned. Preliminary data lend evidence that a support layer made with a more linear polymer, but smaller pores, is a more effective support for forming poly(etherepoxide) active layers with high rejection of small molecule dyes. More crosslinked support membranes with small pores form denser intrinsic active layers without the need for interfacial polymerization and are not easily amenable to interfacial polymerization.

Materials

4'4 Methylene bis cyclohexylamine (MBCHA) was obtained from Acros Organics and used without further preparation. Bisphenol-A-diglycidyl ether (BADGE) and polyethylene glycol (PEG) (Mn 200, Mn 300, and Mn 400) were purchased from Sigma-Aldrich and used as packaged. EPON™ Resin 1031 pellets were obtained from Hexion and used without further treatment. Epoxyease mold-release spray was obtained from Slide Products Inc. Benzene, obtained from Fisher Scientific was dried over molecular sieves. Diethoxy-dimethylsilane from Sigma Aldrich was distilled prior to use. Trans-4-aminocyclohexanol from Sigma Aldrich was sublimed prior to use. Sodium cubes in kerosene were obtained from Sigma Aldrich and a portion washed with benzene prior to use.

A series of membranes were made from BADGE and MBCHA as described in Chapter 1, but without any thin film. Water flux through the membranes was measured gravimetrically and rejection of Rose Bengal and Methylene Blue dyes were determined spectrophotometrically. After evaluating the standalone epoxy membranes, onto each was added an interfacially polymerized EPON active layer. These membranes were viewed under SEM, revealing in part the success of the active layer formation. Tests for flux and rejection were repeated for these membranes. Lastly, the BADGE monomers were replaced with EPON to yield more crosslinked structures. These membranes were similarly tested for flux and rejection. To elucidate the IP mechanism, contact angle and surface porosity measurements were taken. XPS and IR are used for chemical characterization.

Membrane Synthesis:

Epoxy Support Membranes

330 mg of 4,4' methylene bis cyclohexylamine (MBCHA) was dissolved in 3.25 g of polyethylene glycol; MW: 200, 300, 400, or a combination thereof. To the solution was then added 1.0 g of bisphenol-a-diglycidyl ether. The mixture was let to stir at 750 rpm for 3 hours.

1.0 g of EPON™ Resin 1031, tetraphenolethane tetra-glycidylether (EPON), was dissolved in 1.63 g of PEG 200 and 1.63 g of PEG 400. The solution was gently heated and stirred overnight to achieve complete dissolution. At room temperature, 330 mg of MBCHA was added to the solution and left to stir at 750 rpm for 3 hours. Over the course of stirring, the solution became more viscous.

A 7’’ x 7’’x 1/8’’ borosilicate glass sheet was coated with a thin layer of Epoxease mold-release agent. A 11 cm x 14 cm sheet of 6 g/m^2 carbon fiber veil was placed onto the coated glass and impregnated with the desired epoxy resin. The entire substrate was then placed into an oven set to 130 ^{o}C for 4 hours. The cured composite was allowed to cool to room temperature and submerged overnight in a bath of deionized water to remove PEG. If the membrane did not separate from the borosilicate upon soaking in deionized water, the membrane was removed from the substrate by gently peeling by hand.

Membranes made from BADGE ranged from an opaque white color to a transparent blue color depending on the type of porogen used. Membranes made from EPON were transparent yellow in appearance regardless of the porogen.

Interfacial Polymerization

The selected membranes were cut into circular coupons and placed into a custom-made interfacial polymerization reactor such that the smooth side of the membrane (the side that was facing the glass plate) was facing the organic solution. One side of the membrane was contacted to a 1-5% aqueous solution of tetramethyl N,N,N’,N’ tetramethyl-1,6 hexane diamine (TMHD). The organic layer consisted of a 1% solution of EPON resin. The reactor was allowed to sit for 4 hours during which time the TMHD diffused from the organic layer to the aqueous layer, initiating the self-polymerization of the EPON monomer. After 4 hours the coupon was removed from the reactor and placed in a water bath for at least 24 hours before use. The interfacial polymerization (IP) was visually apparent as the membrane took on an opaque yellow color.

SEM: Samples were rendered conductive by sputtering with gold and imaged using a JEOL JSM-6700F FE-Scanning Electron Microscope.

Membrane Testing

Membranes were tested for DI flux and solute rejection in a Sterlitech HP4750 stirred dead-end cell pressurized with compressed nitrogen gas. DI flux was measured gravimetrically.

Dye Rejection

After compacting with DI water, DEC was loaded with 250 mL of 35 µM Rose Bengal (973.67 g/mol), 35 µM of Methylene Blue (319.85 g/mol), or 1 g/L $MgSO_4$. The cell was pressurized to 400 psi. The first ~5 mL of permeate was discarded and the next 50 mL of permeate was collected for analysis. Rejection was determined spectrophotometrically.

Results and Discussion

Rejection and flux can be tuned by changing the porogen system used in fabrication, with lower-molecular weight PEG leading to more porous films with lower rejection, while higher molecular weight PEG leads to a denser structure with higher rejection. The mechanical properties of the BADGE based membranes are superior to the purely EPON membranes. The BADGE membranes are more flexible, even after drying out, while the EPON membranes, as expected for a more crosslinked network, are more brittle and become deformed when dried out.

The DI flux through membranes ranged from 80-1000 LMH/bar, competitive with or far exceeding the solvent flux of commercial membranes with similar MWCO as well as highly novel membranes with much more complex syntheses/fabrication.(29) The membrane with the best permselectivity is the EPON-300 membrane with an average DI Flux of 448 LMH/bar and average rejection of 99.6% and 99.8% of Rose Bengal and Methylene Blue dyes, respectively. DI flux through the BADGE-300 membranes was significantly affected by the presence of the EPON active layer, dropping from an average of 1001 to 458 LMH/bar. The gain in rejection was less dramatic but still significant, increasing from 98.95% to 99.75% and from 66.37 to 75.51 for Rose Bengal and Methylene Blue, respectively, although the variability in rejection increased significantly for the BADGE-300 with an EPON active layer.

The decrease in porosity from changing the support formulation to use PEG 400 rather than PEG 300 as a porogen caused the flux to decrease from an average of 1001 to 661 LMH/bar. The further addition of the EPON active layer resulted in a drop of just under 30 LMH/bar, though, as with the BADGE-300 membranes, the BADGE-400 membrane showed greater variability in flux with an active layer than without an active layer. The drastic increase in MB rejection from 66.37% for BADGE-300 to 96.63% for the BADGE-400 membrane demonstrates that the porosity of the support has a greater effect on the rejection for the membrane than the addition of the active layer. Still, the EPON active layer increases the rejection of MB from 96.63% to 98.30%.

Membranes prepared using epoxy cured in PEG 200 did not result in membranes with significant rejection of either Rose Bengal or Methylene Blue, even with the presence of the EPON active layer. Given the volumetric limits of the DEC system used, the flux was too high to measure. Still, SEM images of these membranes show that a continuous active layer on the surface of the support has formed, with the active layer protruding into the porous layer of the support (Figure 2-6 B). Yet, if the interfacial polymerization occurred mostly within the pores of the BADGE-200 membrane, this result can be correlated with the reduced crosslinking discussed in Sharabati *et al.* In contrast, the active layer of the BADGE-300 membrane appears to be sitting atop the support layer (Figure 2-5 E).

Taking a closer look at the active layer (Figure 2-6 E) of the BADGE 300 membrane where the active layer has been peeled back, the smaller pores of the BADGE-300 support are revealed.

The drastic increases in rejection achieved by reducing the pore size of the epoxy membranes occurs regardless of the presence of an active layer. One option would be to use a PEG of higher molecular weight, but higher molecular weight PEGs below MW 1000 are less common and at the 1000 MW point, PEG melts at temperatures above room temperature, introducing many new variables into the synthesis of epoxies than when compared with lower MW PEG. Instead, we replaced the bi-functional BADGE with the tetra-functional EPON (Figure 2-1).

As expected, the flux through the membranes was greatly reduced. The membranes were still tunable by changing the MW of the porogen, as with the BADGE membranes. Changing the porogen from PEG 300 to PEG 400 showed a more than 5x reduction in flux, dropping from an average of 448 to 84 LMH/bar. Surprisingly, despite the fact that the EPON-based epoxies were much more crosslinked, membranes made with PEG 200 as the porogen showed extremely high flux (water passed through the membranes with very little applied pressure) and negligible rejection of dyes. Despite difficulty in viewing differences in porosity of different EPON-MBCHA membranes (Figure 2-7), the flux data reveal that they are more sensitive to the effects of the change in porogen when compared to the BADGE-based membranes. Interfacial polymerization was only successful when BADGE-MBCHA support membranes were used. When EPON-MBCHA membranes were used, the EPON layer was not well adhered to the support, it was easily damaged on handling or with any shear force on the membrane. This is likely due to the EPON-MBCHA membranes being too dense such that the diffusion of the TMHD was too hindered and thus only a very thin film at the very surface of the support formed. Since the EPON is soluble in toluene, the organic solvent used in the polymerization, it is possible that the toluene is partially dissolving the support layer if full crosslinking was not achieved with curing. Figure 2-8 shows a cross-sectional image of an EPON-

300 support membrane with an interfacially-polymerized active layer. Compared to the membranes in Figure 2-5, the active layer is much thinner, on the scale of hundreds of nanometers.

Despite the drastic changes in flux of the EPON-MBCHA membranes, the differences in rejection of dyes was much less pronounced. Both the EPON-300 and EPON-400 membranes achieved average rejections of RB and MB above 99.7%. This makes the EPON-300 membrane the best option of the fabricated membranes for aqueous separations. Preliminary results show minimal rejection of 1.0 g/L $MgSO_4$, thus the high rejection of RB and MB suggest that additional measurements should be made to determine the exact MWCO for these membranes.

Conclusions

The dense, interfacially-polymerized polyetherepoxide is only amenable to more porous epoxy substrates. The use of more dense substrates leads to very poorly adhered IP layers that could be removed by gentle rubbing with a gloved finger. Still, we demonstrate that the single-material epoxy membranes can achieve the same, if not better, rejection and flux as the IP films. While the BADGE-based membranes show better permeability, the incorporation of the tetra-substituted EPON monomer leads to improved rejection. Monolithic membranes made from BADGE and EPON epoxides can be used to separate low-molecular weight dyes from water. This creates a new path forward for the development of sustainable membrane manufacturing by reducing the amount of solvent necessary during the fabrication process. To complete this work the following experiments will be performed.

- Surface porosity of membranes will be carried out using SEM and Image J Software.
- Contact angels of BADGE 300 and BADGE 400 will be done to see if hydrophilicity of the support layer is contributing to active layer formation.
- Rejection of lower MW dyes will be carried out to determine the actual MWCO of the

monolithic membranes.

Surface porosity will enable further understanding of active layer formation. Uniform pores are known to generate smoother active layers, while a wider dispersity of pore size leads to a more uneven topography as the aqueous layer diffuses toward the organic layer at different rates depending on the pore size. Also, a quantitative measure of pore sizes will enable more precise comparison of membranes with one another, linking direct pore size with performance rather than the formulation and inferred pore structure. Contact angles of water on EPON-based membranes range around 50^o, with little difference between PEG 200, PEG 300, and PEG 400 formulations. If the BADGE-based membranes are, as hypothesized, more hydrophobic because of the methyl-groups that take up a larger share of the total mass of epoxide when compared with EPON-based membranes, this would further explain the pore formation mechanism. The organic layer protrudes further into the support layer during interfacial polymerization when the support is my hydrophobic. This leads to more active layer material forming in the pores rather than atop the support which would lead to higher-flux, lower rejection polymers. Therefore, there would be a “sweet spot” where the small size of the pores would enable more polymerization atop the support and outweigh the effect of a more hydrophobic support. Though preliminary data show negligible rejection of large salts, smaller organics may be removeable given 100% rejection of MB by some membranes in this study. Further optimization may also lead to rejection of large salts.

Degradable Epoxy Membranes

Introduction

For commercial applications, hundreds of square feet of flat sheet membranes are wound into membrane elements that are placed into pressure vessels. The membrane active layers are facing each other between which the feed solution is contacted to the membrane. Therefore, the permeate sides of the membrane are facing each other and the permeate is collected when it reaches the central tube around which the membranes are wound.[24] This water, the permeate, is either collected for use or sent to another set of membrane elements for further treatment in what is called a membrane train. Large desalination plants can contain up to tens of thousands of membrane elements per facility.[26,27] A typical membrane module can have a membrane active layer surface area in the hundreds of square feet.[25-27] Currently though, these membranes are landfilled due to difficulty of recycling. Lawler *et al.* demonstrate how membranes can be diverted from landfills through extensive processing to separate recyclable components; reusing membranes for less intensive separations; and incineration and gasification for electricity generation and to reduce the mass of waste funneled to landfills.[28] They conclude that these methods may offset some of the energy-intense processes and reduce some environmental impacts of transportation, but mention that factors such as the use of petroleum-based solvents for membrane fabrication, etc., make it difficult to gauge the total environmental impact of waste produced during membrane plant operation.

As discussed earlier in this chapter, more chemically tolerant membranes can help reduce the energy impact of membrane separations by reducing the need for extensive pretreatment. Epoxy membranes may be well suited to withstand harsh conditions, but one challenge posed by all heavily crosslinked materials is their inability to be recycled. Addressing this, several novel polymers have been explored as candidates for degradable resins with a wide variety of applications and degradable linkers.[29-31,] Bassampour *et al*. produced epoxy resins made from the reaction of BADGE and organosilane based diamines with varying degrees of degradability in saline, acidic, and basic environments.[9] They conclude that the degradability of the polymers in aqueous environments was based on the crosslinking density of the polymer network (determined by whether the amines were primary or secondary) and the number of labile Si-O bonds. Higher crosslinking and fewer Si-O bonds led to epoxies that did not degrade over the course of the 30-day trial period. While regeneration of Si-O bonds was not demonstrated, the re-formation of covalent linkers between siloxane and hydroxyl-functionalized siloxane can be found throughout the literature, due to the reversible hydrolysis of the Si-O bonds. [34-37]

Carbon fiber (CF) reinforced epoxies are used in many products because of their combined high strength and light weight.[38-40] Because CF is costly, due largely to the petroleum-based precursors, its applications are often limited to high-value products.[39] This has led to an abundance of research in the area of making carbon fiber from more sustainable precursors.[39,40] Still, used carbon fiber composites are typically landfilled due to the difficulty of breaking down the composite matrices such that recycling of fibers (such as by mechanical means) seriously degrades the fibers.[38,41] The development of techniques to improve recyclability of carbon fiber reinforced composites, while maintaining the integrity of the virgin materials, have become increasingly important with the growing use of carbon fiber and the environmental imperative to reduce waste sent to landfill and industry's overall carbon footprint.[38,40-43] Processes that require relatively low energy input (below that of making new fiber from virgin materials) and those that do not employ toxic solvents are most desirable.

Throughout this work, epoxy resins have been used to make high-functioning membranes. Here we consider the end-of-life disposal of membranes and how the already-developed system can be refined to include planned degradation. The use of carbon fiber as a support increases the potential for membrane waste to produce a value-added product. Proposed here is an epoxy with reversible crosslinks that can remain high-functioning in aqueous environments for filtration applications. Diamines analogous to MBCHA, with the types of silane bonds and degree of crosslinking in Baussemer *et al*. that showed the least degradation in aqueous environments, will be incorporated into a BADGE-based resin to produce the hypothetical polymer in Figure 2-9. Hydrolysis of the Si-O bonds creates the alcohols highlighted in yellow. This polymer is linear, and could be removed from carbon fiber with relative ease, without degrading the polymer into oligomers. The crosslinked polymer could potentially be regenerated for use as a membrane by condensation with diethoxy(dimethylsilane) or dimethylsilanol or be used without modification for other applications where strong hydrogen bonding between polymer chains would suffice.

Degradable Monomer Synthesis

5.00 g of trans 4-aminocyclohexanol was added to a dry 2-necked round-bottom flask equipped with condenser with distillation affixed and dissolved in benzene by stirring with heating via a sand-bath under argon. Once completely dissolved, Na metal (treated with benzene) was added to the flask followed by 0.5x equivalence of diethoxy dimethyl silane. The reaction proceeded for 3 days at reflux. The residual Na was removed from the flask and quenched. The product was then cooled foming transparent crystals in benzene. The crystals were then dried via a rotovap to produce pure 4,4'diamino(cyclohexoxy)dimthylsilane (DACHDMS). Purification by chromatography was optimized using basic alumina. The structure was confirmed using NMR and ATR-IR spectroscopy. The disappearance of the ethane CH_2 and CH_3 at 2.18 ppm and 3.75 ppm indicates the substitution of the ethoxy-silane groups, while the appearance of the methyl singlet at about 0.15 ppm indicates retention of the $Si-CH_3$ bonds. Substitution is also provided by the shifts in the CH cyclohexane multiplets from 3.3 ppm and 3.6 ppm to 2.6 ppm and 3.5 ppm as well as the shifts in the CH_2 multiplets downfield when compared to the 1,4-amino(cyclohexanol) (Figure 2-11). At about 1260 cm^{-1}, the sharp peak indicates a $Si-CH_3$ bond in both the DEDMS and the product (Figure 2-12).

Epoxy Resin

Stoichiometric amounts of DACHCMS and BADGE were combined with 3.25 g of PEG 300 and allowed to stir at 750 rpm for three hours (Figure 2-12-A). The resin was poured into an 11 cm x 14 cm piece of 6 g/m^2 carbon fiber atop an Epoxease-coated glass substrate. The prepreg was cured at 130 ^oC for 4 hours. The resulting composite was extremely flexible and opaque (Figure 2-13). ATR-

IR suggests some polymerization by the appearance of the broad O-H stretch near 3300 cm^{-1} . The 2 N-H stretching peaks are indicative of a primary amine as is evident at about 3200 cm^{-1}-3300 cm^{-1} in the DACHDMS sample, the replacement of these with a single peak is indicative of a secondary amine or the lack of a peak due to a tertiary amine is not visible due to the O-H stretch.

Discussion and Conclusions

In this work, the synthesis of a monomer analogous to BADGE and MBCHA was made and polymerized to form a CF composite. The resulting membrane had extremely high flux at the application of very low-pressures, suggesting that the porosity is too high to perform aqueous separations such as ultrafiltration or nanofiltration.

This preliminary work guides us to focus on the following experiments:

The stability of the monomer in PEG needs to be confirmed. A co-solvent should be included to improve dissolution into the PEG and ease polymerization with BADGE. The curing temperature of the resin must be optimized and curing by chemical means should also be considered. Once completed, MWCO will be determined through the rejection of small-molecule dyes. The retrieval of the carbon fiber from the epoxy matrix post-membrane use must be optimized and its effect on the mechanical and chemical properties measured using SEM, XPS, ATR-IR, and single-fiber testing. Retrieval via higher concentrations of aqueous HCl than those used by Bassampour *et al.* and methods to swell the membranes to make the silyl-ether bonds more accessible will be employed such as treatment with minimal organic solvent or by the application of heat. The product generated by reintroduction of a silyl-ester or simply after un-crosslinking the original polymer must be characterized and its ability to be processed to form a new membrane determined. If the incorporation of a cleavable monomer does not prove effective for membrane manufacturing, then the degradation mechanisms mentioned in the introduction must be employed to retrieve the carbon fiber from the spent, traditional epoxy membranes to ensure the relative sustainability of the epoxy membranes as discussed herein.

Figures

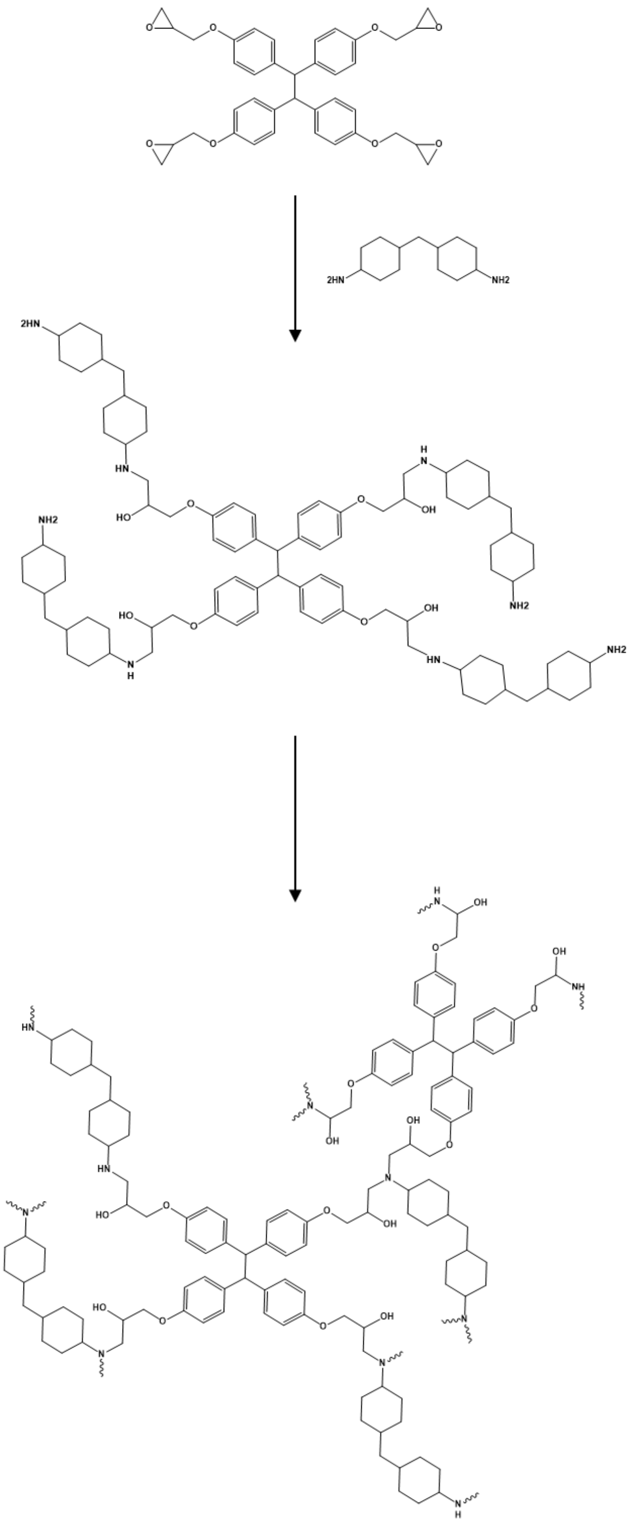

Figure 2-14: Polymerization of EPON with MBCHA.

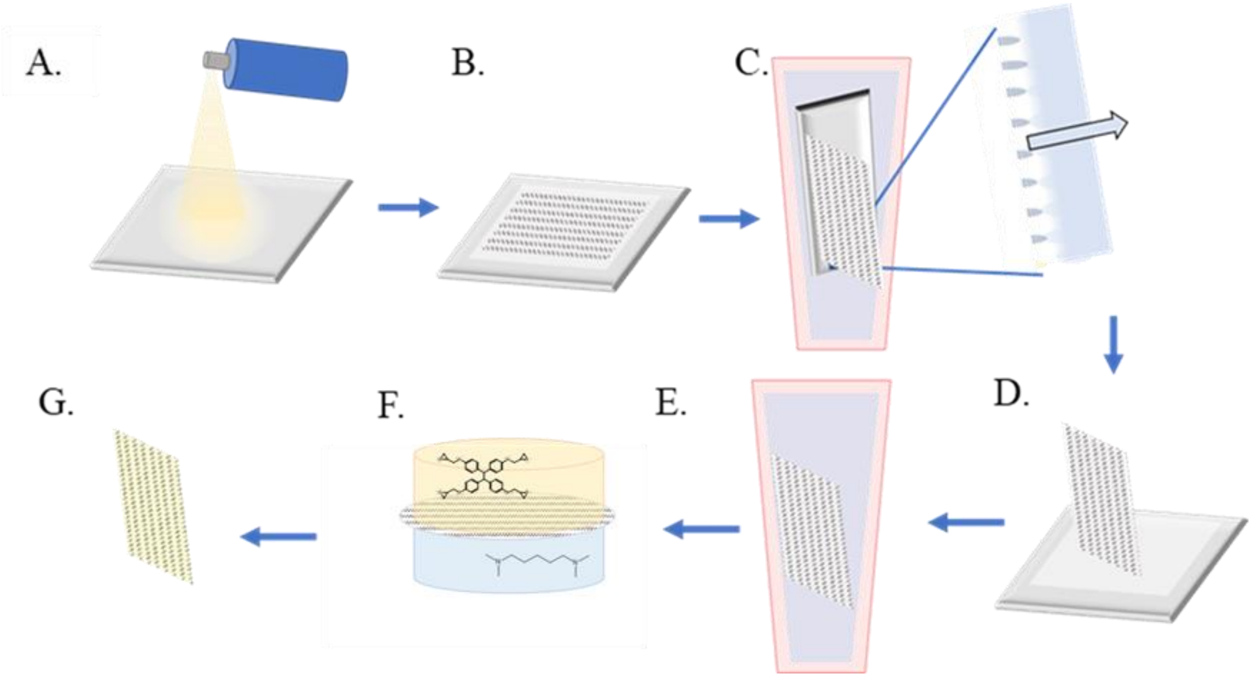

Figure 2-15: Process for making all-epoxy membranes using interfacial polymerization. (A) Coat glass plate with EpoxEase; (B) Cast porogen into fabric and cure; (C) Remove PEG via water bath; (D) Delaminate epoxy support from substrate; (E) Soak substrates in solution of TMHD; (F) Perform interfacial polymerization; and (G) the all-epoxy membrane is complete.

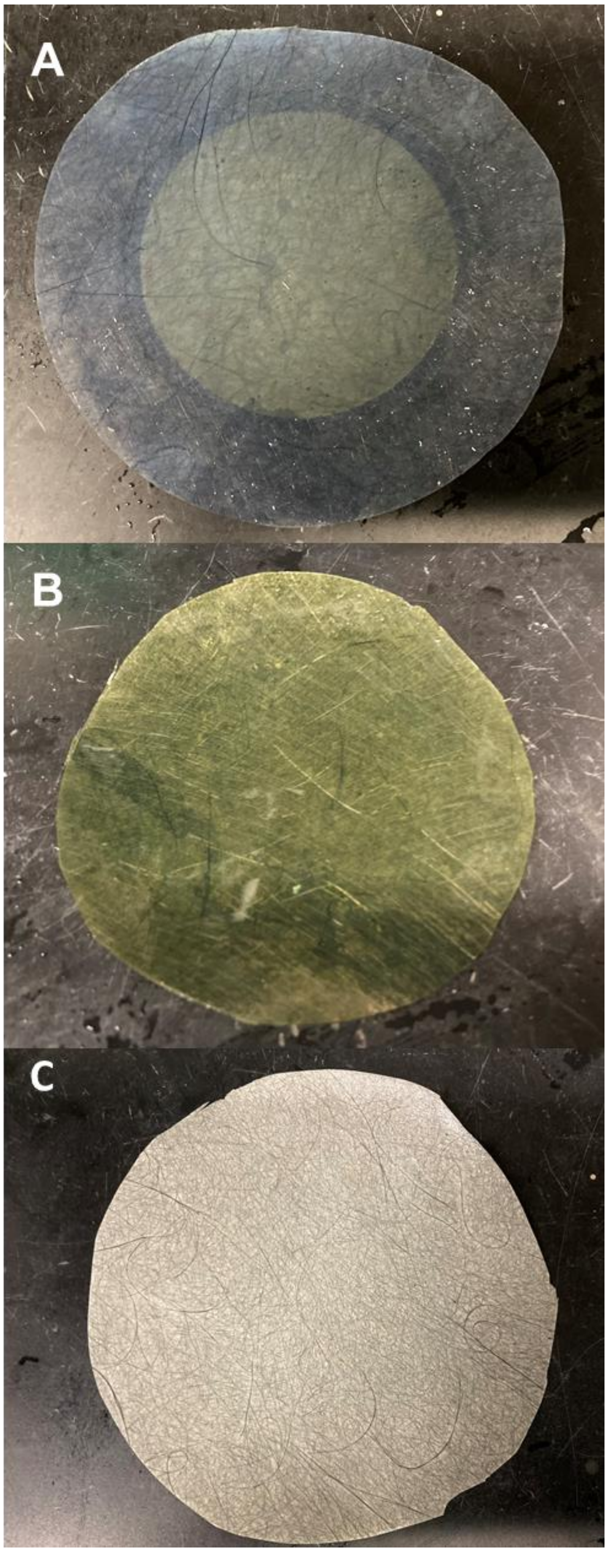

Figure 2-16: (A) Optical image of BADGE-MBCHA-P300 with IP EPON forming inner opaque circle. (B) Optical image EPON-MBCHA-PEG300 membrane (no IP layer) (C) Optical Image of BADGE-MBCHA-P200 with IP EPON active layer (not visible).

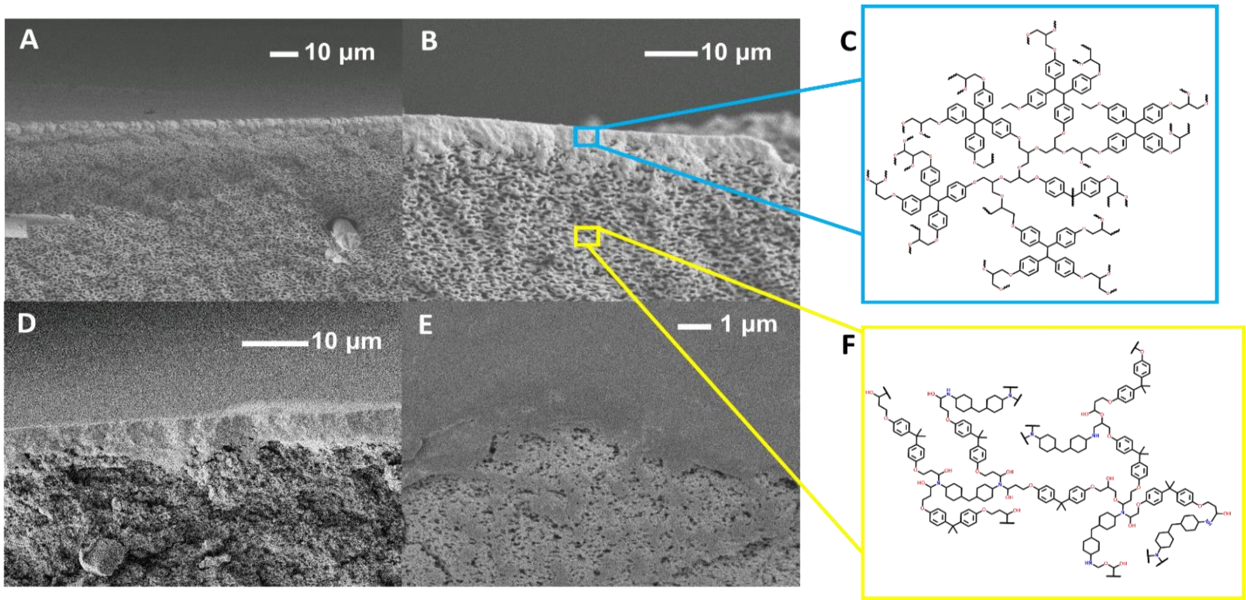

Figure 2-17: (A)-(B) SEM cross-sectional images of IP EPON on a BADGE 200 support membrane. (C) Theoretical structure of the EPON active layer. (D) SEM cross-sectional image of IP EPON on a BADGE-300 support membrane. (E) SEM of a defect on the edge of a BADGE-300 with EPON active layer revealing the porous support structure. (F) Theoretical structure of BADGE-MBCHA support layer.

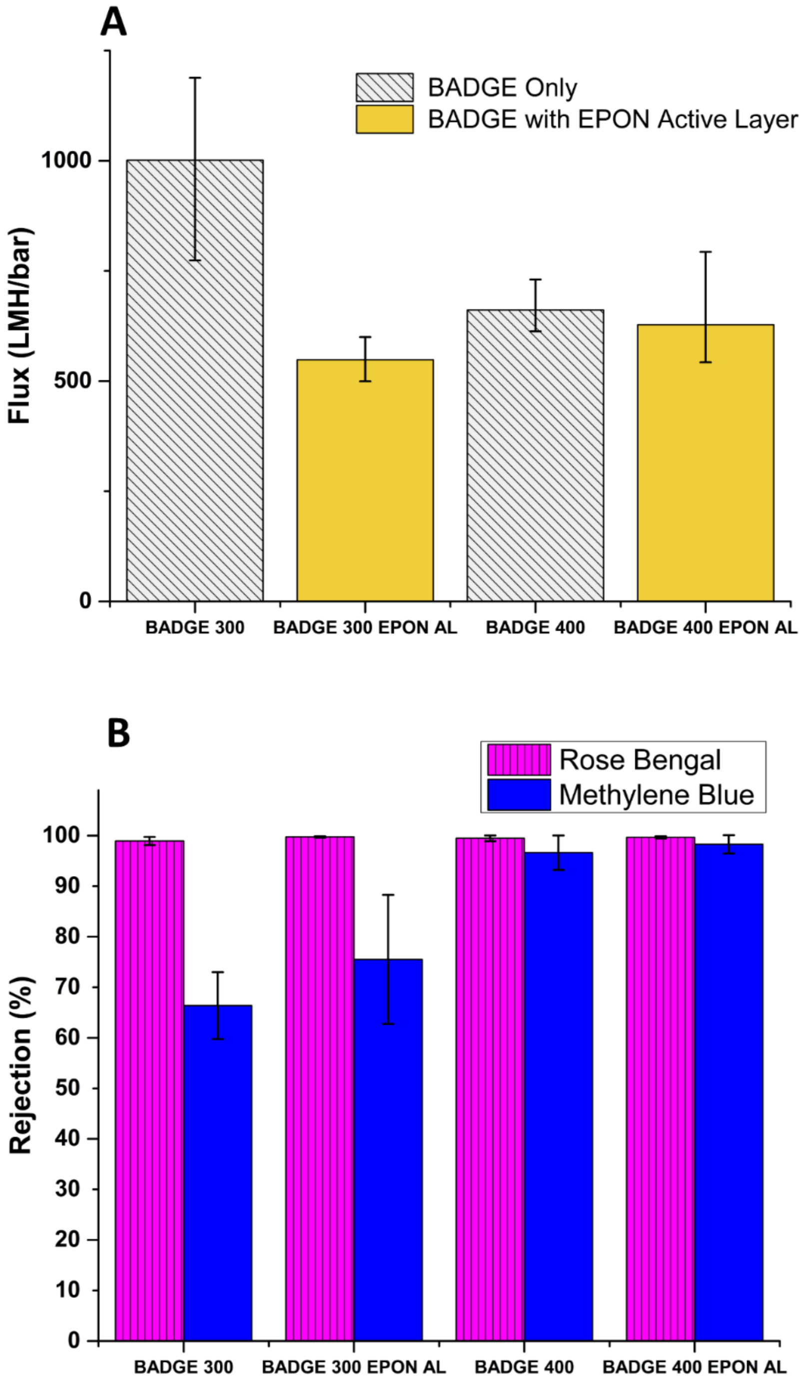

Figure 2-18: (A) Flux through BADGE support layers with and without EPON active layers. (B) Rejection of MB and RB by BADGE support layers with and without EPON active layers.

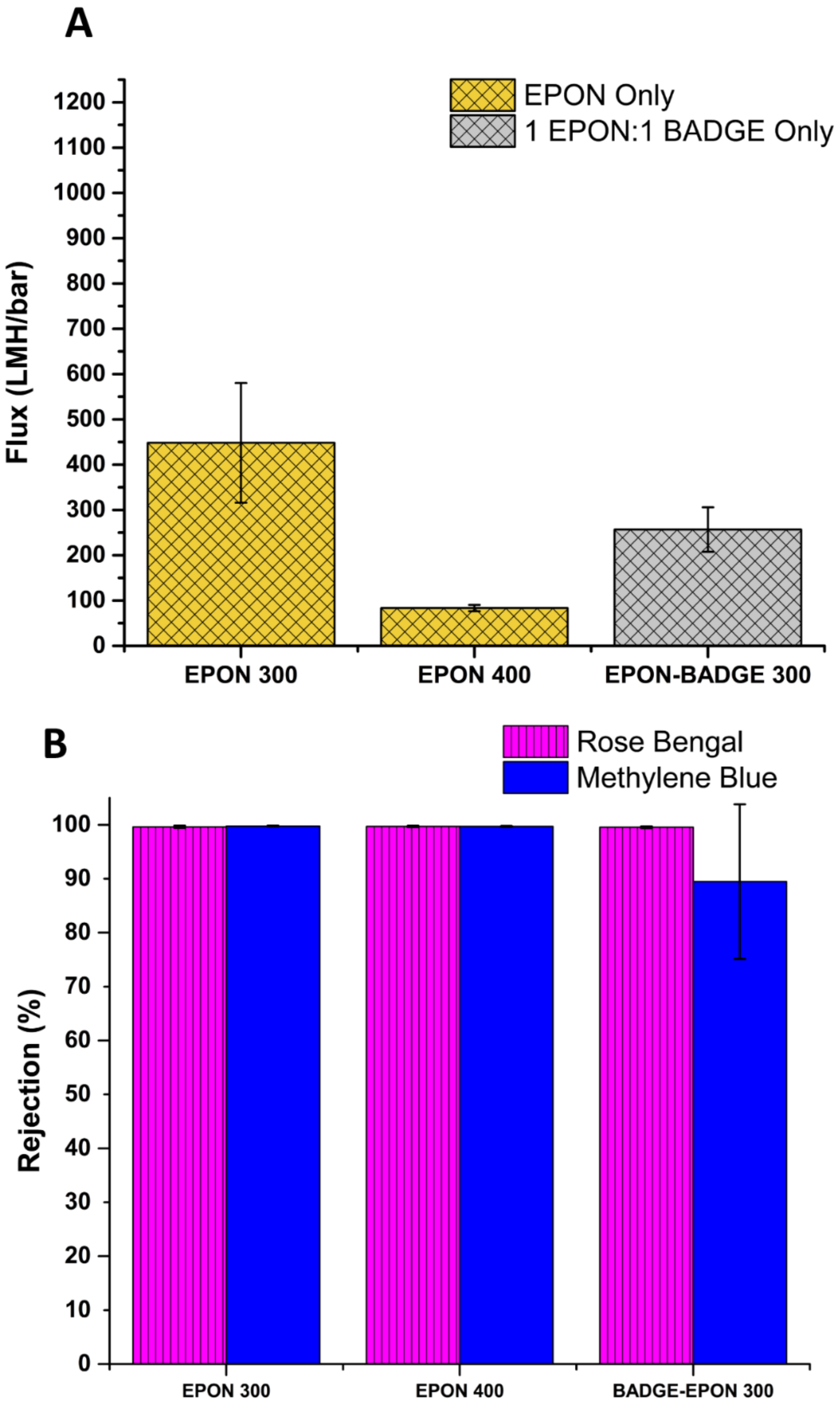

Figure 2-19: (A) Flux through EPON support layers with different porogens (yellow) and a support layer made from both EPON and BADGE epoxide monomers.

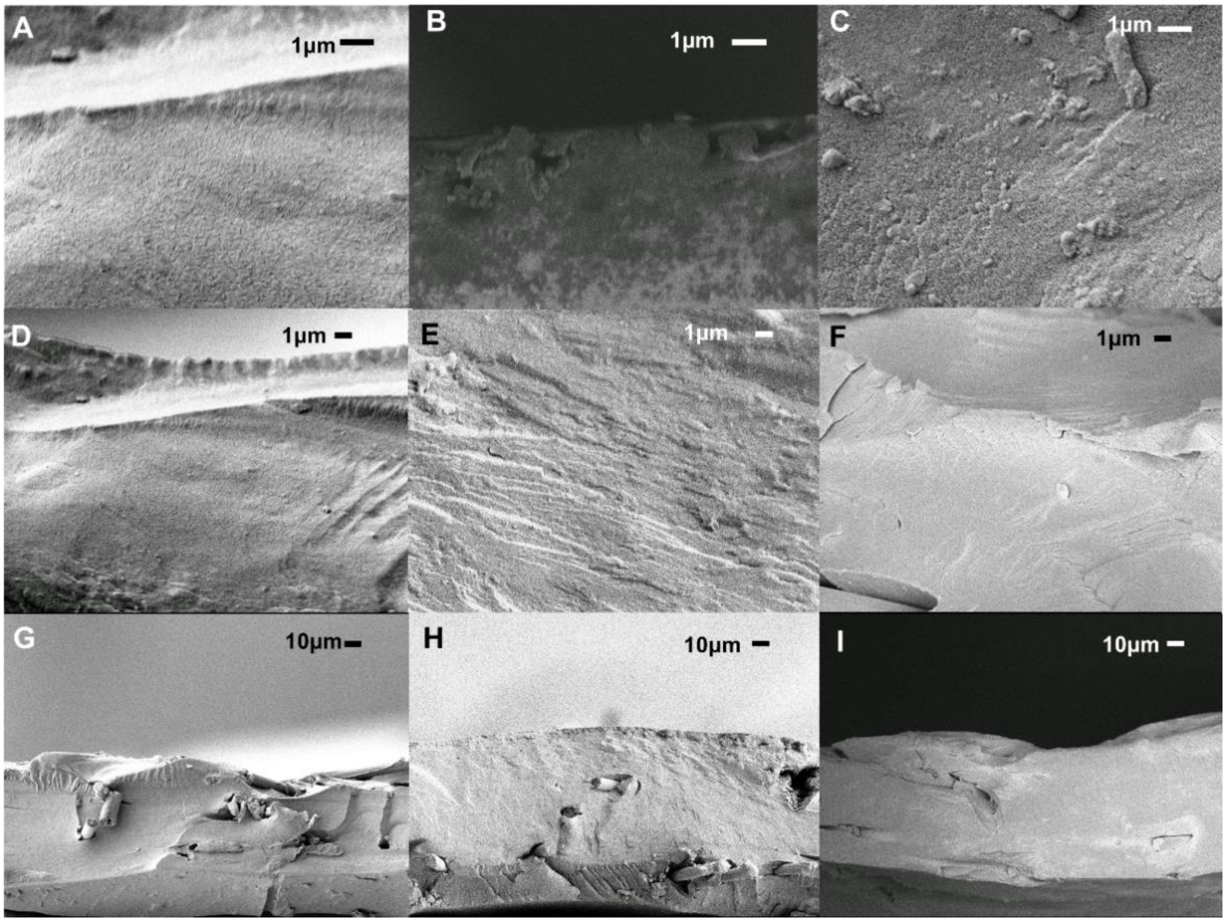

Figure 2-20: (A) SEM cross-section images of an EPON-MBCHA membrane made with PEG-300. (B) SEM image of an EPON-MBCHA membrane made with PEG-400 near the top (substrate-facing) surface.(C) Membrane made from a combination of BADGE and EPON epoxides and MBCHA. (D) Cross section of EPON-MBCHA-PEG 300 membrane near the top of the membrane. (E) Cross section of EPON-MBCHA-PEG400 membrane at reduced magnification. (F) Cross-section of EPON-BADGE-MBCHA-PEG300 at reduced magnification. (G)-(H) SEM images of full cross-sections of EPON-MBCHA-PEG 300, EPON- MBCHA-PEG 400, and EPON-BADGE-MBCHA-PEG 300, respectively.

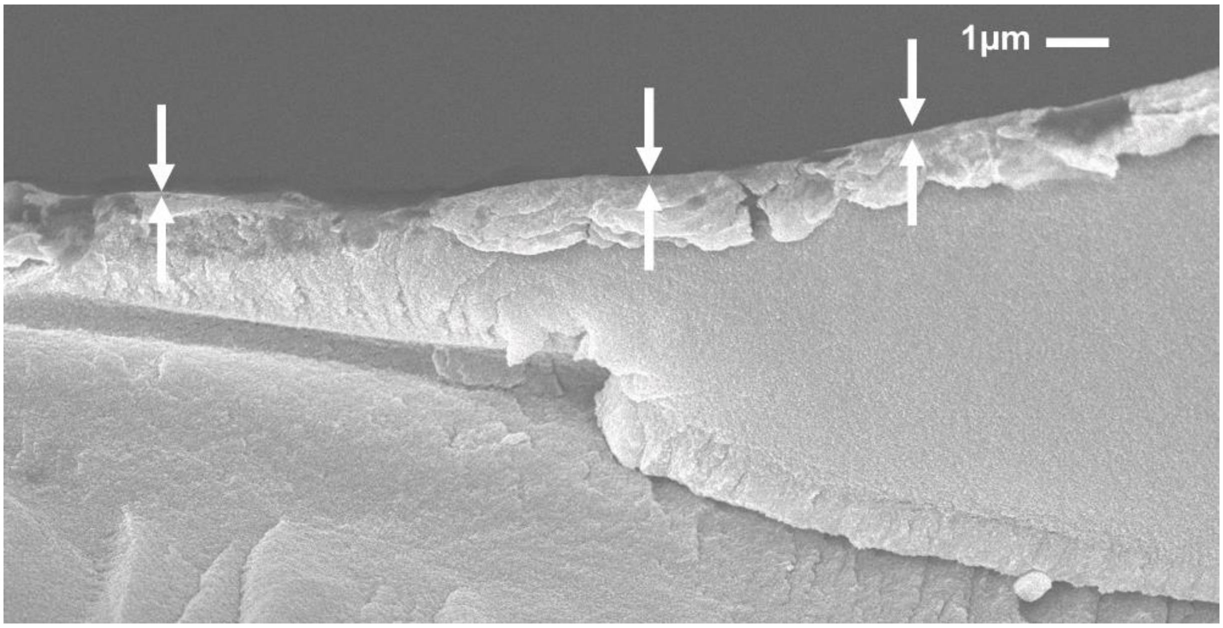

Figure 2-21: SEM cross-section of and EPON-MBCHA-PEG 300 membrane with EPON active layer.

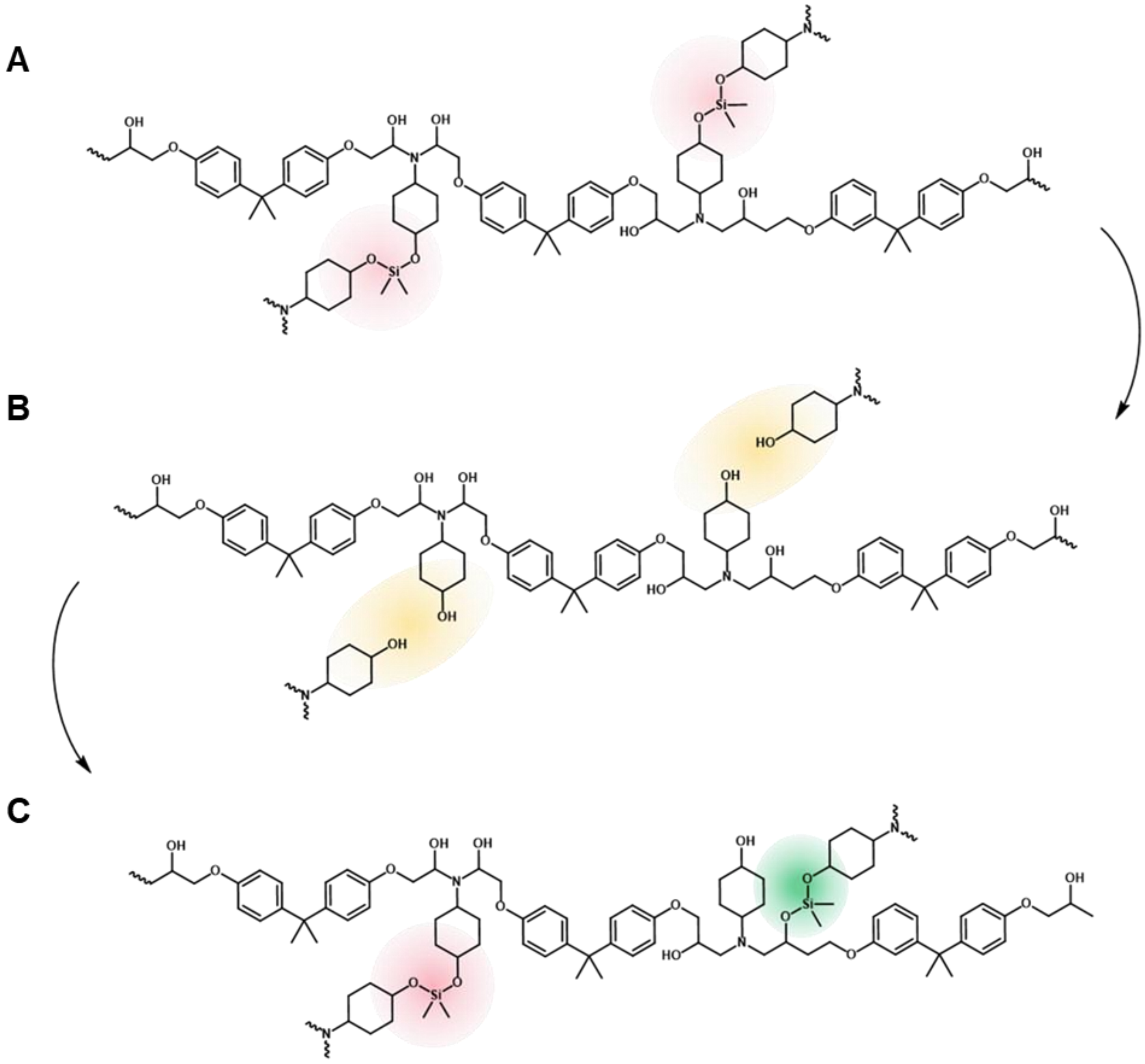

Figure 2-9: (A) Polymer synthesized from DADCHDMS and bispenol-a-diglycidyl ether. (B) Polymer after Si-O bond cleavage. (C) Hypothetical re-crosslinked polymer.

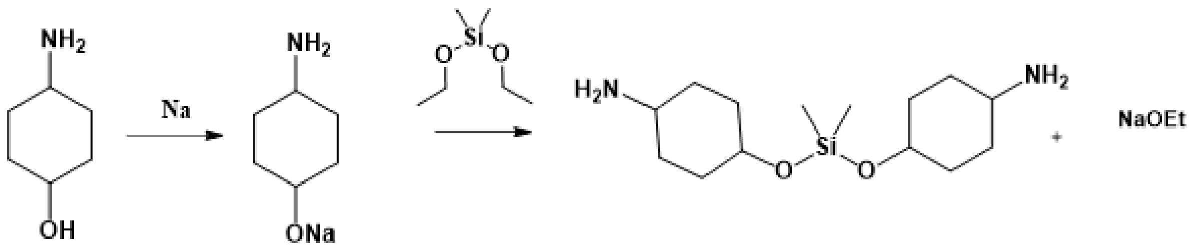

Figure 2-22: The synthesis of silylamine.

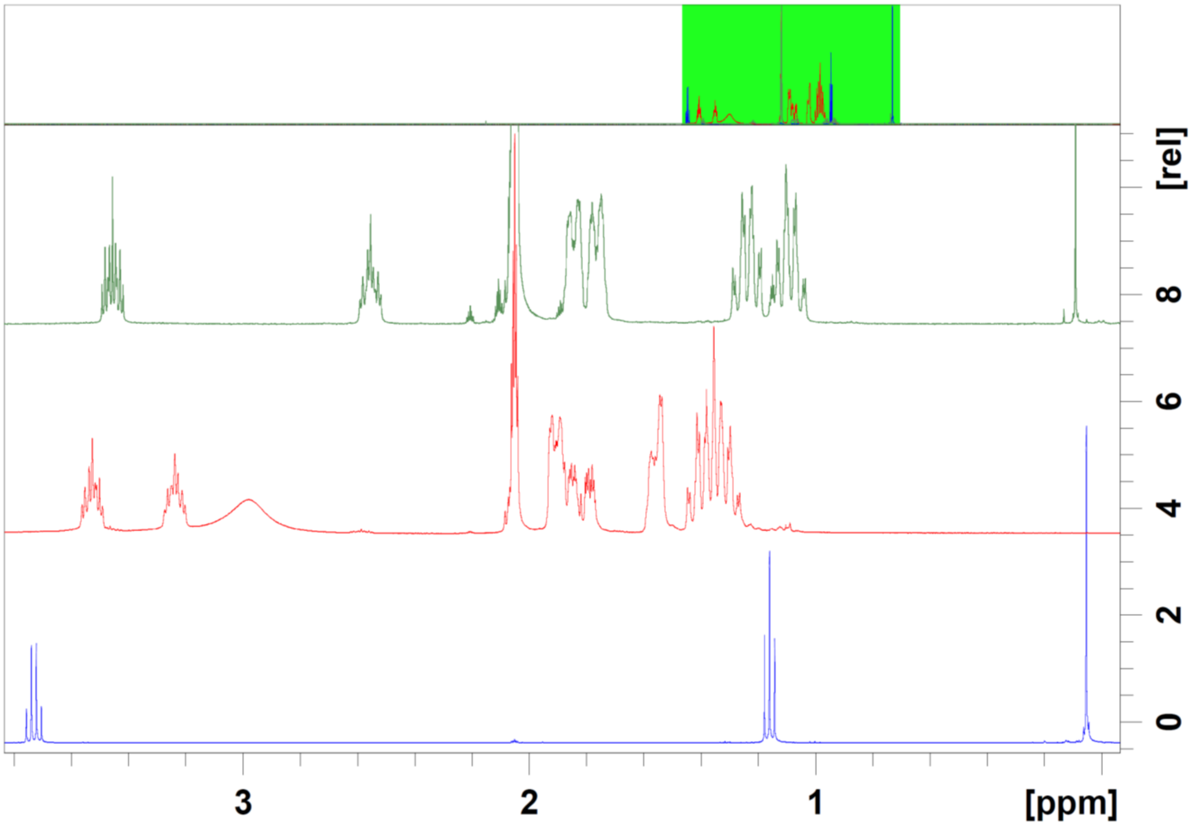

Figure 2-23: DADCHDMS monomer (top), ACH (middle), DEDMS (bottom).

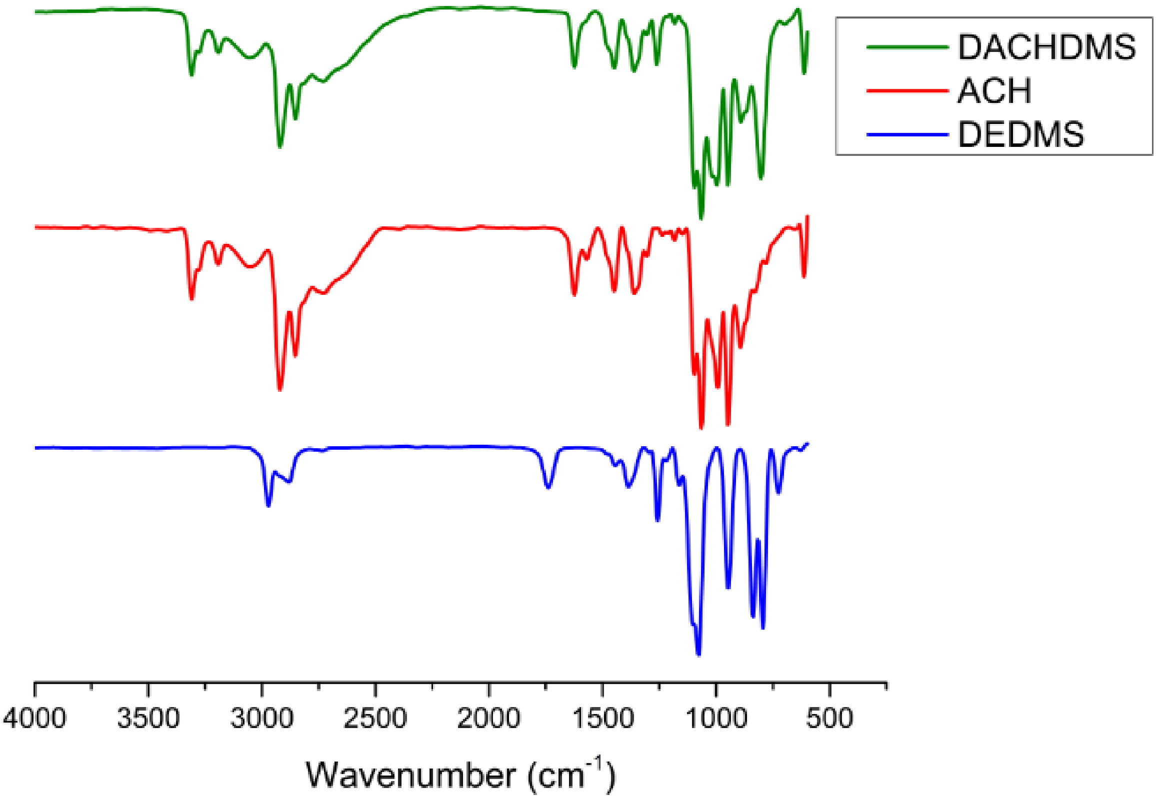

Figure 2-24: DADCHDMS monomer (top), ACH (middle), DEDMS (bottom).

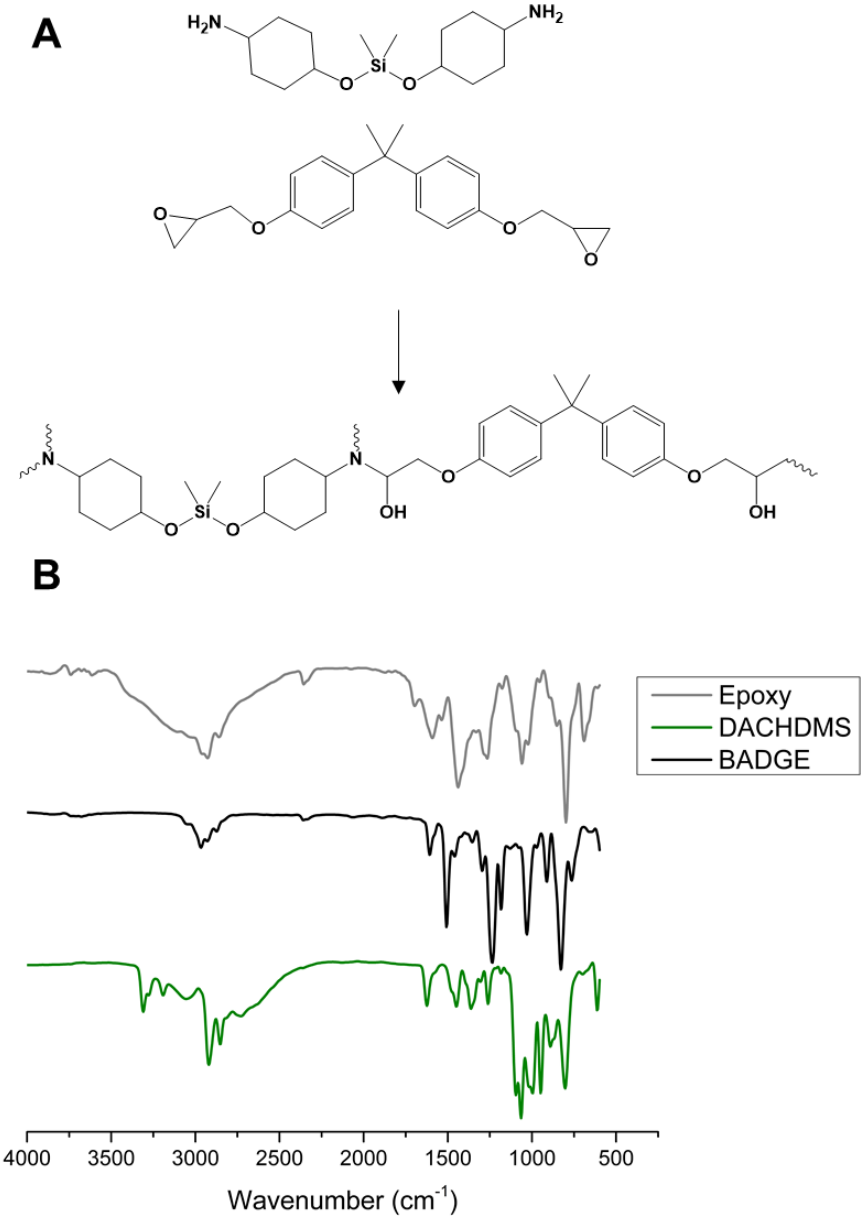

Figure 2- 25 (A) theoretical structure of epoxy. (B) IR of monomers and the resulting epoxy.

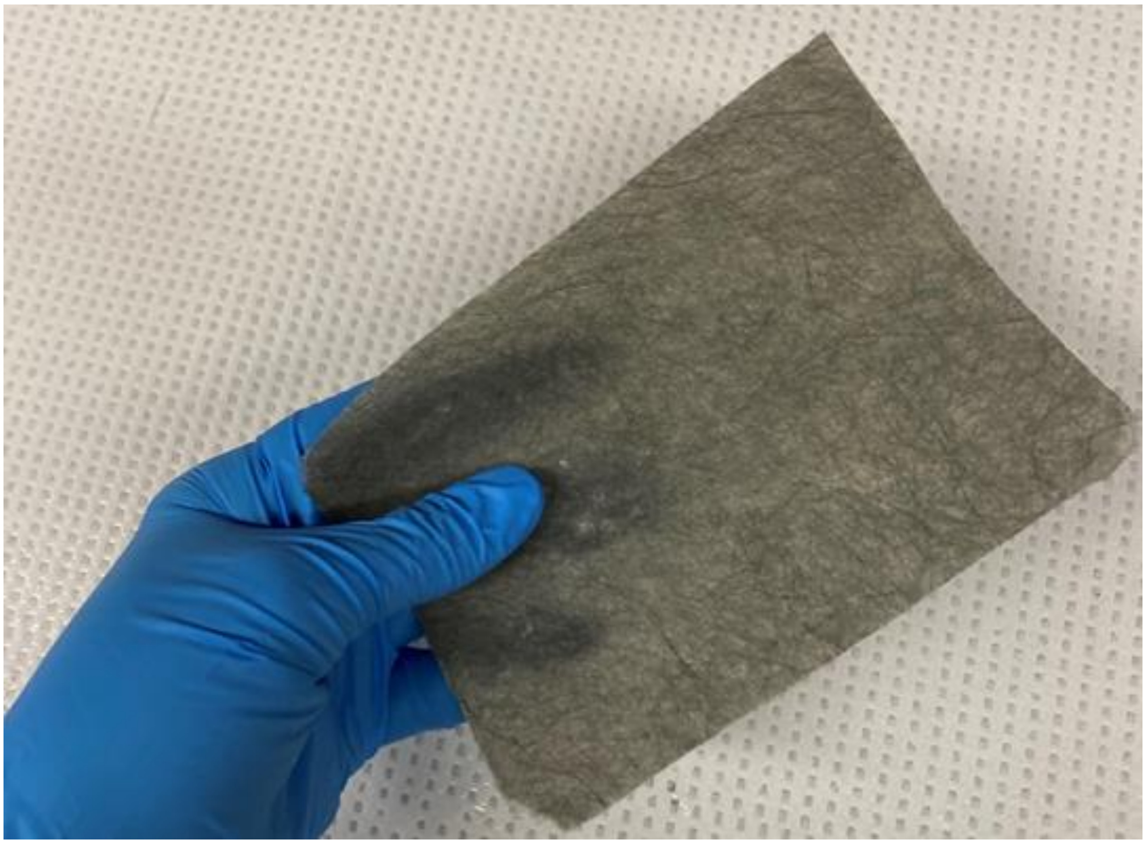

Figure 2- 26 Composite membrane formed by polymerization of BADGE with DACHDMS in an CF matrix.

References

(1) Xu, G., Wang, J., & Li, C. (2013). Strategies for improving the performance of the polyamide thin film composite (PA-TFC) reverse osmosis (RO) membranes : Surface modifications and nanoparticles incorporations. *Desalination*. *328*, 83–100.

(2) Elimelech, M., & Phillip, W. A. (2011). The Future of Seawater and the Environment: Energy, Technology, and the Environment. *Science (New York, N.Y.)*, *333*(August), 712–718.

(3) Do, V. T., Tang, C. Y., Reinhard, M., & Leckie, J. O. (2012). Degradation of polyamide nanofiltration and reverse osmosis membranes by hypochlorite. *Environmental Science and Technology*, *46*(2), 852–859.

(4) Do, V. T., Tang, C. Y., Reinhard, M., & Leckie, J. O. (2012). Degradation of polyamide nanofiltration and reverse osmosis membranes by hypochlorite. *Environmental Science and Technology*, *46*(2), 852–859.

(5) Verbeke, R., Arts, W., Dom, E., Dickmann, M., Egger, W., Koeckelberghs, G., Szymczyk, A., & Vankelecom, I. F. J. (2019). Transferring bulk chemistry to interfacial synthesis of TFC-membranes to create chemically robust poly(epoxyether)films. *Journal of Membrane Science*, *582*(January), 442–453.

(6) Verbeke, R., Seynaeve, M., Bastin, M., Davenport, D. M., Eyley, S., Thielemans, W., Koeckelberghs, G., Elimelech, M., & Vankelecom, I. F. J. (2020). The significant role of support layer solvent annealing in interfacial polymerization: The case of epoxide-based membranes. *Journal of Membrane Science*, *612*(June), 118438.

(7) McVerry, B., Anderson, M., He, N., Kweon, H., Ji, C., Xue, S., Rao, E., Lee, C., Lin, C.-W., Chen, D., Jun, D., Sant, G., & Kaner, R. B. (2019). Next-Generation Asymmetric Membranes Using Thin-Film Liftoff. *Nano Letters*, *19*(8), 5036–5043.

(8) Ji, C., Xue, S., Lin, C.-W., Mak, W. H., Mcverry, B. T., Turner, C. L., Anderson, M., Molas, J. C., Xu, Z., & Kaner, R. B. (2020). Ultrapermeable Organic Solvent Nanofiltration Membranes with Precisely Tailored Support Layers Fabricated Using Thin-Film Liftoff. *ACS Appl. Mater. Interfaces*, *12*, 30796–30804.

(9) Liu, F., Wang, L., Li, D., Liu, Q., & Deng, B. (2019). A review: The effect of the microporous support during interfacial polymerization on the morphology and performances of a thin film composite membrane for liquid purification. *RSC Advances*, *9*(61), 35417–35428.

(10) Singh, P. S., Joshi, S. V., Trivedi, J. J., Devmurari, C. V., Rao, A. P., & Ghosh, P. K. (2006). Probing the structural variations of thin film composite RO membranes obtained by coating polyamide over polysulfone membranes of different pore dimensions. *Journal of Membrane Science*, *278*(1–2), 19–25.

(11) Hermans, S., Bernstein, R., Volodin, A., & Vankelecom, I. F. J. (2015). Study of synthesis parameters and active layer morphology of interfacially polymerized polyamide-polysulfone membranes. *Reactive and Functional Polymers*, *86*, 199–208.

(12) Ghosh, A. K., & Hoek, E. M. V. (2009). Impacts of support membrane structure and chemistry on polyamide-polysulfone interfacial composite membranes. *Journal of Membrane Science*, *336*(1–2), 140–148.

(13) Vilakati, G. D., Wong, M. C. Y., Hoek, E. M. V, & Mamba, B. B. (2014). *Relating thin film composite membrane performance to support membrane morphology fabricated using lignin additive*. 469, 216-24.

(14) Ramon, G. Z., Wong, M. C. Y., & Hoek, E. M. V. (2012). Transport through composite membrane, part 1: Is there an optimal support membrane? *Journal of Membrane Science*, *415–416*, 298–305.

(15) Dong, X., Lu, D., Harris, T. A. L., & Escobar, I. C. (2021). Polymers and Solvents Used in Membrane Fabrication: A Review Focusing on Sustainable Membrane Development. *Membranes 2021, Vol. 11, Page 309*, *11*(5), 309.

(16) Alqaheem, Y., & Alomair, A. A. (2020). Minimizing Solvent Toxicity in Preparation of Polymeric Membranes for Gas Separation. *ACS Omega*. 5, 12, 630-6335.

(17) Ong, C., Falca, G., Huang, T., Liu, J., Manchanda, P., Chisca, S., & Nunes, S. P. (2020). Green Synthesis of Thin-Film Composite Membranes for Organic Solvent Nanofiltration. *ACS Sustainable Chemistry and Engineering*, *8*(31), 11541–11548.https://doi.org/10.1021/ACSSUSCHEMENG.0C02320/ASSET/IMAGES/LARGE/SC0C02320_0005.JPEG

(18) Cheng, C., & Gupta, M. (2020). Solvent-Free Synthesis of Selectively Wetting Multilayer and Janus Membranes. *Advanced Materials Interfaces*, *7*(20), 2001103. https://doi.org/10.1002/ADMI.202001103

(19) Waldman, R. Z., Yang, H. C., Mandia, D. J., Nealey, P. F., Elam, J. W., & Darling, S. B. (2018). Janus Membranes via Diffusion-Controlled Atomic Layer Deposition. *Advanced Materials Interfaces*, *5*(15), 1800658.

(20) Jang, H.-J., Shin, C. Y., & Kim, K.-B. (2015). Safety Evaluation of Polyethylene Glycol (PEG) Compounds for Cosmetic Use. *Toxicol. Res*, *31*(2), 105–136.

(21) Dipalma, J. A., Deridder, P. H., Orlando, R. C., Kolts, B. E., & Cleveland, M. V. (2000). A randomized, placebo-controlled, multicenter study of the safety and efficacy of a new polyethylene glycol laxative. *American Journal of Gastroenterology*, *95*(2), 446–450.

(22) Musgrave, C. S. A., & Fang, F. (2019). Contact Lens Materials: A Materials Science Perspective. *Materials*. *12*(2), 261.

(23) Jimenez, Y. P., Alele, N., Galleguillos, H. R., & Ulbricht, M. (2013). Nanofiltration

Separation of Aqueous Polyethyleneglycol – Salt Mixtures. *Separation Science and Technology*. 48, 1298–1307.

(24) McKeen, L. W. (2017). Markets and Applications for Films, Containers, and Membranes. *Permeability Properties of Plastics and Elastomers*. 4, 61–82.

(25) Souza-Chaves, B. M., Alhussaini, M. A., Felix, V., Presson, L. K., Betancourt, W. Q., Hickenbottom, K. L., & Achilli, A. (2022). Extending the life of water reuse reverse osmosis membranes using chlorination. *Journal of Membrane Science*, *642*, 119897.

(26) *Ashkelon Seawater Reverse Osmosis (SWRO) Plant, Israel - Water Technology*. (n.d.). Retrieved May 3, 2022, from https://www.water-technology.net/projects/israel/

(27) *Hydranautics to supply RO membrane to world's biggest seawater desalination plant in Israel*. (2010). Water World. https://www.waterworld.com/print/content/16220856

(28) Lawler, W., Alvarez-Gaitan, J., Leslie, G., & Le-Clech, P. (2015). Comparative life cycle assessment of end-of-life options for reverse osmosis membranes. *Desalination*, *357*, 45–54.

(29) Bowman, C. N., & Kloxin, C. J. (2012). Covalent adaptable networks: reversible bond structures incorporated in polymer networks. *Angew Chem Int Ed*, *51*(18), 4272–4274.

(30) Xie, Y., Hill, C. A. S., Xiao, Z., Militz, H., & Mai, C. (2010). Silane coupling agents used for natural fiber/polymer composites: A review. *Composites Part A: Applied Science and Manufacturing*, *41*(7), 806–819.

(31) Chen, X., Dam, M. A., Ono, K., Mal, A., Shen, H., Nutt, S. R., Sheran, K., & Wudl, F. (2002). A thermally re-mendable cross-linked polymeric material. *Science*, *295*(5560), 1698–1702.

(32) Bassampour, Z. S., Budy, S. M., & Son, D. Y. (2017). Degradable epoxy resins based on bisphenol A diglycidyl ether and silyl ether amine curing agents. *Journal of Applied Polymer Science*, *134*(12), 44620.

(33) Abdelmouleh, M., Boufi, S., Salah, A. Ben, Belgacem, M. N., & Gandini, A. (2002). Interaction of silane coupling agents with cellulose. *Langmuir*, *18*(8), 3203–3208.

(34) Gadhave, R. V, Mahanwar, P. A., & Gadekar, P. T. (2019). Cross-linking of Polyvinyl Alcohol/Starch Blends by Epoxy Silane for Improvement in Thermal and Mechanical Properties. *bioResources*. 14(2). 3833-3843.

(35) Ishida, H., & Koenig, J. L. (1980). EFFECT OF HYDROLYSIS AND DRYING ON THE SILOXANE BONDS OF A SILANE COUPLING AGENT DEPOSITED ON E-GLASS FIBERS. *Journal of Polymer Science. Part A-2, Polymer Physics*, *18*(2), 233–237.

(36) Witucki, G. L. (n.d.). *A Silane Primer: Chemistry and Applications of AIkoxy Silanes*.

(37) Gelest, & Inc. (2014). *Silane Coupling Agents Connecting Across Boundaries Metal Primers Bind Biomaterials Provide Crosslinking Immobilize Catalysts Improve Polymer and Particle Dispersion Enhance Adhesive Bonding Increase Electrical Properties Maximize Composite Strength Increase Mechanical Properties Version3 .0: Water-borne Silanes New Coupling Agents: Cyclic Aza-Silanes, Azido-Silanes, Dipodal Silanes Oligomeric Hydrolysates*. http://www.kellychemical.com

(38) Kumar, S., & Krishnan, S. (2020). Recycling of carbon fiber with epoxy composites by chemical recycling for future perspective: a review. *Chemical Papers*, *74*(11), 3785–3807.

(39) Baker, D. A., & Rials, T. G. (2013). Recent advances in low-cost carbon fiber manufacture from lignin. *Journal of Applied Polymer Science*, *130*(2), 713–728.

(40) Baker, D. A., Gallego, N. C., & Baker, F. S. (2012). On the characterization and spinning of an organic-purified lignin toward the manufacture of low-cost carbon fiber. *Journal of Applied Polymer Science*, *124*(1), 227–234.

(41) Jody, B. J., Pomykala, J. A., Daniels, E. J., & Greminger, J. L. (2004). A process to recover carbon fibers from polymer-matrix composites in end-of-life vehicles. *JOM 2004 56:8*, *56*(8), 43–47.

(42) Bai, Y., Wang, Z., & Feng, L. (2010). Chemical recycling of carbon fibers reinforced epoxy resin composites in oxygen in supercritical water. *Mater Des*, *31*(2), 999–1002.

(43) Dang, W., Kubouchi, M., Yamamoto, S., Sembokuya, H., & Tsuda, K. (2002). An approach to chemical recycling of epoxy resin cured with amine using nitric acid. *Polymer*, *43*(10), 2953–2958.

CHAPTER 3: Toward a Systematic Tuning of Thin-Film Composite Membrane Selectivity

Polybenzimidazole (PBI) represents a unique class of polymers that are known for being solvent tolerant, difficult to degrade, and mechanically tough.[1] The chemical tolerance of PBI has made it of great interest to those making membranes for water or organic solvent purification.[2-15] Still, much of the focus of PBI membranes is for their use as fuel cell membranes due to chemical tolerance and high proton conductivity when doped with acid.[15-20] By protonation of the imidazole groups, PBI immobilizes a polyprotic acid such that protons can "hop" through the membrane matrix from free acid, to immobilized acid, to water.[16,22] Unlike sulfonated fluoropolymers, like Nafion, PBI membranes do not require strict control of temperature and humidity for fuel cell operaton.[17] The need to keep the polymers from separating from the aqueous phase of the cell has led to an array of covalent and non-covalent crosslinking techniques.[23-27]

The use of PBI for water purification is not new.[1,12-14] Linear polybenzimidazoles were tested for desalination in the 1970's in both flat-sheet and hollow fiber formats and showed great potential for brackish water and seawater desalination.[13] Still, the same properties that make PBI great for fuel cell membranes complicate their use for aqueous applications where rejection of salts is largely based on the pH of the water to be filtered. Lv, *et al*. demonstrated the effects of pH on rejection of ions in water that have complex equilibria. The rejection values vary from ion-to-ion because the pH of the feed solution changes both the surface properties of the PBI as well as the charge and size of the ions in water.[11] Studies like this are crucial to the advancement of membrane technology as attention is turning away from solely focusing on reducing the energy used for RO toward improving selectivity.

Membrane selectivity is dependent on how attracted the membrane is to itself relative to the attraction of a solute or solvent is to the membrane. The cohesive energy density of a substance, or, the free energy needed to separate a material from itself can be described as:

$$\gamma_i \equiv -\frac{1}{2}\Delta G_{ii}^{coh}$$

Equation 3-1

where γ is the surface tension of substance i and ΔG is the cohesive energy density of the material. Therefore, for a solid membrane (m) and liquid (s), the cohesion can be represented as the difference in attractive cohesion and self-cohesion:[28]

$$\Delta G_{\mathrm{ms}} = \gamma_{\mathrm{ms}} - \gamma_{\mathrm{m}} - \gamma_{\mathrm{s}}$$

Equation 3-2

Now, the value γ is comprised of three components that are representative of van der Waals, hydrogen bonding, and acid/base interactions. This energy of cohesion can be found for a solid, such as a polymer membrane, by measuring the degree of attraction between liquids of known surface tensions, the degree of contact measured in terms of the angle θ that a drop of a liquid has with a material.[28] The total interfacial attraction between a liquid and a solid can be expressed as:

$$(1 + cos\theta)\gamma_{\mathrm{l}}{}^{TOT} = -\Delta G_{\mathrm{ml}}{}^{LW} - \Delta G_{\mathrm{ml}}{}^{AB}$$

Equation 3-3

where LW indicates the Lishfitz-van der Waals interaction and AB indicates the acid-base interaction. In order to find the cohesive energy of a material with itself, each interfacial energy between liquid and solid must be broken down into either LW attraction or acid-base base-acid attraction between the two.[28] After the appropriate combinatorial treatments, one yields:

$$((1+cos\theta)\gamma_L^{TOT} = 2\sqrt{\gamma_S^{LW}\gamma_L^{LW}} + \sqrt{\gamma_S^{+}\gamma_L^{-}} + \sqrt{\gamma_S^{-}\gamma_L^{+}}$$

Equation 3-4

γ^+ and γ^- is sometimes combined into one term γ^{AB}, by Equation 3-5.

$$y_i^{AB} = 2\sqrt{\gamma_i^{+}\gamma_i^{-}}$$

Equation 3-5

In this case, three liquids of known cohesivities can be used to acquire contact angles with a single material. By solving the system of equation based on each $\gamma_L{}^{TOT}$, one can obtain the cohesive energy of the membrane active layer material. Since the solubility of a solute relative to the solubility of its solvent in an active layer determines the perm-selectivity of the membrane, the separation mechanism can only be tuned based on an understanding of the balance of forces around the solvated solute. From there, the contribution of each cohesive force can be broken down and correlated (or not) to the rejection of a particular solute.

This work addresses the question of how PBI’s might be altered to improve rejection of ions across the pH scale and if the amphoteric nature of derivatives of PBI might broaden the operating pH scale for PBI membranes. A simple system of monovalent ions and four different PBIs were tested for rejection of NaCl at high, low, and neutral pH. Rejection of ions at both seawater and low salinity were measured along with a variety of surface properties.

Figure 3-1 shows the structures of the 4 PBI’s used in this study and how they may adopt different charged states depending on the pH of the water they’re immersed in. Celazole (PBI) (Figure 3-1-A) can adopt a positive charge at low pH. Sulfonated PBI (SPBI) (Figure 3-1-B) can adopt a positive charge at low pH and a negative charge at high pH. Nitrated PBI (NPBI)

(Figure 3-1-C) adopts a positive charge at low pH as PBI does, but has the added hydrophilicity due to the nitro groups on the benzene portions. Lastly, aminated PBI (APBI) (Figure 3-1-D) does not have a charge at high pH, but can adopt additional positive charges at low pH. Though rejection of ions by membranes can be highly dependent on charges at the surface, which causes ions to be repelled from the membrane at the surface or experience additional drag when permeating through a membrane, the rejections observed here do not directly correspond to whether the polymer should theoretically possess a charge.

The last section of this work demonstrates the tuning of membrane active layer diffusivity and surface energies by changing the ratio of PBI and polystyrene sulfonic acid (PSSA) in a polymer blend (Figure 3-2). PBI being basic and water-insoluble and PSSA being acidic and water soluble presents a unique polymer system where surface energies and water diffusivity can be tuned. Upon heating, the sulfonic acids and benzene ring undergo a Friedel-Crafts reaction to create covalent crosslinks.[24] This may be a valuable approach to designing polymers with tailored selectivity, without having to use a new type of polymer.

Materials

Celazole (PBI) was obtained from Performance Products Inc. A 10% PBI solution in DMAc was dialyzed against water to remove the solvent and stabilizers. The precipitated polymer was then freeze-dried to remove any residual water. Sulfuric acid and nitric acid were obtained from Fisher Scientific and used without modification. A 10% aqueous solution of PSSA was obtained from Sigma Aldrich and freeze-dried to form a powder prior to use. Solvents and all other reagents were obtained from Sigma Aldrich and used without further purification.

Synthesis

Four different PBIs were used in this work. Celazole was use directly. Three other derivatives were synthesized from Celazole – sulfonated PBI (SPBI), nitrated PBI (NPBI), and aminated PBI (APBI). Celazole was dissolved in sulfuric acid and heated at 180 ^{o}C for 48 hours. The product was dialyzed against water for several days and lyophilized to produce a yellow powder. To produce NPBI, Celazole was dissolved in 5:1 HNO_3:H_2SO_4 and heated at 180 ^{o}C for 4 hours. The solution was dialyzed against water for several days. The resulting bright-orange polymer was vacuum filtered to remove water and rinsed several times with DI water followed by drying in a vacuum oven at 60 ^{o}C for several hours. The resulting NPBI was dissolved in DMAc with a catalytic amount of palladium on carbon under H_2 gas for 48 hours. The solution was filtered to remove Pd/C and precipitated with DI water. The product was rinsed several times with deionized water with vacuum filtration. The amber-colored product was dried in a vacuum oven at 60 ^{o}C to remove any residual water. All four powders are shown in Figure 3-4. Modifications were confirmed using ATR-IR spectroscopy. The C=N stretch along with the C-H blend of a benzene remain present in all PBI samples. The appearance of peaks corresponding with N-O stretching; a primary amine N-H bend and C-N stretch; and the S=O stretch indicate successful derivatization. The XPS analysis (Table 3-1) indicates appropriate changes in elemental composition when comparing each derivative to unmodified PBI. Comparing the atomic composition between derivatives does not appear as consistent, the aminated PBI seems to have too high of oxygen and sulfur content relative to the SPBI sample. This suggests that either APBI is slightly contaminated with sulfuric acid left over from the nitration step prior to hydrogenation or that the APBI is very sensitive to contamination with acids due to the primary amine moieties.

Methods

Contact Angle

Sessile drop contact angle measurements were taken using deionized water, ethylene glycol, and diiodomethane as probe liquids using a contact angle goniometer. The average of 10 measurements taken 10 s after deposition were used. Surface tension components were calculated using Equation 3-4.

ζ-Potential

ζ-potential measurements were obtained using an Anton Parr SurPASS Electrokinetic analyzer equipped with an adjustable gap cell. Automatic titration was performed with the addition of either HCl or NaOH.

A three mil doctor blade was used to cast polymers onto glass slides and dried on a hot plate set to 60 °C for contact angle and ζ-potential analysis. Membranes were made using T-FLO as described in Chapter 1, where the active layers were cast from 5 wt. % solutions using a 0.3 mil, fixed-height doctor blade and dried on a hot plate at 60 °C. Supports were made using PEG 300 as the porogen.

Blends of PBI and poly(styrenesulfonic) acid were prepared by dissolving PBI and PSSA in DMAc at 10 wt.%. PBI and 5 mL of PSSA solution were combined according to the specific ratios as described later in this chapter, resulting in the precipitation of the polymer due to acid-base interactions. The blend was re-dissolved by the addition of 1 mL of 1-methyl imidazole. Solutions were cast onto glass slides for contact angle and XPS analysis.

Membranes were made by casting the aforementioned solutions onto glass substrates and lifted off using T-FLO where the epoxy resin was dissolved in 50% PEG 200 and 50% PEG 400. For crosslinked samples, the active layers were allowed to cure at 180 °C for 4 hours prior to T-FLO. Table 3-2 gives the XPS-derived O:S ratio for blends and crosslinked blends. The O:S ratio decreases after crosslinking due to the loss of O-H from the sulfonic acid group that is transformed into a sulfone group.

Salt-Rejection Measurements

A dead-end stirred cell was used to determine salt-rejection of each membrane. The membranes were compacted with deionized water and flux measured gravimetrically. Subsequently, 250 mL of feed solution was loaded into the cell, which was then pressurized to 800 psi. The first 5 mL of permeate was discarded. The next 25 mL was collected. Rejection was determined by comparing the conductivity of the permeate solution with that of the feed.

Discussion

ζ-Potential can be used to measure the amount of charge on a solid surface in different aqueous environments. ζ-potential between -10 mV and +10 mV is considered somewhat neutral, while values above 10 mV indicate a positively charged surface and those below -10 mV, a negative surface charge. As expected, PBI has a strong positive charge at pH values below 7 and is most positive below pH 5. SPBI, on the other hand, has less positive charge than PBI, beginning at a pH of less than 5. PBI has a negative surface charge above pH 8, but this decreases much more slowly with increasing pH when compared to the other PBIs. It is not surprising that SPBI has the greatest negative charge and the smallest window of neutral charge of all of the PBIs as it can adopt a true negative charge via sulfonate. NPBI does not get charged at high or low pH when compared to SPBI and PBI. This makes sense as the nitro group cannot add protons or become negative. The basic imidazole groups are in-part shielded by the electron density of the nitro groups. The measurements of APBI surface charge do not align with chemical intuition. It was expected that APBI would have the most positive surface charge at low pH because of the primary amines. Instead, APBI more closely tracks with NPBI, having a slightly positive charge only below pH 4 and avvery negative charge above pH 5. The discrepancies between ζ-potential and rejection show that for highly amphoteric systems, surface charge alone is not the best indicator for rejection.

PBI and SPBI follow the same trend of decreasing salinity with increasing pH. APBI and NPBI performed better separations at either high or low pH and worse at neutral pH. At high salinity, these trends were less obvious for SPBI and APBI, which were relatively constant across the pH range.

It is generally accepted that surface charge on a membrane is only relevant to rejection at low salinity. Otherwise, there is too much shielding of the membrane surface by the ions in solution for permeating ions to be substantially repelled by the surface charges. Overall, the rejection of salt was lower when the feed was at 3.5% and the variability for SPBI and APBI was diminished. This is not surprising for linear polymers, but PBI and NPBI appear to have a pH dependency for rejection at both low and high salinity. NPBI has even higher rejection at low pH for the high salinity trials versus the low salinity trials.

Hydrophilic membranes are thought to hold a layer of water at the surface of the membrane, preventing hydrophobic foulants from adhering to the surface and increasing rejection of solutes because of the higher diffusivity of water in these samples. **Table 3-3** contains contact angles of deionized water (DI), ethylene glycol (GL), and diiodomethane (DM), for each polymer. A lower contact angle indicates a surface's higher affinity for the solvent, therefore contact angles with DI are indicative of which polymers are most hydrophilic. APBI is the most hydrophilic, followed by NPBI, PBI, and SPBI. If self-neutralization is occurring within the SPBI polymer (sulfonic acid with imidazole), this may explain the lower hydrophilicity of SPBI as hydrogen-bonding sites would be reduced. The combination of lone pairs on the N atoms and polar, hydrogen bonding N-H bonds, providing two modalities for H-bonding with water, may best explain the overall highest hydrophilicity of APBI. Following the same logic, N-PBI simply has more sites for hydrogen bonding than PBI alone.

Hydrophilicity alone is not indicative of rejection at high or low pH, but interfacial surface tension components can be determined for each membrane by using a series of probe liquids (water, ethylene glycol, and diiodomethane) that have known surface energy. These data can then be used to solve for the membrane surface energy components using Equation 3-4. The results of these calculations are summarized in Figure 3-7D.

The rejection of 0.2% NaCl and 3.5% NaCl at pH 2, pH 7, and pH 10 by each membrane is summarized in Figures 3-7A and 3-7B, respectively. These membranes are not highly crosslinked like traditional RO membranes, therefore, rejection at >99% is not expected. Although this work sheds light on how chemically tolerant RO membranes might be designed, the rejection of NaCl is being used to study the materials, not for the optimization of an RO membrane. At low salinity, SPBI is the highest performing membrane, except at pH 10 where NPBI is highest performing. For seawater levels of NaCl, rejection is much lower and the differences in performance of each membrane are more uniform, especially at pH 7. However, NPBI appears to better reject salts at both concentrations if at pH 2 or pH 10.

At low salinity, APBI and NPBI appear to reject salt better at high or low pH than at neutral pH. PBI and SPBI have the highest rejection at low pH, which worsens as the pH increases. At low pH, the PBI derivatives reject salt in order of increasing surface charge according to zeta potential. PBI is worse despite having the highest surface charge at low pH. A corresponding trend does not exist at neutral pH or high pH. Despite being the most negatively charged at neutral pH according to ζ-potential, APBI shows the poorest salt rejection at this pH.

NPBI and SPBI have the greatest γ^{AB} values, at 12.5 and 12.4, respectively, which may correlate with their superior rejection at low and high pH. PBI has the lowest γ^{AB}, at 7.0. For SPBI, γ^{-} is a larger contributor to γ^{AB} than γ^{+} with values of 3.7 and 10.3. NPBI is less skewed toward γ^{-}, with γ^{-} and γ^{+} of 8.4 and 4.6. NPBI has the highest γ^{LW}. Since charged states have less of an effect at high salinity, it may be that γ^{LW} drag, due to dispersion forces, may have a key role in rejection of highly saline solutions. Comparatively, PBI and APBI have the highest γ^{-} values, but significantly lower γ^{+} values.

PBI has the highest γ^- at 18.3, while a γ^+ of only 0.7. It may be that the best salt rejection is achieved by having high γ^{AB}, but the contribution to γ^{AB} according to Equations 3-3 thorugh 3-5 must be evenly distributed between γ^- and γ^+; thus, it is not sufficient to consider just $\gamma^{AB.}$.

While the above trends hold true for this small data set, these properties are intrinsically linked and the direct relationship of one or two variables is not always obvious. To summarize these observations, a correlation matrix was generated (Figure 3-8). The degree of correlation between two variables is defined in Equation 3-6, where x_i and y_i are two variables for one sample and $\overline{x}_i$ and $\overline{y}_i$ are the mean of all of the variables in the sample set.

$$Correlation\ Coefficient = \frac{\Sigma(x_i - \overline{x}_i)(y_i - \overline{y}_i)}{\sqrt{\Sigma(x_i - \overline{x}_i)^2 \Sigma(y_i - \overline{y}_i)^2}}$$

Equation 3-6

The result is the correlation coefficient, a number between 0-1 that describes the degree of positive and negative correlation. If a correlation coefficient between two variables is zero, their relationship is random. The color bar in Figure 3-8 represents the degree of correlation between two variables, where teal is neutral, yellow is the highest positive correlation, and dark blue is the most negative correlation. On either axis are the rejection at different pH and salinity values, the elemental analysis from XPS, the surface tension components, and certain ζ-potential values. Rejection of 3.5% NaCl at pH 2 is abbreviated as “pH2 3.5”, all of the rejection values follow this abbreviation. The elemental analysis is labelled by the electron orbital used for XPS quantitation corresponding to each element (e.g., carbon atomic % is labelled “C1s”). The surface energy components are labelled “g” with the type (tot., LW, etc.) as superscripts. Contact angles are labelled “CA” followed by the probe liquid; EG is ethylene glycol, DM is diiodomethane, and DI is deionized water. IEP stands for isoelectronic point and zeta potential values are labelled “ZP” followed by the pH value at which it was measured.

For simplicity, the rejection components on the y-axis and the rest of the mentioned elements are visible while the rest of the matrix is partially covered. Each set of components on the y-axis are boxed in red for ease of reading.

Rows 2 and 5 are correlation values for pH 7 and 3.5% NaCl and 0.2% NaCl, respectively. In elemental analysis, there is a positive correlation between carbon content and rejection, while all other elements are negatively correlated. For surface energies, all are negatively correlated except γ^-, which has a strong positive correlation, especially at high salinity. All of the contact angles and ζ-potential values are negatively correlated.

When looking at the other rows (1,3,4, and 6) corresponding to high and low pH at both salinities, the correlations (in general) are the reverse what they were with the pH 7 values. Carbon is negatively correlated with rejection, while all of the other elements (with the exception of S2p at 3.5% and pH 2) become positively correlated. All surface energy components become positively correlated, except γ^+. Rejection of 3.5% NaCl at pH 2 shows the weakest positive and negative correlations, but the trends remain the same.

To create a crosslinked network for improved salt rejection, blends of PBI and PSSA were fabricated into membranes. The ratio of PBI to PSSA in each film is summarized in Figure 3-6D. This appears to give the ability to tune the hydrophilicity and the γ^- and γ^+ values for the polymer film. Decreasing the amount of PSSA increased the hydrophilicity of the membrane. Doing so also caused an increase in γ^- and a decrease in γ^+; although, doing this does not have as great of an effect on the net γ^{AB}. These membranes experienced a decrease in γ^{LW} upon curing, which may make them good candidates for RO at neutral pH.

The performance of these membranes are summarized in Table 3-4. These results cannot be directly compared to those of the aforementioned PBI derivatives as their membrane supports and pH conditions were slightly different. Additionally, only rejection of 3.5% NaCl was measured. Only S1 and PBI were used in this experiment. PBI shows the same trend of decreasing rejection with increasing pH as shown in Figure 3-7B. PBI/PSSA gives the opposite trend. The γ^- values for the PBI/PSSA blends are much lower than for the PBI derivatives. Although it is possible that S1 may be following the same trend as the derivatives when it comes to higher rejection at high pH, the distinctly lower rejection at low pH may have to do with some relationship between γ values beyond the scope of these data.

Conclusions

PBI, SPBI, NPBI, and APBI have varying properties. When used to reject salt at pH 7, the γ^+ surface energy component was most important. At low and high pH, it was most important to have a lower γ^+, and the contributions of γ^+ and γ^- to be more equal in magnitude. ζ -potential values for neutral feed solutions should be more positive, while at *either* low or high pH, lower ζ -potential values appear more advantageous. Blending PBI with PSSA to create a more crosslinked network gives good handles for optimization in terms of γ^+ and γ^-, but not for γ^{LW}. Curing of the blend to form covalent crosslinks does not appear to have a uniform effect on γ values. Increasing the amount of PSSA in the blend and crosslinking cause the hydrophilicity of the films to decrease. These experiments show that at both high and low salinity, the same membrane may not be able to perform well at both neutral and non-neutral pH, however, PBIs are good candidates for high rejection at both high and low pH.

To further this work, several more validation tests must be performed using the same polymers as well as the polymer derivatives made with differing degrees of functionalization. The exact location of functionalities along the PBI chains must be determined using NMR to confirm that changes in surface energy components have to do with the added functionalities in general or with functionalities along certain locations on either the benzene or benzimidazole portions of the polymer.

Making polymer blends gives some systematic control over the γ values for membranes, as shown with PBI/PSSA. Additional blends need to be tested to see if a highly entropic membrane, with regions of variable γ values, might be used to perform well across the range of salinity and extreme pH levels tested here. For example, would a blend of NPBI and PBI be able to have high rejection at both low and high pH, while also providing reasonable rejection at neutral pH? Would creating block co-polymers of PBIs build a better entropic membrane than just a blend of the polymers?

Preliminary work (not included here) shows that SPBI is much more crystalline than PBI or a blend of PBI and PSSA. Since crystallinity creates regions in the polymer that are impenetrable, that means that it is in the voids surrounding the crystalline regions that determine the separation. A degree of crystallinity may be determined using traditional XRD. A method of peak fitting should be employed to quantify the FWHM values and relative intensity of the peaks. More in-depth analysis of crystallinity may help create a more representative correlation matrix. To gain better insight into the pore-sizes of dense PBI films, positron annihilation lifetime spectroscopy (PALS) may be used. Optical techniques may be limited or impossible to determine pore sizes of dense films as the pores are simply the voids between polymer chains, requiring the use of more intensive techniques.

Additionally, this study employed the same procedure for making the support membrane for each sample. This may be eliminating the potential for better separation by polymer films that could be brought about by optimizing the support membrane individually. Eventually, these variables must also be incorporated, but confirmation of the present trends must be validated before adding in additional variables. In order for any of these correlations to be accepted, many more experiments must be carried out. This data set is really only suitable for demonstration purposes. After doing so, more scrutiny must be applied to the absolute values of correlation and perhaps a more sophisticated model for correlation adapted. Though it is the opinion of the author that using data such as these to predict the performance of membranes may be very far off, building data sets such as these may help guide the design of new membranes within the same class (in this case, linear PBIs).

In the following section, it is demonstrated that by using phase-inverted films as opposed to dense films, more functional membranes may be made.

Nonsolvent Induced Phase Separation (NIPS) to Form Porous PBI Thin Films

Introduction

In Chapter 1, Thin-Film Lift Off (T-FLO) was used to lift dense thin films onto porous epoxy substrates in order to simplify the fabrication of complex asymmetric membranes. A two-layer crosslinked PBI-PSSA membrane was highly effective at salt removal and maintained high rejection under harsh conditions. Despite low flux relative to commercial membranes, the membrane is in itself valuable, especially for niche applications. T-FLO remains a good technique for making asymmetric membranes of novel materials and then optimize them for compaction resistance. In theory, if active layers could be cast thinner and thinner, flux can be greatly increased and the same separation achieved. In practice, directly casting dense polymer films on the scale of tens of nanometer thick skin layers of interfacially-polymerized active layers poses challenges including creating continuous thin films on a large scale when working with extremely dilute polymer solutions. These challenges lead to a high dispersity of rejection values for higher-flux T-FLO membranes. There is still work to be done in this area, but this section will briefly discuss the use of nonsolvent initiated phase separation (NIPS) in tandem with T-FLO. Normally, membranes made using NIPS are made by casting a polymer solution onto a support followed by immersion into a bath to precipitate the completed membrane. Here, the active layer will be generated by immersing a polymer thin film into a nonsolvent and then casting an epoxy support onto the film for lift off.

The asymmetric structure and the pore size of a NIPS membrane is based on the relative affinity of the nonsolvent for the polymer solvent as well as the polymer.[29-35] If solvent and non-solvent are highly miscible, the rapid permeation through the solid phase of the solvent often leads to elongated finger-like pores. If the solvent and the nonsolvent are less miscible, the structure will be more sponge-like.[30] Typically the side of the film that first contacts the non-solvent will be the densest due to rapid precipitation. This dense portion serves as the active layer. Ideally, this work would allow continuous films of the polymers made earlier in this chapter, but with much thinner active layers. Here the active layer is determined by the polymer-solvent-non-solvent system, rather than the height of the doctor blade and the concentration of polymer dope solution.

In this work, thin films are cast onto glass plates and precipitated using NIPS without removal from the plate. These films can be peeled from the glass and used for pore-structure analysis or formed into asymmetric membranes using T-FLO. Secondly, different non-solvents are tested including isopropanol, water, and acetone; to observe their effect on pore structure. Lastly, films of different PBI derivatives are tested using the same solvent system to observe how slight changes in the polymer affects the resultant film morphology.

Experimental

PBI films for SEM

A 20% PBI solution was prepared by dissolving PBI powder in DMAc at 50 ºC for 24 hrs. Thin films were cast onto glass substrates using a 3-mil fixed-height doctor blade, which were then submerged into deionized water to precipitate the PBI. Films were not removed from the glass plates, but were then either heated at 60 ºC or air-dried to remove solvents. Small portions of the dried films were peeled off of the plate, freeze-fractured, sputtered with gold, and imaged using a JEOL JSM-6700F FE-Scanning Electron Microscope.

T-FLO of Phase Inverted Films

A 20% or 5% solution of PBI, APBI, NPBI, or SPBI was made in DMAc. Solutions were cast onto glass plates with a 3-mil doctor blade and immediately submerged, membrane-side-down, into the nonsolvent. Some material was lost upon removal of the films from the water. Films were air-dried. The complete process for making T-FLO membranes is described in the previous chapter. The version incorporating NIPS is summarized in **Figure 3-12**.

DI flux was determined gravimetrically as described in Chapter 2.

Discussion and Conclusions

The side facing away from the plate has a much smaller pores, while the film facing the plate was smooth but with larger pores. The film morphology for the solvent-facing sides of the films are shown in Figure 3-12AC. The glass-facing side, as expected, has a smoother morphology with some porosity (Figure 3-12D). Cross-sectional images do not indicate a large-scale asymmetric structure with a visible active layer; therefore, higher resolution imaging is needed. T-FLO membranes with NIPS active layers were fabricated and tested for DI flux. While phase inversion performed using water showed the most porous structure from SEM, when thinner films were used, acetone was better in terms of processing. Films precipitated in water often came off of the plate upon removal from water. Therefore, acetone was selected as the most practical solvent for making large-area samples.

Figure 3-13 includes crossesctions of T-FLO membranes with active layers formed by precipitation in IPA, deionized water, and acetone, respectively. The most porous structure appears to be the water-precipitated sample, followed by the acetone and IPA. IPA does not appear to generate the same degree of interconnected pores as water and acetone. The higher viscocity of water compared to acetone makes it a more difficult solvent to use for phase inversion of thinner films.

Images of thinner phase-inverted films after T-FLO are given in Figure 3-13. The top images have active layers made from phase-inverted PBI, while the bottom two images are taken from phase-inverted APBI. The PBI films have a greater asymmetry, while the APBI films appear denser. Although, in Figure 3-13B, small pores in the active layer cross section can be seen toward the bottom of the image.

Table 3-5 gives the flux for T-FLO membranes made with dense films and the flux for membranes images in Figure 3-13. Both membranes saw an increase in flux, as expected, when NIPS was used in membrane fabrication. APBI, which already exhibited greater flux than PBI films, had a much larger change, however, the change was proportional to the change in PBI at about 14-fold.

The new membranes did not exhibit rejection of monovalent salts, as expected given the pores visible in Figure 3-12. Still, this demonstrates that phase inversion may be highly applicable to T-FLO membranes and be a way forward for applying the fundamentals discussed in part 1 of this chapter to real-world membranes. Additional experiments must be performed in this area. All PBI derivatives (APBI, NPBI, and SPBI) must be tested to better understand the effects of different non-solvents on film structure. Once monovalent salt-rejecting membranes are made using this technique, the trends observed earlier in this chapter must be confirmed.

Fog-point titrations need to be performed to generate ternary phase diagrams for each polymer (PBI, SPBI, NPBI, and APBI) solvent-non-solvent system that will be useful for deterministically designing a membrane. Analysis of pore size and pore-size distribution should be observed using SEM.

Tables

Table 3-2 Elemental Analysis Based on XPS Survey Scans

Atomic %	**O**	**N**	**C**	**S**
PBI	1.13	7.71	91.16	0
N-PBI	4.15	9.98	85.87	0
A-PBI	9.9	13.8	74.74	1.57
S-PBI	4.49	6.88	86.27	2.36

Figures

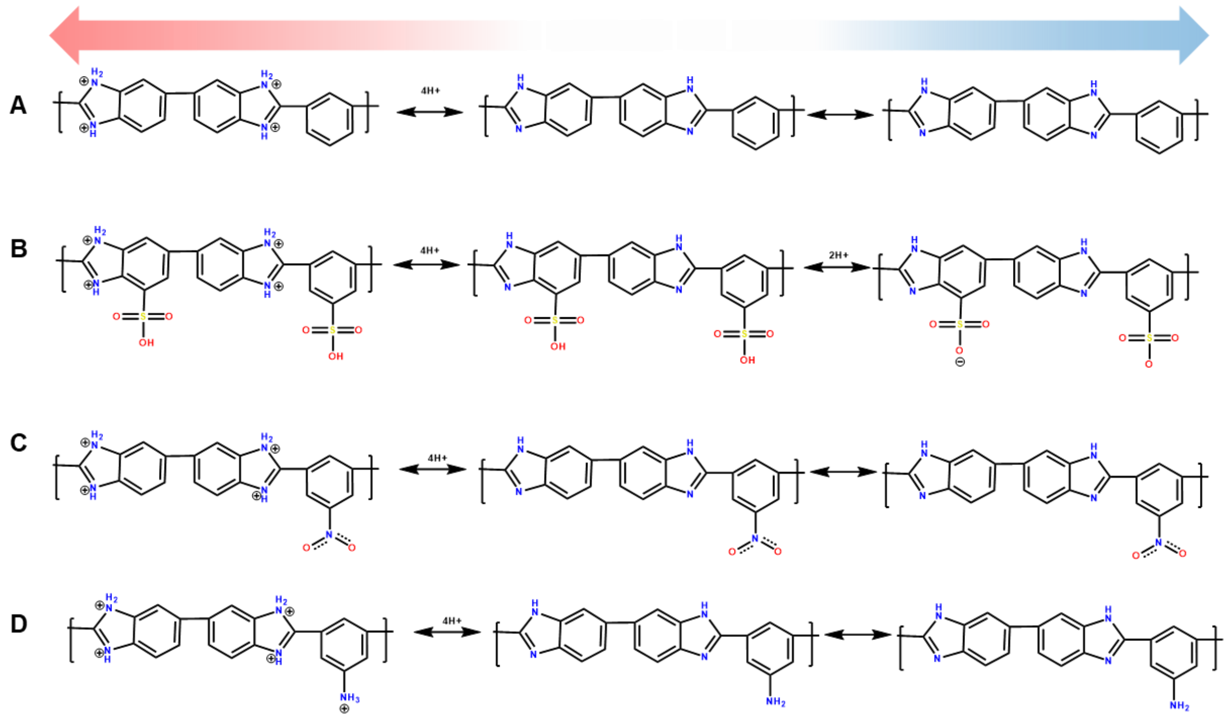

Figure 3-12: Schematics of (A) PBI (B) SPBI (C) NPBI (D) APBI with charged states at varying pH.

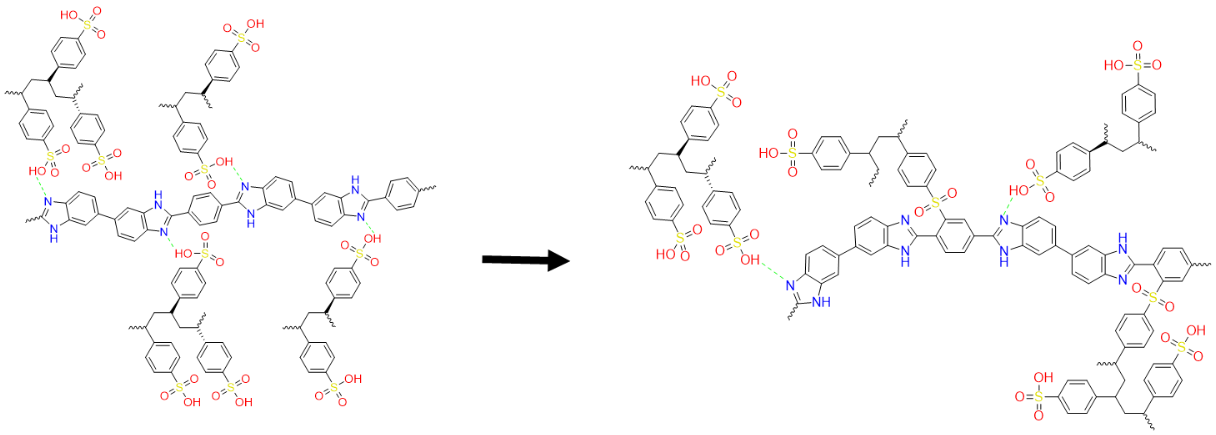

Figure 3-13: Crosslinking of PBI with SPBI

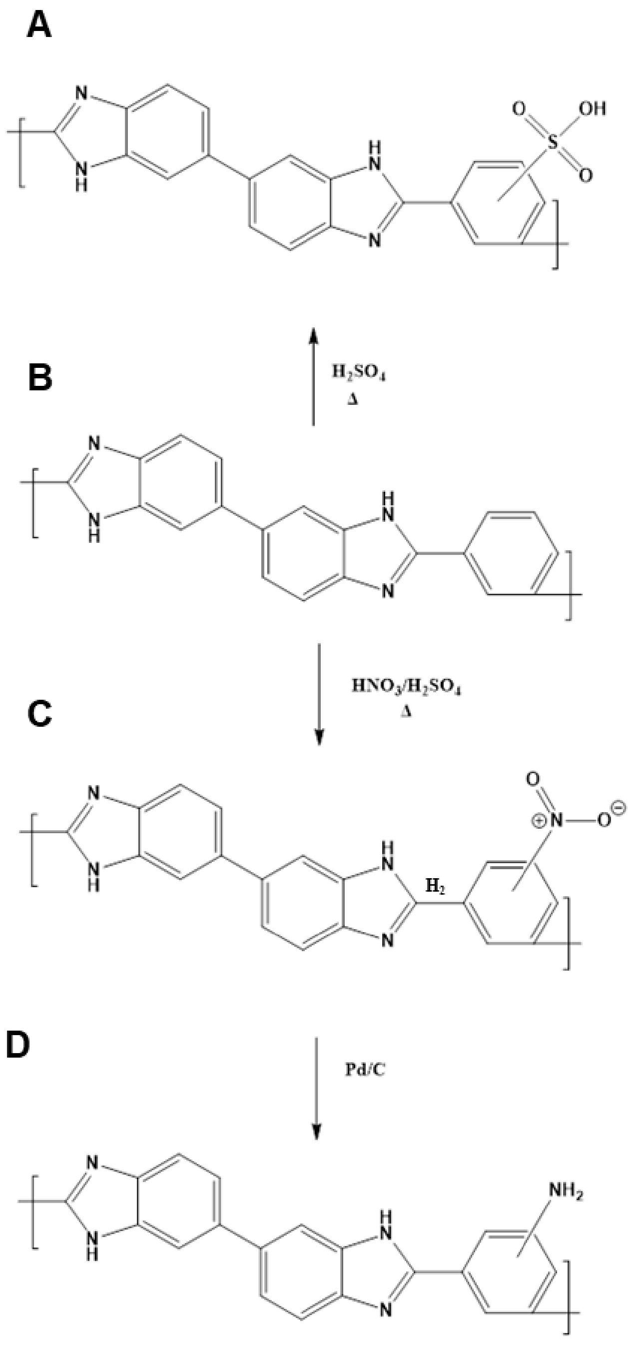

Figure 3-3: Synthesis of (A) SPBI (B) PBI (C) NPBI (D) APBI

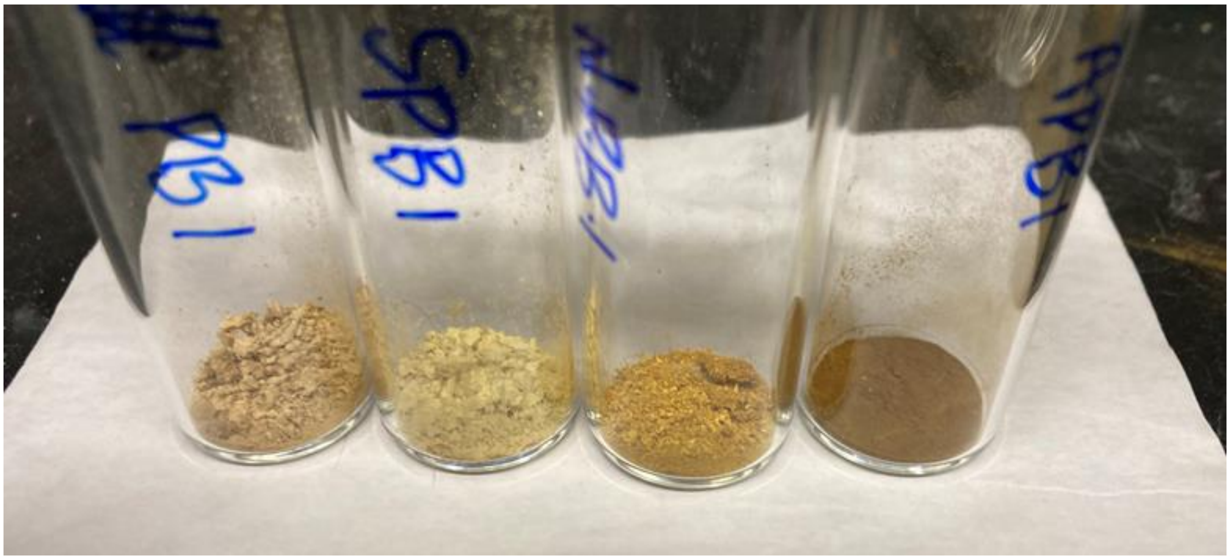

Figure 3- 14 Powders of PBI, SPBI, NPBI, and APBI (left-to-right).

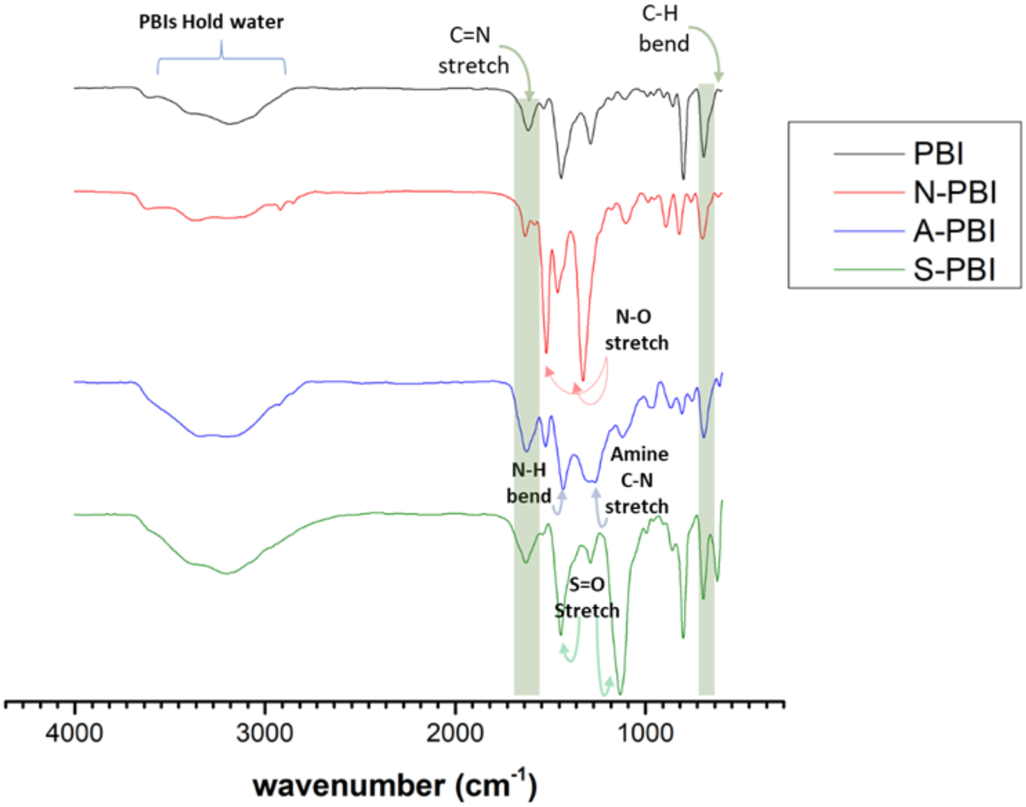

Figure 3- 15: IR spectra of selected polymer powders.

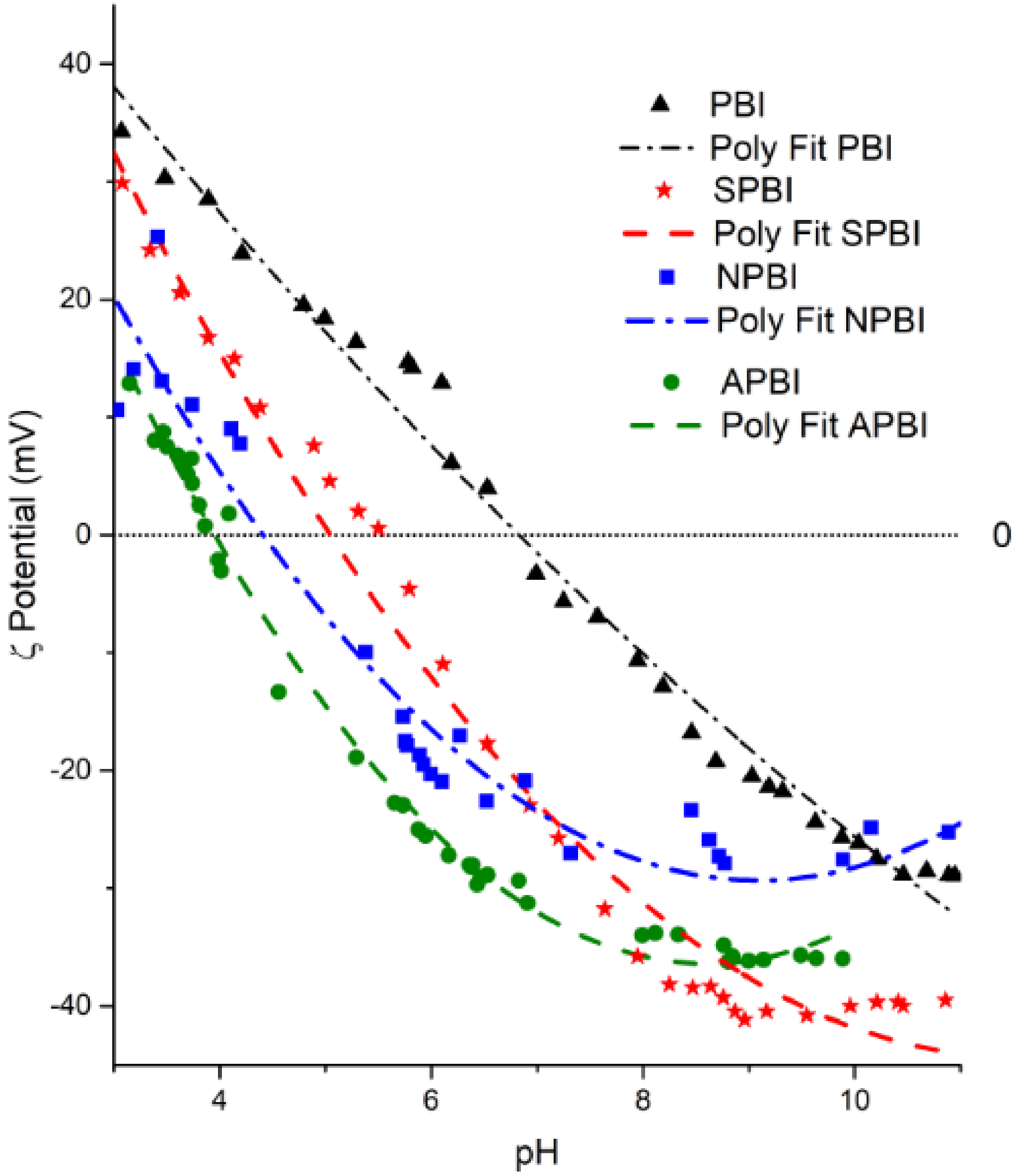

Figure 3-16 ζ-potential measurements for thin films of PBIs.

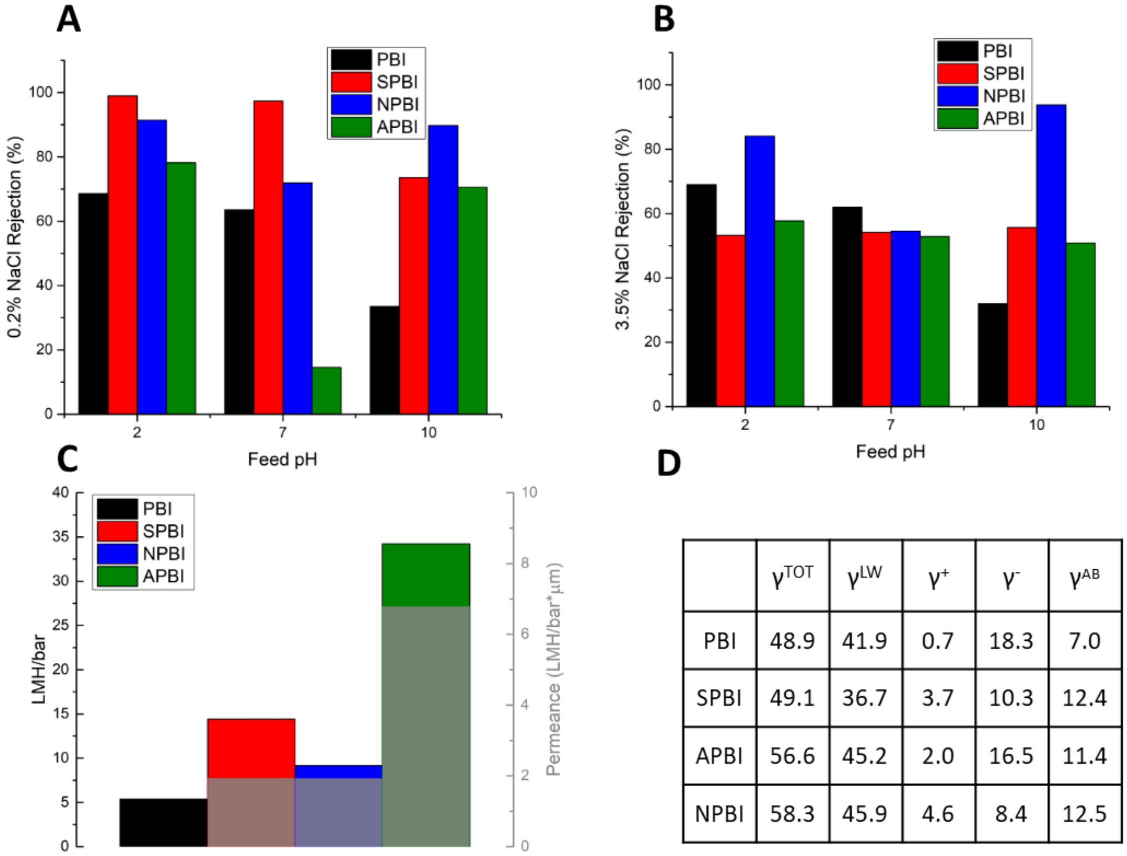

	γ^{TOT}	γ^{LW}	γ^{+}	γ^{-}	γ^{AB}
PBI	48.9	41.9	0.7	18.3	7.0
SPBI	49.1	36.7	3.7	10.3	12.4
APBI	56.6	45.2	2.0	16.5	11.4
NPBI	58.3	45.9	4.6	8.4	12.5

Figure 3-17: (A) Rejection of 0.2% NaCl at pH 2, pH 7, and pH 10. (B) Rejection of 3.5% NaCl at pH 2, pH 7, and pH 10. (C) DI flux and permeance, flux divided by thickness of active layer. (D) Interfacial surface tension values determined by contact angle.

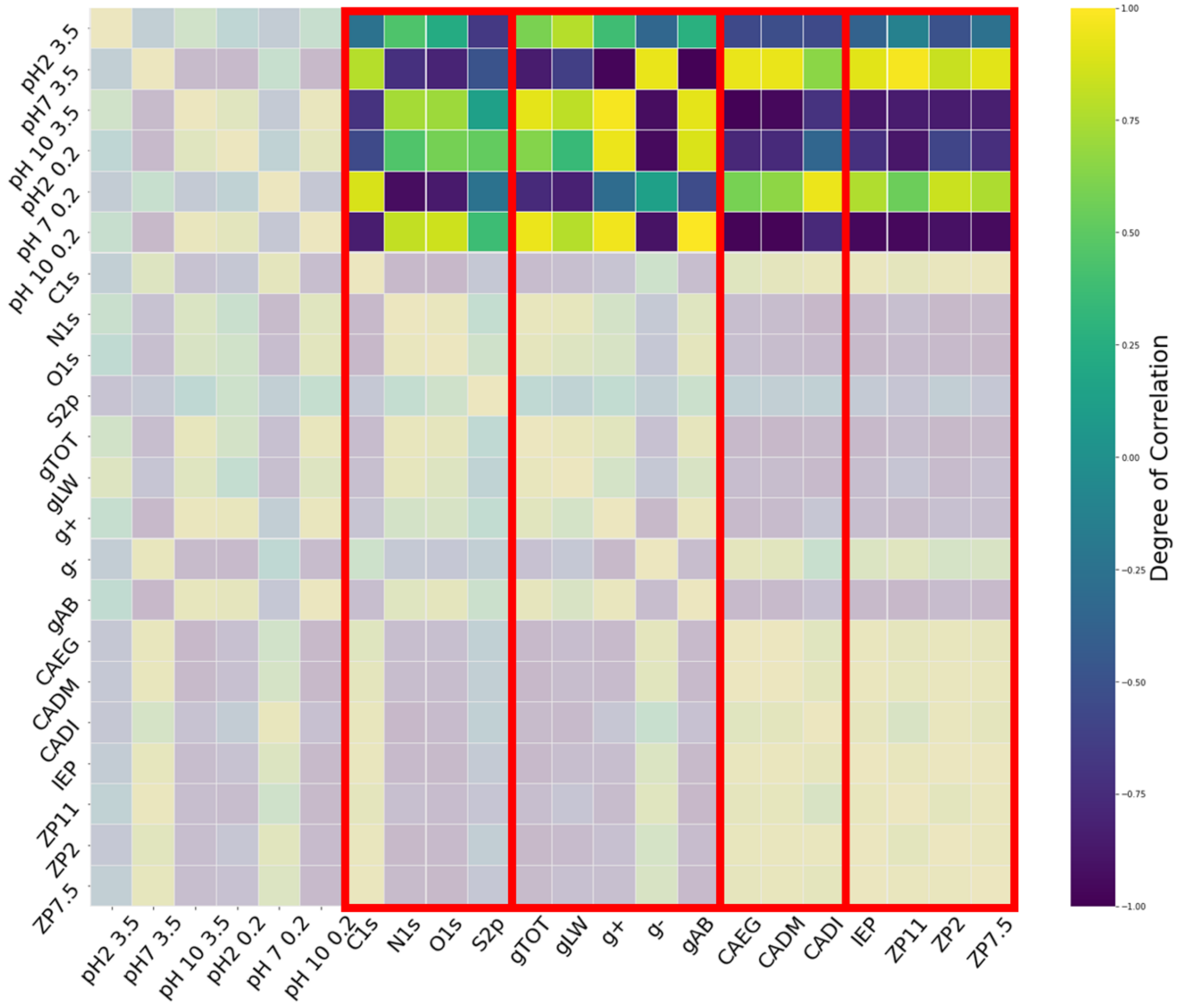

Figure 3-18: Correlation table for membrane surface properties and rejection at pH 2, pH 7, and pH 10 of 0.20% NaCl and 3.5% NaCl.

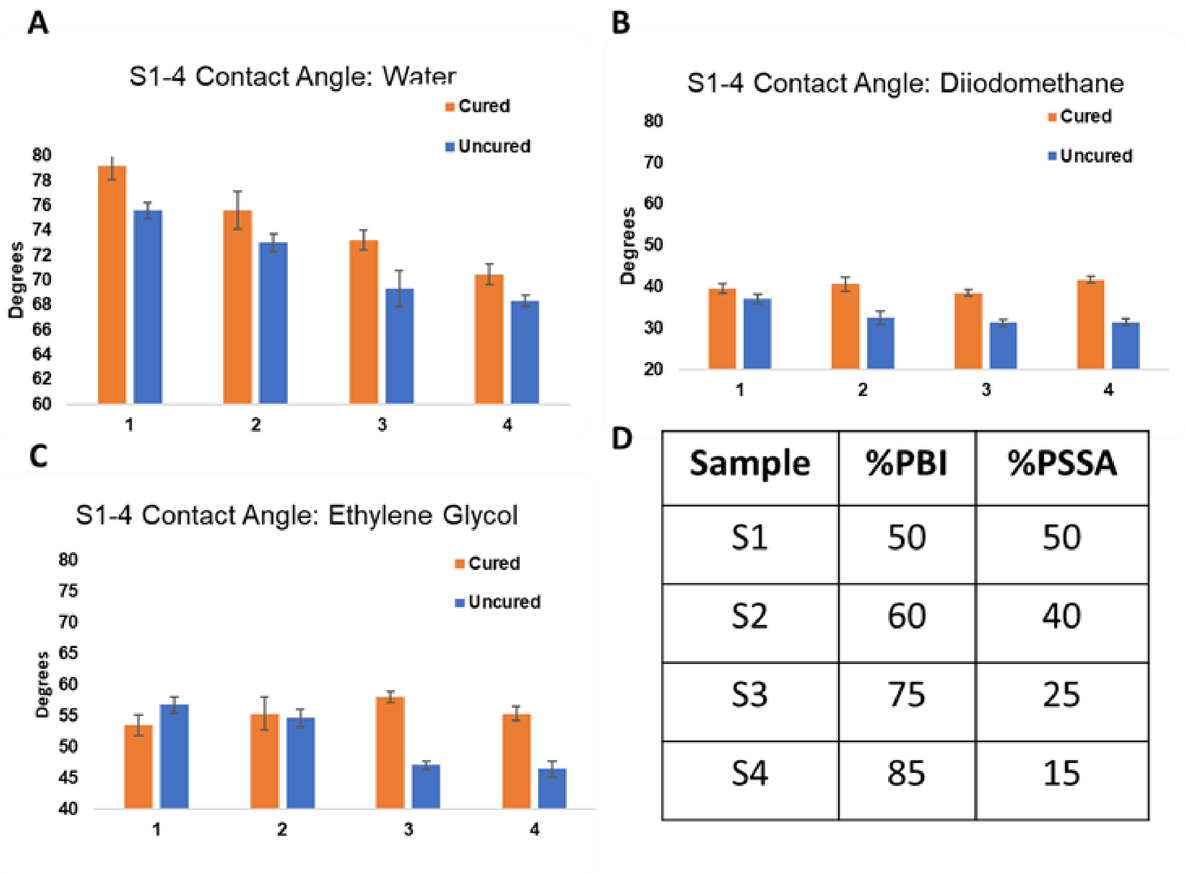

Sample	%PBI	%PSSA
S1	50	50
S2	60	40
S3	75	25
S4	85	15

Figure 3-9: Contact angles with (A) deionized water (B) diiodo methane (C) and ethylene glycol. (D) Composition of active layers for the 4 membranes analyzed.

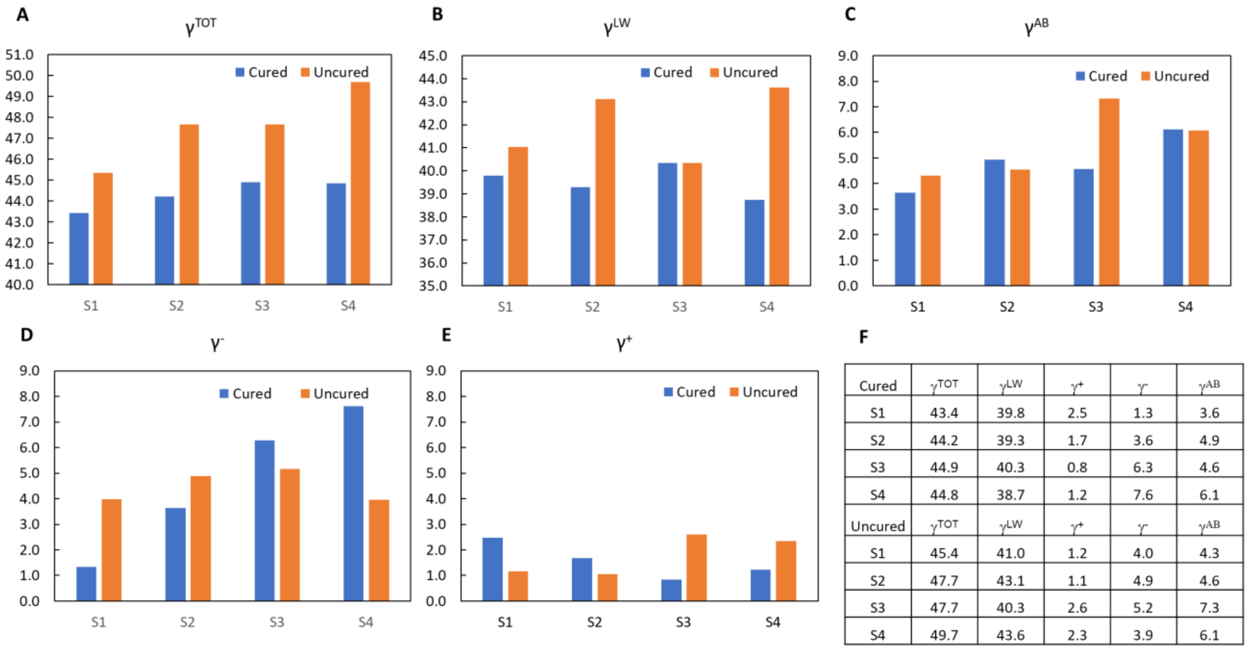

Cured	γ^{TOT}	γ^{LW}	γ^{+}	γ^{-}	γ^{AB}
S1	43.4	39.8	2.5	1.3	3.6
S2	44.2	39.3	1.7	3.6	4.9
S3	44.9	40.3	0.8	6.3	4.6
S4	44.8	38.7	1.2	7.6	6.1
Uncured	γ^{TOT}	γ^{LW}	γ^{+}	γ^{-}	γ^{AB}
S1	45.4	41.0	1.2	4.0	4.3
S2	47.7	43.1	1.1	4.9	4.6
S3	47.7	40.3	2.6	5.2	7.3
S4	49.7	43.6	2.3	3.9	6.1

Figure 3-10: The (A) total (B) Lifshitz van der Waals (C) acid-base (D) electron donating and (E) electron accepting interfacial surface tension values for each membrane summarized in 3-9-C after curing to form sulfone crosslinks or before curing. (D) summary of values.

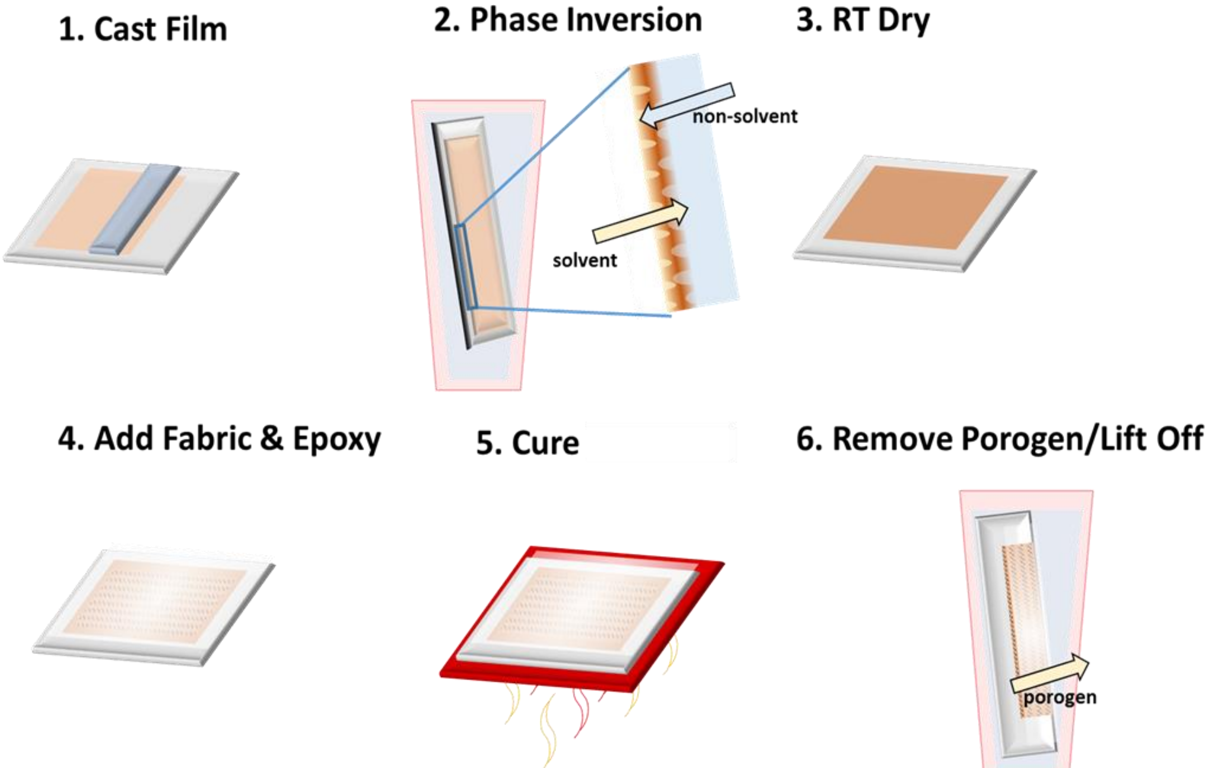

Figure 3-19: T-FLO method incorporating NIPS.

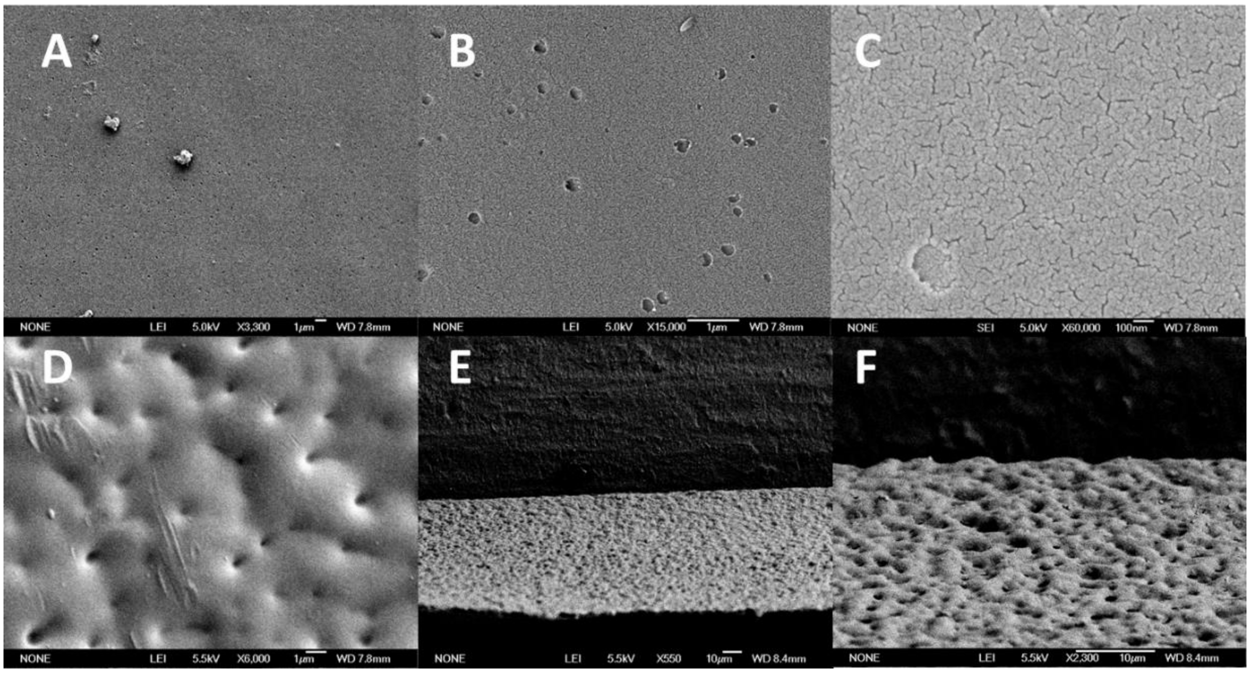

Figure 3-20: SEM images of phase-inverted PBI membrane active layers with reduced density for T-FLO membrane fabrication. Non-solvent-facing side: A 3,300x; B 15,000x; C 60,000x; Glass substrate-facing side; D 6,000x Cross-sections of ~40 µm “active-layer”.

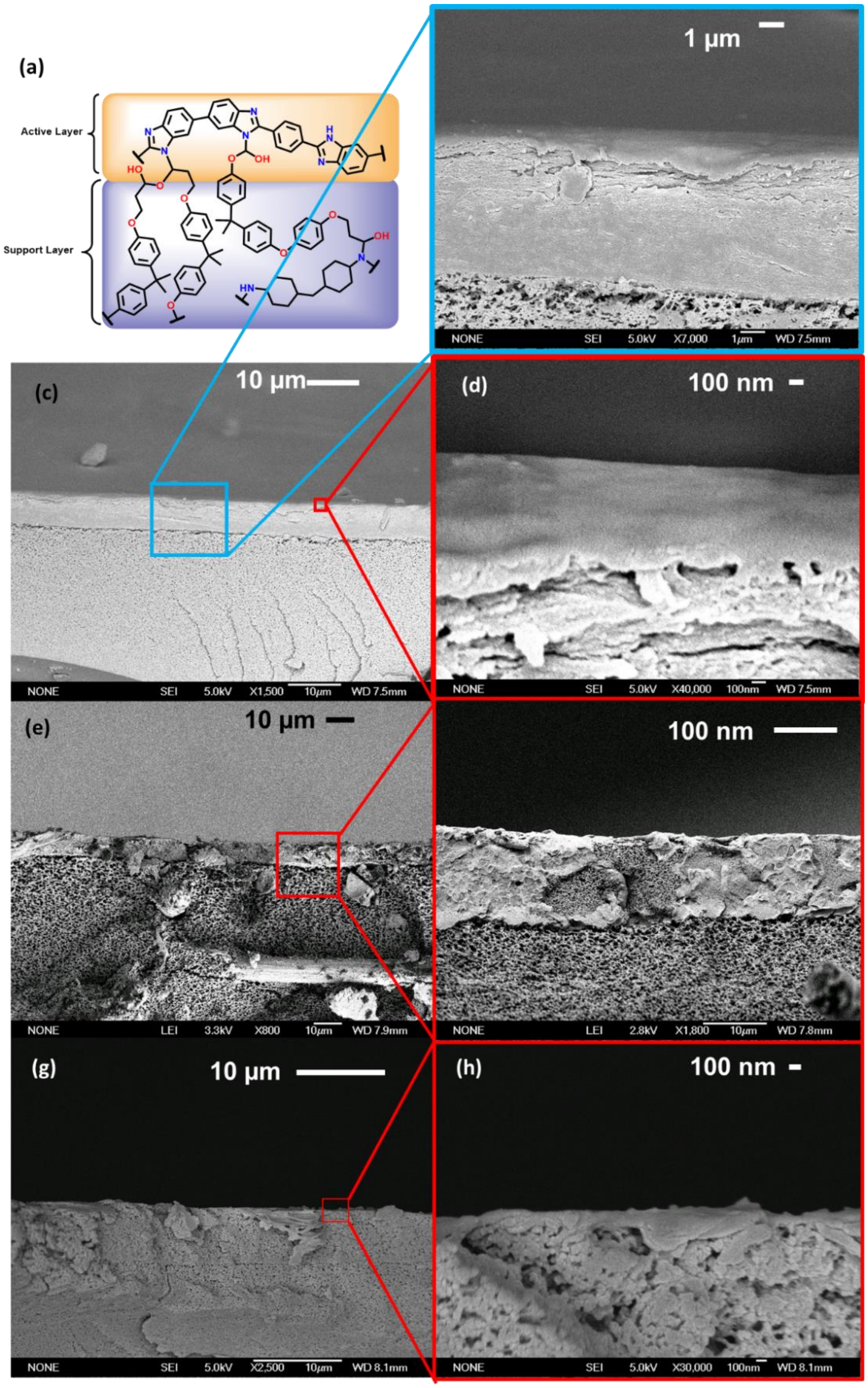

Figure 3-21: (a) Chemical composition of active and support layers. (b-d)NIPS films made into T-FLO membranes where IPA was the nonsolvent at varying magnification. (c) nonsolvent is water (d) nonsolvent is acetone.

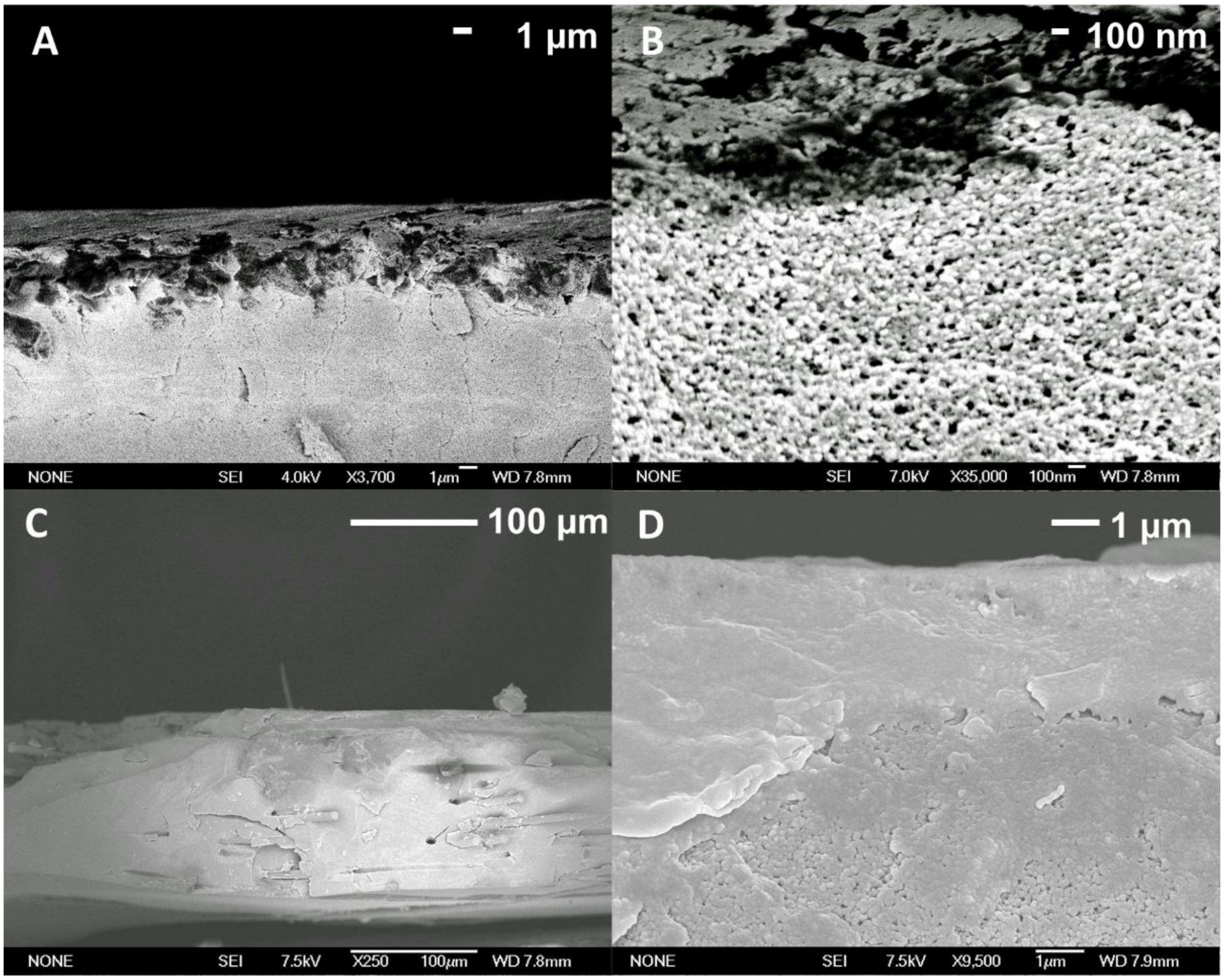

Figure 3-14: (A) SEM cross-section of T-FLO membrane with PBI active layer after phase separation upon immersion in acetone. (B) SEM image of membrane in (A) focusing on interface between active layer and support layer. (C) SEM cross-section of T-FLO membrane with APBI active layer after phase separation upon immersion in acetone.(D) SEM image of membrane in (C) focusing on active layer.

References

(1) Chung, T.-S. (1997). A Critical Review of Polybenzimidazoles. *Journal of Macromolecular Science, Part C: Polymer Reviews*. *37*(2), 277–301.

(2) Mohammad, A. W., Teow, Y. H., Ang, W. L., Chung, Y. T., Oatley-Radcliffe, D. L., & Hilal, N. (2015). Nanofiltration membranes review: Recent advances and future prospects. *Desalination*. *356*, 226–254.

(3) Zhu, W. P., Sun, S. P., Gao, J., Fu, F. J., & Chung, T. S. (2014). Dual-layer polybenzimidazole/polyethersulfone (PBI/PES) nanofiltration (NF) hollow fiber membranes for heavy metals removal from wastewater. *Journal of Membrane Science*. *456*, 117–127.

(4) Flanagan, M. F., & Escobar, I. C. (2013). Novel charged and hydrophilized polybenzimidazole (PBI) membranes for forward osmosis. *Journal of Membrane Science*. *434*, 85–92.

(5) Asadi Tashvigh, A., Luo, L., Chung, T. S., Weber, M., & Maletzko, C. (2018). Performance enhancement in organic solvent nanofiltration by double crosslinking technique using sulfonated polyphenylsulfone (sPPSU) and polybenzimidazole (PBI). *Journal of Membrane Science*. *551*, 204–213.

(6) Székely, G., Valtcheva, I. B., Kim, J. F., & Livingston, A. G. (2015). Molecularly imprinted organic solvent nanofiltration membranes - Revealing molecular recognition and solute rejection behaviour. *Reactive and Functional Polymers*. *86*, 215–224.

(7) Hausman, R., Digman, B., Escobar, I. C., Coleman, M., & Chung, T.-S. (2010). Functionalization of polybenzimidizole membranes to impart negative charge and hydrophilicity. *Journal of Membrane Science*. *363*, 195–203.

(8) Valtcheva, I. B., Kumbharkar, S. C., Kim, J. F., Bhole, Y., & Livingston, A. G. (2014). Beyond polyimide: Crosslinked polybenzimidazole membranes for organic solvent nanofiltration (OSN) in harsh environments. *Journal of Membrane Science*. 457, 62–72.

(9) Wang, K. Y., Xiao, Y., & Chung, T.-S. (2006). Chemically modified polybenzimidazole nanofiltration membrane for the separation of electrolytes and cephalexin. *Chemical Engineering Science*. 61, 5807–5817.

(10) Valtcheva, I. B., Marchetti, P., & Livingston, A. G. (2015). Crosslinked polybenzimidazole membranes for organic solvent nanofiltration (OSN): Analysis of crosslinking reaction mechanism and effects of reaction parameters. *Journal of Membrane Science. 493*, 568–579.

(11) Lv, J., Wang, K. Y., & Chung, T.-S. (2008). Investigation of amphoteric polybenzimidazole (PBI) nanofiltration hollow fiber membrane for both cation and anions removal. *Journal of Membrane Science*. 310, 557–566.

(12) Davis, H. J., Soehngen, J. W. (1981). Chlorine Resistant PBI RO Permselective Membranes. *UA Army Mobility Equipment Research and Development Command.* 1-57.

(13) Model, F. S., & Lee, L. A. (1972). PBI Reverse Osmosis Membranes: An Initial Survey. In Reverse Osmosis Membrane Research. *Springer US*. 285-297.

(14) Sawyer, L. C., & Jones, R. S. (1984). Observations on the Structure of First Generation Polybenzimidazole Reverse Osmosis Membrane. *Journal of Membrane Science*. 20, 147-166.

(15) Petersen, R. J. (1993). Composite reverse osmosis and nanofiltration membranes. *Journal of Membrane Science*, *83*(1), 81–150.

(16) Asensio, J. A., Sa´nchezsa´nchez Ab, E. M., & Go´mezgo´mez-Romero, P. (2010). Proton-conducting membranes based on benzimidazole polymers for high-temperature PEM fuel cells. A chemical quest. *Chemical Society Reviews*. 39, 3210-3239.

(17) Mack, F., Aniol, K., Ellwein, C., Kerres, J., & Zeis, R. (2015). Novel phosphoric acid-doped PBI-blends as membranes for high-temperature PEM fuel cells. *Journal of Materials Chemistry A*. 3, 10864-10874.

(18) Xia, Z., Ying, L., Fang, J., Du, Y. Y., Zhang, W. M., Guo, X., & Yin, J. (2017). Preparation of covalently cross-linked sulfonated polybenzimidazole membranes for vanadium redox flow battery applications. *Journal of Membrane Science*. 525, 229–239.

(19) Kulkarni, M. P., Peckham, T. J., Thomas, O. D., & Holdcroft, S. (2013). Synthesis of highly sulfonated polybenzimidazoles by direct copolymerization and grafting. *Journal of Polymer Science Part A: Polymer Chemistry*. 51(17), 3654–3666.

(20) Pan, H., Chen, S., Jin, M., Chang, Z., & Pu, H. (2018). Preparation and properties of sulfonated polybenzimidazole-polyimide block copolymers as electrolyte membranes. *Ionics*. 24, 1629–1638.

(21) Jouanneau, J., Mercier, R., Gonon, L., & Gebel, G. (2007). Synthesis of sulfonated polybenzimidazoles from functionalized monomers: preparation of ionic conducting membranes. *Macromolecules*, *40*(4), 983–990.

(22) Norby, T. (n.d.). *Materials for Electrochemical Energy Conversion and Storage*. 1–63.

(23) Dickson, J., Krishnan, N. N., Henkensmeier, D., Jong, A., Jang, H., Choi, S. H., Kim, H.-J., Han, J., Woo, S., & Ac, N. (2017). Thermal crosslinking of PBI/sulfonated polysulfone based blend membranes. *Journal of Materials Chemistry A. 5,* 409-417.

(24) Wu, Q., Xiao, G., & Yan, D. (2008). Synthesis of soluble sulfonated polybenzimidazoles derived from 2-sulfonate terephthalic acid. 073. *E-Polymers*. 073, 1-14.

(25) Choi, J. H., Lyoo, W. S., Ha, W. S., & Rossbach, V. (1995). Characterization of nitro-substituted polybenzimidazole synthesized by the reaction with nitric acid. *Journal of Macromolecular Science, Part A*. 32(11), 1875–1891.

(26) Solution sulfonation of a novel polybenzimidazole. A proton electrolyte for fuel cell application. *Journal of Membrane Science*. 314(1–2), 247–256.

(27) Kumbharkar, S. C., & Kharul, U. K. (2009). N-substitution of polybenzimidazoles: Synthesis and evaluation of physical properties. *European Polymer Journal*. 45(12), 3363–3371.

(28) Hurwitz, G., Guillen, G. R., & Hoek, E. M. V. (2010). Probing polyamide membrane surface charge, zeta potential, wettability, and hydrophilicity with contact angle measurements. *Journal of Membrane Science*. 349(1–2), 349–357.

(29) Wijmans, J. G., Kant, J., Mulder, M. H. V., & Smolders, C. A. (1985). Phase separation phenomena in solutions of polysulfone in mixtures of a solvent and a nonsolvent: relationship with membrane formation. *Polymer*. 26(10), 1539–1545.

(30) Guillen, G. R., Pan, Y., Li, M., & Hoek, E. M. V. (2011). Preparation and Characterization of Membranes Formed by Nonsolvent Induced Phase Separation: A Review. *Industrial and Engineering Chemistry Research*, *50*(7), 3798–3817.

(31) Hołda, A. K., & Vankelecom, I. F. J. (2015). Understanding and guiding the phase inversion process for synthesis of solvent resistant nanofiltration membranes. *Journal of Applied Polymer Science*, *132*(27), n/a-n/a.

(32) Ho, A. K., & Vankelecom, I. F. J. (2014). Integrally skinned PSf-based SRNF - membranes prepared via phase inversion — Part B : Influence of low molecular weight additives. *Journal of Membrane Science*. *450*, 499–511.

(33) Wei, J., Qiu, C., Tang, C. Y., Wang, R., & Fane, A. G. (2011). Synthesis and characterization of flat-sheet thin film composite forward osmosis membranes. *Journal of Membrane Science*, *372*(1–2), 292–302.

(34) Guillen, G. R., Ramon, G. Z., Kavehpour, H. P., Kaner, R. B., & Hoek, E. M. V. (2013). Direct microscopic observation of membrane formation by nonsolvent induced phase separation. *Journal of Membrane Science*. *431*, 212–220.

(35) Sadrzadeh, M., & Bhattacharjee, S. (2013). Rational design of phase inversion membranes by tailoring thermodynamics and kinetics of casting solution using polymer additives. *Journal of Membrane Science*. *441*, 31–44.

CHAPTER 4: Fast response electrochemical capacitor electrodes created by laser reduction of carbon nanodots

Adapted with permission from Strauss, V., Anderson, M., Turner, C. L., & Kaner, R. B. (2019). Fast response electrochemical capacitor electrodes created by laser-reduction of carbon nanodots. *Materials Today Energy*. 11, 114–119. Copyright 2019 Elsevier

Abstract

The conversion of small bio-based molecules into electro-active functional carbon nanomaterials such as carbon nanodots or graphene is attracting increasing interest. In this communication we demonstrate the use of laser-reduced carbon nanodots (lrCND) as electrodes for electrochemical capacitors. A CO_2-laser- assisted process is utilized to convert CNDs into highly conductive 3D-carbon monoliths. Exclusion of molecular oxygen from the reaction environment has a positive effect on device parameters and particularly on the frequency response. Using this simple and inexpensive method, an extremely fast RC time constant of 0.29 ms and a capacitance of 0.259 mF cm^{-2} at 120 Hz were obtained. This can be attributed to an effective conversion of CNDs into graphitic carbon in an oxygen-free environment and the presence of unconverted CNDs in the 3D-carbon network acting as doping agents.

Introduction

During the past few years, carbon-based electrodes, in particular, graphene and carbon nanotubes, have been extensively investigated as active materials in high-frequency electric double layer capacitors (HF-EDLCs).[1] Due to the wide variety of carbon materials and their high electronic conductivity, flexibility, and tunable porosity, they are considered promising materials for high-speed capacitor applications, such as AC-line filtering.[2] Fine-tuning the architecture of graphene-based electrodes can lead to remarkably short RC time constants for the electrodes, on the order of a few milliseconds [3-5].

The RC time constants (τ_{RC}), i.e. the product of resistance (R) and the capacitance (C) at a given frequency, are a characteristic parameter of EDLCs and relate to the frequency at which the electric response of a device switches from resistive to capacitive.[6,7] In general, a fast τ_{RC} is preferable since this allows for very fast charging and discharging, but more than this, a fast frequency response can enable applications for AC-line filtering. Decisive factors to achieve low τ_{RC} are low electronic and ionic series resistance throughout the device. This can be enabled by *a*) low charge transport resistance in the active material, *b*) low electrolyte/electrode and electrode/current collector interface resistance, *c*) absence of micropores in the active materials to avoid ionic resistance, and *d*) avoiding slow-kinetic pseudocapacitive reaction sites. A perspective on important device parameters for HF-EDLCs is given in a recent review article.[7]

A range of examples demonstrate that by proper alignment of carbon materials, low t_{RC} can be achieved. Carbon materials applicable for HF-EDLCs include onion-like carbon (26 ms)[8], chemical vapor deposited carbon nanotubes (0.19 ms)[9], and electrochemically reduced graphene oxide (1.35 ms).[10] Additionally, composite materials consisting of graphene oxide/carbon nanotubes (4.8 ms)[11] or printable graphene/conducting polymer hybrids (0.47 ms)[12] were found to have extraordinarily short frequency response times. Another material developed for HF-EDLC applications is porous conducting poly(3,4-ethylenedioxythiophene) with a t_{RC} of 0.8 ms.[13] Also highly porous materials like electro- chemically reduced graphene oxide and carbon black have been shown to possess low t_{RC} of only 0.35 ms. [10-14]Among the most promising materials are vertically aligned graphene sheets or nitrogen-doped holey graphene, offering high capacitance, yet very low t_{RC} of only 0.2 ms.[15,16] Among the more abundant and thus economic materials is carbon black with RC time constants as low as 0.35 and remarkably high areal capacitance of 0.56 $mFcm^{-1}$.[14] A comprehensive overview of active materials for HF EDLCs has been reviewed recently. [7]

Most of these examples utilize rather elaborate or costly fabrication techniques. In contrast, our standard laser-assisted reduction process represents a simple template-free, and fast one-step conversion process.[17,18] Using this method we have demonstrated that films of graphene oxide, carbon nanodots (CND) and com- posites thereof can be converted into functional 3D-carbon electrodes for HF-EDLCs.[19-33] We found that the laser-reduction of CND into 3D-turbostratic graphene yields electrodes with remarkably low τ_{RC}.[19] Notably, CNDs are made of natural small molecules and, therefore, represent a way to convert renewable carbon sources into functional electronic materials.[3-24] Previously, they have mainly been investigated as photoactive com- pounds for a range of optical and charge-transfer applications, but they are increasingly being used as feedstock for charge storage materials.[25,26] For example, their relatives, graphene quantum dots (GQD), have been successfully integrated as active material in interdigitated Au electrodes exhibiting τ_{RC} of <0.1 ms in aqueous electrolytes.[27]

In this paper we show that a change of the reaction environment and the laser power for the laser-assisted reduction of annealed carbon nanodots (CND300, annealed at 300 ^{O}C) leads to improvements of the frequency response of the resulting 3D-carbon electrodes. The electrochemical properties of this 3D-carbon in EDLC electrodes were examined focusing on the frequency response. The main factors for improvement of τ_{RC} are the absence of molecular O_2 in the reaction environment and the presence of unconverted material in the carbon network. By improvement of these parameters, RC time constants as low as 0.29 ms were obtained.

Results and Discussion

CNDs are a few nanometers in size and feature an sp^2-hybridized p-conjugated carbon core and a variety of functional groups on their surfaces.[19,25] Typical functional groups in annealed CNDs (CND300) are hydroxyls and carboxylates and the C:O atomic ratio is ~2:1. In the CO_2-laser-assisted reduction process, CNDs are con- verted into electronically conductive, porous 3D-graphene networks.[19] The CO_2-laser irradiation causes the material to heat up to several hundred degrees Celsius and then rapidly cool down to room temperature. Upon laser impact, the functional groups are cleaved and turned into gases leading to rapid expansion, reduction and vaporization of the CND300. Subsequently, the reduced CND300 reacts in the gas phase upon rapid cooling to form extended graphitic sheets. This process is illustrated in the schematic diagram presented in Figure 4-1.

Li et al. reported a significant influence of the reaction environment during laser reduction on the resulting material.[28] We used a similar laser reaction chamber in our experiments (see Experimental Section) to test the influence of the reaction medium during the laser reduction of CND300.

First, the materials properties of lrCND300 reduced under O_2 or Ar were analyzed in terms of mass loss, accessible surface areas, and sheet conductivities. The mass loss during the laser-reduction process is ~60% in both reaction environments (Figure. 4-2e). Laser- reduction under O_2 leads to a slightly increased specific surface area of 351 $m^2\ g^{-1}$ compared to 333 $m^2\ g^{-1}$ under Ar. In the absence of O_2 a higher sheet conductivity of 295 Sm^{-1} compared to with 248 $S\ Sm^{-1}$ under O_2 is achieved. In the SEM images in Fig. 4-2, the same elementary structural features are observed independent of the reaction medium. A closer look reveals some small differences. During laser-conversion in an O_2 atmosphere, a greater occurrence of open pores was found on the surface of the lrCND300. Exclusion of O_2 from the reaction atmosphere prevents the opening of the pores. lrCND300(Ar) exhibits a porous structure with graphitic surface features.

To elucidate the chemical structure, the products of the laser reduction in both Ar and O_2 atmospheres were characterized by XPS and Raman spectroscopy. The XPS spectra of lrCND300 reduced under Ar and O_2 with an emphasis on the C_{1s} region are shown in Figure 4-2-c. All products show a dominant peak at 284.6 eV indicating that the majority of carbon in the samples is sp^2-hybridized. The two lrCND300 samples have a similar composition with a carbon content of 84%

for reduction in both argon and oxygen environments. The final sp^2-carbon content is higher under Ar with 78% sp^2-carbon compared to 74% under O_2.

The Raman spectra of both samples show the same set of peaks, namely the D-, the G-, D^0, and G^0-peak at ~1329, ~1578, ~1609, and ~2652 cm^{-1}, respectively (Figure 4-2-f). The intensities of the D and D^0- bands relate to defects in the graphitic lattice. Notably, the film reduced under O_2 shows a significantly enhanced D-band, indicating a higher number of defects. The I_D/I_G ratio is 1.47 under O_2 and 0.97 under Ar. When taking a closer look at the G-band, a bathochromic shift of the G-band of 3 cm^{-1} from 1584 (O_2) to 1581 cm^{-1} (Ar) is noted, indicating an increase in electron density when turning from O_2 to Ar as the reaction medium. The G-band is sensitive to both electron doping and the size of the crystalline domains. A downshift of the G-band originates either from a shift of electron density into the conduction band of graphene/graphite or a higher degree of crystallinity of the sp^2-phases in the graphitic sample.[29,30] Presumably, the oxygen containing functional groups provide electron trap states and withdraw electron density from the conjugated sp^2-network.

We tested the electrochemical performance of lrCND300 reduced under O_2 or Ar in EDLCs using 0.1 M $TBAPF_6$ in acetonitrile. Two representative cyclic voltammograms of mass normalized symmetric lrCND300 cells using 0.1 M $TBAPF_6$/MeCN as the electrolyte solution at 100 mVs^{-1} are shown in Figure 4-3a. Both cells show a capacitive curve shape without redox peaks. The shape of the CV curve is more rectangular for lrCND300(Ar) than for lrCND300(O_2) as a result of lower series resistance. The capacitance increases by a factor of 1.5 in an oxygen environment. The rectangular line shape for lrCND300(Ar) is retained even at high scan rates up to 100 V s^{-1} (Fig. 3b). Both cells show excellent cycling stability (Figure 4-3-c). Over 20,000 cycles, only 2% of the initial capacitance of lrCND300(Ar) is lost. Interestingly, in the O_2 reduced cell, the capacitance increases by 3% after 20,000 cycles. This can be attributed to atmospherically adsorbed O_2 onto the electrode before immersion into the electrolyte solution. Upon application of the voltage the O_2 desorbs or decomposes and exposes the new sites to the electrolyte.

The Nyquist plots in Figure 4-3-d shows the corresponding frequency response of the lrCND300 HF-EDLCs under O_2 and Ar. A positive polarization effect is reflected in the impedance plot where a lower maximum phase angle of 84° is observed for lrCND300(Ar) and only ~79° for lrCND300(O_2). The abnormal behavior in the high frequency region is due to instrumental artifacts.[31] Moreover, the phase angle plot in Figure 4-3-e shows that a wider capacitive frequency window ranging from ~0.1e100 Hz is available in the Ar reduced cells. The yellow shaded area indicates the frequency window typically used for the characterization of EDLCs using CV scan rates between 10 and 500 mV s^{-1}. At frequencies of <0.1 Hz, the phase angle drops towards lower values as leakage resistance becomes dominant, rendering this frequency region impractical for EDLC applications. For the CND300 based EDLCs, the frequency range showing capacitive characteristics is 1000e100,000 mVs^{-1}. The frequency at which the phase angle is 45°, i.e. where the device transitions from resistive to capacitive behavior, is 955 or 495 Hz corresponding to relaxation times (t_0) of 1.05 or 2.02 ms. At 120 Hz, areal capacitances of 0.259 and 0.342 mF cm^{-2} and RC-time constants (τ_{RC}) of 0.29 ms and 0.77 ms were obtained for lrCND300(Ar) and lrCND300(O_2), respectively (Figure 4-3-f). The phase angles at 120 Hz are 78° in lrCND300(Ar) and only ~60° in lrCND300(O_2).

Based on the presented results we conclude that the absence of O_2 during the laser reduction process has a positive effect on the frequency response of lrCND300-based HF-EDLCs. In the absence of oxygen the formation of micropores is prevented, which facilitates fast ion transport and a higher electrical conductivity due to lower defect density in the active material.

The electrochemical parameters, in particular the frequency response, are also affected by unconverted CND300 remaining within the porous 3D-carbon network during the laser conversion (Figure 4-1). These were removed from the graphitized 3D-carbon network by washing the electrodes with either *N*-methyl-2- pyrrolidone (NMP) or aqueous KOH solution. A scanning electron micrograph of the top-side and the bottom-side of the carbon film after washing is presented in Figure 4-4-a. From the cyclic voltammograms of these electrodes, a 2.25 times higher capacitance compared to unwashed electrodes was determined (Figure 4-4-b). However, the less ideal curve shape indicates a higher series resistance; this was confirmed with impedance measurements that show a dramatically increased minimum phase angle of 57^{o} and a frequency at 45^{o} of 48 Hz compared to 955 Hz in the unwashed lrCND300(Ar) electrodes (Figure 4-4-c). CND300 is composed of charged particles attached to the surface of the electrode, likely via pep- stacking (Figure 4-4-d). Thus, the charges are located on the electrode/ electrolyte interface and are accessed by applying bias. The pep interactions prevent CND300 from diffusing, which reduces diffusion resistance. The unconverted parts of CND300 can act as doping agents or solid-state electrolytes keeping the charges immediately at the electrode/electrolyte interface and thus reducing the τ_{RC} of the overall device. Removal of these unreacted particles makes the electrode surfaces and micropores accessible to the electrolyte, which increases the capacitance, but also the series resistance. Therefore, the use of organic electrolyte systems in which CND300 is entirely insoluble are essential for the high frequency response of the devices.

Different concepts to achieve HF-EDLCs based on carbon materials have been introduced in the literature. Typical procedures for the fabrication of HF-EDLCs include several steps such as photolithography, chemical vapor deposition, and electrodeposition. The most common substrates are noble metals such as gold. A list of carbon-based materials and device architectures with significantly low τ_{RC} is given in Table 4-1. Interestingly, most of the concepts introduced include fabrication by electrodeposition which generally provides a better contact between the substrate and the active material. To decrease the internal series resistance, graphene buffer layers in vertically grown CNT carpets have been grown to support conduction between the active CNT layer and the substrate.[9] Usually EDLCs optimized for low τ_{RC} feature comparatively small active layer thicknesses of only a few hundred nanometers. As the thickness of the active material increases, the t_{RC} increases as a result of the longer ion diffusion length.[9,12,32] For example, it was found that the series resistance in carbon nanotube/carbon black based HF-EDLCs was significantly lower when the stainless-steel substrate was roughened, which improves the contact be- tween the active material and the substrate.[32] A decisive advantage of our lrCND300 electrodes is the simple fabrication procedure and the eco-friendly nature of the starting material. In comparison to carbon black based HF-EDLCs,[14] the laser-assisted method provides the possibility of micropatterning.

Conclusions

We have described the influence of the reaction medium on the final product of the laser-assisted reduction process of carbon nanodot films. In the presence of oxygen, changes in the morphology of the pores in the 3D-carbon monolith are observed. These are associated with higher defect densities in the material as determined by Raman spectroscopy. Higher defects and open pores cause a decrease in sheet conductivity and an increase in capacitance. In the absence of atmospheric oxygen, higher structural integrity of the 3D-carbon films are achieved, subsequently leading to better frequency response in HF-EDLCs. A minimum phase angle of 84° and an RC time constant of 0.29 ms make the electrodes interesting candidates for line filtering applications.

Experimental

Sample preparation

CNDs were synthesized according to previously published protocols.[19,35] CNDs were synthesized by reacting citric acid and urea in a 1:1 mass ratio in deionized H_2O heated in a standard 700 W microwave oven until the solvent evaporated. The CNDs from this reaction were annealed at 300 °C (CND300) under argon for 2 h. 100 mg of CND300 was suspended in 10 mL of a 1:1 (v/v) mixture of *N*-methyl-2-pyrrolidone (NMP) and propan-2-ol (*i*- PrOH) by vigorous stirring overnight. Films were prepared by drop- casting 0.025 mL onto stainless-steel discs and evaporating the solvent at 150 ºC. The uniform films were then converted with a Full Spectrum laser engraver in a laser-reaction chamber based on the example discussed in reference 27. The gas inlet was opposite to the gas outlet. A 50 mm diameter zinc selenide window was incorporated in the reaction chamber lid, allowing the CO_2 laser (10.6 mm) to pass into the gas-reaction chamber. The sample was placed in the center of the chamber. A continuous gas flow of 0.1 L s^{-1} during the reaction was used. The substrate-supported films were washed by immersing into either NMP or 1 M KOH. After the unreacted CND300 was dissolved, the electrodes were thoroughly rinsed with deionized water and methanol.

Characterization

Raman spectra were recorded with a Renishaw InVia Raman Microscope using a 633 nm laser as the excitation source. The spectra shown are averaged from 49 spots on a film. Scanning electron microscopy (SEM) was conducted on a Jeol JSM-6700F with an electron acceleration voltage of 3 kV. Samples were pre- pared on stainless steel substrates. XPS spectra were recorded using a Kratos Axis Ultra DLD spectrometer equipped with a mono- chromatic Al Kα X-ray source (hn 1486.6 eV). High-resolution spectra were calibrated using carbon tape (Ted Pella) with a known C1s binding energy of 284.6 eV. Raw data were processed using CasaXPS software (version 2.3.16). C1s spectra were fit using GaussianeLorentzian line-shapes for all spectral components except for the sp^2 C-C component, which was fitted with an asymmetric line shape to reflect the metallic character of the respective samples. Conductivity measurements were performed on a defined area on a Si substrate. Active surface areas were determined by stirring measured amounts of lrCND300 in solutions of methylene blue in DI water with known concentrations for at least 24 h.[36] The suspended material was then removed by centrifugation at 16 kG and UVevis absorption spectra of the supernatant recorded. The number of methylene blue molecules adsorbed onto the surfaces was calculated from the difference in absorption at 665 nm with respect to the reference solution. Every methylene blue molecule was assumed to occupy 1.35 nm^2 of active surface area.[37] For all experiments, polypropylene beakers and vials were used.

EDLCs were assembled in coin cells with electrode diameters of 15 mm and tested under sealed conditions. Electrochemical measurements were conducted on a Biologic VMP3 electrochemical workstation. The areal capacitance C_A was obtained from electro- chemical impedance measurements. The RC time constants were determined from the product of the resistance and the capacitance

at 120 Hz according to $\tau_{\mathrm{RC}} = RC = \mathrm{Z}' \bullet 1 = 2\pi f \bullet Z''$.

Acknowledgments

This work was supported by the Deutsche For- schungsgemeinschaft (German Academic Research Society), grant number STR1508/1-2 (V.S.) and the UCLA Dr. Myung Ki Hong Endowed Chair in Materials Innovation (R.B.K.). We thank the mi- croscopy facility in the UCLA Department of Materials Science and Engineering led by Dr. S.V. Prikhodko for use of their Raman spectrometer.

Tables

Table 4-1: Summary of carbon-based EDLCs featuring fast tRC.

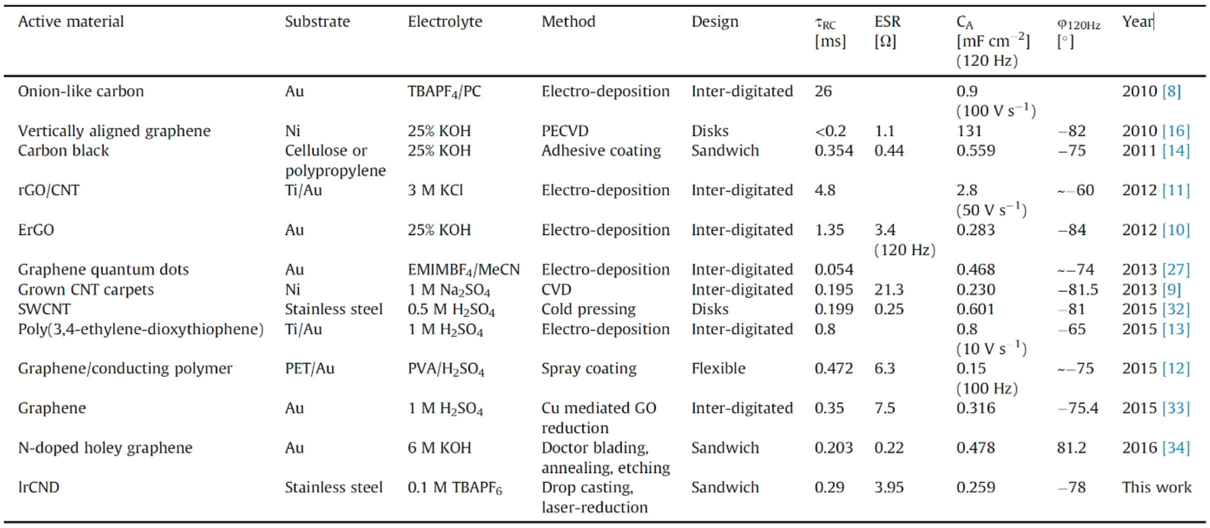

Active material	Substrate	Electrolyte	Method	Design	τ_{RC} [ms]	ESR [Ω]	C_A [mF cm^{-2}] (120 Hz)	φ_{120Hz} [°]	Year
Onion-like carbon	Au	$TBAPF_4$/PC	Electro-deposition	Inter-digitated	26		0.9 (100 V s^{-1})		2010 [8]
Vertically aligned graphene	Ni	25% KOH	PECVD	Disks	<0.2	1.1	131	−82	2010 [16]
Carbon black	Cellulose or polypropylene	25% KOH	Adhesive coating	Sandwich	0.354	0.44	0.559	−75	2011 [14]
rGO/CNT	Ti/Au	3 M KCl	Electro-deposition	Inter-digitated	4.8		2.8 (50 V s^{-1})	~−60	2012 [11]
ErGO	Au	25% KOH	Electro-deposition	Inter-digitated	1.35	3.4 (120 Hz)	0.283	−84	2012 [10]
Graphene quantum dots	Au	$EMIMBF_4$/MeCN	Electro-deposition	Inter-digitated	0.054		0.468	~−74	2013 [27]
Grown CNT carpets	Ni	1 M Na_2SO_4	CVD	Inter-digitated	0.195	21.3	0.230	−81.5	2013 [9]
SWCNT	Stainless steel	0.5 M H_2SO_4	Cold pressing	Disks	0.199	0.25	0.601	−81	2015 [32]
Poly(3,4-ethylene-dioxythiophene)	Ti/Au	1 M H_2SO_4	Electro-deposition	Inter-digitated	0.8		0.8 (10 V s^{-1})	−65	2015 [13]
Graphene/conducting polymer	PET/Au	PVA/H_2SO_4	Spray coating	Flexible	0.472	6.3	0.15 (100 Hz)	~−75	2015 [12]
Graphene	Au	1 M H_2SO_4	Cu mediated GO reduction	Inter-digitated	0.35	7.5	0.316	−75.4	2015 [33]
N-doped holey graphene	Au	6 M KOH	Doctor blading, annealing, etching	Sandwich	0.203	0.22	0.478	81.2	2016 [34]
lrCND	Stainless steel	0.1 M $TBAPF_6$	Drop casting, laser-reduction	Sandwich	0.29	3.95	0.259	−78	This work

Figures

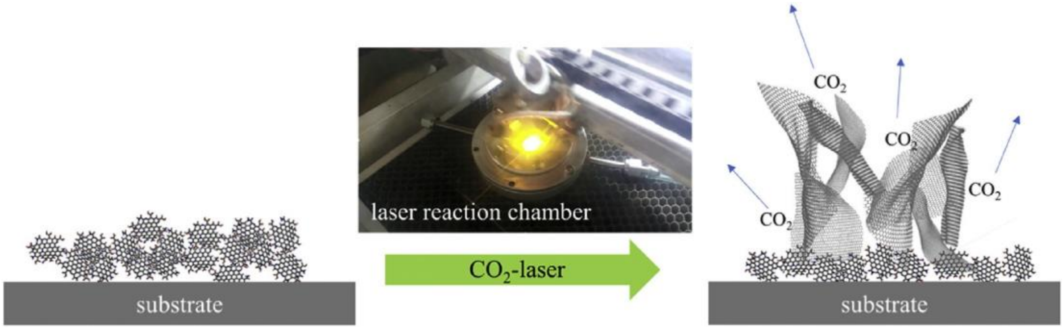

Figure 4-1: Illustration of the CO_2-laser conversion process for CND300; Inset image: photograph of the gas reaction chamber using a benchtop CO_2-laser.

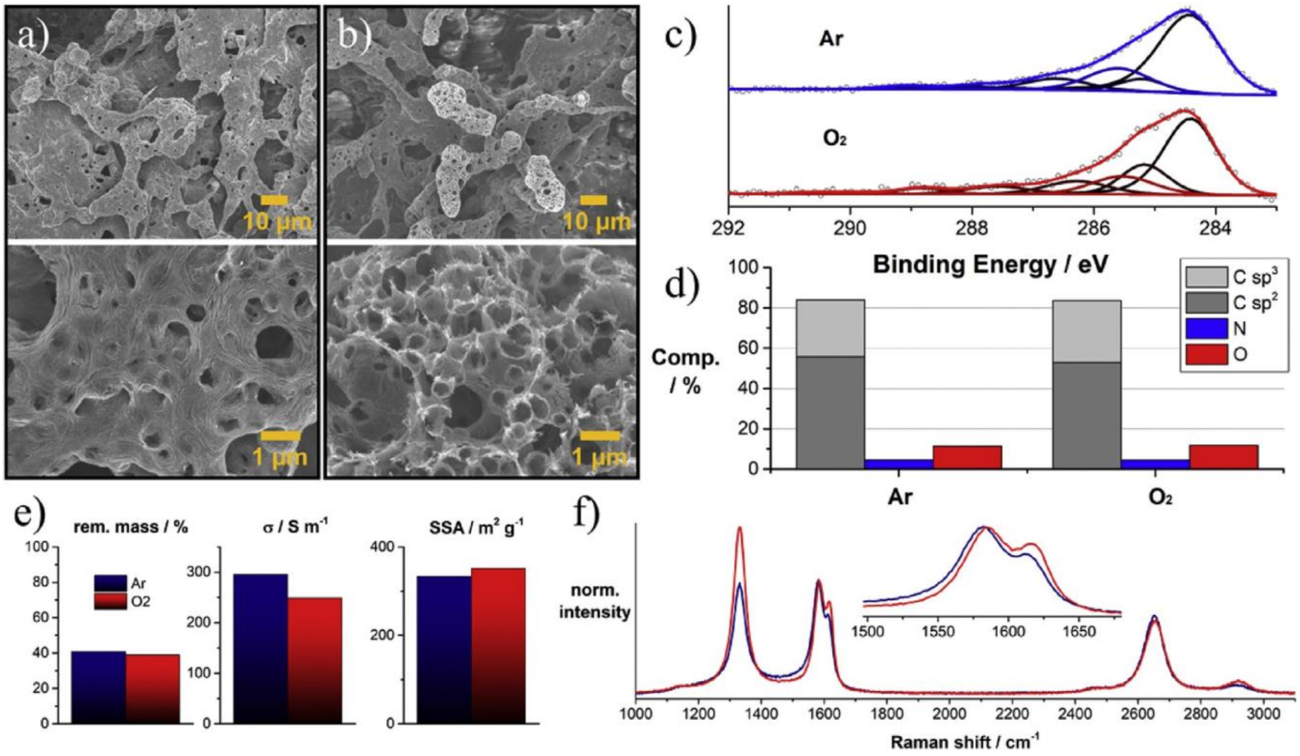

Figure 4-2:. Characterization of the lrCND300 film; a) Scanning electron micrographs of lrCND300(Ar); b) Scanning electron micrographs of lrCND300(O_2); c) XPS spectra of the C$_{1s}$ region of lrCND300 reduced in Ar and O_2 atmosphere, respectively; d) Elemental composition of lrCND300 reduced in Ar and O_2 atmosphere, respectively; e) remaining mass after laser reduction of CND300 under argon (blue) and oxygen (red) using the same laser parameters, sheet conductivity of lrCND300 reduced under argon (blue) and oxygen (red), and specific surface area of lrCND300 reduced under argon (blue) and oxygen (red); f) Raman spectra of lrCND300 reduced in Ar (blue) and O_2 (red) atmosphere obtained upon excitation at 633 nm.

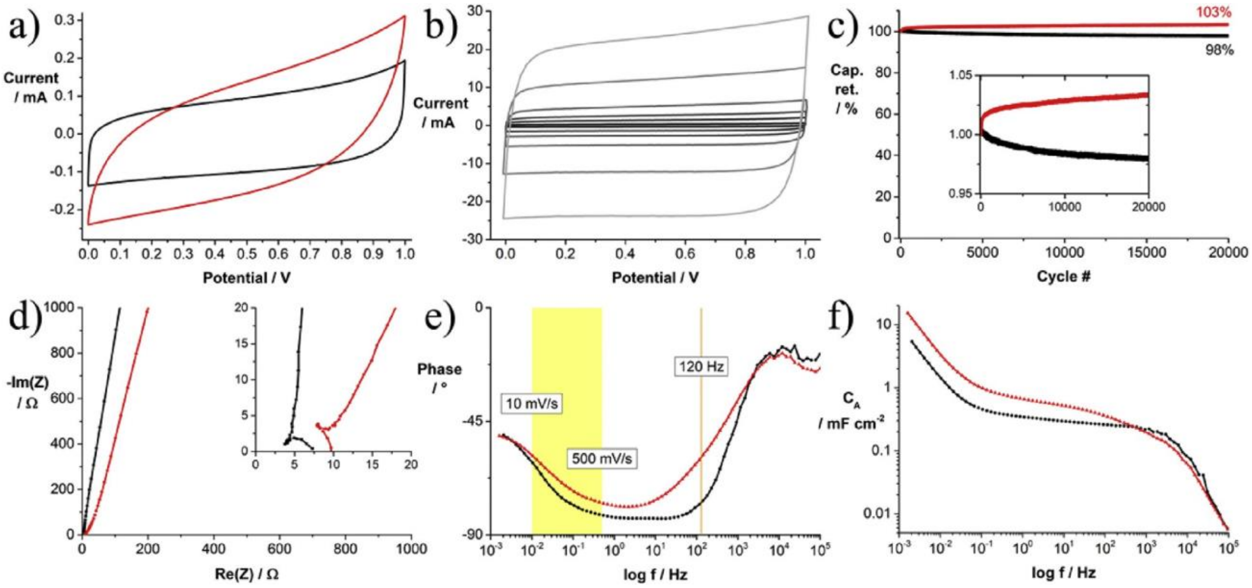

Figure 4-3: a) Cyclic voltammograms of two EDLCs assembled with lrCND300(Ar) (black) and lrCND300(O$_2$) (red) electrodes in 0.1 M TBAPF$_6$/MeCN as electrolyte at a scan rate of 100 mV s ^{1}; b) Cyclic voltammograms of a lrCND300(Ar) EDLC in 0.1 M TBAPF$_6$/MeCN as the electrolyte at different scan rates between 1 and 100 V s ^{1}; c) Cycling stability of lrCND300(Ar) (black) and lrCND300(O$_2$) (red) over 20,000 cycles at a current density of 8 A g ^{1} or 750 mA cm ^{3}, i.e. 60 Hz; d) Nyquist impedance plots of two EDLCs assembled with lrCND300(Ar) (black) or lrCND300(O$_2$) (red) in 0.1 M TBAPF$_6$/MeCN as the electrolyte; e) Phase angle plots of two EDLCs assembled with lrCND300(Ar) (black) or lrCND300(O$_2$) (red) in 0.1 M TBAPF$_6$/MeCN as the electrolyte; f) Specific areal capacitance at different scan rates obtained from electrochemical impedance measurements.

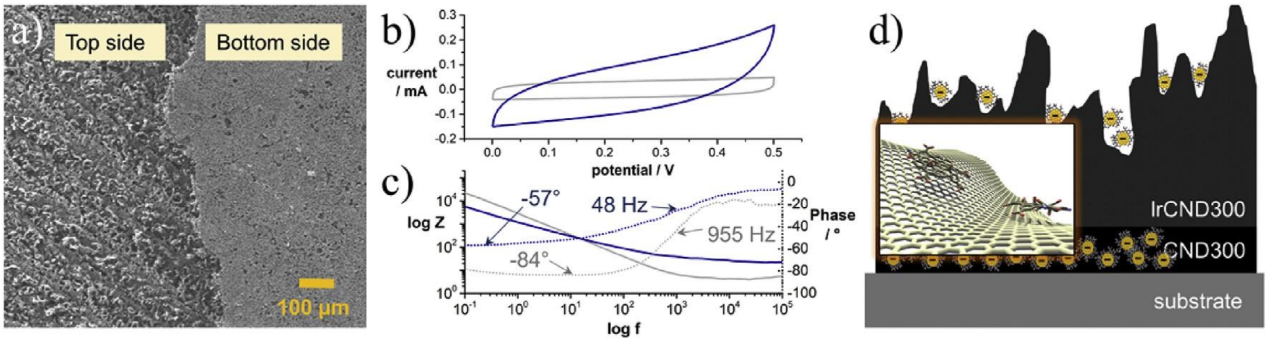

Figure 4-4: a) Scanning electron micrograph comparing the top and the bottom sides of a lrCND300 film after removing from the substrate by KOH washing; b) Cyclic voltammograms of EDLCs with washed (blue) and unwashed (gray) lrCND300(Ar) in 0.1 M TBAPF$_6$/MeCN as electrolyte at a scan rate of 100 mV s ^{1}; c) Bode impedance plot of EDLCs with washed (blue) and unwashed (gray) lrCND300(Ar) in 0.1 M TBAPF$_6$/MeCN as electrolyte; d) Illustration of the structure of lrCND300 film; Inset: Illustration of CND300 interacting with lrCND300.

References

(1) F. Wang, X. Wu, X. Yuan, Z. Liu, Y. Zhang, L. Fu, Y. Zhu, Q. Zhou, Y. Wu, W. Huang, Latest advances in supercapacitors: from new electrode materials to novel device designs, Chem. Soc. Rev. 46 (2017) 6816-6854.

(2) D. Premathilake, R.A. Outlaw, S.G. Parler, S.M. Butler, J.R. Miller, Electric double layer capacitors for ac filtering made from vertically oriented graphene nanosheets on aluminum, *Carbon* 111 (2017) 231-237.

(3) Z. Gao, Y. Zhang, N. Song, X. Li, Biomass-derived renewable carbon materials for electrochemical energy storage, Mater. Res. Lett. 5 (2017) 69-88.

(4) Q. Wang, J. Yan, Z. Fan, Carbon materials for high volumetric performance supercapacitors: design, progress, challenges and opportunities, *Energy Environ. Sci*. 9 (2016) 729-762.

(5) Q. Ke, J. Wang, Graphene-based materials for supercapacitor electrodes e a review, J. Mater. 2 (2016) 37-54.

(6) P.L. Taberna, P. Simon, J.F. Fauvarque, Electrochemical characteristics and impedance spectroscopy studies of carbon-carbon supercapacitors, *J. Electrochem. Soc*. 150 (2003) A292.

(7) Z. Fan, N. Islam, S.B. Bayne, Towards kilohertz electrochemical capacitors for filtering and pulse energy harvesting, *Nano Energy* 39 (2017) 306-320.

(8) D. Pech, M. Brunet, H. Durou, P. Huang, V. Mochalin, Y. Gogotsi, P.-L. Taberna, P. Simon, Ultrahigh-power micrometre-sized supercapacitors based on onion- like carbon, *Nat. Nanotechnol*. 5 (2010) 651-654.

(9) J. Lin, C. Zhang, Z. Yan, Y. Zhu, Z. Peng, R.H. Hauge, D. Natelson, J.M. Tour, 3-Dimensional graphene carbon nanotube carpet-based microsupercapacitors with high electrochemical performance, *Nano Lett.* 13 (2013) 72-78.

(10) K. Sheng, Y. Sun, C. Li, W. Yuan, G. Shi, Ultrahigh-rate supercapacitors based on eletrochemically reduced graphene oxide for ac line-filtering, Sci. Rep. 2 (2012), https://doi.org/10.1038/srep00247.

(11) M. Beidaghi, C. Wang, Micro-supercapacitors based on interdigital electrodes of reduced graphene oxide and carbon nanotube composites with ultrahigh power handling performance, Adv. Funct. Mater. 22 (2012) 4501e4510, https://doi.org/10.1002/adfm.201201292.

(12) Z.-S. Wu, Z. Liu, K. Parvez, X. Feng, K. Müllen, Ultrathin printable graphene supercapacitors with AC line-filtering performance, Adv. Mater. 27 (2015) 3669e3675, https://doi.org/10.1002/adma.201501208.

(13) N. Kurra, M.K. Hota, H.N. Alshareef, Conducting polymer micro-supercapacitors for flexible energy storage and Ac line-filtering, Nano Energy 13 (2015) 500e508, https://doi.org/10.1016/j.nanoen.2015.03.018.

(14) P. Kossyrev, Carbon black supercapacitors employing thin electrodes, J. Power Sources 201 (2012) 347e352, https://doi.org/10.1016/j.jpowsour.2011.10.106.

(15) M. Cai, R.A. Outlaw, R.A. Quinlan, D. Premathilake, S.M. Butler, J.R. Miller, Fast response, vertically oriented graphene nanosheet electric double layer ca- pacitors synthesized from C_2H_2, ACS Nano 8 (2014) 5873e5882, https:// doi.org/10.1021/nn5009319.

(16) J.R. Miller, R.A. Outlaw, B.C. Holloway, Graphene double-layer capacitor with ac line-filtering performance, Science 329 (2010) 1637e1639, https://doi.org/ 10.1126/science.1194372.

(17) Y. Zhou, Q. Bao, B. Varghese, L.A.L. Tang, C.K. Tan, C.-H. Sow, K.P. Loh, Microstructuring of graphene oxide nanosheets using direct laser writing, Adv. Mater. 22 (2010) 67e71, https://doi.org/10.1002/adma.200901942.

(18) V. Abdelsayed, S. Moussa, H.M. Hassan, H.S. Aluri, M.M. Collinson, M.S. El- Shall, Photothermal deoxygenation of graphite oxide with laser excitation in solution and graphene-aided increase in water temperature, *J. Phys. Chem. Lett.* 1 (2010) 2804e2809.

(19) V. Strauss, K. Marsh, M.D. Kowal, M.F. El-Kady, R.B. Kaner, A simple Route to porous graphene from carbon nanodots for supercapacitor applications, *Adv. Mater*. 30 (2018) 1704449.

(20) R.B. Kaner, Embedding hollow Co_3O_4 nanoboxes into a three-dimensional macroporous graphene framework for high-performance energy storage de- vices, Nano Res. 11 (2018) 2836-2846.

(21) V. Strong, S. Dubin, M.F. El-Kady, A. Lech, Y. Wang, B.H. Weiller, R.B. Kaner, Patterning and electronic tuning of laser scribed graphene for flexible all-carbon devices, *ACS Nano* 6 (2012).

(22) M.F. El-Kady, R.B. Kaner, Scalable fabrication of high-power graphene micro-supercapacitors for flexible and on-chip energy storage, *Nat. Commun*. 4 (2013) 1475,

(23) J.Y. Hwang, M.F. El-Kady, M. Li, C.-W. Lin, M. Kowal, X. Han, R.B. Kaner, Boosting the capacitance and voltage of aqueous supercapacitors via redox charge contribution from both electrode and electrolyte, *Nano Today* 15 (2017) 15-25.

(24) V. Strauss, A. Roth, M. Sekita, D.M. Guldi, Efficient energy-conversion mate- rials for the future: understanding and tailoring charge-transfer processes in carbon nanostructures, *Chem 1* (2016) 531-556.

(25) V. Strauss, A. Kahnt, E.M. Zolnhofer, K. Meyer, H. Maid, C. Placht, W. Bauer, T.J. Nacken, W. Peukert, S.H. Etschel, M. Halik, D.M. Guldi, Assigning electronic states in carbon nanodots, *Adv. Funct. Mater*. 26 (2016) 7975-7985.

(26) V. Strauss, Ecofriendly carbon nanomaterials for future electronic applications, Chem 2

(2017) 319-321.

(27) W.-W. Liu, Y.-Q. Feng, X.-B. Yan, J.-T. Chen, Q.-J. Xue, Superior micro- supercapacitors based on graphene quantum dots, *Adv. Funct. Mater*. 23 (2013) 4111-4122.

(28) Y. Li, D.X. Luong, J. Zhang, Y.R. Tarkunde, C. Kittrell, F. Sargunaraj, Y. Ji, C.J. Arnusch, J.M. Tour, Laser-induced graphene in controlled atmospheres: from superhydrophilic to superhydrophobic surfaces, *Adv. Mater*. 29 (2017) 1700496.

(29) L.M. Malard, M.A. Pimenta, G. Dresselhaus, M.S. Dresselhaus, Raman spectroscopy in graphene, *Phys. Rep*. 473 (2009) 51-87.

(30) A.C. Ferrari, J. Robertson, Raman spectroscopy of amorphous, nanostructured, diamond-like carbon, and nanodiamond, *Philos. Trans. A Math. Phys. Eng. Sci*. 362 (2004) 2477-2512.

(31) The “high-frequency hooks” are artefacts due to inaccurate calibration of the instrument, very likely a inductive effect from the cable. The Non-zero Capacitance at Zero Potential Is Due to a Defect Electrical Connection in the Instrument., (n.d.).

(32) Y. Rangom, X. (Shirley) Tang, L.F. Nazar, Carbon nanotube-based super- capacitors with excellent ac line filtering and rate capability via improved interfacial impedance, *ACS Nano* 9 (2015) 7248e7255.

(33) Z. Wu, L. Li, Z. Lin, B. Song, Z. Li, K.-S. Moon, C.-P. Wong, S.-L. Bai, Alternating current line-filter based on electrochemical capacitor utilizing template- patterned graphene, *Sci. Rep.* 5 (2015) 10983, https://doi.org/10.1038/ srep10983.

(34) Q. Zhou, M. Zhang, J. Chen, J.D. Hong, G. Shi, Nitrogen-doped holey graphene film-based ultrafast electrochemical capacitors, *ACS Appl. Mater. Interfaces* 8 (2016) 20741-20747.

(35) J.T. Margraf, F. Lodermeyer, V. Strauss, P. Haines, J. Walter, W. Peukert,

R.D. Costa, T. Clark, D.M. Guldi, Using carbon nanodots as inexpensive and environmentally friendly sensitizers in mesoscopic solar cells, *Nanoscale Horiz.* 1 (2016) 220e226.

(36) S. Naeem, V. Baheti, J. Wiener, J. Marek, Removal of methylene blue from aqueous media using activated carbon web, *J. Text. Inst*. 108 (2017) 803-811.

(37) P.T. Hang, Methylene blue absorption by clay minerals. Determination of sur- face areas and cation exchange capacities (clay-organic studies XVIII), *Clays Clay Miner*. 18 (1970) 203-212.

CHAPTER 5: Self-Assembled Functionally Graded Graphene Films with Tunable Compositions and Their Applications in Transient Electronics and Actuation

Adapted with permission from Bhatkar, O., Smith, D., Kowal, M. D., Anderson, M., Rizvi, R., & Kaner, R. B. (2019). Self-Assembled Functionally Graded Graphene Films with Tunable Compositions and Their Applications in Transient Electronics and Actuation. *ACS Applied Materials and Interfaces.*11, 2346-23473. Copyright 2018 American Chemical Society

Abstract

The facile fabrication of functionally graded all-graphene films using a single-step casting process is reported. The films consist of a self- assembled graphene oxide (GO) precursor that can be reduced to different levels on an active metal substrate. Control of processing conditions such as the underlying substrate metal and the film-drying environment results in an ability to tailor the internal architecture of the films as well as to functionally grade the reduction of GO. A gradient arrangement within each film, where one side is electrically conductive reduced GO (rGO) and the other side is insulating GO, was confirmed by scanning electron microscopy, Raman, X-ray diffraction, Fourier transform infrared, and X-ray photoelectron spectroscopy characterization studies. All-graphene-based freestanding films with selectively reduced GO were used in transient electronic applications such as flexible circuitry and RFID tag antennas, where their decommissioning is easily achieved by capitalizing on GO's ability to readily dissociate and create a stable suspension in water. Furthermore, the functionally graded structure was found to exhibit differential swelling behavior, and its potential applications in graphene-based actuators are outlined.

Introduction

Functionally graded materials (FGMs) consist of two or more distinct substances, engineered such that the distribution of each constituent changes continuously with spatial variables. The chemical, material, and microstructural gradients of FGMs can tailor the overall thermal, mechanical, and electrical properties in an inhomogeneous manner, making the behavior of FGMs quite distinct from that of homogeneous materials and traditional composites.[1,2] Furthermore, FGMs substitute the sharp interface between two discrete materials with a gradient interface, thereby improving the bonding strength and eliminating the residual stresses between materials.[3] FGMs have potential applications in numerous fields such as biomedicine, defense, energy, aerospace, automobile, electronics, and optoelectronics.[2,4] As a recent example, Bartlett et al.[5] designed a functionally graded robot whose body transitions from a rigid core to a soft exterior. Another study by Hu et al.[6] reported an in- situ fabrication process of static magnetic field that led to an understanding of the effects of solute migration and temperature distribution on the crystal growth during directional solidification.

Graphene, a two-dimensional (2D) carbon material arranged in an sp^2-bonded hexagonal network, possesses high surface area[7] along with excellent in-plane thermal,[8] mechanical,[9] and electrical[10] properties. These attributes of graphene have spurred significant research into its applications such as energy storage devices,[11,12] chemical and biosensors,[13] electronic and photonic devices,[14] and electromechanical systems.[15] How- ever, the development of large-scale graphene films with economically scalable processing as well as the integration of these films into functional devices is still a technical barrier for any value-added economical end-use application of graphene. Graphene oxide (GO) is an oxidized derivative of graphene having oxygen-containing functional groups on its basal plane and edges. GO is a common precursor that can be used for the large-scale production of graphene at relatively low cost, considering the abundance of graphite and GO’s simple yet scalable chemical synthesis and the ability to be dispersed in an aqueous environment.[16,17] Due to its hydrophilic nature and dispersibility, GO membranes have been shown to be applicable in selectively controlled water permeation,[18] humidity sensing,[19] and actuation.[20] Graphene oxide can be converted to its electrically conducting variant, reduced graphene oxide (rGO), through a variety of reduction approaches such as chemical,[21] thermal,[22] hydrothermal,[23] photothermal,[24] and electrochemical.[25,2] Moreover, graphene- oxide-based paperlike flexible films can be fabricated with appreciable mechanical properties. For example, Dikin et al.[27] demonstrated a freestanding graphene oxide film, which outperformed other paperlike materials in stiffness and flexibility.

Self-assembly of graphene oxide sheets or reduced graphene oxide sheets is recognized as an attractive approach to construct 2D and three-dimensional (3D) graphene-based structures.[23,28,29] Recent studies have successfully demonstrated self-assembled graphene networks on different substrates via single- or multiple-step processes.[30,31] These assembly approaches include layer-by-layer,[32] Langmuir−Blodgett,[33] evaporation-induced,[34] template-directed,[35] and flow-direc- ted.[27] Interestingly, GO sheets can be effectively reduced and self-assembled in the presence of metal (e.g., Al, Fe, Cu, Ni) powders and foils.[36,37] For example, a large-area graphene film was fabricated via a metal-assisted (Cu foil) reduction method of graphene oxide followed by high-temperature (900 °C) annealing in a H_2-containing atmosphere, as reported by Huang et al.[38] Another study by Hu et al.[39] reported the spontaneous assembly of a 3D graphene network using substrate-assisted reduction, including active and inert metals, semiconducting Si, nonmetallic carbon, and indium tin oxide glass. Reduced GO was spontaneously deposited on these various substrates when immersed in a 1 mg/mL GO solution for a certain period of time at room temperature. Cao et al.[17]

carried out a similar approach where a freestanding paperlike reduced graphene film was produced using a solution-based route, where a piece of metal foil (e.g., copper, nickel, cobalt, iron, or zinc) was submerged into a GO solution with a concentration of 0.1−0.5 mg/mL. In contrast to the aforementioned techniques of indiscriminate self-assembly and reduction of graphene oxide, efforts to produce a compositional grading between graphene oxide and reduced graphene oxide have been more limited. Owing to the outstanding properties of both graphene and graphene oxide, a carbonaceous media where both forms of graphene are functionally graded would be desirable. A more recent study by Liu et al.[40] prepared bilayer films of reduced GO/GO through moderate flash reduction of graphene oxide films. A partial photothermal reduction of GO was observed on the irradiated side of the films, as confirmed by the selective removal of oxygen-containing functional groups.

In this study, we report a facile and one-step metal-assisted film-casting process for producing all-graphene-based functionally graded films (FGG) and their applications. Control of processing conditions, such as the underlying metal substrate and the film-drying environment, results in an ability to tailor the internal architecture of the films as well as to functionally grade the reduction of GO with tunable compositions. The resulting film chemical composition and microstructure were mechanistically linked to the various metallic substrates and parameters employed during processing. Furthermore, the ability to create masks for the selective reduction of GO on metal interfaces is also demonstrated. All-graphene-based freestanding films with applications in transient electronics and differential swelling-based actuation are demonstrated. Their decommissioning was easily achieved through immersion in an aqueous environment, which capitalizes on GO’s ability to readily dissociate and create a stable suspension in water.

Experimental

Graphene Oxide Preparation.

Graphene oxide was synthesized using a modified Hummer's method.[41,42] In a typical reaction, 10 g of graphite powder (Bay Carbon, SP-1 grade, 325 mesh) was added to cold sulfuric acid (500 mL). Potassium permanganate (60 g) was then added slowly, keeping the temperature below 10 °C. After mixing for 2 h, 500 mL of deionized water was added slowly while keeping the temperature of the reaction below 50°C. The reaction was stirred for 1 h and then quenched with 1 L of distilled water and 30 mL of H_2O_2 (30%). After the color of the solution changed from brown to orange and gas evolution ceased, the solution was filtered and washed with 4 equiv of deionized water to produce a 5 wt % gelatinous solution of graphene oxide with a pH in the range of 3−4.

Graphene Oxide Film Deposition and Reduction

A highly concentrated graphene oxide (50 mg/mL) paste was doctor- blade-coated onto various polished metallic substrates. The substrates investigated were Cu, Ni, Pb, Al, and Zn metals. The thin sheet metal foils were adhered to a flat glass plate using a Kapton pressure adhesive. Various blade gaps were set and calibrated using feeler gauges. The GO gel paste was deposited at one end of the metal substrate and was manually coated using the doctor blade in a uniform manner. The entire coating assembly was then air-dried at various temperatures and humidity conditions. After drying, the film was easily peeled off from the metal substrate and was found to be a freestanding functionally graded graphene (FGG) film.

Characterization

The morphology and elemental analyses of FGG samples were characterized by scanning electron microscopy (SEM, FEI Quanta 3D FEG dual beam electron microscope). Raman spectra were recorded using a Jobin Yvon Horiba confocal Raman spectrometer in a backscattering configuration with a 632 nm He−Ne laser excitation. An Olympus BX41 microscope with 50× magnification was used during the Raman analysis. X-ray diffraction (XRD) measurements were performed with a Rigaku Ultima III high- resolution X-ray diffractometer with small-angle X-ray scattering. Cu Kα radiation (λ = 0.154 nm) was utilized in the 2θ range from 5 to 80° with a scanning speed of 1 °/min. X-ray photoelectron spectroscopy (XPS) measurements of the samples were carried out on a Kratos analytical high-sensitivity XPS using focused monochromatized Al Kα radiation ($h\nu$ = 1486.6 eV), which was corrected by the C 1s line at 284.6 eV. The sheet resistance values of the samples were measured using a Siglent SDM 3055 digital multimeter with a Signatone SP^4 four-point probe at room temperature.

Results and Discussion

A typical experimental procedure of fabricating paperlike functionally graded graphene films, henceforth referred to as M−FGG (where M denotes the substrate metal), is shown in Figure 5-1. A high concentration of GO paste (50 mg/mL) was coated uniformly on a metal substrate (i.e., zinc, aluminum foil, nickel, copper, or lead) using a doctor blade (Figure 5-2). The final FGG film thickness is dependent on the deposited thickness, which can be controlled using the gap between the blade and the metal substrate. After drying at 40 °C for 3 h in the presence of 60% relative humidity (RH), a freestanding, paperlike FGG film could be readily peeled off from the metal substrate. The remaining metal substrate can be recycled (Figure 5-3) for use in the next round of fabrication. An FGG structure, where one side is primarily the electrically conductive rGO, henceforth referred to as M−rGO, while the opposite side is the electrically insulating GO, henceforth referred to as M−GO, can be prepared by either controlling (1) the concentration of GO, (2) the underlying metal substrate, (3) the film deposition thickness, (4) the film-drying temperature, and/or (5) the film-drying humidity. Figure: 5-1-b illustrates an FGG film deposited on an Al foil, which exhibits a reflective graphitic surface where it came in contact with the Al foil and dull brownish-black color, characteristic of GO, on the top, air-dried surface of the film. The FGG film can be prepared in any shape and size using an active metal substrate in a one-step coating method. The final film is mechanically robust and freestanding as demonstrated by its ability to be significantly bent without fracturing. Using a template at the interface between the GO and the metal substrate allows only the select portion of GO exposed to the active metal substrate to undergo reduction and FGG formation. Figure: 5-1-c demonstrates an example of such selective reduction of GO, where the institutional logos UT and UCLA have been imprinted and reduced on the overall GO substrate. The cross- sectional image of an Al-foil-assisted FGG film obtained by scanning electron microscopy (SEM) is presented in Figure 5-5-d. The cross-sectional morphology of the film reveals that the GO sheets have assembled into a well-packed layered microstructure of graphene and graphene oxide sheets. The nonconducting nature of graphene oxide becomes particularly apparent by the charged zones during SEM, which are more concentrated at the air-exposed side of the FGG films.

Unlike other GO reduction processes where the GO is reduced indiscriminately,[17,39] the FGG films in the present method transition from being electrically conductive at one face to becoming insulating at the opposite face. The underlying metallic substrate was found to play an important role in directing the reduction of the GO and the overall microstructure of the FGG film. FGG films were fabricated on Zn, Al, Pb, Ni, and Cu substrates by coating a concentrated GO paste

(50 mg/mL) with a thickness of 300 μm, followed by drying at 50 °C in a 60% RH environment. Of these metallic substrates, the FGG films formed on Zn were observed to have a unique porous microstructure and thus were the subject of a further detailed investigation. A Zn−FGG film (thickness = 126 μm, Figure 5-4) was simply peeled off using a piece of cellophane tape to obtain a transition zone, lying somewhere between the metal interface (reduced) side and the air-exposed side. The thickness of the transition zone was measured to be ∼50 μm from the reduced side of the Zn− FGG film, obtained by accounting for the thickness of the Scotch tape as well as the peeled film using a micrometer. The differences in reduction between the three regions of the films were characterized by Raman spectroscopy (Figure 5-5). The Zn−FGG films exhibit the characteristic D and G bands in their Raman spectra in all three regions (Figure 5-5-a). The D band is a disorder-activated shift attributed to defects disrupting the sp^2 hybridization of carbon, while the G band is the primary in-plane vibration mode for a hexagonal network of C atoms.[43] The pristine GO without reduction shows a G peak at around 1604 cm^{-1}, which is expected to shift toward 1580 cm^{-1} (graphite) after reduction.[43,44] A slight reverse shift of the G band is observed after the reduction of GO on zinc, which can be attributed due to the presence of metal elements on the FGG film.[17,45] The intensity ratio of the D and G bands (I_D/I_G) offers insights into the extent of reduction through the liberation of oxygen-containing point and edge defect sites.

The intensity ratios of the D to G peaks (I_D/I_G) were determined to be 1.14, 1.51, and 1.84 on the nonreduced, transition zone, and reduced side of the Zn−FGG film, respectively, indicating a graded composition from one side to the other of the FGG film. The I_D/I_G ratio for pristine GO is 1.01, which is lower than either side of the Zn−FGG film. The increase in the ID/IG ratio is the result of a decrease in the average size of the sp^2 domains upon reduction of the GO, which would cause a large number of structural edge defects.[44,46]

The differential reduction of a Zn−FGG film was further confirmed by X-ray diffraction (XRD), as shown in Figure 5-5-b. Pristine GO possesses a characteristic peak at 10.88° with a *d*-spacing of 0.81 nm, attributable to the presence of oxygen- containing functional groups separating the graphitic layers.[43] Three distinct diffraction peaks corresponding to the (002) basal plane are present on the nonreduced side of the Zn− FGG film at around $2\theta = 8.6$, 10.75, and 23.65° with *d*-spacings of 1.03, 0.82, and 0.37 nm, respectively. In contrast, the diffraction peaks of the reduced side are found at 8.84° (0.99 nm), 10.88° (0.81 nm), and 24.32° (0.36 nm). The highest intensity peak (10.75°) on the nonreduced side of the Zn−FGG film with an expanded interlayer distance (0.82 nm) can be attributed to the oxygen-containing functional groups and intercalated water molecules between the GO sheets.[38,43] The opposing side of the Zn−FGG film still exhibits this peak but at a significantly reduced intensity in comparison to the other more prominent peaks at 8.84 and 24.32°. The broader peak at 24.32° corresponds to an interlayer spacing of 0.36 nm, which is close to pristine graphite's interlayer spacing of 0.335 nm. The highest intensity diffraction peak on the reduced GO side occurs at 8.84° (*d*-spacing = 0.99 nm), which according to previous reports[47,48] corresponds to the intercalation of metal ions between the GO sheet basal planes. The increase of the interlayer distance from 0.81 nm (pristine GO peak) to 0.99 nm provides strong evidence for the intercalation of metal ions between the GO sheets.

The chemical structures of the GO film and both the reduced and the nonreduced sides of the Zn−FGG were studied using FTIR spectroscopy (Figure 5-5-c). The intensity of the broad peak between 2800 and 3600 cm^{-1} is caused by both graphene oxide. Both adsorbed water and hydroxyl (−OH) groups.49 The peak at 1724 cm^{-1} is associated with the carbonyl (C=O) stretching mode found in carboxylic acid, ketone, and aldehyde functionalities. The fingerprint region (800−1500 cm^{-1}) of the spectra are both broad and overlapping, making them difficult to assign to specific organic functionalities; however, it can be said with certainty that intense absorption in this region of the spectra shows that the material is highly functionalized with a wide variety of covalently bonded oxygen. Here, we are defining that the peaks at 1045, 1400, and 1620 cm^{-1} correspond to epoxides, carboxyl, and aromatic groups, respectively.[17,50] Comparing the spectrum of pristine GO to the "nonreduced" side of the Zn−FGG film, very little change in the spectra is observed. However, the peak at 1724 cm^{-1} becomes significantly weaker. This is indicative of the removal of carbonyls despite the air-exposed side not being in direct contact with the Zn metal substrate. In contrast, the spectrum of pristine GO compared to the reduced side of the Zn−FGG film shows significant changes to the FTIR absorption spectra. The fingerprint region shows little to no absorption, indicating that most oxygen functionalities have been removed. The only significant peaks are a broad set of overlapping peaks from ∼1300 to 1400 cm^{-1} and another set from ∼1600 to 2000 cm^{-1}, likely caused by the few remaining oxygen functionalities, which are possibly involved with metal-ion crosslinking. [47] In a similar fashion to the Zn−FGG films, the Al− FGG films also exhibit a functionally graded reduction of GO, as confirmed by Raman, XRD, and FTIR spectroscopy (Figure 5-6). A cross-sectional image of an FGG film on zinc (Figure 5-5-d) indicates a graded microstructure between graphene and graphene oxide. The bottom surface of the film, which is in contact with the metal, reveals a porous structure, whereas the nonreduced side consists of a densely packed structure (Figure 5-7). The energy-dispersive X-ray (EDX)-based elemental mapping reveals that atomic zinc is well distributed throughout the film. These results along with the XRD and FTIR observations suggest a metal− graphene coupling throughout the FGG film.

The reduction of GO is associated with redox reactions occurring at the interfaces of the active metal and the GO particles in solution. Thus, the recovery of sp^2 hybridization during reduction should depend on the reduction potential values of the various metal substrates, as per their position in the electrochemical series. Hence, a metal with the lowest reduction potential should be able to reduce GO most effectively. This hypothesis was tested by characterizing the conductive face of FGG films reduced on Zn, Al, Pb, Ni, and Cu substrates. The Raman spectra of reduced graphene oxide at the interface of various metallic substrates are shown in Figure 5-8-a. A pristine GO film dried on an inert substrate (polyimide) possesses a D band at 1336 cm^{-1} and a G band at 1604 cm^{-1}, whereas Ni, Pb, Cu, Al, and Zn metal-assisted rGOs exhibit G bands at Raman shifts of 1601, 1599, 1595, 1587, and 1595 cm^{-1}, respectively. The red shifting of the G band shows the development of in-plane sp^2 carbon domains.[38,51] Compared to pristine GO films, the intensity ratios of the D band to G band for various metal-assisted rGOs have increased. Moreover, the Zn−FGG film shows the highest intensity ratio ($I_D/I_G = 1.84$) when compared to other metal-assisted reduced films, implying the highest extent of reduction of GO on Zn.

Figure 5-5-b illustrates the normalized XRD patterns of GO and rGO reduced on various active metals. Ni−FGG, Pb− FGG, Cu−FGG, Al−FGG, and Zn−FGG samples exhibit relatively lower intensity peaks at 10.5, 11.0, 10.5, 10.3, and 10.8°, respectively, which correspond to the GO interlayer separation. In addition, all of the reduced GO samples show a broader peak between 20 and 25° corresponding to a significantly lower interlayer distance (∼0.4 nm), which indicates that the graphitic structure is partially recovered. In the case of the Zn−FGG films, the intensity of the broad graphitic peaks is higher compared to that of other metals, denoting a significant recovery of sp^2 hybridization and subsequently greater extent of reduction of GO. The intensity of these broad peaks gradually diminishes as the reduction efficiency decreases in other metal-based FGG films. An additional peak at 8.8° (*d*-spacing of 0.99) appears in the Zn− FGG sample, corresponding to the cross-linking of metal ions within the graphitic layers. This peak is not noticeable in the XRD pattern of other reduced samples, indicating an absence of such crosslinking. The corresponding metal contents in these other metals based on XPS measurements (Tables 5-1 and 5-2) are drastically lower (<0.7 atom %), when compared to those of the Zn−FGG film (~4.4 atom % for Zn). It should also be noted that the multiple peaks at 23.3, 25.5, 26.8, 27.7, 29.7, 43.8, and 44.6° on the Pb−rGO sample correspond to PbO that was apparently transferred onto the FGG film.[52]

The FTIR spectra for the reduced side of the FGG film coated on various metals are shown in Figure 5-8-c and compared to the original GO FTIR spectrum. The FGG films on nickel, lead, and copper show strong absorption bands in the fingerprint region (900−1500 cm^{-1}) as well as carbonyl (~1700 cm^{-1}), aromatic/water (1625 cm^{-1}), and hydroxyl 2500−3500 cm^{-1}) regions. The presence of these bands indicates that the material, while being mildly deoxygenated, still maintains a high amount of oxygen functionalities on its surface. In contrast, the GO samples that were coated onto zinc and aluminum show greatly diminished absorption in the fingerprint region as well as the OH stretching region (2500− 3500 cm^{-1}) due to the conversion of GO to a highly deoxygenated and dehydrated reduced GO.

The FTIR spectra of the FGG films indicate a strong interaction between the trapped water molecules and the oxygen-containing functional groups on GO, which could possibly be directing the self-assembly process. To investigate this further, the trapped moisture within the various FGG films was quantified by thermogravimetric measurements. FGG films, as well as pristine GO films, were cut into 10 x 10 mm^2 samples and dried in a convection oven at 150 °C with the weight loss being recorded over time. The percentage of weight loss as a function of time for pristine GO and FGG films reduced on various metals is illustrated in Figure 5-8-d. A sharp drop in mass loss is observed over a short, initial period, which becomes steady afterward for all cases, characteristic of absorbed water within the films. However, in contrast to the rest of the metals (~40% mass loss), the Zn−FGG film contains significantly less water (~20% loss), suggesting a significant loss of oxygen-containing functional groups to either the conversion to rGO or to the metal-ion cross-links during processing, since it is these functional groups that facilitate the water absorption capability of the GO films.

The electrical conductivity of the reduced side of the FGG films was investigated by depositing a 300 μm thick GO paste with a concentration of 50 mg/mL on Zn, Al, Pb, Ni, and Cu substrates using a doctor blade followed by air-drying at 50 °C with 60% RH. The average dried film thicknesses were measured to be 126, 30, 29, 36, and 24 μm for Zn, Al, Pb, Ni, and Cu, respectively. Comparison between the reduced film thickness and its effect on sheet resistance for the Zn−FGG and Al−FGG films is plotted in Figure 5-9. A linear and exponential decline in the sheet resistance with increasing thickness is observed in the case of Zn−FGG and Al−FGG, respectively. The increase in conductivity can be attributed to additional delocalized π-electrons available for charge transfer in subsequent layers of graphene oxide. A plot of sheet resistance, measured using a four-point probe, is shown in Figure 5-8-e corresponding to the reduced side of the various FGG films. The lowest sheet resistance of 108.7 Ω/sq is observed on the Zn−FGG film followed by the Al−FGG (187.7 Ω/sq), the Pb−FGG (2600.2 Ω/sq), the Ni−FGG (4782.5 Ω/sq), and the Cu−FGG (7095.1 Ω/sq) films. On the other hand, the sheet resistances of the insulating faces of the FGG films show very high values (>10 MΩ/sq or in some cases “over range”) denoting the absence of reduction (Figure 5-10). The lower values of sheet resistance on the reduced faces, along with Raman, XRD, and FTIR results, indicate that the elimination of oxygen functionalities from the Zn−FGG film is significantly higher than that of the other metal-assisted reduced films. The standard reduction potentials of Al/Al^{3+}, Zn/Zn^{2+}, Ni/Ni^{2+}, Pb/Pb^{2+}, and Cu/Cu^{2+} are −1.66,

−0.76,−0.26, −0.13, and 0.34 V, respectively, vs. SHE, while the reduction potential of GO is reported to be about −0.4 V vs SHE in a pH 4 solution.[50] Based on standard potential values, the Al substrate should reduce GO more effectively, and consequently, it should have the lowest sheet resistance when compared to the other metals. Table 5-1 shows that the sheet resistance of Al is higher than that of Zn; similarly, Ni shows a higher value of sheet resistance than Pb. To elucidate the reduction mechanism(s) of the FGG films, we designed a galvanic cell with an electrolyte at pH 4.0 (Figure 5-11). In such a cell, the redox reactions can be divided into two half reactions:

Anode: $M = M^{(n+)} + ne^{-1}$

Cathode: $nGO + 2nH^{+} + 2ne^{-1} = nrGO + nH_2O$

Total Redox: $nGO + 2nH^{+} + M = nrGO + M^{(n+)} + nH_2O$

The overall reduction potentials of the metal substrates tested in the custom cell are listed in Table 1. Zinc was found to have the lowest reduction potential of −1.09 V among the listed metals, followed by Al (−0.76 V), Pb (−0.50 V), Ni (−0.36 V), and Cu (−0.12 V). The greater reduction potential of Al (in comparison to Zn) is attributed to the well-known passivating behavior of Al. A lower reduction potential implies a greater driving force for Zn to lose electrons to the GO, hence explaining the more effective reduction of GO observed using the Zn metal substrate.

The precise chemical compositions of pristine GO and FGG films reduced on the different active metals were analyzed using X-ray photoelectron spectroscopy (XPS) (Figure 5-12, 5-13) with the results summarized in Tables 5-1 – 5-4. High- resolution scans of sp^2 (284.5 ± 0.1 eV), sp^3 (285.3 ± 0.1 eV), C−OH (287.1 ± 0.1 eV), C−O−C (287.7 ± 0.1 eV), and COOH (288.6 ± 0.1 eV) groups.[38,39] The relative area of the deconvoluted peaks was used to determine the relative atomic abundance of each orbital/moiety, where an abundance of sp^2 carbon relative to sp^3 carbon and to other functional groups implies a higher degree of reduction/deoxygenation, respectively. [53] Films reduced on a zinc substrate show markedly different oxygen functionalities on either opposing sides (Figure 4b−d and Table S3). The spectra corresponding to the side in contact with the metal substrate (Zn−rGO) show few oxygen functionalities (Figure 5-12-d), whereas the air-exposed side of the film is abundant in oxygen functionalities, indicative of minimally reduced GO (Figure 5-12-b). Survey scans (0−1204 eV) provide relative atomic percentages of metals, carbon, and oxygen in each sample as well as film cross sections. The fully oxygenated film precursor (pristine GO) has a carbon-to- oxygen ratio (C:O) of approximately 2.3:1 (Table 5-1), which can be contrasted with the C:O ratios measured through the profile of the Zn−FGG film. In the Zn−FGG films, the C:O ratio was determined to be approximately 2.5:1 for Zn−GO (nonreduced side), 3.02:1 for the transition region, and 3.4:1 for Zn−rGO (reduced side) (Figure 5-12-f and Table 5-1), thus indicating an asymmetric degree of deoxygenation across the film. Taken together with the Raman, XRD, and FTIR observations, the XPS results suggest that the elimination of oxygen-containing functional groups and the restoration of the π-conjugated structure are not uniform throughout the film, resulting in a functionally graded conductive rGO and insulating GO distribution within a single film. The graded graphene networks in the FGG films can be tailored through the control of the underlying metal substrates as well as the film's drying environment. As shown in Figures 5-12 and 5-13, all films reduced on Al, Pb, Cu, and Ni undergo reduction from contact with the metal foil, as indicated by the increase in sp^2 carbon at ∼284.5 eV and the decrease in sp^3 carbon as well as oxygen functional groups corresponding to the peaks at 285.5−289.0 eV (see Tables 5-1 and 5-2). This deoxygenation trend directly corresponds to the reduction potential of the metals, as observed from the galvanic cell experiments. The survey scans also show the amount of metal ions that was dispersed throughout the film during the reduction process (Table 5-1, 5-2), which, as discussed earlier, was significantly higher for Zn (4.4 atom %) vs the other metals (e.g., Al, 0.7 atom %). With the precise chemical composition of the films, the water uptake behavior, and the relative galvanic positions of the metallic-reducing agents known, a complete mechanistic picture of the GO/rGO functional grading and the ensuing film morphology can be illuminated (Figure 5-14).The functional grading observed in these films is caused by a competition between the kinetics of film drying and the redox reaction between the metal and the GO. This competition is facilitated by the high concentration of GO (30−50 mg/mL), which exhibits a gel-like behavior,[54] used in our process. Similarly, processed films on a Zn substrate, but using dilute concentrations of GO (e.g., 10 mg/mL or less), did not exhibit any functional grading. Instead, such films reduced throughout their thickness indiscriminately upon either drying or freeze-drying, a behavior that is well known.[17,38,39] Furthermore, we found that highly concentrated GO films were also reduced indiscriminately throughout their thickness when processed in a high humidity environment (90−100% RH) for 24 hr, followed by air-drying (40% RH), thus implying a role of drying kinetics. The indiscriminate reduction occurs because of the high water content in dilute GO suspensions or in a highly humid environment, where the GO flakes and their polar functional groups are well solvated. An indiscriminately reduced Zn−rGO film in the presence of high RH (95%) is shown in Figure 5-15. Due to prolonged drying and indiscriminate reduction throughout the thickness, the film loses its freestanding nature, and loosely connected flakes of coagulated GO particles are observed on the base metal surface. In the other case, where the films are dried at a low RH (<30%), the drying is accomplished at a faster rate, and significant lateral strains develop between the layers resulting in a ruptured film surface (Figure 5-15-b). Contrast this with the GO flakes in the topmost layers of a concentrated dispersion with a paste/gel-like rheology, which will begin to dehydrate rapidly due to evaporation at moderate humidity (40−60% RH). Once dehydrated, the GO flakes do not participate in the redox reactions, due to the immobilization of the H^+ and M^{n+} ions, and consequently remain in an oxidized form. At the same time, the bottom regions of the GO film, which remain hydrated, get reduced as per the redox reactions described earlier. Once reduced, the GO flakes deposit on the conductive surfaces forming a reduction front whose continued propagation upwards is facilitated by the inherent electrical conductivity of the rGO itself.

A consequence of the galvanic reduction of GO is the presence of liberated cations from the metallic substrate, which must react for an overall neutral charge balance once the film has dried. Previous work has indicated that negatively charged oxygen moieties within GO are favorable sites for metal ions, which can form chemical cross-links between any adjacent GO flakes because of their multivalent nature.[47] These cross-links are known to occur with either a plane-to-plane configuration through a ring-opening reaction with the epoxide groups present on the graphitic basal plane or with an edge-to-edge configuration where a cross-link is formed with the carboxyl and hydroxyl groups that are present on the graphitic edges. The abundance of metal ions in our FGG films as observed in EDX (Figure 5-16) and XPS (Figure 5-12), as well as the selective disappearance of certain functional groups from FTIR observations (Figure 5-8-c), suggests a significant degree of cross-linking within the dried FGG films. Furthermore, these results imply that the nature of the cross-links is selective to the type of a metal substrate that the FGG films are cast upon. According to their FTIR spectra, the Zn-based films are mainly devoid of any epoxide functionalities at 1045 cm^{-1}, which are otherwise present in other metallic substrates including Al. At the same time, the carboxyl functionalities at 1400 cm^{-1} are completely absent from Al−FGG films and weakly expressed in other metallic substrates. In contrast, the carboxyl groups are prominent in the Zn−FGG films despite the high level of reduction and electrical conductivity observed in them. This indicates that Zn^{2+} binding on GO is through epoxide ring opening, resulting in a basal plane-to-plane cross-linking (Figure 5-14-b). The XRD spectra of the Zn−FGG films (5-8-b) exhibit a second (002) peak at a lower 2θ value of ∼8.8° as opposed to the single (002) peak at ∼11° observed in GO and other metal-reduced films, indicating a basal plane interlayer expansion in the Zn−FGG films due to the accommodation of these cross-links. The plane-to-plane cross-links are what cause the flakes to coagulate and expel water, which results in a porous morphology (Figure 5-14 a,c), where the pores are formed by the water channels as they dry out. The thermogravimetric data (Figure 5-8-d), which show that the dried Zn−FGG films have significantly lower water content, support this hypothesis. In contrast, the FGG films cast upon other metals (including Al) create an edge-to-edge cross-linking that results in a layer- stacking type of self-assembly and a smooth interface (Figure 5-14-d) during the drying process. Thus, the final film micro- structure and functional grading are directed by the underlying metal substrate.

The recently conceived concept of transient electronics calls for functional electronic components that can undergo a programmed decommissioning/destruction. Such a capability is required under multiple scenarios, such as crypto-hardware designs,[55] medical devices,[56] and environmentally benign electronics for mitigating e-waste.[57] Transient electronics are typically multicomponent systems constructed using conductive and usually reactive metals (e.g., Mg, Fe, Mo, W, and Zn), semiconductors (e.g., doped Si), and insulators (e.g., MgO, SiO_2, and Si_3N_4), which are all held together by a water- or acid-soluble encapsulation layer (e.g., poly(vinyl alcohol), polyvinylpyrrolidone, polylactic acid, polycaprolactone, or poly(phthalaldehyde)).[58,59] Graphene-oxide-based electronics are not designed with transient operations in mind. However, the dispersibility of graphene oxide in water can facilitate the design of all-graphene-based electronics with transient properties. The selective reduction of GO offers the ability to construct well-defined patterns and connections required in electronic circuits and devices. A schematic of an all-graphene-based selectively reduced GO for an RFID tag antenna is demonstrated in Figure 5-17-a. A mask of the desired pattern is employed at the interface of the metal substrate and GO paste to restore the conjugated sp^2 networks selectively. A silhouette portrait electronic cutting tool can be used to create masks with thin polymer sheets or papers. After creating the desired templates, the thin polymer masks were transferred and adhered onto the metal substrate through the application of industrial spray glue (Easy Tack) on the mask surface. The GO paste was then coated on the masked metal substrate through a doctor-blading technique, as described in Figure 5-17-a. Only the selective portions of GO that are in contact with the metal substrate will be transformed into rGO, while the remaining portions covered with the mask will stay as GO. The GO paste along with the mask was dried under controlled temperature and humidity conditions to obtain a smooth film without any cracks. An image of an RFID tag antenna based on an all- graphene construct prepared by a one-step coating process is shown in Figure 5-17-a. The RFID tag antenna is mechanically robust and flexible. Moreover, the inexpensive graphene-based RFID tag antenna can be disintegrated/decommissioned by an external stimulus with minimal impact on the surrounding environment. To demonstrate the transient effect, we prepared a U-shaped reduced GO conductive path (30 x 20 x 3 mm^3) imprinted on a GO substrate (60 x 40 mm^2) with a thickness of $\sim$25 μm. The film was immersed in distilled water in such a manner that half of the film was immersed in the liquid, while the rest, which included the probes of the ohm-meter, remained above the liquid surface. The ohmic resistance values were recorded during the dissolution process. The GO sheets absorb water and swell because of their hydrophilic nature, whereas the rGO sheets repel water due to their hydrophobic nature. As a result, the U-shaped conductive circuit disintegrates into small pieces of rGO over time and loses its functionality. We studied the transient behavior of this U-shaped conductive path under different environmental conditions, including the temperature of the water, agitation of the liquid, and the pH, as well as the film thickness. As can be seen in Figure 5-17-c,d, increasing the water temperature, inducing a weak agitation of the liquid, lowering the pH value, or reducing the thickness of the film all favor the dissolution process. Images from the transience experiments at different stages of disintegration are presented in Figure 5-17-g. While the GO starts to disintegrate in water through swelling after approximately 2 min, the electrically conductive path is completely disrupted only after 6.3 min. All of the graphene-based electrical circuits shown in this study can also be disintegrated without submersing the films under water. For instance, placing a few drops of water on the conductive path can disrupt the circuit within a few minutes (Figure 5-18).

The bilayer-like arrangement of the GO and rGO structures in these FGG films is evident by their differential swelling behavior when immersed in water. GO is highly hydrophilic and rapidly swells by absorbing water, whereas rGO, without the oxygen moieties, is hydrophobic and repels water. As can be observed, Al−FGG, Pb−FGG, Ni−FGG, and Cu−FGG films curl when they are submerged in distilled water (Figure 5-18-a, Figure 5-19), indicating the presence of bilayer-like arrangements originating from the graded structure. The increased volume of GO through water absorption on the nonreduced side concomitant with a poor absorption on the rGO side causes the FGG films to macroscopically curl. The curling effect is not observed with the Zn−FGG films, which might be due to the high density of Zn cross-links throughout the film combined with its porous structure.

The FGG films are mechanically robust and flexible and can be cut into slender strips that display hygromorphism, a shape deformation in the presence of a moist environment. Hygromorphism is also observed in nature, e.g., in the case of pine cones that respond to changes in the surrounding humidity.[60,61] Increase in the mechanical strength and flexibility of the FGG films upon reduction is evident through their response to the dynamic stress−strain tests (Figure 5-21). The ultimate tensile strength of pristine GO films increased by 65% after reduction on an aluminum substrate, making them ideal for hygromorphic actuation. To demonstrate their actuation, a 30 x 5 mm^2 Al−FGG film was placed in a custom-made transparently controlled humidity chamber. For different values of RH, the FGG films display different extents of bending (Figure 5-19-b,c). The oxygen-containing functional groups of GO control the expansion/contraction of the film through the absorption and repulsion of water molecules. At 100% RH, GO sheets absorb water molecules that induce an obvious expansion of GO sheets and hence develop a mismatch force between GO and rGO sheets. As a result, the FGG film bends toward the rGO face in a moist environment. In contrast, when the value of the RH is decreased, the bending of the FGG film is shifted toward the GO face due to the repulsion of water molecules by the GO sheets. The FGG films have also proven to exhibit a consistent bending curvature for multiple cycles of varying RH (30−95%), denoting the repeatability of the actuation mechanism (Figure 5-19-d). The mechanically strong, flexible, hygromorphic FGG actuators could be attractive for a wide variety of applications, such as soft robotics and artificial muscles.[62,63]

Conclusions

All-graphene-based functionally graded films were developed by a single-step film coating process on various active metal substrates. The functionally graded reduction of GO film, where one side was electrically conductive rGO and the opposite side was insulating GO, can be produced by tuning the underlying substrate metal and the film-drying environment. Based on SEM, EDX, Raman, XRD, FTIR, XPS, and sheet resistance results, the reduction of GO on a Zn substrate was very effective in restoring the conjugated sp^2 network while removing the oxygen-containing functional groups, followed by Al, Pb, Ni, and Cu substrates. All-graphene- based freestanding RFID tag antennas that possess disintegration characteristics under distilled water have been demonstrated. The mechanically robust, flexible FGG films with a bilayer-like arrangement of GO and rGO structures are sensitive to humidity and are shown to be applicable as hygromorphic actuators. We believe that the large-scale FGG films developed by a facile, cost-effective, recycling, and environmentally friendly approach combined with their transient and hygromorphic behaviors could find many applications including low-cost, flexible electronic devices and sensors.

Tables

Table 5-1: The chemical compositions of reduced, transition, and non-reduced side of Zn-FGG and Al- FGG films derived from C1s XPS spectra.

Sample	Reduced side				Transition GO/rGO region				Non-reduced side			
	C (%)	O (%)	atomic (%)	C/O ratio	C (%)	O (%)	atomic (%)	C/O ratio	C (%)	O (%)	atomic (%)	C/O ratio
Zn-FGG	73.4	21.4	4.4 (Zn)	3.4	71.5	23.8	4.0 (Zn)	3.0	71.0	27.9	0.7 (Zn)	2.5
Al-FGG	85.7	13.2	0.7 (Al)	6.5	68.3	28.7	0.7 (Al)	2.4	69.2	28.5	0.6 (Al)	2.4

Table 5-2: The chemical compositions of pristine GO and reduced and non-reduced side of various FGG films derived from C1s XPS spectra.

Sample	Reduced side				Non-reduced side			
	C (%)	O (%)	Atomic (%)	C/O ratio	C (%)	O (%)	Atomic (%)	C/O ratio
Pristine GO	-	-	-	-	69.9	29.9	-	2.3
Pb-FGG	61.4	27.5	3.4 (Pb)	2.3	71.5	27.5	0 (Pb)	2.6
Ni-FGG	76.7	21.0	0.4 (Ni)	3.6	69.9	28.9	0 (Ni)	2.4
Cu-FGG	74.4	24.2	0.1 (Cu)	3.1	69.0	29.7	0 (Cu)	2.3

Table 5-3: The fitted results of C1s XPS spectra of reduced, transition, and non-reduced side of FGG films reduced on Zn and Al active metal substrates.

Sample		**Zn- FGG**	**Al- FGG**
Reduced side	C=C (sp^2) (%)	48.3	59.4
	C-C (sp^3) (%)	33.9	29.4
	C-O (%)	8.9	6.7
	C-O-C (%)	3.3	2.8
	C=O (%)	0	0
	HO-C=O (%)	2.8	1.7
Transition GO/rGO region	C=C (sp^2) (%)	40.3	22.6
	C-C (sp^3) (%)	39.9	25.3
	C-O (%)	8.6	32.9
	C-O-C (%)	3.4	15.9
	C=O (%)	0.4	0
	HO-C=O (%)	3.4	3.3
Non-reduced side	C=C (sp^2) (%)	18.9	22.2
	C-C (sp^3) (%)	29.2	27.2
	C-O (%)	38.6	37.6
	C-O-C (%)	8.6	8.5
	C=O (%)	0	0
	HO-C=O (%)	2.5	2

Table 5-4: The fitted results of C1s XPS spectra of pristine GO film and reduced and non-reduced side of FGG films reduced on various active metal substrates

Sample	**Reduced side**						**Non-reduced side**					
	C=C(sp^2) (%)	C-C (sp^3) (%)	C-O (%)	C-O-C (%)	C=O (%)	HO- C=O (%)	C=C (sp^2) (%)	C-C (sp^3) (%)	C-O (%)	C-O- C (%)	C=O (%)	HO- C=O (%)
Pristine GO	-	-	-	-	-	-	11.7	25.5	47.8	10.2	0.0	3.9
Pb-FGG	28.9	43.1	17.3	7.2	0.0	1.5	5.5	42.1	35.3	11.3	0.8	2.0
Ni-FGG	39.4	26.6	18.7	8.3	0.5	4.5	13.7	30.9	40.7	10.0	0.0	3.4
Cu-FGG	27.4	30.8	28.1	8.1	0.2	2.3	8.6	32.1	37.9	12.4	2.6	4.2

Figures

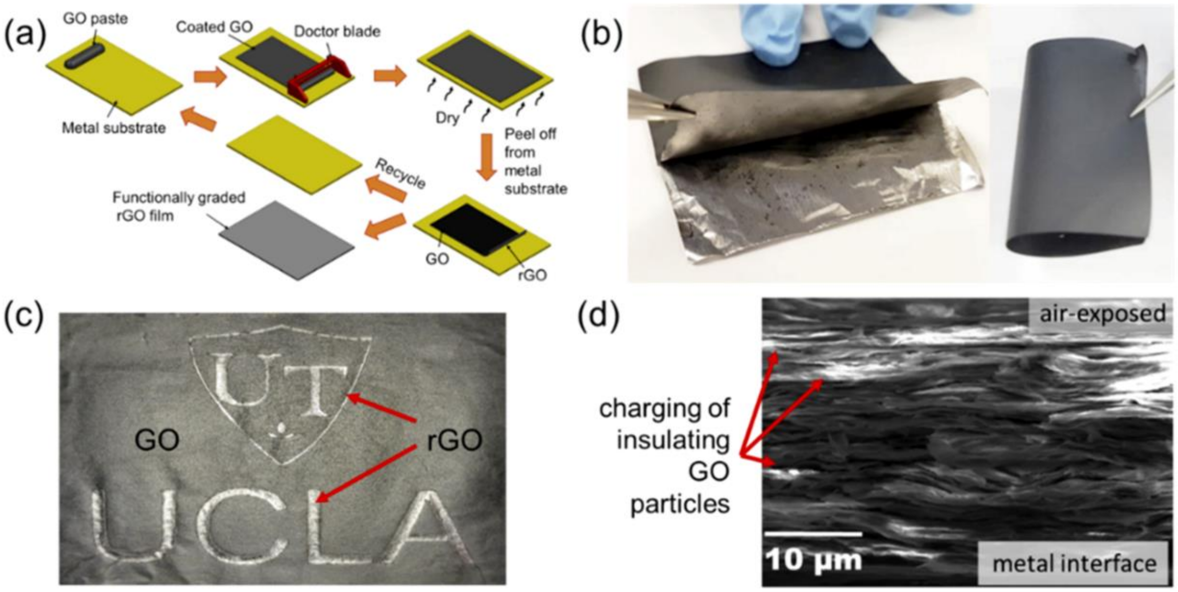

Figure 5-1: (a) Schematic drawings of the reduction process of a GO film on a metal substrate. Photographs of (b) an FGG film on an Al foil illustrating the shiny rGO luster created on the side interfacing with the metal as well as the flexibility of the overall film. (c) Selective reduction of GO with imprinted institutional logos and the (d) SEM image of the cross section of an Al−FGG film.

Figure 5-2: The deposition and reduction process of graphene oxide film. A 50 mg/mL concentrated graphene oxide paste was doctor blade coated on various polished metallic substrates. Various blade gaps were set and calibrated using feeler gauges. The GO gel paste was deposited at one end of the metal substrate and was manually coated using the doctor blade in a uniform manner. The entire coating assembly was then air-dried at various temperatures and humidity conditions. After drying, the film was easily peeled-off from the metal substrate and was found to be a free-standing functionally graded graphene (FGG) film.

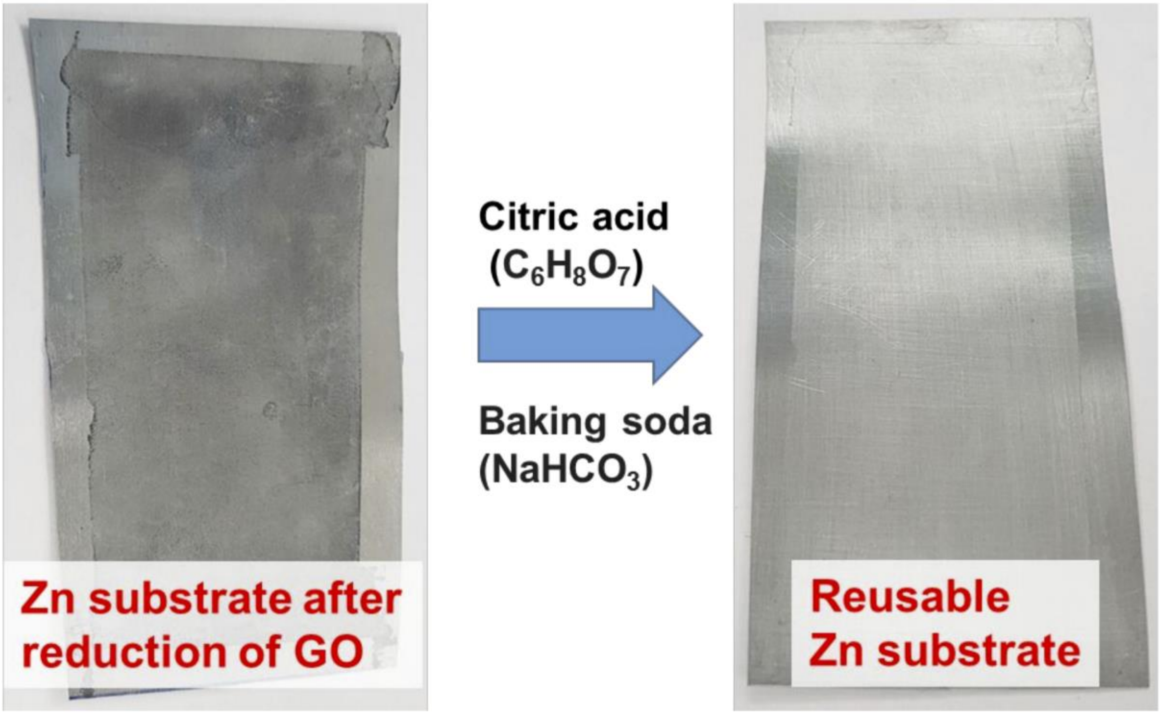

Figure 5-3: Recycling process of metal substrate for use in the next round of fabrication. The leftover rGO was cleaned by applying a little amount of baking soda (around half teaspoon) and citric acid (3~4 drops). After scrubbing and rinsing with water, the metal substrate was dried at room temperature.

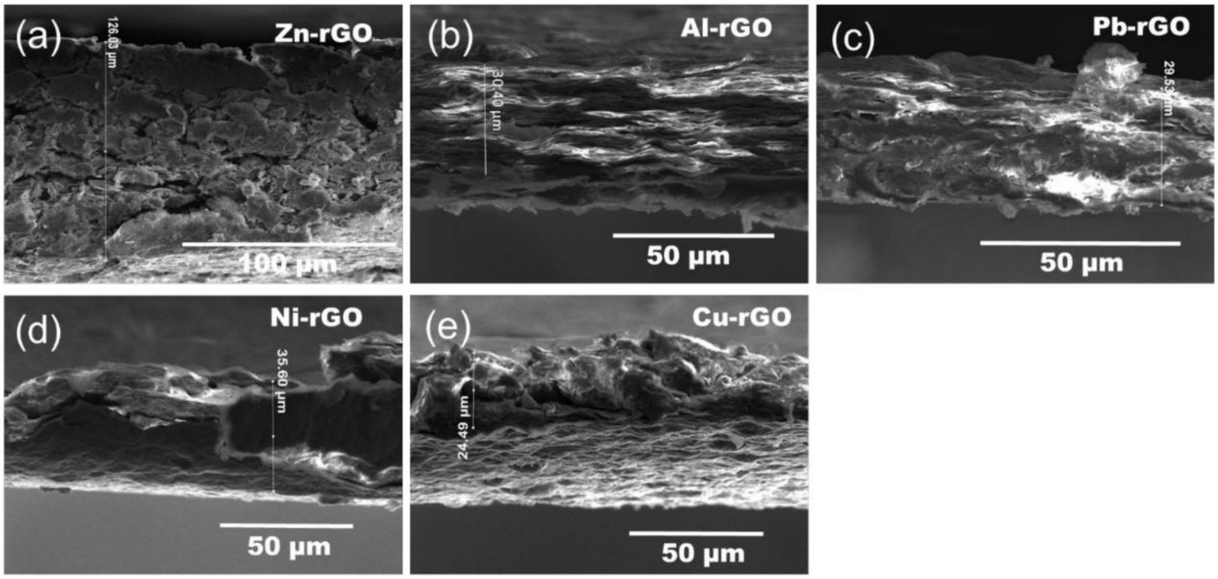

Figure 5-4: Cross-sectional SEM images of FGG films reduced on (a) Zn, (b) Al, (c) Pb, (d) Ni, and (e) Cu.

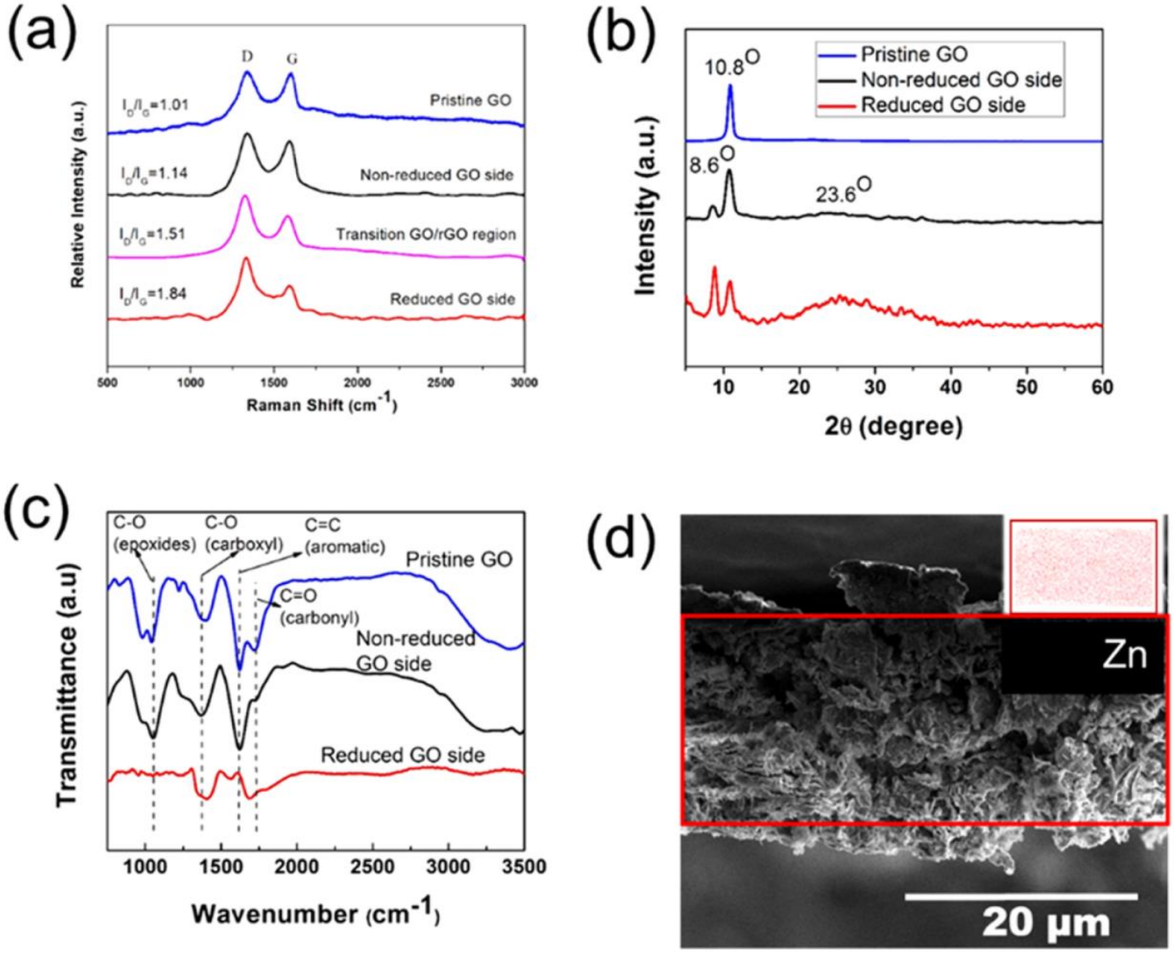

Figure 5-5: Structural characterization of a pristine GO and an FGG film reduced on Zn using (a) Raman spectra, (b) XRD patterns, and (c) Fourier transform infrared (FTIR) spectra; (d) cross-sectional SEM image and elemental mapping of Zn, within a Zn−FGG film.

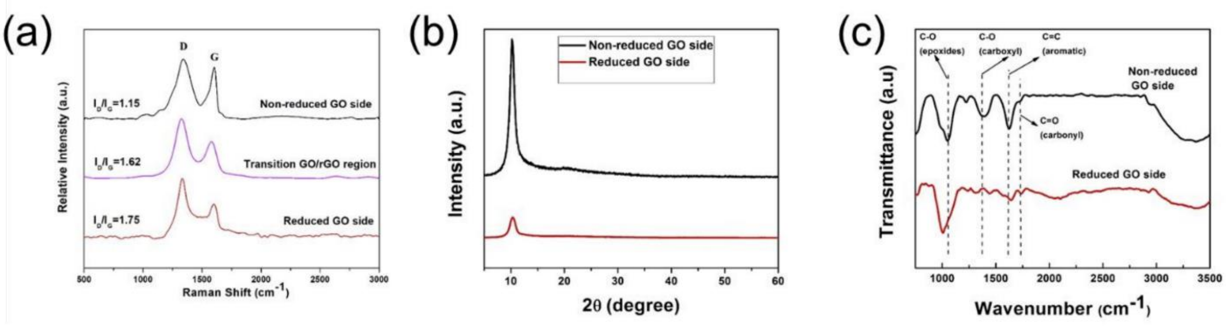

Figure 5-6: Structural characterization of Al-FGG film using (a) Raman spectra, (b) XRD patterns, and (c) FTIR spectra.

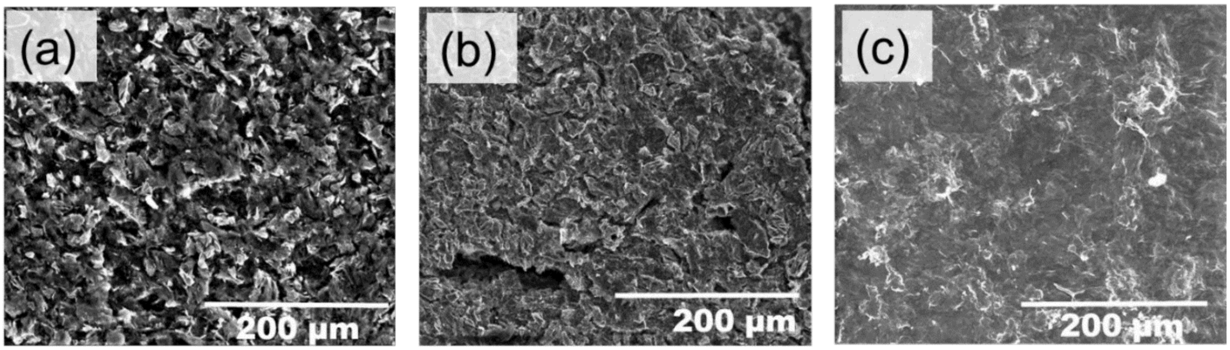

Figure 5-7: SEM image of the surface morphology of (a) reduced side, (b) transition region, and (c) nonreduced side of FGG film on Zn.

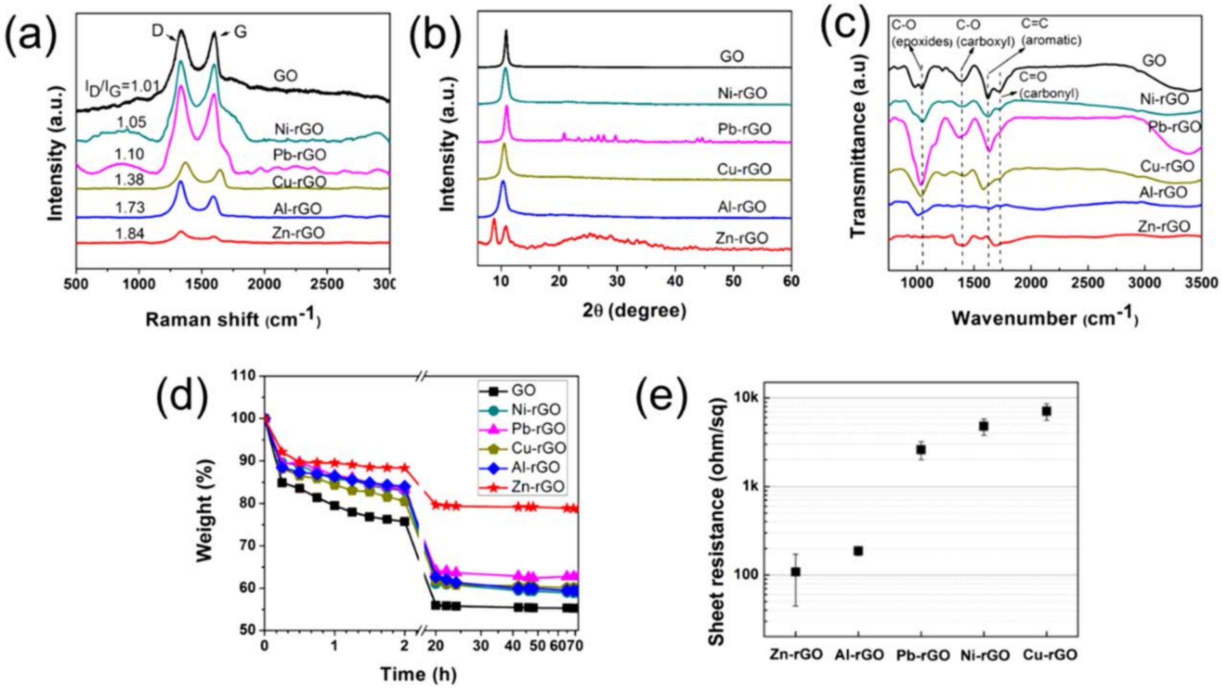

Figure 5-8: (a) Raman spectra, (b) XRD patterns, and (c) FTIR spectra of GO and the reduced side of Ni−FGG, Pb−FGG, Cu−FGG, Al−FGG, and Zn−FGG films; (d) thermogravimetric characterization of FGG films; and (e) sheet resistance of Ni−FGG, Pb−FGG, Cu−FGG, Al−FGG, and Zn−FGG films.

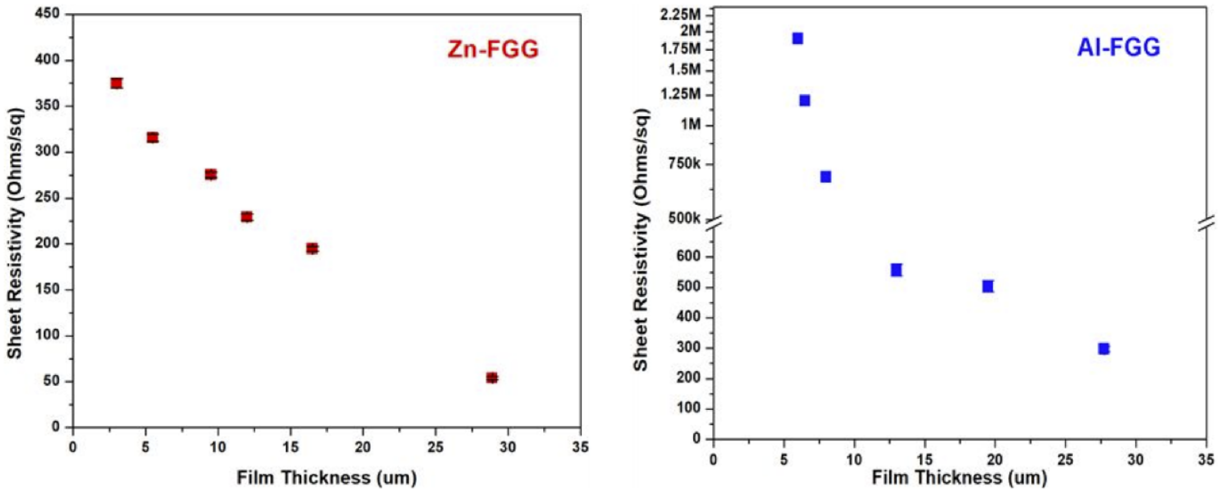

Figure 5-9:. The effect of film thickness on the sheet resistivity of the film grown on Zn and Al substrate.

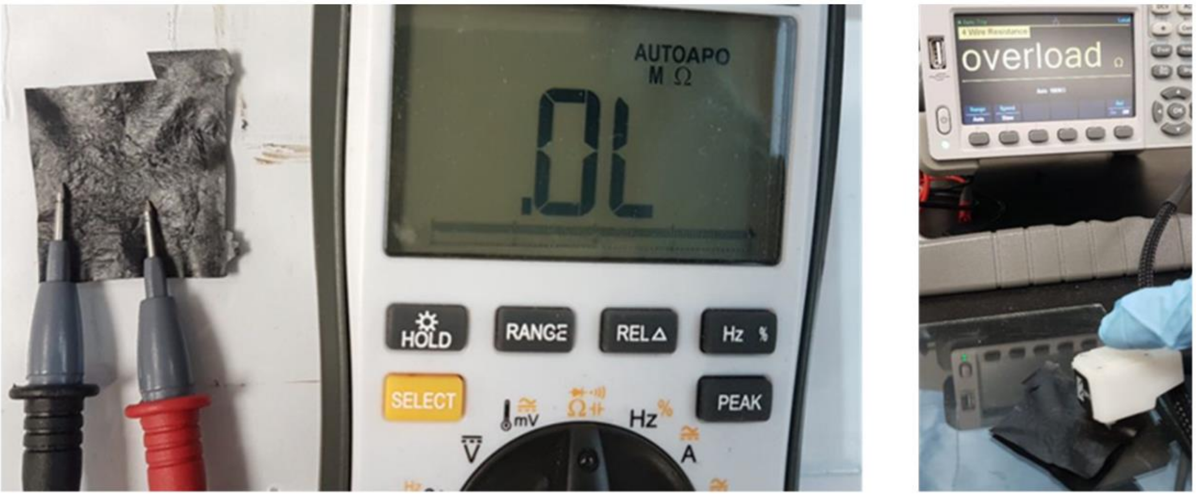

Figure 5-10: Resistance measurements using 2pt and 4pt probes displaying a very high value (Overload) of sheet resistance on non-reduced (GO) face of the FGG films denoting absence of reduction.

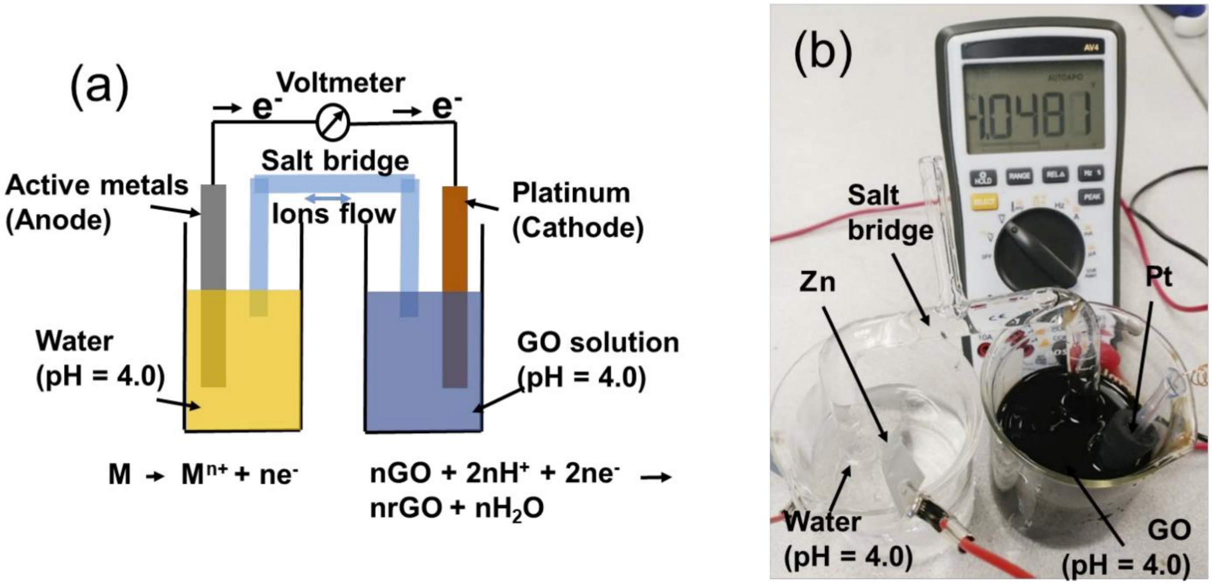

Figure 5-11: (a) Schematic illustration of a model voltaic cell, (b) an image of an experimental setup of a voltaic cell. An active metal substrate and an inert platinum plate were used as the anode and the cathode, respectively, which were connected by a salt bridge (NaCl) to facilitate the flow of metal ions across the half-cells. The anode was immersed in water with a pH of 4.0 and the cathode was immersed in a GO solution with a pH of 4.0. At the anode, the metal substrate oxidized into metal ions by releasing electrons, which were acquired by the GO at the cathode.

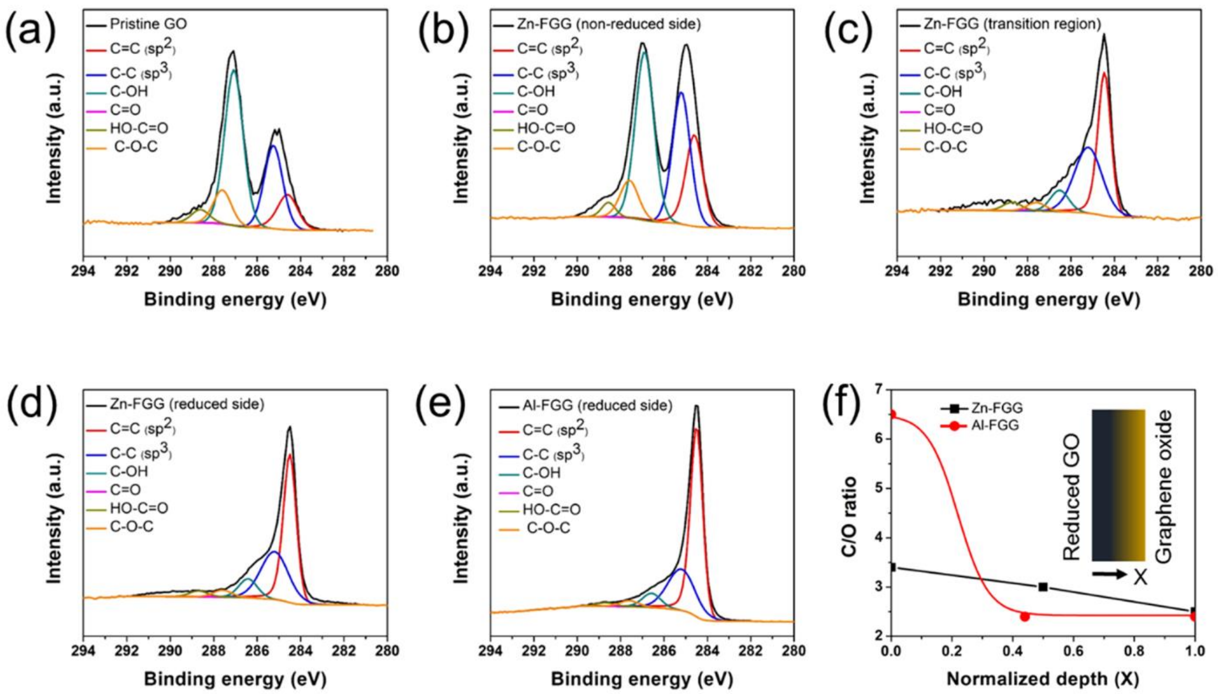

Figure 5-12: C 1s spectra of (a) pristine GO, (b) the nonreduced side, (c) the transition region, and (d) the reduced side of the Zn−FGG film, and the reduced side of (e) the Al−FGG film. (f) Carbon-to-oxygen ratio as a function of the depth of FGG films reduced on Zn and Al showing graphene networks can be tuned in a controlled manner.

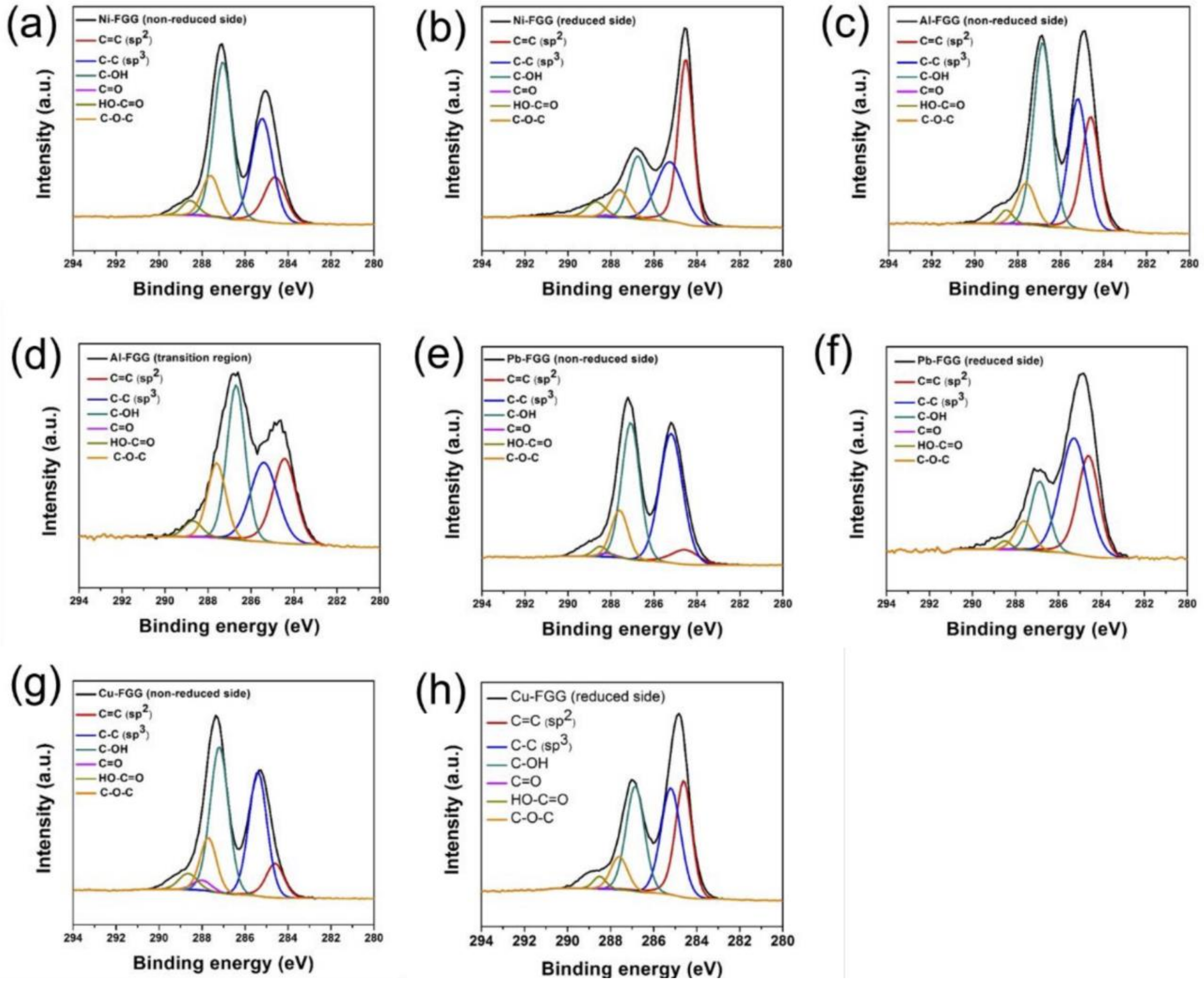

Figure 5-13: C1s spectra of (a) non-reduced side and (b) reduced side of Ni-FGG film, (c) non-reduced side and (d) transition region of Al-FGG film, (e) non-reduced side and (f) reduced side of Pb-FGG film, and (g) non-reduced side and (h) reduced side of Cu-FGG film.

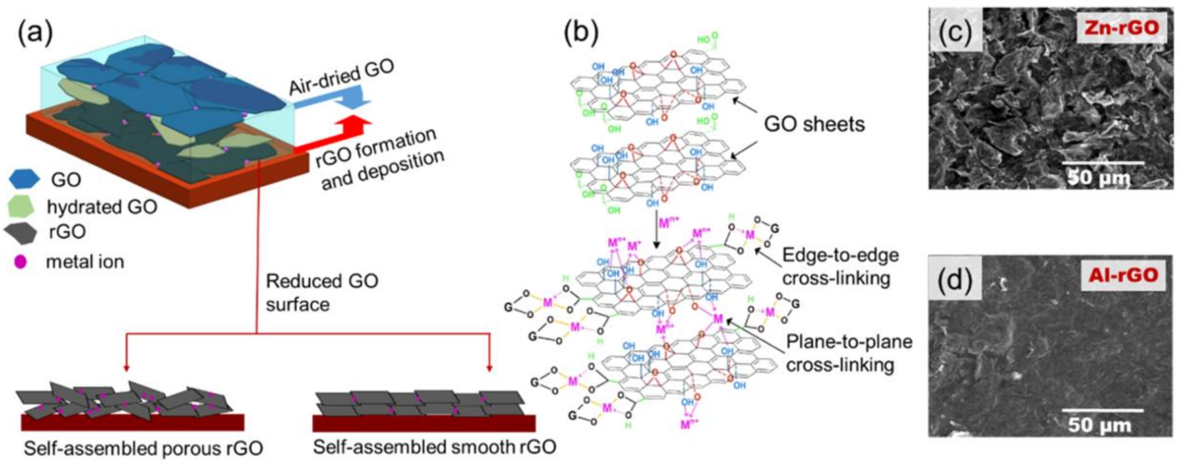

Figure 5-14: Schematic illustrations of (a) reduction and (b) metal-ion cross-linking in FGG films. SEM images of the reduced side of FGG films developed on (c) Zn and (d) Al substrates.

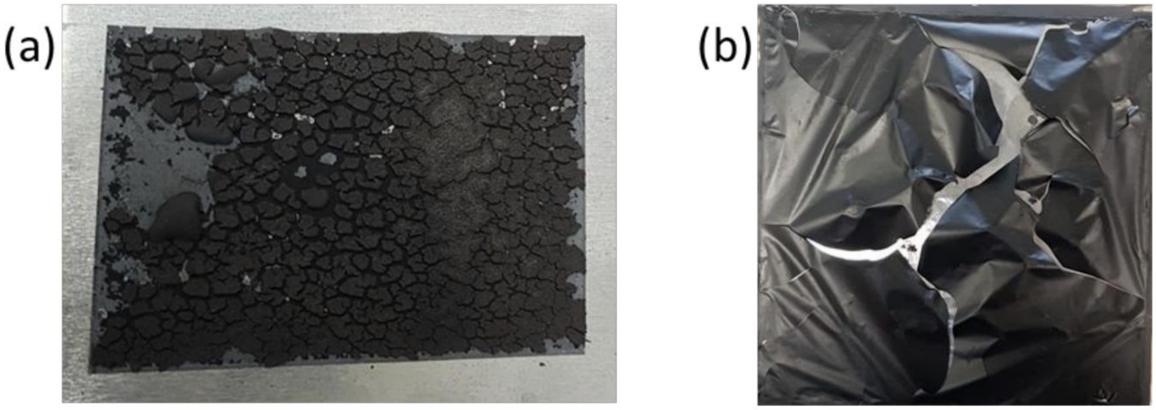

Figure 5-15: (a) Indiscriminately reduced Zn-FGG film under high RH (95%) yielding coagulated flakes of RGO that are loosely packed on the surface of metal. (b) Formation of differential layer strains upon drying in the Al-FGG film resulting in a ruptured surface at a low RH (<30%).

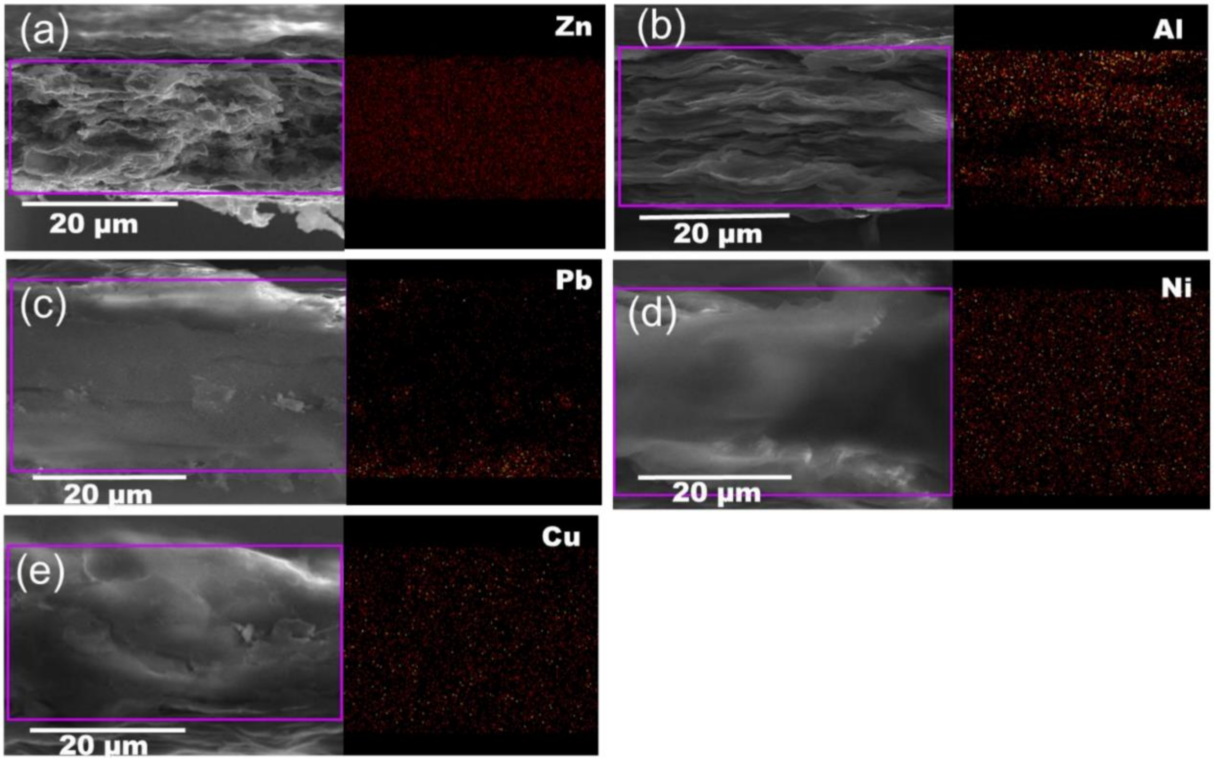

Figure 5-16: The elemental mapping of FGG films reduced on (a) Zn, (b) Al, (c) Pb, (d) Ni, and (e) Cu. The metal elements were distributed uniformly throughout the films.

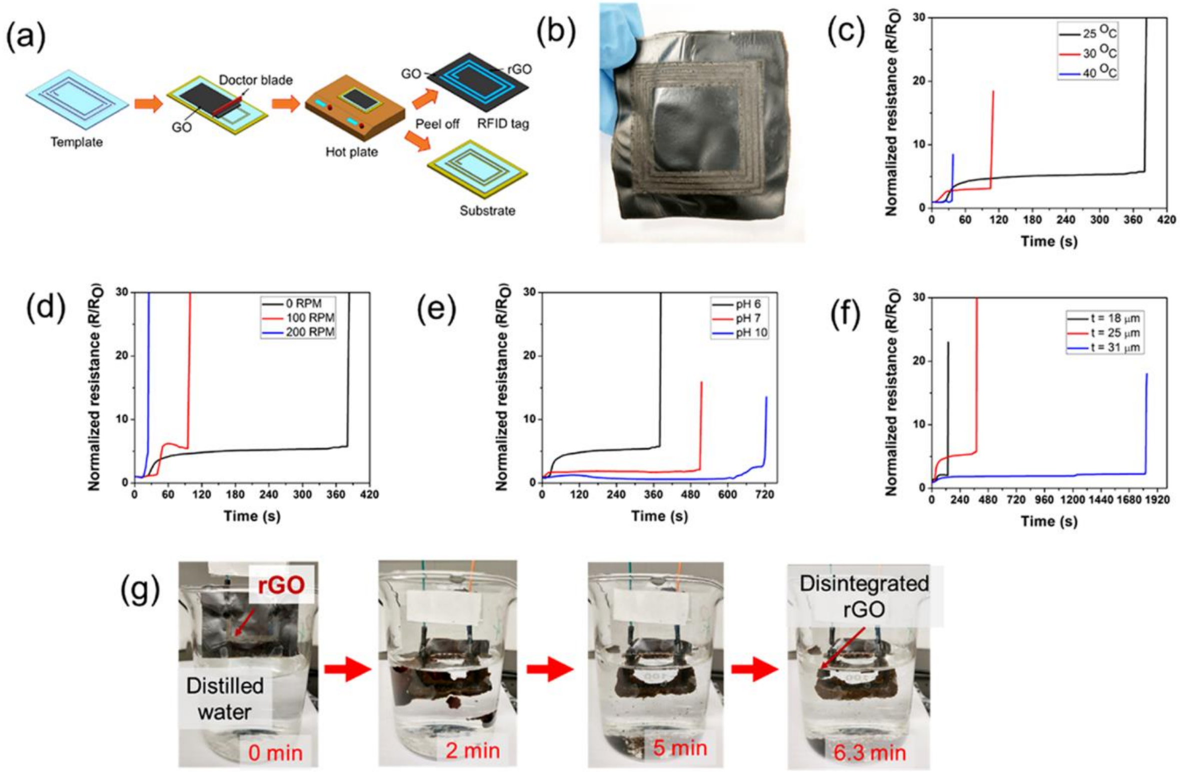

Figure 5-17: (a) Schematic drawing of selectively reduced GO for an RFID tag antenna; (b) photograph showing an all-graphene-based RFID tagantenna developed on Al; (c) changes in normalized ohmic resistance of U-shaped rGO recorded as a function of time during swelling in distilled water for different (c) temperatures, (d) agitation rates, (e) pH, and (f) thicknesses of the films; and (g) photographs at different stages of the disintegration process of the U-shaped rGO imprinted on GO films.

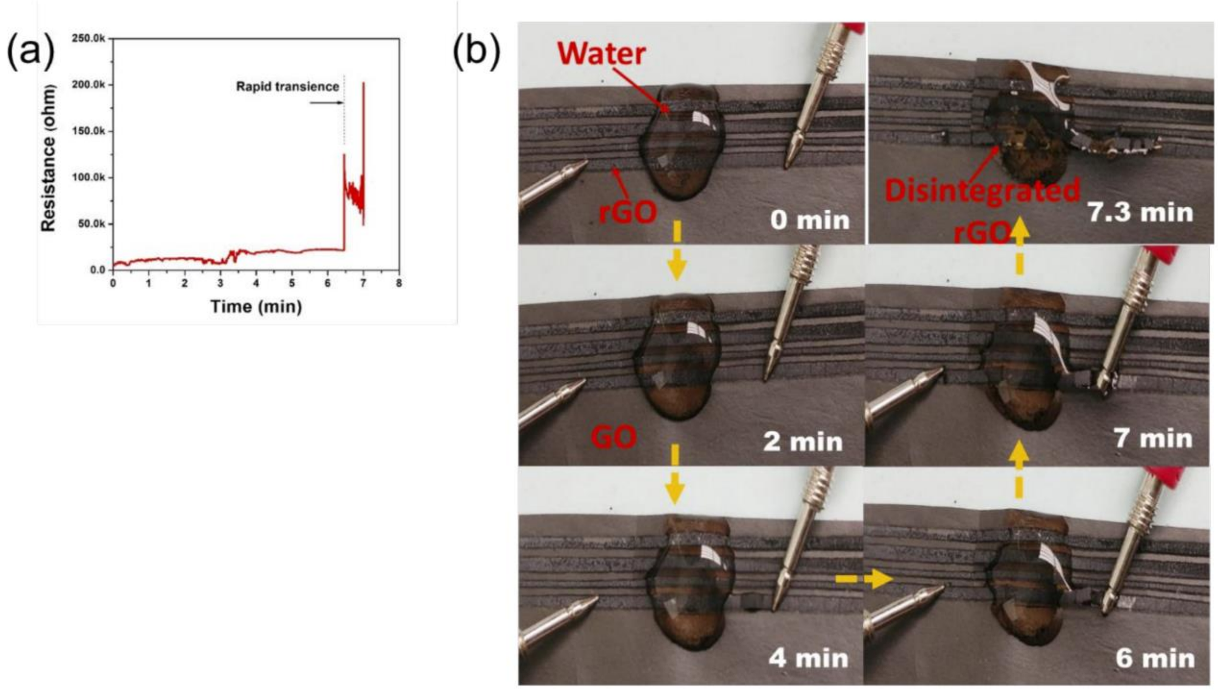

Figure 5-18: (a) The ohmic resistance values during swelling of distilled water at room temperature; (b) photographs at different stages of disintegration process of electrically conductive RFID antenna.

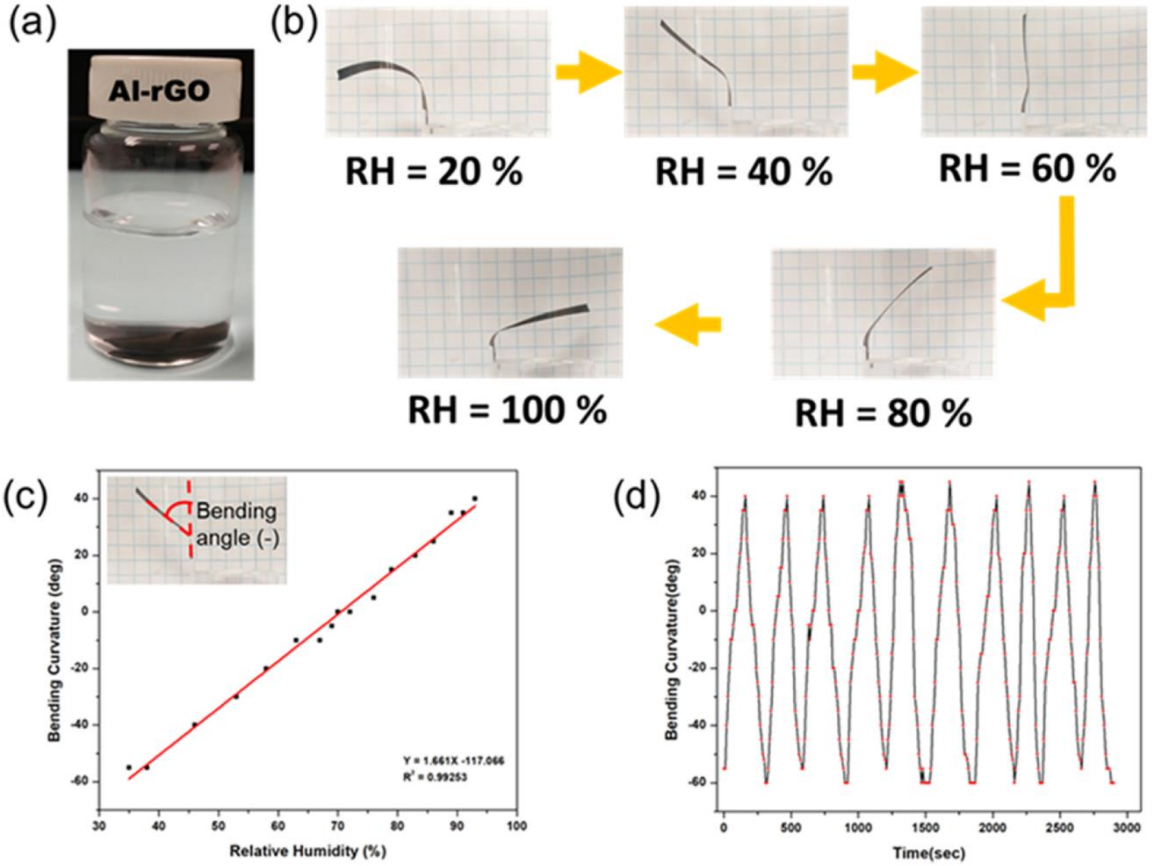

Figure 5-19: Curling behavior of a bilayer-like arrangement of the GO and rGO structures in the Al−FGG films during (a) immersion in distilled water and (b) under different humidity conditions. (c) Bending curvature of an FGG actuator as a function of RH and (d) for multiple cyclic change in humidity levels (RH = 30−95%).

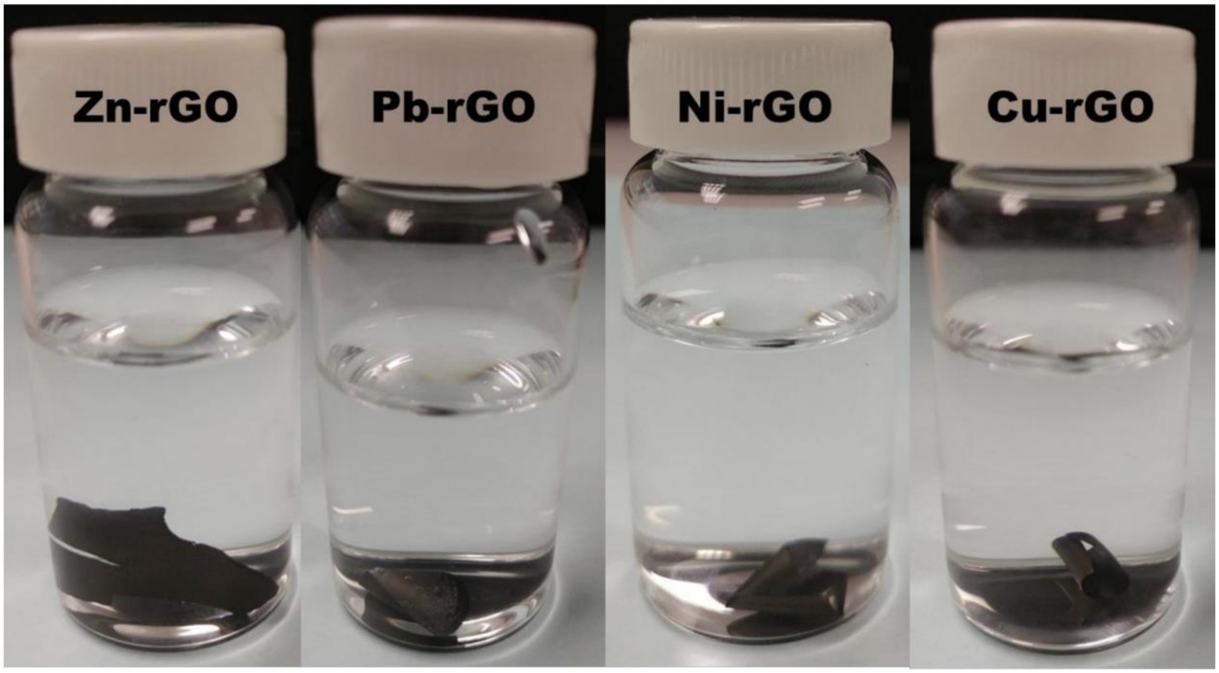

Figure 5-20: The curling behavior of bilayer-like arrangement of the GO and rGO structures in the FGG films during immersion in distilled water.

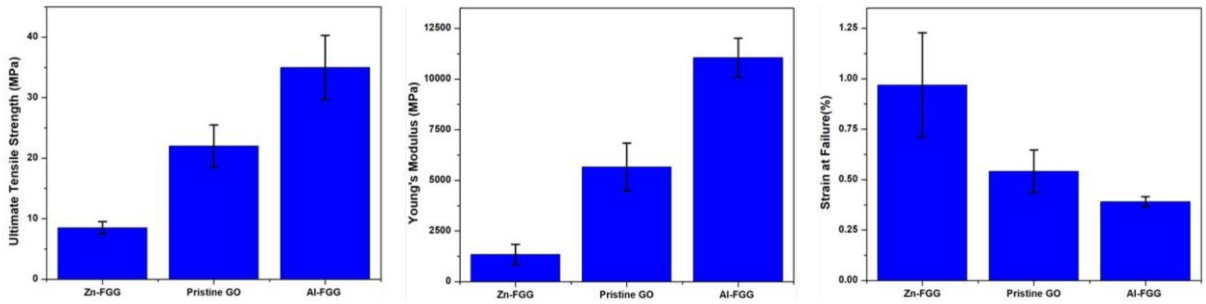

Figure 5-21: Mechanical Properties of Pristine GO films and functionally graded films coated on Aluminum and Zinc substrate.

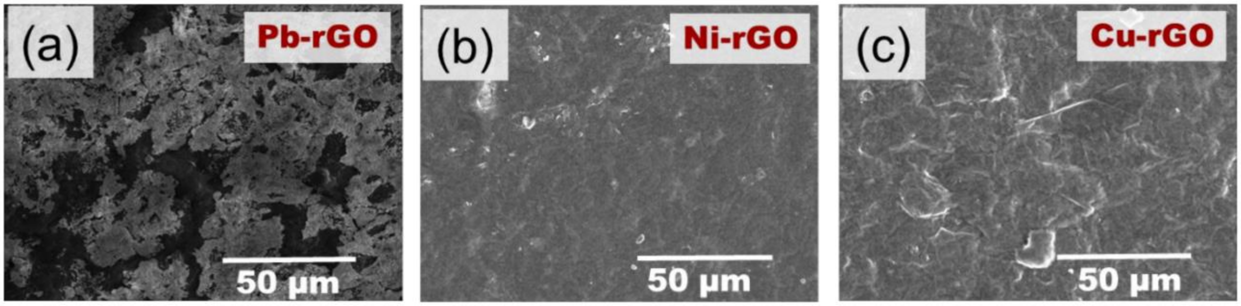

Figure 5-22: SEM images of reduced side of FGG film developed on (a) Pb, (b) Ni, and (c) Cu substrates.

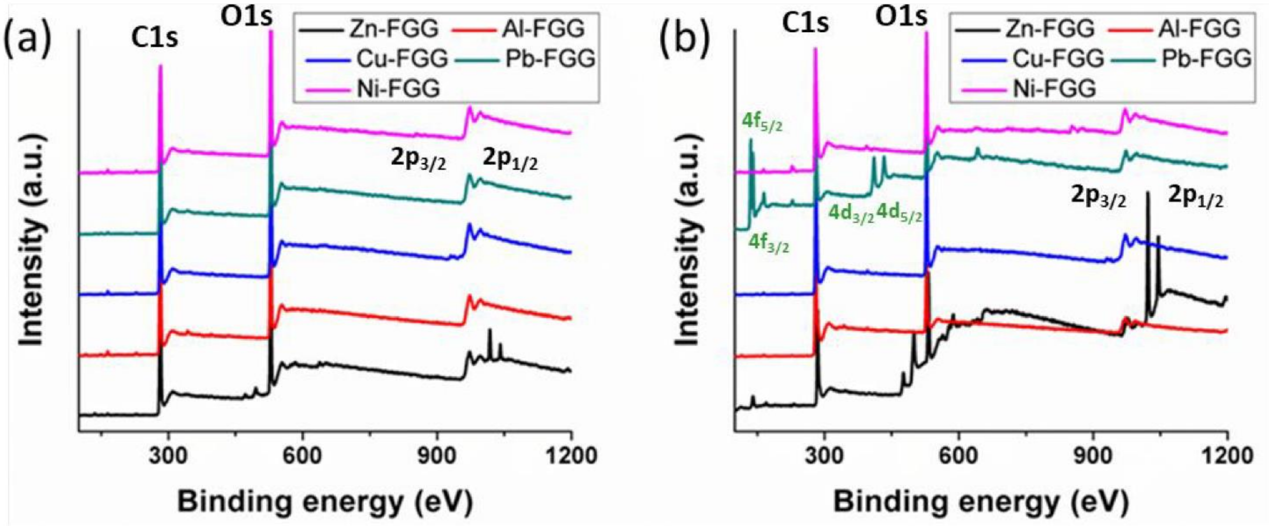

Figure 5-23. Comparison between XPS spectra on the (a) non-reduced side and (b) reduced side of the FGG films showing presence of metal-ion intercalation post-reduction.

References

(1) Kieback, B.; Neubrand, A.; Riedel, H. Processing techniques for functionally graded materials. *Mater. Sci. Eng., A* 2003, *362*, 81−106.

(2) Miyamoto, Y.; Kaysser, W.; Rabin, B.; Kawasaki, A.; Ford, R. G. *Functionally Graded Materials: Design, Processing and Applications*; Springer Science & Business Media, 2013; Vol. *5*.

(3) Gupta, A.; Talha, M. Recent development in modeling and analysis of functionally graded materials and structures. *Prog. Aerosp. Sci.* 2015, *79*, 1−14.

(4) Wegst, U. G.; Bai, H.; Saiz, E.; Tomsia, A. P.; Ritchie, R. O. Bioinspired structural materials. *Nat. Mater.* 2015, *14*, No. 23.

(5) Bartlett, N. W.; Tolley, M. T.; Overvelde, J. T. B.; Weaver, J. C.; Mosadegh, B.; Bertoldi, K.; Whitesides, G. M.; Wood, R. J. A 3D- printed, functionally graded soft robot powered by combustion. *Science* 2015, *349*, 161.

(6) Hu, S.; Gagnoud, A.; Fautrelle, Y.; Moreau, R.; Li, X. Fabrication of aluminum alloy functionally graded material using directional solidification under an axial static magnetic field. *Sci. Rep.* 2018, *8*, No. 7945.

(7) Stankovich, S.; Dikin, D. A.; Dommett, G. H.; Kohlhaas, K. M.; Zimney, E. J.; Stach, E. A.; Piner, R. D.; Nguyen, S. T.; Ruoff, R. S. Graphene-based composite materials. *Nature* 2006, *442*, 282−286.

(8) Balandin, A. A.; Ghosh, S.; Bao, W.; Calizo, I.; Teweldebrhan, D.; Miao, F.; Lau, C. N. Superior thermal conductivity of single-layer graphene. *Nano Lett.* 2008, *8*, 902−907.

(9) Lee, C.; Wei, X.; Kysar, J. W.; Hone, J. Measurement of the elastic properties and intrinsic strength of monolayer graphene. *Science* 2008, *321*, 385−388.

(10) Novoselov, K. S.; Geim, A. K.; Morozov, S. V.; Jiang, D.; Zhang, Y.; Dubonos, S. V.; Grigorieva, I. V.; Firsov, A. A. Electric field effect in atomically thin carbon films. *Science* 2004, *306*, 666−669.

(11) Shao, Y.; El-Kady, M. F.; Wang, L. J.; Zhang, Q.; Li, Y.; Wang, H.; Mousavi, M. F.; Kaner, R. B. Graphene-based materials for flexible supercapacitors. *Chem. Soc. Rev.* 2015, *44*, 3639−3665.

(12) Xu, Y.; Lin, Z.; Zhong, X.; Huang, X.; Weiss, N. O.; Huang, Y.; Duan, X. Holey graphene frameworks for highly efficient capacitive energy storage. *Nat. Commun.* 2014, *5*, No. 4554.

(13) Shao, Y.; Wang, J.; Wu, H.; Liu, J.; Aksay, I. A.; Lin, Y. Graphene based electrochemical sensors and biosensors: a review. *Electroanalysis* 2010, *22*, 1027−1036.

(14) Avouris, P. Graphene: electronic and photonic properties and devices. Nano Lett. 2010, 10, 4285−4294.

(1) He, Q.; Wu, S.; Yin, Z.; Zhang, H. Graphene-based electronic sensors. Chem. Sci. 2012, 3, 1764−1772.

(2) Stankovich, S.; Dikin, D. A.; Piner, R. D.; Kohlhaas, K. A.; Kleinhammes, A.; Jia, Y.; Wu, Y.; Nguyen, S. T.; Ruoff, R. S. Synthesis of graphene-based nanosheets via chemical reduction of exfoliated graphite oxide. Carbon 2007, 45, 1558−1565.

(3) Cao, X.; Qi, D.; Yin, S.; Bu, J.; Li, F.; Goh, C. F.; Zhang, S.; Chen, X. Ambient fabrication of large-area graphene films via a synchronous reduction and assembly strategy. Adv. Mater. 2013, 25, 2957−2962.

(4) Zhou, K. G.; Vasu, K. S.; Cherian, C. T.; Neek-Amal, M.; Zhang, J. C.; Ghorbanfekr-Kalashami, H.; Huang, K.; Marshall, O. P.; Kravets, V. G.; Abraham, J.; Su, Y.; Grigorenko, A. N.; Pratt, A.; Geim, A. K.; Peeters, F. M.; Novoselov, K. S.; Nair, R. R.

Electrically controlled water permeation through graphene oxide membranes. Nature 2018, 559, 236−240.

(5) Borini, S.; White, R.; Wei, D.; Astley, M.; Haque, S.; Spigone, E.; Harris, N.; Kivioja, J.; Ryhańen, T. Ultrafast Graphene Oxide Humidity Sensors. ACS Nano 2013, 7, 11166−11173.

(6) Ji, M.; Jiang, N.; Chang, J.; Sun, J. Near-Infrared Light-Driven, Highly Efficient Bilayer Actuators Based on Polydopamine-Modified Reduced Graphene Oxide. Adv. Funct. Mater. 2014, 24, 5412−5419.

(7) Chua, C. K.; Pumera, M. Chemical reduction of graphene oxide: a synthetic chemistry viewpoint. Chem. Soc. Rev. 2014, 43, 291−312.

(8) Zhu, Y.; Stoller, M. D.; Cai, W.; Velamakanni, A.; Piner, R. D.; Chen, D.; Ruoff, R. S. Exfoliation of graphite oxide in propylene carbonate and thermal reduction of the resulting graphene oxide platelets. ACS Nano 2010, 4, 1227−1233.

(9) Xu, Y.; Sheng, K.; Li, C.; Shi, G. Self-assembled graphene hydrogel via a one-step hydrothermal process. ACS Nano 2010, 4, 4324−4330.

(10) Mukherjee, R.; Thomas, A. V.; Krishnamurthy, A.; Koratkar, N.Photothermally reduced graphene as high-power anodes for lithium- ion batteries. ACS Nano 2012, 6, 7867−7878.

(11) Shao, Y.; Wang, J.; Engelhard, M.; Wang, C.; Lin, Y. Facile and controllable electrochemical reduction of graphene oxide and its applications. J. Mater. Chem. 2010, 20, 743−748.

(12) (26) Morant-Miñana Maria, C.; Heidler, J.; Glasser, G.; Lu, H.; Berger, R.; Gil-Gonzalez, N.; Müllen, K.; de Leeuw, D. M.; Asadi, K. Spatially resolved solid-state reduction of graphene oxide thin films. Mater. Horiz. 2018, 5, 1176−1184.

(13) Dikin, D. A.; Stankovich, S.; Zimney, E. J.; Piner, R. D.; Dommett, G. H.; Evmenenko, G.; Nguyen, S. T.; Ruoff, R. S. Preparation and characterization of graphene oxide paper. Nature 2007, 448, 457.

(14) Shao, J. J.; Lv, W.; Yang, Q. H. Self-assembly of graphene oxide at interfaces. Adv. Mater. 2014, 26, 5586−5612.

(15) Yuan, Z.; Xiao, X.; Li, J.; Zhao, Z.; Yu, D.; Li, Q. Self-Assembled Graphene-Based Architectures and Their Applications. Adv. Sc. 2017, 5, No. 1700626.

(16) Chen, Z.; Ren, W.; Gao, L.; Liu, B.; Pei, S.; Cheng, H.-M. Three-dimensional flexible and conductive interconnected graphene networks grown by chemical vapour deposition. Nat. Mater. 2011, 10, 424.

(17) Maiti, U. N.; Lim, J.; Lee, K. E.; Lee, W. J.; Kim, S. O. Three- dimensional shape engineered, interfacial gelation of reduced graphene oxide for high rate, large capacity supercapacitors. Adv. Mater. 2014, 26, 615−619 505 .

(18) Han, S. T.; Zhou, Y.; Wang, C.; He, L.; Zhang, W.; Roy, V. Layer-by-layer-assembled reduced graphene oxide/gold nanoparticle hybrid double-floating-gate structure for low-voltage flexible flash memory. Adv. Mater. 2013, 25, 872−877.

(19) Cote, L. J.; Kim, F.; Huang, J. Langmuir Blodgett assembly of graphite oxide single layers. J. Am. Chem. Soc. 2009, 131, 1043−1049.

(20) Huang, S.-Y.; Zhao, B.; Zhang, K.; Yuen, M. M.; Xu, J.-B.; Fu, X.-Z.; Sun, R.; Wong, C.-P. Enhanced reduction of graphene oxide on recyclable Cu foils to fabricate graphene films with superior thermal conductivity. *Sci. Rep.* 2015, *5*, No. 14260.

(21) Chen, P. Y.; Liu, M.; Valentin, T. M.; Wang, Z.; Spitz Steinberg, R.; Sodhi, J.; Wong, I. Y.; Hurt, R. H. Hierarchical Metal Oxide Topographies Replicated from Highly Textured Graphene Oxide by Intercalation Templating. *ACS Nano* 2016, *10*, 10869−10879.

(22) Fan, Z.; Wang, K.; Wei, T.; Yan, J.; Song, L.; Shao, B. An environmentally friendly and efficient route for the reduction of graphene oxide by aluminum powder. *Carbon* 2010, *48*, 1686−1689.

(23) Liu, Q.; He, M.; Xu, X.; Zhang, L.; Yu, J. Self-assembly of graphene oxide on the surface of aluminum foil. *New J. Chem.* 2013, *37*, 181−187.

(24) Huang, S. Y.; Zhao, B.; Zhang, K.; Yuen, M. M.; Xu, J. B.; Fu, X. Z.; Sun, R.; Wong, C. P. Enhanced Reduction of Graphene Oxide on Recyclable Cu Foils to Fabricate Graphene Films with Superior Thermal Conductivity. *Sci. Rep.* 2015, *5*, No. 14260.

(25) Hu, C.; Zhai, X.; Liu, L.; Zhao, Y.; Jiang, L.; Qu, L. Spontaneous reduction and assembly of graphene oxide into three- dimensional graphene network on arbitrary conductive substrates. *Sci. Rep.* 2013, *3*, No. 2065.

(26) Liu, Y.-Q.; Ma, J.-N.; Liu, Y.; Han, D.-D.; Jiang, H.-B.; Mao, J.- W.; Han, C.-H.; Jiao, Z.-Z.; Zhang, Y.-L. Facile fabrication of moisture responsive graphene actuators by moderate flash reduction of graphene oxides films. *Opt. Mater. Express* 2017, *7*, 2617−2625.

(27) Marcano, D. C.; Kosynkin, D. V.; Berlin, J. M.; Sinitskii, A.; Sun, Z.; Slesarev, A.; Alemany, L. B.; Lu, W.; Tour, J. M. Improved Synthesis of Graphene Oxide. *ACS Nano* 2010, *4*, 4806−4814.

(28) Hummers William, S., Jr.; Offeman, R. E. Preparation of graphitic oxide. *J. Am. Chem. Soc.* 1958, *80*, 1339.

(29) Wang, M.; Duong, L. D.; Oh, J.-S.; Mai, N. T.; Kim, S.; Hong, S.; Hwang, T.; Lee, Y.; Nam, J.-D. Large-area, conductive and flexible reduced graphene oxide (RGO) membrane fabricated by electro- phoretic deposition (EPD). *ACS Appl. Mater. Interfaces* 2014, *6*, 1747−1753.

(30) Wu, Z.-K.; Lin, Z.; Li, L.; Song, B.; Moon, K.-s.; Bai, S.-L.; Wong, C.-P. Flexible micro-supercapacitor based on in-situ assembled graphene on metal template at room temperature. *Nano Energy* 2014, *10*, 222−228.

(31) Ferrari, A. C.; Meyer, J.; Scardaci, V.; Casiraghi, C.; Lazzeri, M.; Mauri, F.; Piscanec, S.; Jiang, D.; Novoselov, K.; Roth, S.; Geim, A. K. Raman spectrum of graphene and graphene layers. *Phys. Rev. Lett.* 2006, *97*, No. 187401.

(32) Bo, Z.; Shuai, X.; Mao, S.; Yang, H.; Qian, J.; Chen, J.; Yan, J.; Cen, K. Green preparation of reduced graphene oxide for sensing and energy storage applications. *Sci. Rep.* 2014, *4*, No. 4684.

(33) Park, S.; Lee, K.-S.; Bozoklu, □G.; Cai, W.; Nguyen, S. T.; Ruoff, R. S. Graphene oxide papers modified by divalent ions enhancing mechanical properties via chemical cross-linking. *ACS Nano* 2008, *2*, 572−578.

(34) Turgut, H.; Tian, Z. R.; Yu, F.; Zhou, W. Multivalent Cation Cross-Linking Suppresses Highly Energetic Graphene Oxide’s Flammability. *J. Phys. Chem. C* 2017, *121*, 5829−5835.

(35) Acik, M.; Lee, G.; Mattevi, C.; Pirkle, A.; Wallace, R. M.; Chhowalla, M.; Cho, K.; Chabal, Y. The Role of Oxygen during Thermal Reduction of Graphene Oxide Studied by Infrared Absorption Spectroscopy. *J. Phys. Chem. C* 2011, *115*, 19761−19781.

(36) Mei, X.; Ouyang, J. Ultrasonication-assisted ultrafast reduction of graphene oxide by zinc powder at room temperature. *Carbon* 2011, *49*, 5389−5397.

(37) Dong, X.; Fu, D.; Fang, W.; Shi, Y.; Chen, P.; Li, L. J. Doping single-layer graphene with aromatic molecules. *Small* 2009, *5*, 1422− 1426.

(38) Ma, C.; Shu, Y.; Chen, H. Recycling lead from spent lead pastes using oxalate and sodium oxalate and preparation of novel lead oxide for lead-acid batteries. *RSC Adv.* 2015, *5*, 94895−94902.

(39) Dimiev, A. M.; Eigler, S. *Graphene Oxide: Fundamentals and Applications*, John Wiley & Sons, 2016.

(40) Naficy, S.; Jalili, R.; Aboutalebi, S. H.; Gorkin Iii, R. A.; Konstantinov, K.; Innis, P. C.; Spinks, G. M.; Poulin, P.; Wallace, G. G. Graphene oxide dispersions: tuning rheology to enable fabrication. *Mater. Horiz.* 2014, *1*, 326−331.

(41) Yin, L.; Cheng, H.; Mao, S.; Haasch, R.; Liu, Y.; Xie, X.; Hwang, S. W.; Jain, H.; Kang, S. K.; Su, Y.; et al. Dissolvable metals for transient electronics. *Adv. Funct. Mater.* 2014, *24*, 645−658.

(42) Hwang, S. W.; Song, J. K.; Huang, X.; Cheng, H.; Kang, S. K.; Kim, B. H.; Kim, J. H.; Yu, S.; Huang, Y.; Rogers, J. A. High- Performance Biodegradable/Transient Electronics on Biodegradable Polymers. *Adv. Mater.* 2014, *26*, 3905−3911.

(43) Lee, G.; Kang, S. K.; Won, S. M.; Gutruf, P.; Jeong, Y. R.; Koo, J.; Lee, S. S.; Rogers, J. A.; Ha, J. S. Fully Biodegradable Microsupercapacitor for Power Storage in Transient Electronics. *Adv. Energy Mater.* 2017, *7*, No. 1700157.

(44) Fu, K. K.; Wang, Z.; Dai, J.; Carter, M.; Hu, L. Transient electronics: materials and devices. *Chem. Mater.* 2016, *28*, 3527− 3539.

(45) Cheng, H.; Vepachedu, V. Recent development of transient electronics. *Theor. Appl. Mech. Lett.* 2016, *6*, 21−31.

(46) Reyssat, E.; Mahadevan, L. Hygromorphs: from pine cones to biomimetic bilayers. *J. R. Soc., Interface* 2009, *6*, 951−957.

(47) Holstov, A.; Bridgens, B.; Farmer, G. Hygromorphic materials for sustainable responsive architecture. *Constr. Build. Mater.* 2015, *98*, 570−582.

(48) Xu, G.; Zhang, M.; Zhou, Q.; Chen, H.; Gao, T.; Li, C.; Shi, G. A small graphene oxide sheet/polyvinylidene fluoride bilayer actuator with large and rapid responses to multiple stimuli. *Nanoscale* 2017, *9*, 17465−17470.

(49) Cheng, H.; Liu, J.; Zhao, Y.; Hu, C.; Zhang, Z.; Chen, N.; Jiang, L.; Qu, L. Graphene Fibers with Predetermined Deformation as Moisture-Triggered Actuators and Robots. *Angew. Chem., Int. Ed.* 2013, *52*, 10482−10486.